Research in Optoelectronics (A)

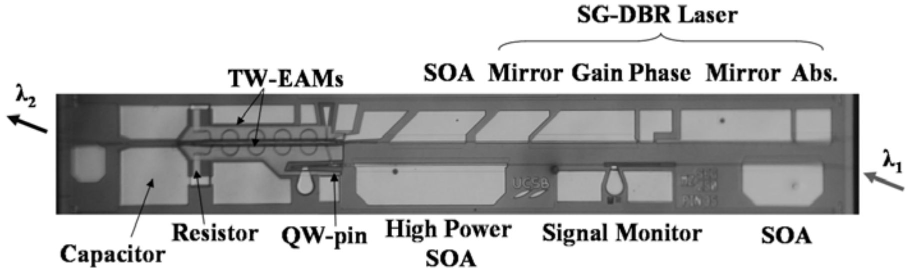

2008 Reprints of

Professor Larry A. Coldren

and Collaborators

ECE Technical Report 09-01
Department of Electrical & Computer Engineering
University of California, Santa Barbara

Research in Optoelectronics (A)

Reprints published in 2008

by

Professor Larry A. Coldren

and Collaborators

Published as

Technical Report # ECE 09-01

of

The Department of Electrical & Computer Engineering

The University of California

Santa Barbara, CA 93106

Phone: (805) 893-4486
Fax: (805) 893-4500
E-mail: coldren@ece.ucsb.edu
http://www.ece.ucsb.edu/Faculty/Coldren/home.htm

Introduction:

Welcome to the 2008 edition of the articles published by Professor Coldren's group at UC-Santa Barbara. Also included are articles by collaborators on which Prof. Coldren was a named co-author. As in recent years the work has a focus on III-V compound semiconductor materials for photonic devices—mostly diode lasers and photonic integrated circuits. The work spans efforts from basic materials and processing technology, through device physics and design, to device formation, characterization, and insertion into systems demonstrations.

The reprints have been grouped into three areas: **I. Photonic IC Technology & Devices; II. Vertical-Cavity Surface-Emitting Lasers; and III. Cavity QED and Single-Photon Emitters.** The majority of the work is in the first area, which has been further subdivided into *A. PIC Technology and Transmitters; B. Wavelength Converter and Packet Switching PICs; and C. RF-Photonics, Filters, and Analog PICs.* Each area contains materials research, device physics, device design and process development, device fabrication, and device characterization. In some cases devices are inserted into more advanced systems, so that their performance can be evaluated in a more rigorous environment. The epitaxial growth activity is strongly supported by Prof. DenBaars (MOCVD) and Prof. Gossard (MBE), who co-advise the students involved in these areas. Thus, their contributions have been invaluable to the research, even when they do not appear as co-authors on the device oriented papers.

The work was performed with funding from several grants from industry and government, some gifts funds from industry, and support from the Kavli Endowed Chair in Optoelectronics and Sensors. Specific projects included one on wavelength converters and photonic networks under the DARPA DoDN program (Prof. Blumenthal, PI); an analog receiver project sponsored by DARPA Phorfront (Prof. Bowers, PI); two projects to create very high-speed, high-efficiency optical sources for optical interconnects, one an STTR with Ziva Corp. and one an extension of the DARPA C2OI program, both to support our vertical-cavity surface-emitting laser work; and a new project on programmable optical filters supported by the DARPA-PhASER program.

The first group of reprints (*IA.*) summarizes our work on photonic IC technology and more specifically our efforts to make highly-functional and efficient widely-tunable transmitters using some of the integration platforms developed at UCSB over the past several years. This group consists of seven papers, including two journal papers and five conference papers. Of the conference papers, three were invited, and two of these were invited tutorials. In order to better summarize the content of these extensive tutorials, copies of the slides for the last one (ECOC '08) are included in this edition.

Figure 1 illustrates an integrated widely-tunable transmitter that incorporates a sampled-grating distributed-Bragg-reflector (SG-DBR) laser with a traveling-wave electro-absorption modulator (TW-EAM) on InP. It is representative of the work in Section *IA.* In this case, both the load resistor and the rf-bypass capacitor are also integrated on the PIC. The TW-EAM uses a meander-line velocity matching technique. Open eyes at 40

Gb/s for a variety of wavelengths indicate the success of this technique. This transmitter will be used in the all photonic wavelength converter (or transceiver) shown in Fig. 2. Fig. 1 demonstrates that any wavelength over a 40 nm wavelength band can be encoded with NRZ data up to 40 Gb/s. Such transmitters are desired in wavelength-division multiplexed (WDM) communication systems.

Figure 1. Widely-tunable transmitter incorporating a velocity-matched traveling wave EAM following an SGDBR laser. Open eye diagrams verify successful operation across a wide wavelength range.

Figure 2 illustrates a single-chip wavelength all-photonic wavelength converter in which an input signal of nearly arbitrary data rate and various intensity modulation formats over some wavelength range can be converted (and regenerated to some extent) to a desired output wavelength. This is representative of the work in Section *IB*. The transmitter stage is similar to that shown in Fig. 1; the receiver stage consists of a two-stage high-gain, high-saturation-power semiconductor-optical-amplifier (SOA) preceding a high-saturation current photodiode (PD). The photocurrent from the photodiode directly modulates the TW-EAM of the transmitter, so that no rf needs to be coupled on or off of the chip. A separate absorber is used for data monitoring if so desired. It was developed for use in all-optical networking experiments.

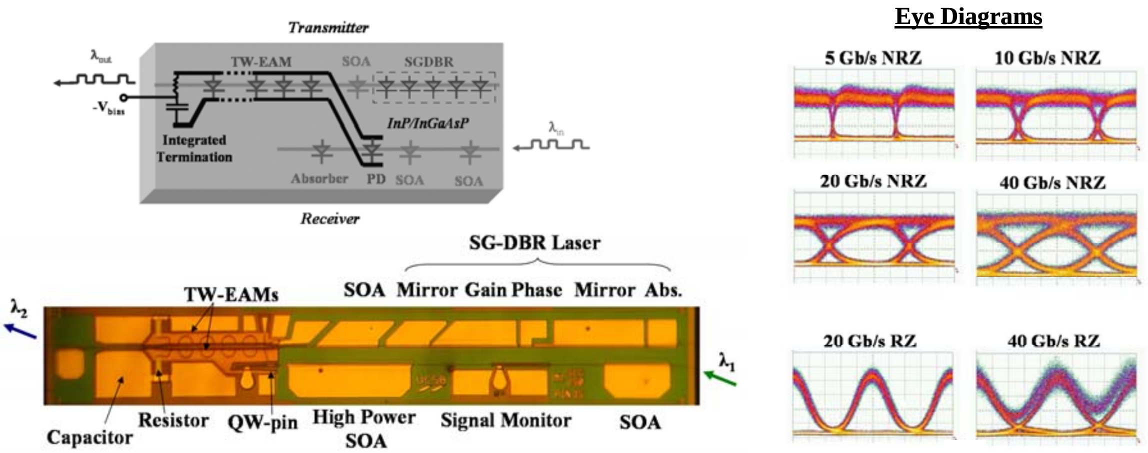

Figure 2. All-photonic widely-tunable data-format and data-rate transparent wavelength converter that integrates an SGDBR—TW-EAM transmitter with an SOA-PIN receiver. Schematic and photo of PIC shown on left; eye diagrams of data at various rates and formats shown at right.

Figure 3 is another example from Section *IB* that illustrates a different 40 Gb/s wavelength converter. In this case the transmitter section uses a Mach-Zehnder interferometer (MZI) instead of a TW-EAM. Such devices primarily use phase modulation instead of absorption modulation, and they can be design to manage chirp, so that transmission distances can be greatly extended. In fact, in this case the MZI uses a series-connected design for higher impedance, so that the photocurrent can generate a higher electric field for better efficiency.

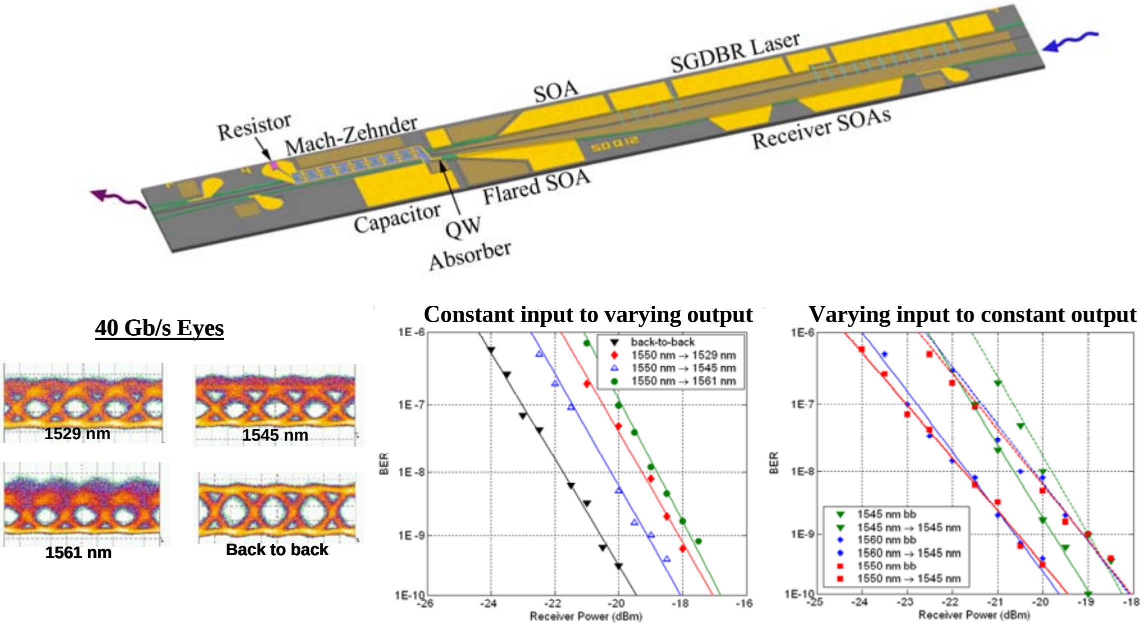

Figure 3. All-photonic widely-tunable wavelength converter that integrates an SGDBR—MZI transmitter with an SOA-PIN receiver. Operation to 40 Gb/s demonstrated across 32 nm.

Work in the RF-Photonics, Filters, and Analog PICs area (*IC*) has expanded into a number of new areas in 2008, although most of the publications remain from the work on integrated phase demodulators. These consist of a coherent optical receiver PIC that incorporates a pair of differentially-driven tracking modulators, a 3 dB coupler, and a differential detector pair together with an electronic IC that provides feedback from the detector pair to the modulator pair. Figures 4 & 5 summarize some of the recent work. Figure 4 gives the latest results with our 'uni-traveling-carrier' (UTC) high-saturation power photodetectors that must remain linear in this application to very high photocurrents, and Fig. 5 gives initial results from a more compact PIC that uses grating beam-splitters to shorten the feedback path. A short feedback path is necessary to limit loop delay and increase the stable bandwidth of the feedback loop. The feedback loop limits the magnitude of the detector output to avoid nonlinearities, even with phase modulation depths of many radians in the input signal. For good balance the coupler should have a 50 : 50 splitting ratio, so it is a key design parameter for Fig. 5. As shown in Fig. 4, 1 dB photodetector saturation currents > 70 mA, and an output third-order intercept point (OIP3) ~ 45 dBm was observed for one design at 60-70 mA, which indicates very good linearity and is a excellent result for such waveguide photodetectors.

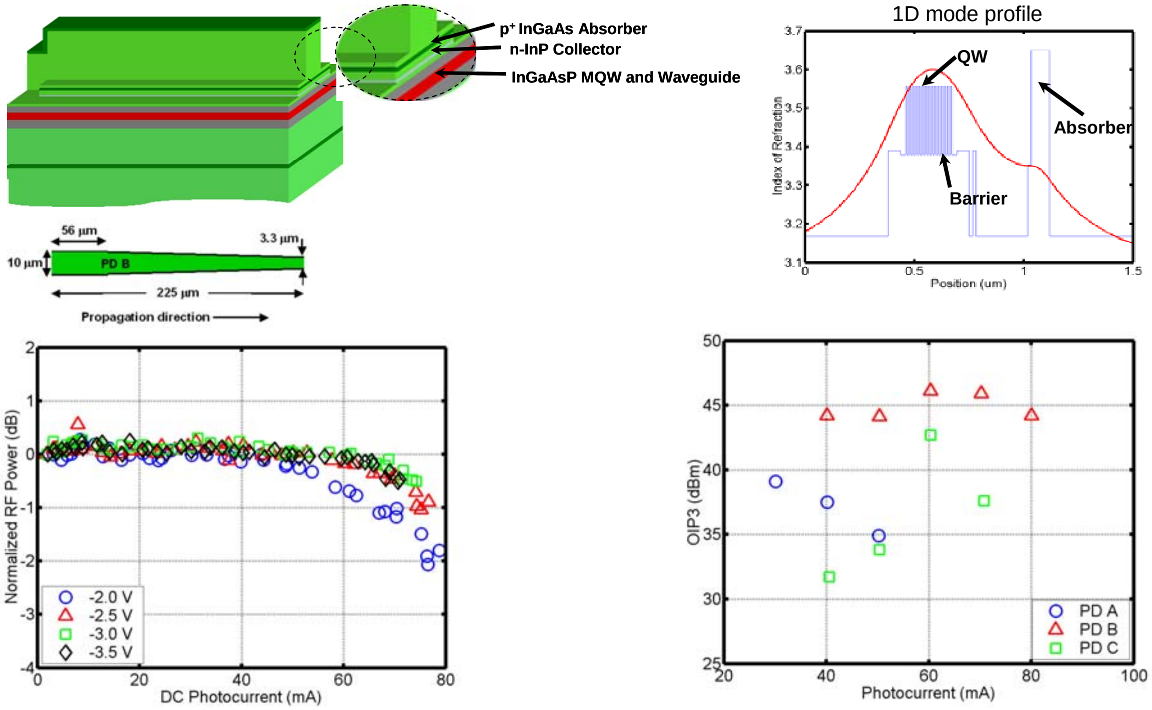

Figure 4. Waveguide UTC photodetector design (top) and results (bottom). Top schematic and transverse plot shows design of tapered off-set absorber, ridge waveguide UTC. Lower-left gives output power relative to linear vs. photocurrent current for several biases; lower-right gives the output 3rd order intercept point for three different designs.

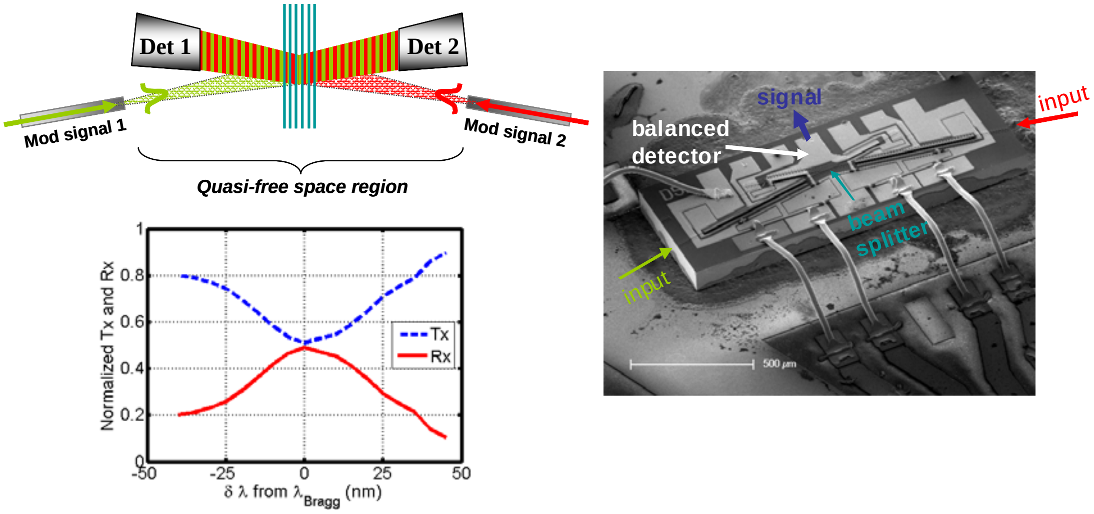

Figure 5. Phase demodulator PIC with a grating beam splitter to combine two input signals on a pair of detectors. SEM-photo illustrates wire-bonded chip; plot shows near 50 : 50 beam splitting ratio for 15 µm long grating.

Figure 6 gives a schematic and SEM cross section of the 980 nm VCSEL that has given record high-speed modulation efficiency results. This represents the work in Section **II**. As can be seen, lateral oxidation is used to simultaneously form 1) a tapered aperture of a desired shape to limit optical loss and minimize the optical mode volume as well as confine the current injection region, and 2) additional deep oxidation layers above the tapered current and photon confinement aperture to limit the parasitic capacitance without introducing unwanted series resistance. By reducing the modal volume without increasing the modal loss compared to our prior work with ultra-low-cavity-loss VCSELs, these devices demonstrated threshold currents of 0.115 mA and differential efficiencies of 65% at room temperature. The threshold approximately doubles and the differential efficiency drops by ~20% at 85 °C. The total power dissipation at room temperature is 10 mW for a bias current of 4.4 mA with an average output power of 2.7 mW. Error-free data transmission up to 35 Gb/s was demonstrated at this point. This corresponds to 286 pJ/bit of power dissipation/bit of data transmitted. The modulation voltage used in these experiments was 0.84 V peak-peak, and this drove a differential device load impedance of 200 Ω, which corresponds to an average switching energy of 50 pJ/bit, dividing by 2 for equal numbers of ones and zeros as a function of time. (Of course, if we use a 50 Ω load, we get four times this number.)

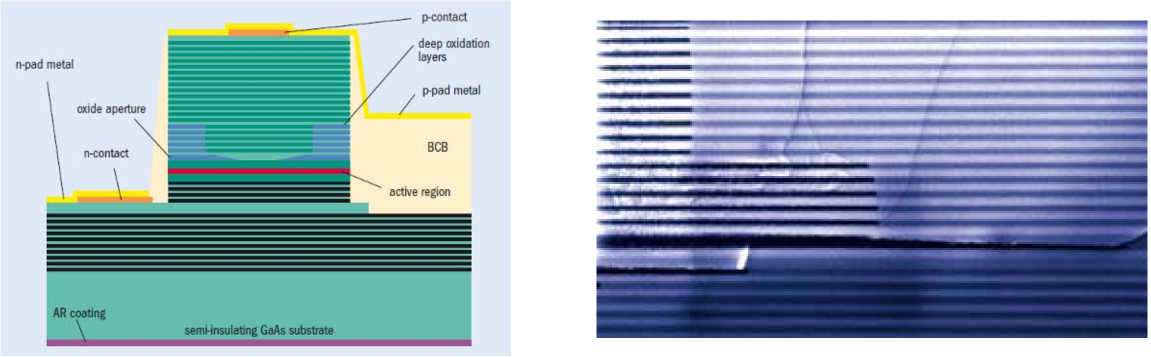

Figure 6. Schematic and SEM cross section of highly-efficient, high-modulation speed VCSEL.

The final group of papers on Cavity QED and Single-Photon Emitters is reported in Section **III.** It lists one paper that utilized GaAs-based MBE material and devices formed in our group. This work was led by other faculty members both at UCSB and elsewhere. Thus, we will not highlight it to a larger extent in this reprint collection. We continue to be receptive to outside collaborations that can use our expertise to some advantage.

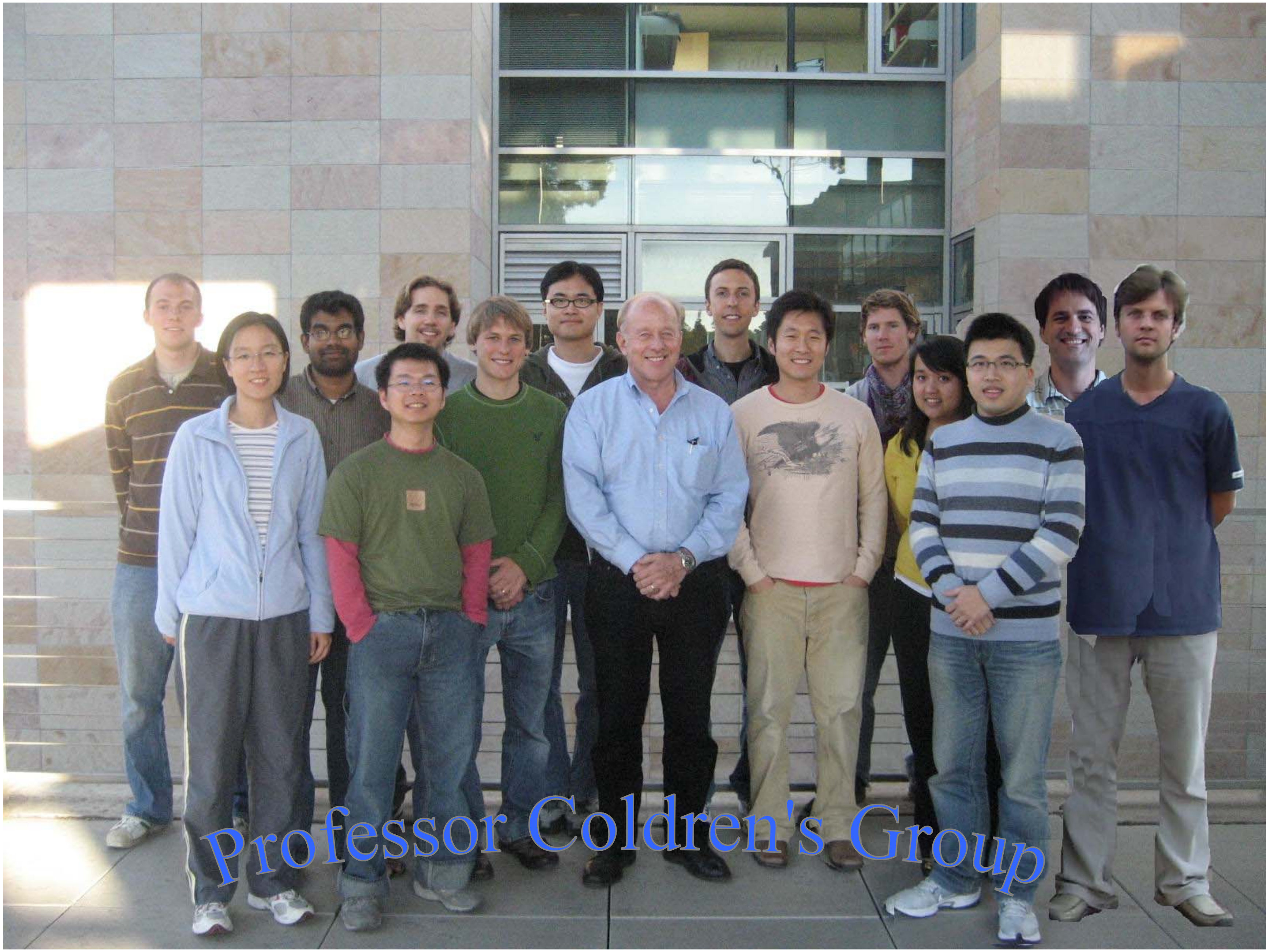

Back Row: Chad Althouse, Uppili Krishnamachari, Steve Nicholes, Chin-Han Lin, John Parker, Erik Norberg, Sasa Ristic
Front Row: Janet Chen, Joseph, Chang, Rob Guzzon, Larry Coldren, Yan Zheng, Jeannine Roson, Andy Hung, Leif Johansson
Not Pictured: Ashish Bhardwaj

Professor Coldren's Group

I. *Researchers*

A. Bhardwaj	Visiting Scientist, UCSB
L. Johansson	Associate Research Engineer, UCSB
S. Ristic	Post Doctoral Researcher, UCSB

II. *Students*

C. Althouse	M.S. Program
Y. Chang	Ph.D. Program
C. Chen	Ph.D. Program
M. Dummer	Ph.D. Program, now at Vixar Inc.
R. Guzzon	Ph.D. Program
J. Klamkin	Ph.D. Program, now at Lincoln Labs
U. Krishnamachari	Ph.D. Program
C. Lin	Ph.D. Program
S. Nicholes	Ph.D. Program
E. Norberg	Ph.D. Program
J. Parker	Ph.D. Program
J. Raring	Ph.D. Program, now at Sandia National Labs
N. Stoltz	Ph.D. Program, now at UCLA
A. Tauke-Pedretti	Ph.D. Program, now at Sandia National Labs
Y. Zheng	Ph.D. Program

III. *Staff*

D. Cohen	Principal Development Engineer, reports to Prof Nakamura
J. Roson	Center Assistant, OTC

Collaborators

I. *Faculty*

D. Blumenthal	UCSB
D. Bouwmeester	UCSB
J. Bowers	UCSB
S. DenBaars	UCSB
P. Petroff	UCSB
M. Rodwell	UCSB
J. Shynk	UCSB
S. Strauf	Stevens Institute of Technology

II. *Researchers*

Y. Akulova	JDSU
J. Barton	Post Doctoral Researcher, UCSB (Blumenthal)
Y. Choi	Post Doctoral Researcher, UCSB (Hu)
H. Chou	Post Doctoral Researcher, UCSB (Bowers), now at Luminent
C. Coldren	JDSU
R. John	IBM T.J. Watson Research Center
D. Kuchta	IBM T.J. Watson Research Center
M. Masanovic	Post Doctoral Researcher, UCSB (Blumenthal)
S. Nakagawa	IBM Tokyo Research Laboratory
H. Poulsen	Post Doctoral Researcher, UCSB (Blumenthal)
C. Schow	IBM T.J. Watson Research Center
M. Sysak	Post Doctoral Researcher UCSB (Bowers)
C. Wang	Ph.D. Program, now at Aerius Photonics, LLC
D. Zibar	Post Doctoral Researcher UCSB (Bowers), now at Com-DTU, Institute for Communication, Optics and Materials; Denmark

Collaborating Students

E. Burmeister	UCSB (Bowers)

B. Koch	UCSB (Bowers)
J. Mack	UCSB (Blumenthal)
N. Nunoya	UCSB (Bowers)
M. Rakher	UCSB (Bouwmeester)
A. Ramaswamy	UCSB (Bowers)
C. Sheldon	UCSB (Rodwell)
J. Summers	UCSB (Blumenthal)
Y. Wang	UCSB (Shynk)

Table of Contents:

I. Photonic IC Technology and Devices Page

IA. PIC Technology and Transmitters

L.A. Johansson, and L.A. Coldren, "Transmission of 10 Gbps Duobinary Signals Using an Integrated Laser-Mach Zehnder Modulator," *Proc. OFC/NFOEC*, OThC4, San Diego, CA (February 24-28, 2008)

M.M. Dummer, J. Klamkin, E.J. Norberg, J.W. Raring, A. Tauke-Pedretti, and L.A. Coldren, "Periodic Loading and Selective Undercut Etching for High-Impedance Traveling-Wave Electroabsorption Modulators," *Proc. OFC/NFOEC*, OThC6, San Diego, CA (February 24 – 28, 2008)

L.A. Coldren, "InP-Based Photonic Integrated Circuits," *Proc. CLEO/QELS*, CTuBB1, San Jose, CA (May 4-9, 2008) INVITED Tutorial

M.M. Dummer, J. Klamkin, J.P. Mack, and L.A. Coldren, "Widely Tunable 40 Gbps Transmitter Utilizing a High-Impedance Traveling-Wave EAM and SG-DBR Laser," *Proc. Integrated Photonics and Nanophotonics Research and Applications,* IMA2, (July 13-16, 2008) INVITED Paper

S.C Nicholes, J.W. Raring, E.J. Norberg, C.S. Wang, M.M. Dummer, S.P. DenBaars, and L.A. Coldren, "Highly Polarized Single-Chip ELED Sources Using Oppositely Strained MQW Emitters and Absorbers," *IEEE Photonics Technology Letters*, **20**, (14), pp. 1267-1269 (July 15, 2008)

M.M. Dummer, J. Klamkin, E.J. Norberg, A. Tauke-Pedretti, J.W. Raring, and L.A. Coldren, "Transmission Line Characterization of Undercut-Ridge Traveling-Wave Electroabsorption Modulators," *IEEE Photonics Technology Letters*, **20**, (15), pp. 1302-1304 (August 1, 2008)

Larry A. Coldren, "Multi-function Integrated InP-Based Photonic Circuits," *Proc. European Conference on Optical Communication*, Tu.1.A.2., Brussels, Belgium (September 21-25, 2008) INVITED Tutorial

M.M. Dummer, J.R. Raring, J. Klamkin, A. Tauke-Pedretti, and L.A. Coldren, "Selectively Undercut Traveling-Wave Electroabsorption Modulators Incorporating a p-InGaAs Contact Layer," *Optics Express*, **16**, (25), pp. 20388-20394 (December 8, 2008)

IB. Wavelength Converter and Packet Switching PICs

A. Tauke-Pedretti, M.M. Dummer, M.N. Sysak, J.S. Barton, J. Klamkin, J.W. Raring and L.A. Coldren, "Separate Absorption and Modulation Mach-Zender Wavelength Converter," *Journal of Lightwave Technology*, **26**, (1), pp. 91-98 (January-February 2008)

E.F. Burmeister, J.P. Mack, H.N. Poulsen, J. Klamkin, L.A. Coldren, D.J. Blumenthal, and J.E. Bowers, "SOA Gate Array Recirculating Buffer for Optical Packet Switching," *Proc. OFC/NFOEC*, OWE4, San Diego, CA (February 24-28, 2008)

M.M. Dummer, M.N. Sysak, A. Tauke-Pedretti, J.W. Raring, J. Klamkin, and L.A. Coldren, "Widely Tunable Separate Absorption and Modulation Wavelength Converter With Integrated Microwave Termination," *Journal of Lightwave Technology*, **26**, (8), pp. 938-944 (April 15, 2008

M.L. Masanovic, E.F. Burmeister, A. Tauke-Pedretti, B.R. Koch, M.M. Dummer, J.A. Summers, J.S. Barton, L.A. Coldren, J.E. Bowers, and D.J. Blumenthal, "Photonic Integrated Circuits for Optical Routing and Switching Applications," *Proc. Integrated Photonics and Nanophotonics Research and Applications*, IWC5, (July 13-16, 2008) INVITED Paper

J.S. Barton, M.L. Masanovic, M.M. Dummer, A. Tauke-Pedretti, E.F. Burmeister, B.R. Koch, J.A. Summers, L.A. Coldren, J.E. Bowers, and D.J. Blumenthal, "Recent Progress on LASOR Optical Router and Related Integrated Technologies," *Proc. International Conference on Photonics in Switching*, D-01-4, Sapporo, Japan (August 4-7, 2008) INVITED

M.M. Dummer, J. Klamkin, A. Tauke-Pedretti, and L.A. Coldren, "40 Gb/s Widely Tunable Wavelength Converter with a Photocurrent-Driven High-Impedance TW-EAM and SGDBR Laser," *Proc. IEEE International Semiconductor Laser Conference*, WB2, Sorrento, Italy (September 14-18, 2008)

M.M Dummer, J. Klamkin, A. Tauke-Pedretti, and L.A. Coldren, "A Bit-Rate-Transparent Monolithically Integrated Wavelenght Converter," *Proc. European Conference on Optical Communication*, Th.2.C.1., Brussels, Belgium (September 21-25, 2008) INVITED

IC. RF-Photonics, Filters and Analog PICs

A. Ramaswamy, L.A. Johansson, J. Klamkin, H.-F Chou, C. Sheldon, M.J. Rodwell, L.A. Coldren, and J.E. Bowers, "Integrated Coherent Receivers for High-Linearity Microwave Photonics Links," *Journal of Lightwave Technology*, **26**, (1), pp. 209-216 (January 1, 2008)

C.-H. Chen, J. Klamkin, L.A. Johansson, and L.A. Coldren, "Design and Implementation of Ultra-Compact Grating-Based 2x2 Beam Splitter for Miniature Photonic Integrated Circuits," *Proc. OFC/NFOEC*, OTuC5, San Diego, CA (February 24-28, 2008)

J. Klamkin, Y.-C. Chang, A. Ramaswamy, L.A. Johansson, J.E. Bowers, S.P. DenBaars, and L.A. Coldren, "Output Saturation and Linearity of Waveguide Unitraveling-Carrier Photodiodes," *Journal of Quantum Electronics*, **44**, (4), pp. 354-359 (April 2008)

L.A. Johansson, Y.A. Akulova, C. Coldren, and L.A. Coldren, "Improving the Performance of Sampled-Grating DBR Laser-Based Analog Optical Transmitters," *Journal of Lightwave Technology*, **26**, (7), pp. 807-815 (April 1, 2008)

A. Ramaswamy, L.A. Johansson, J. Klamkin, D. Zibar, L.A. Coldren, M.J. Rodwell, and J.E. Bowers, "Optical Phase Demodulation of a 10GHz RF Signal using Optical Sampling," *Proc. Coherent Optical Technologies and Applications Topical Meeting*, CTuC3, Boston, MA (July 13-16, 2008)

C.-H. Chen, A. Ramaswamy, J. Klamkin, L.A. Johansson, J.E. Bowers, and L.A. Coldren, "Optical Phase Demodulation using a Coherent Receiver with an Ultra-Compact Grating Beam Splitter," *Proc. Asia Optical Fiber Communication & Optoelectronic Conference*, SaN3, Shanghai, China (October 20 – November 2, 2008) Outstanding Student Presentation Award

Y. Wang, J.J. Shynk, and L.A. Coldren, "Filter Designs for a Reconfigurable Photonics Integrated Circuit," *Proc. Asilomar Conference on Signals, Systems, And Computers*, TP8b2-3, Pacific Grove, CA (October 26-29, 2008)

A. Ramaswamy, J. Klamkin, N. Nunoya, L.A. Johansson, L.A. Coldren, and J.E. Bowers, "Three-Tone Characterization of High-Linearity Waveguide Uni-Traveling-Carrier Photodiodes," *Proc. LEOS Annual Meeting*, TuR3, Newport Beach, CA (November 9-13, 2008)

II. Vertical-Cavity Surface-Emitting Lasers

S. Nakagawa, D. Kuchta, C. Schow, R. John, L.A. Coldren, and Y.-C. Chang, “1.5mW/Gbps Low Power Optical Interconnect Transmitter Exploiting High-Efficiency VCSEL and CMOS Driver,” *Proc. OFC/NFOEC*, OThS3, San Diego, CA (February 24-28, 2008)

L.A. Coldren and Y.-C. Chang, “Small Optical Sources with Improved Speed/Power Dissipation,” *Proc. HP Labs Photonics Interconnect Forum*, San Jose, CA (May 12, 2008)

Y-C Chang, and L. A. Coldren, “Ultrafast VCSELs promise to turbocharge chip communication,” *Compound Semiconductor*, **14** (5) pp29-31 (June, 2008) INVITED Paper

Y.-C. Chang and L.A. Coldren, “Optimization of VCSEL Structure for High-Speed Operation,” *Proc. IEEE International Semiconductor Laser Conference*, ThA1, Sorrento, Italy (September 14-18, 2008)

III. Cavity QED and Single-Photon Emitters

S. Strauf, M. T. Rakher, N.G. Stoltz, L.A. Coldren, P.M. Petroff, and D. Bouwmeester, “High Frequency Single Photon Sources,” *Proc. LEOS Annual Meeting*, WY1, Newport Beach, CA (November 9-13, 2008) INVITED

I. Photonic IC Technology and Devices

A. PIC Technology and Transmitters

Transmission of 10 Gbps Duobinary Signals Using an Integrated Laser-Mach Zehnder Modulator

L.A. Johansson and L.A. Coldren
Department of Electrical and Computer Engineering, University of California, Santa Barbara, CA 93106.
Email: leif@ece.ucsb.edu

P.C. Koh Y.A. Akulova and G.A. Fish
JDSU, 7404 Hollister Ave, Goleta, CA 93117

Abstract: Generation and transmission of 10 Gbps duobinary signals is demonstrated using an integrated widely-tunable SGDBR laser and Mach-Zehnder modulator over a wavelength range of 1538nm – 1564nm.

OCIS codes: (250.5300) Photonic Integrated Circuits; (060.2330) Fiber Optics Communications

1. Introduction

Duobinary modulation has the advantage of more compact modulated optical spectral width compared to standard NRZ modulation [1]. This provides improved dispersion tolerance and longer transmission distances over non-dispersion managed fiber. It also allows greater spectral efficiency, allowing closer spacing of optical channels, or reduced requirements for wavelength multiplexing components [2]. A second advantage is the possibility of using lower speed drive electronics to generate very high data rates, optical generation of up to 107 Gbps duobinary signals has been demonstrated [3]. Duobinary transmission using $LiNbO_3$ MZ modulators have been long demonstrated, allowing transmission of 10Gbps data over 200 km of standard singlemode fiber [4]. More recently, demonstrations using InP MZ modulators have been performed, demonstrating a similar performance with generally lower drive voltage [5,6].

In this paper, we demonstrate generation and transmission of 10 Gbps duobinary signals using an integrated widely-tunable SGDBR laser and Mach-Zehnder modulator over a wavelength range of 1538nm – 1564nm. This is the first demonstration of 200km reach with an integrated laser-Mach Zehnder (ILMZ). Previous work either did not use integrated devices [5,6] or it was performed using standard NRZ modulation with lower reach; 100km [7].

2. Device and Experiment

The device used in this work consists of a sampled-grating DBR laser integrated to an SOA and a dual-drive Mach-Zehnder modulator. All sections of the device are integrated onto one single Indium-Phosphide chip using an offset quantum-well structure to define sections with optical gain. The sampled-grating DBR laser can be tuned throughout the C-band and the integrated SOA provides power leveling over this wavelength range and compensates for cavity and modulator losses. The Mach-Zehnder modulator consist of two optical waveguide segments with RF electrodes situated in-between two multimode interference couplers. More details of this type of device can be found in [7] where transmission of negative-chirp 10 Gbps NRZ signals over 100km standard singlemode fiber was demonstrated.

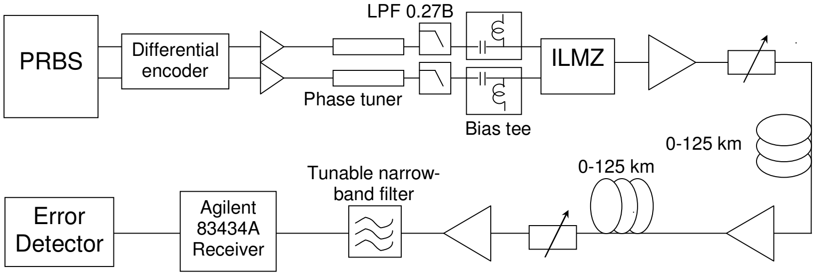

Fig. 1. Schematic of experimental arrangement used to generate and transmit 10 Gbps duobinary modulation using the integrated SGDBR laser – Mach-Zehnder modulator

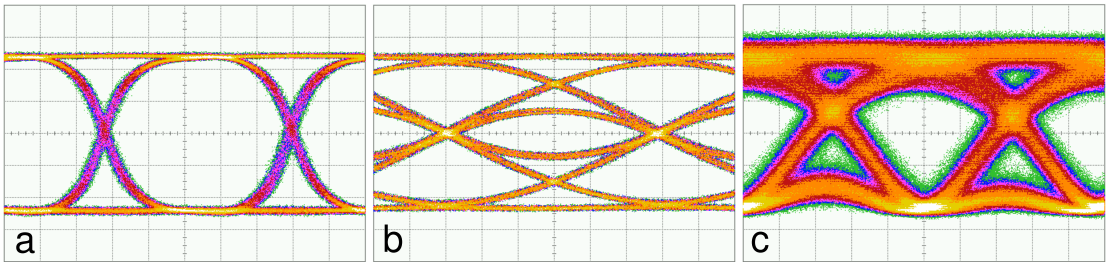

Fig. 2a: Eye diagram of output of PRBS. 2b: filtered electrical duobinary drive signal. 2c. Corresponding optical eye.

Figure 1 shows the experimental arrangement used to generate and transmit the 10 Gbps duobinary optical modulation. The two complementary outputs from a 10 Gbps pseudo-random bit sequencer (PRBS) were differentially encoded, amplified and synchronized. Figure 2a shows that output eye diagram of the PRBS. A 0.27B risetime filter (156ps risetime) was used to filter the NRZ eye diagram and to generate the duobinary drive signal shown in Fig. 2b. After push-pull drive of the InP modulator (2x3.6V) the optical eye is formed and shown in Fig. 2c. The optical signal was transmitted through up to 250km of standard singlemode fiber (200km Corning SMF-28, 50 km Lucent SMF). Booster, inline and receiver optical amplification were used where required.

3. Results

Figure 3 shows captured eye diagrams after transmission through 0km to 250 km of standard singlemode fiber at 1551nm wavelength. Open eye diagrams are obtained at 250km. At transmission distances above 200km, the required launch power was in the 10 dBm range which causes pulse compression and a corresponding shift in power penalty compared to purely dispersion limited performance.

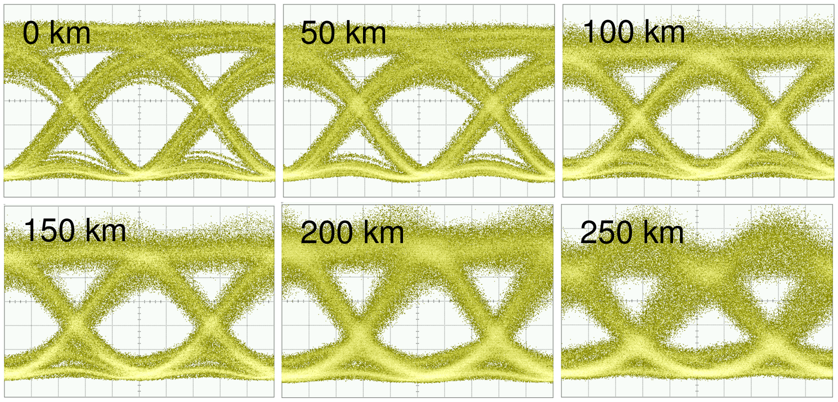

Fig. 3: Received optical eye diagrams at 1551nm after transmission through 0km, 50km, 100km, 150km, 200km and 250 km fiber, respectively.

Figure 4, left shows bit-error-rate performance for 0-250km transmission distance at 1551 nm wavelength using a 2^7-1 PRBS signal. Error-free transmission using long word-lengths (eg. 2^{31}-1) was not possible. The exact cause for this has not been established, but several factors can contribute, including electrical or optical crosstalk, thermal effects, or pattern dependence in the electronic drive circuitry. The receiver sensitivity varies over a ~2dB range with a small further degradation at 250km transmission. The lowest penalty was observed in the 100km-150km range. No error floor could be detected at any transmission distance.

The fiber transmission performance was also verified at the lower and higher end of the laser tuning range, 1538nm, and 1568nm respectively. The power penalty at a BER of 10^{-9} versus transmission distance for all three wavelengths is summarized in fig. 4, right. A similar trend in power penalty can be observed over all wavelengths with a mid-range optimum around 100-150km. Indications of better performance at longer wavelengths can be observed, both in the point of lowest power penalty and the transmission penalty at 250 km.

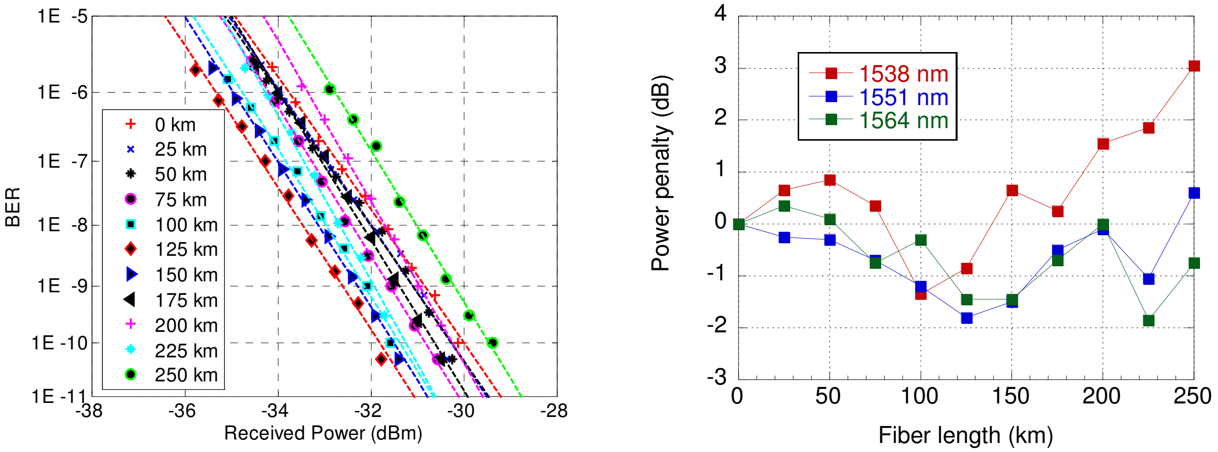

Fig. 4: Left: Detected error rates at the preamplifier optical receiver at 1551nm for different fiber transmission distances. Right: equivalent power penalty at a BER of 10^{-9} at 1538nm, 1551nm and 1564 nm optical wavelength.

4. Conclusion

We demonstrated generation and transmission of 10 Gbps duobinary signals using an integrated widely-tunable SGDBR laser and Mach-Zehnder modulator over a wavelength range of 1538nm – 1564nm. Transmission up to 250 km of standard singlemode fiber with low power penalty and no error floor was achieved. This is the first time an integrated laser-Mach Zehnder is used to transport 10 Gbps signals over 200km of standard singlemode fiber.

5. References

[1] X. Gu and L. C. Blank, “10 Gb/s unrepeatered three-level optical transmission over 100 km of standard fiber,” Electron. Lett., vol. 29, pp. 2209–2211, 1993.

[2] M. Duelk, J. Cripp, J. Simsarian, A. Bhardwaj, P. Bernasconi, M. Zirngibl, 0. Laznicka "Fast Packet Routing in a 2.5 Tb/s Optical Switch Fabric with 40 Gb/s Duobinary Signals at 0.8 b/s/Hz Spectral Efficiency," in Optical Fiber Communication Conference on CD-ROM (Optical Society of America, Washington, DC, 2003), PD8-1.

[3] P.J. Winzer, G. Raybon, M. Duelk, "107-Gb/s optical ETDM transmitter for 100G Ethernet transport," 31st European Conference on Optical Communication, 2005. Vol. 6, pp:1-2, 25-29 Sept. 2005.

[4] K. Yonenaga and S. Kuwano, "Dispersion-Tolerant Optical Transmission System Using Duobinary Transmitter and Binary Receiver," IEEE J. Lightwave Technol., vol. 15, no. 8, pp. 1530-1537, 1997.

[5] R. A. Griffin, A. Tipper and I. Betty, "Performance of MQW InP Mach-Zehnder Modulators for Advanced Modulation Formats," in Optical Fiber Communication Conference on CD-ROM (Optical Society of America, Washington, DC, OFC 2005), OTuL5.

[6] Takeshi Kurosaki, Yasuo Shibata, Nobuhiro Kikuchi, Ken Tsuzuki, Wataru Kobayashi, Hiroshi Yasaka, and Kazutoshi Kato, "200-km 10-Gbit/S Optical Duobinary Transmission Using An N-I-N Inp Mach-Zehnder Modulator," 2007 International Conference on Indium Phosphide and Related Materials, Matsue, Japan, 14-18 May, 2007, WeBI-3.

[7] Y. A. Akulova, G. A. Fish, P. Koh, P. Kozodoy, M. Larson, C. Schow, E. Hall, H. Marchaod, P. Abraham, L. A. Coldren, "10 Gb/s Mach-Zehnder modulator integrated with widely-tunable sampled grating DBR Laser," in Optical Fiber Communication Conference on CD-ROM (Optical Society of America, Washington, DC, 2003), TuE4.

Periodic Loading and Selective Undercut Etching for High-Impedance Traveling-Wave Electroabsorption Modulators

Matthew M. Dummer[1], Jonathan Klamkin[1], Erik J. Norberg[1], James W. Raring[2],
Anna Tauke-Pedretti[3], and Larry. A. Coldren[1]
[1]*Department of Electrical and Computer Engineering, University of California, Santa Barbara, CA 93106*
[2] *Sandia National Laboratories, Abuquerque, NM 87185 USA*
[3]*Air Force Research Laboratory, Kirtland AFB, Albuquerque, NM 87117*
dummer@ece.ucsb.edu

Abstract: For the first time, selective undercut etching and periodically loaded electrodes are combined to improve impedance and velocity matching for traveling-wave electroabsorption modulators. These devices are fabricated in a platform compatible with widely tunable lasers.

OCIS codes: (250.7360) Waveguide modulators. (230.7020) Traveling-wave devices

1. Introduction

Indium Phosphide based electroabsorption modulators (EAMs) offer a compact solution for efficient, high-speed modulation of optical signals. The utilization of traveling wave (TW) electrodes for EAMs has led to significantly increased bandwidths compared to traditional lumped-element type devices. However, one drawback of TW-EAMs is the low characteristic impedance of the transmission line compared with 50 Ω electrical drivers, due to the high capacitive loading of the p-n junction. This high capacitance also results in slow-wave mode propagation [1] of the electrical signal, which limits the maximum interaction length between the electrical and optical waves. Recently, several methods have been reported for reducing the capacitance per unit length of TW-EAMs including periodic transmission line loading [2], as well as selective undercutting of the active region [3]. For the first time, we have simultaneously utilized both of these techniques to develop high–impedance TW-EAMs which are compatible for integration with sampled-grating (SG) DBR lasers. These TW-EAMs exhibit twice the characteristic impedance compared with previous designs as well as significantly improved return loss and velocity matching. An average impedance of 40 Ω and open eye diagrams at 40 Gb/s with a 1.6 V drive are demonstrated.

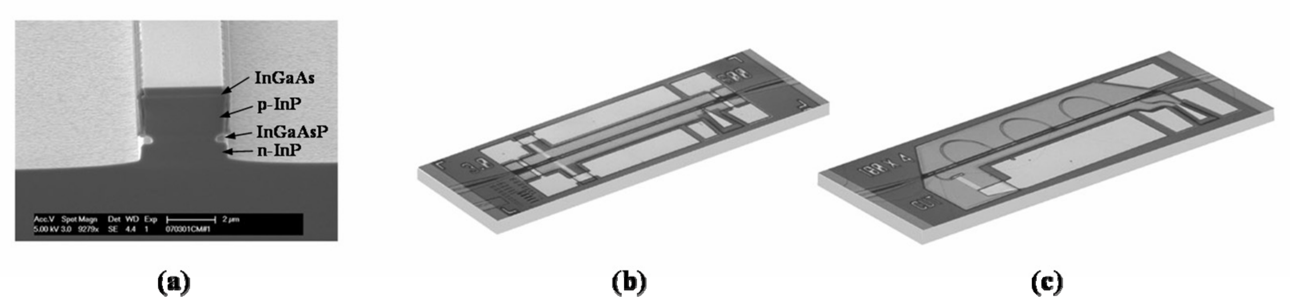

Fig. 1 (a) SEM cross section of undercut EAM structure. (b) Continuously loaded TW-EAM design with integrated termination. (c) Periodically loaded TW-EAM design with integrated termination.

2. Design and Fabrication

The TW-EAM material design was based on the dual quantum well (DQW) epitaxial layer structure for SG-DBR laser integration [4]. These modulators were designed as a proof of concept and, although no lasers have yet been integrated, the entire fabrication process is completely compatible with integrated transmitters. The devices were fabricated on a conducting substrate with a 350 nm InGaAsP waveguide layer, containing 10 quantum wells, between upper and lower InP cladding layers. The photoluminescence peak of the multi-quantum-well stack was 1465 nm. A cross section of the waveguide structure is shown in Fig. 1 (a). The deeply-etched ridge was fabricated first by a combination of dry and wet etching to stop at the quaternary layer. A sidewall mask of SiN was then formed on the upper cladding before dry etching the ridge through the waveguide and lower cladding layer. The waveguide was undercut using a selective wet etch of sulfuric acid and peroxide to reduce the quaternary width from

978-1-55752-855-1/08/$25.00 ©2008 IEEE

3.5 µm to 1.9 µm. The sidewall mask was essential to preserve the p^+-InGaAs contact layer during the selective wet etch. The modulator ridges were buried with a low-k dielectric, Benzocyclobutene, before metallization.

EAMs fabricated with continuously loaded and periodically loaded transmission lines are presented in Fig. 1 (b) and (c), respectively. These devices make use of an on-chip NiCr resistor followed by a DC-blocking capacitor to terminate the traveling wave electrode. The resistor was designed to match the impedance of the TW electrode to prevent electrical reflections. EAMs with coplanar waveguides terminating both sides were also fabricated to allow for two-port S-parameter characterization. The active optical length for both the continuous and periodic TW-EAMs was 400 µm. The periodic electrode was separated into four EAM segments connected by high impedance microstrip lines. Of the total electrode length, only 25% was capacitively loaded, and the path lengths of the unloaded optical and electrical segments were designed to match the propagation distance of the two velocity-mismatched waves.

3. S-Parameter Characterization

We have measured and compared three modulator structures: (1) the continuously loaded TW-EAM with a deeply etched ridge, (2) the continuously loaded TW-EAM with an undercut active region and (3) the periodically loaded design, also with the selective undercut etch. The electrical properties of the different EAM designs were examined by two-port S-Parameter measurements using an HP 8510C network analyzer. The magnitudes of the S-parameter measurements are shown in Fig. 2 (a) at -2.5 V bias. Both undercut designs demonstrate significant improvement over design (1) in both electrical bandwidth and reflected power. The S_{11} measurement shows the return loss of the periodic TW-EAM is well below -10 dB up to 20 GHz, demonstrating better impedance matching to the 50 Ohm electrical drive.

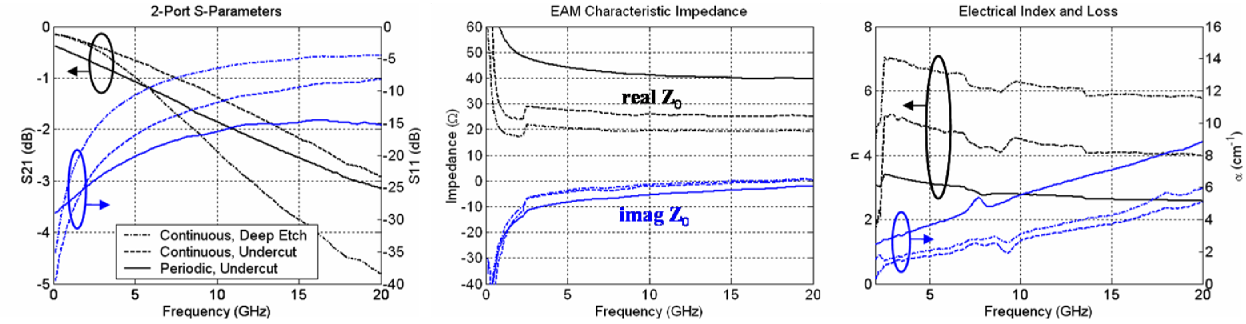

(a) (b) (c)

Fig. 2 (a) Two-port electrical S-parameter measurements, (b) Characteristic impedance vs. frequency, and (c) microwave index and attenuation of the three TW-EAM designs at -2.5 V DC bias.

From the S-Parameter measurements we have extracted the transmission line properties of the three structures using the ABCD matrix method [5]. Figure 2 (b) and (c) show the average characteristic impedance as well as microwave index and loss for the different TW-EAMs. The undercut alone increases the impedance of the transmission line from 20 to 26 Ω, and with the addition of the periodic electrode an average impedance of 40 Ω is achieved. The undercut etch also reduces the electrical effective index from 6 to 4, which closely matches the optical group velocity for this waveguide structure. The average electrical index of the periodic electrode is further reduced to nearly 3. This shows good agreement with design simulations which allow for the optical and electrical propagation distances to be matched along the entire device length. For comparison, the microwave loss values of the periodic device are normalized to reflect the loss per active optical length. The loss of the periodic TW-EAM is higher due to the extra 1.2 mm of passive electrode length.

4. Optical Measurements

Optical measurements of the devices have been performed using an external tunable laser source and lensed fibers to couple the light at both facets. Because they are intended to be integrated with a laser, there was no effort to make the EAMs polarization independent so it was necessary to optimize the polarization of the input light for maximum modulation efficiency in these measurements. Small signal electrical to optical (E-O) measurements were made to compare the optical bandwidth of the three TW-EAM designs and to measure the traveling wave effects. Figure 3

(a) shows the normalized frequency response of the three EAMs at -3.0 V bias up to 50 GHz. The values of the on-chip terminations for the continuous and periodic TW-EAMs were 26 Ω and 38 Ω, respectively. The 3-dB bandwidths of the deep-etched, undercut, and periodic designs were 23 GHz, 40 GHz, and 30 GHz, which clearly demonstrates the benefit of the selective undercut etch. The 25% reduction in the bandwidth of the periodic structure is due to the higher microwave loss compared with the continuous, undercut TW-EAM. However, the higher impedance of the device allows for larger voltage swings and less electrical reflections compared with the continuous design. Higher bandwidths can be achieved by terminating the periodic structure with a resistor lower than the characteristic impedance to induce a voltage reflection that results in an enhancement of the frequency response. With 22 Ω terminating the periodic EAM, the bandwidth is increased to 40 GHz.

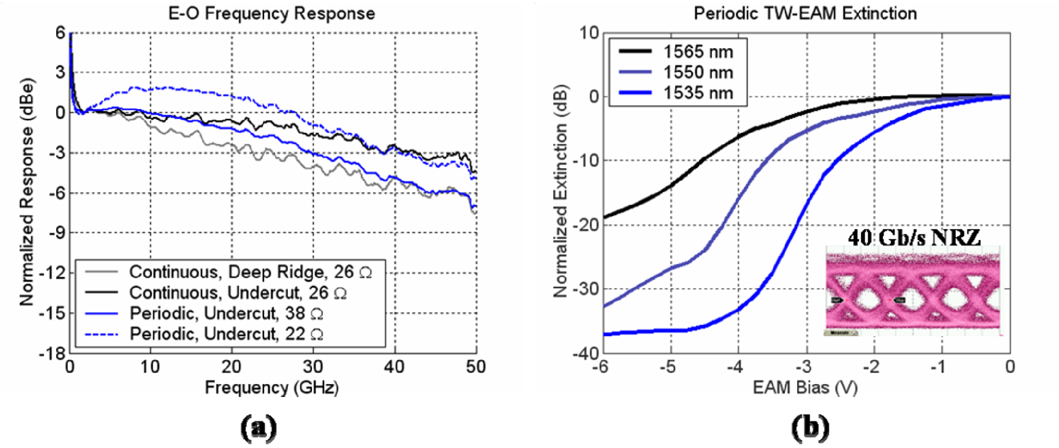

Fig. 3 (a) Optical to electrical frequency response of the different TW-EAM designs for various integrated resistor values.
(b) DC extinction vs. wavelength for the periodically loaded TW-EAM. Inset: 40 Gb/s eye diagram.

We have measured DC extinction for the periodic TW-EAM for wavelengths of 1565, 1555, and 1535 nm, shown in Figure 3 (b). The maximum slope efficiencies were 8, 16, and 20 dB/V, respectively. To demonstrate large signal operation of the periodic TW-EAM, we have performed digital data modulation at 40 Gb/s non-return to zero. The device was biased at -3.8 V and terminated with 38 Ω. The inset in Figure 3 (b) shows the observed optical eye diagram at 1550 nm. The dynamic extinction ratio was measured as 6.0 dB for an electrical drive voltage of 1.6 V peak-to-peak.

5. Conclusion

We have demonstrated the first traveling wave EAM to incorporate periodic transmission line loading with selective undercut etching of the active region. This design increases the characteristic impedance by a factor of two, and exhibits excellent velocity matching characteristics. Periodically loading the device improves the return loss by 10 dB at 20 GHz and exhibits an optical bandwidth of 30 GHz for a 400 um long active length. The device demonstrated modulation of digital data up to 40 GB/s with 1.6 V drive. We are currently integrating these EAMs with SG-DBR lasers for tunable transmitters. Future work will focus on reducing the microwave loss to increase the bandwidth, as well as raising the characteristic impedance to 50 Ω to further improve impedance matching.

The authors acknowledge the funding support of the DARPA/MTO/ARL DOD-N program under the LASOR project award number W911NF-04-9-0001.

References

[1] Walker, R.G. *IEEE Journal of Quantum Electronics*, vol. 27, pp 654-667, (1991)
[2] Lewen, R. *et al. Journal of Lightwave Technology,* vol. 22, pp 172-179, (2004)
[3] Chiu, Y. J. *et al. Photonics Technology Letters, IEEE,* vol. 17, pp 2065-2067, (2005)
[4] Sysak, M.N. *et al. Photonics Technology Letters, IEEE* vol. 18, pp 1630-1632, (2006)
[5] Spickermann, R. *et al. Trans. on Microwave Theory and Techniques, IEEE* vol. 42, pp 1918-1924, (2004)

InP-Based Photonic Integrated Circuits

Larry A. Coldren
ECE and Materials Departments
University of California, Santa Barbara, CA 93106
coldren@ece.ucsb.edu

Abstract: The monolithic integration of a number of photonic components on a single InP chip for increased functionality and reliability as well as decreased power dissipation and cost is becoming an accepted goal for most component vendors. This tutorial will review current integration approaches and results, emphasizing our UCSB work.

1. Introduction

InP-based Photonic Integrated Circuits (PICs) have been discussed and researched since the late 1970s when the InP based materials were still in an early stage of development[1-3]. A significant amount of work in the 1980s and early 1990s demonstrated many of the integration techniques still in use today[3-8]. However, for many years success with hybrid integration techniques has slowed the commercial adoption of PICs, except for a few limited examples, such as the integration of an electro-absorption modulator (EAM) with a DFB laser (the so-called EML). In fact, some have argued that PIC approaches would rarely replace feasible hybrid approaches for many years to come. Recently, these 'hybrid-integration-forever' advocates seem to have gone quiet, and some have even had the epiphany that 'PICs are now the only way to go'. Clearly, there have been some recent existence proofs of complex PICs that appear to have numerous advantages over hybrid approaches[9,10]. Time will tell, but the thesis of this tutorial will be that PICs are now seen as the preferred approach for many applications, and as such, they will be the subject of intense R & D at many commercial component vendors in the next couple of years. It is even possible that some new PIC technologies, such as quantum-well intermixing (QWI)[11], will gain widespread acceptance for real commercial applications.

2. Integration Platforms

At the core of most PICs is a basic active-passive waveguide integration technique, and this largely determines the viability of the resulting integration platform. Figure 1 illustrates several active-passive integration approaches that have been used with some success. Of course, by 'passive' we may be referring to a modulator region or a truly passive interconnecting waveguide.

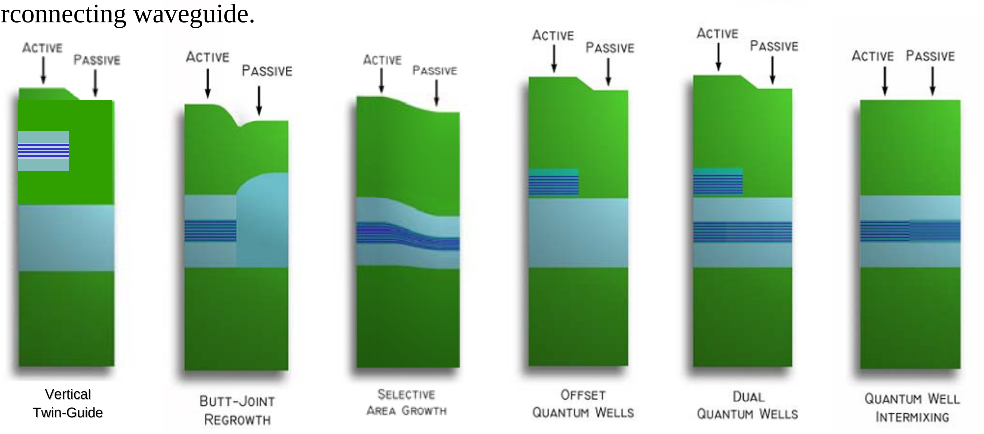

Figure 1. Schematics of six integration platforms. All have been used in commercial products.

Pros and Cons of each of the integration platform shown in Fig. 1 include the following: the vertical twin guide allows for independent properties in the upper and lower guides, but a long coupling length is needed to accomplish the vertical light transfer; the butt-joint regrowth approach also allows for independent properties in the active and passive sections, but a critical alignment of the regrown waveguides is necessary; the selective area growth technique provides a scaling of the vertical dimensions to change the absorption edge of the quantum-wells, but the properties of each are still linked and the patterned growth results in some transition length as well as being critically dependent on the lateral diffusion properties of the precursors; the offset quantum-well approach only requires an unpatterned blanket regrowth over a small step after etching away the active wells, but offsetting the gain results in a reduced net gain for the mode; the dual quantum-well case adds higher bandgap wells in the waveguide to provide better modulators in the 'passive' guide; the quantum-well intermixing approach can provide multiple bandgaps from a single growth with multiple diffusion steps, but for higher saturation power SOAs or detectors additional blanket regrowths are necessary.

3. Example PICs

Figures 2 & 3 show schematics and results from two example 40 Gb/s PICs fabricated in the authors group. Figure 2 describes a single-chip all-photonic transceiver that includes a high-gain, high-saturation power SOA-UTC receiver and a widely tunable transmitter that combines an SGDBR laser with an electroabsorption modulator (EAM) [12]. The QWI platform is used. Figure 3 describes the use of the dual QW (DQW) platform to form a single-chip wavelength converter with a flared SOA-PIN receiver directly interconnected to a widely tunable SGDBR—Mach-Zehnder modulator (MZM) for the transmitter stage [13].

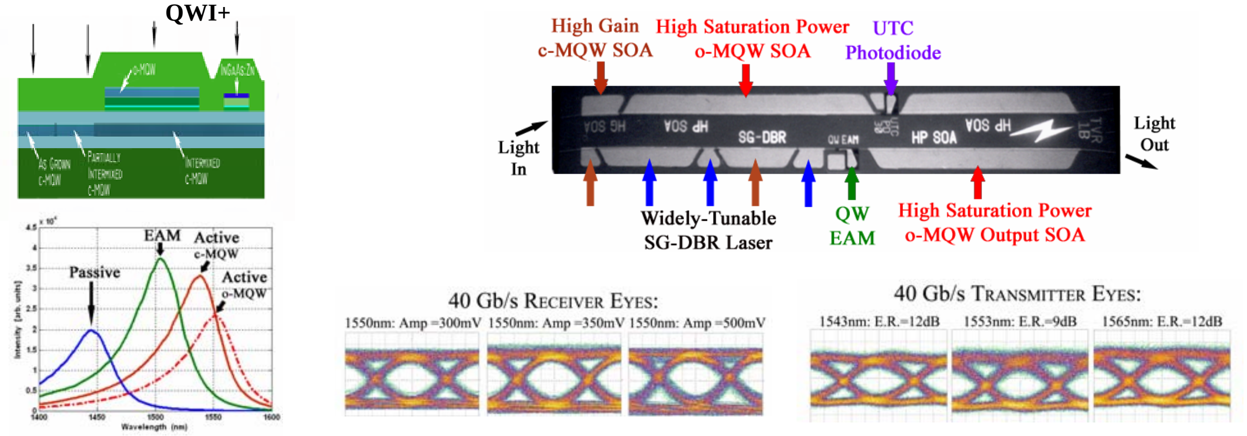

Figure 2. 40Gb/s single-chip transceiver fabricated with quantum-well intermixing (QWI) and blanket regrowths. A schematic device cross section and top view, photoluminescence plots of the various sections, and receiver and transmitter eye diagrams are shown. Receiver sensitivity @ 10^{-10} is -19.8 dBm; error-free wavelength conversion across a 32 nm range demonstrated.

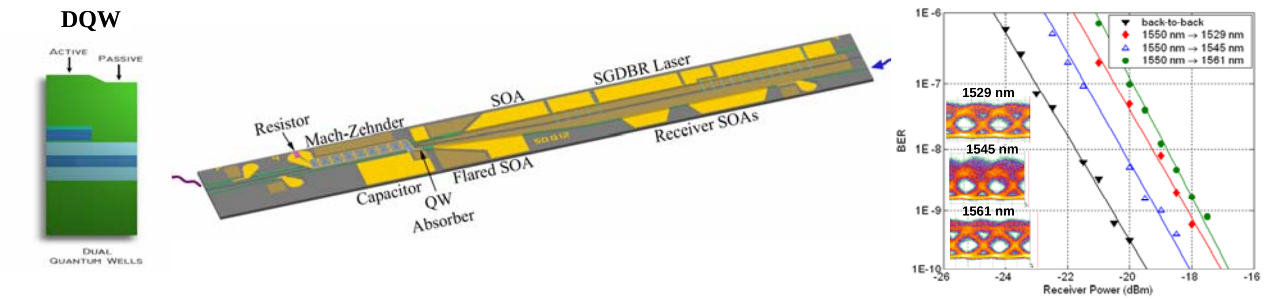

Figure 3. 40Gb/s single-chip wavelength converter fabricated with the "dual QW" integration platform. A series-connected traveling-wave MZM design is employed for chirp management. Only dc biases applied to chip for error free wavelength conversion over a 33 nm range.

References

[1] R. F. Leheny, R. E. Nahory, M. A. Pollack, A. A. Ballman, E. D. Beebe, J. C. DeWinter, R. J. Martin, *Electron. Letts*. **16**, 353 (1980).
[2] L.A. Coldren, B. I. Miller, K. Iga, and J.A. Rentschler, *Appl. Phys. Letts*, **38** (5) 315-317 (1981).
[3] Y. Abe, K. Kishino, Y Suematsu, and S. Arai, *Electron. Letts*. **17** (25) 945-947 (1981).
[4] M. Suzuki, Y. Noda, H. Tanaka, S. Akiba, Y. Kushiro, and H. Isshiki, *IEEE J. Lightwave Tech*., **LT-5**, 1277-1285 (1987)
[5] W.C. Dautremont-Smith, R. J. McCoy, R.H. Burton, and A.G. Baca, *AT&T Tech. J*., **68**, 64-82 (1989).
[6] T. L. Koch, U. Koren, R. P. Gnall, F.S. Choa, R. Hernandez-Gil, C.A. Burrus, et al, *Electron. Letts*., **25**, 1621-1622 (1989).
[7] R. C. Alferness, T.L. Koch, L.L. Buhl, F. Storz, F. Heismann, and M. Martyak, *Appl. Phys. Letts*., **55**, 2011-2013 (1989).
[8] T. L. Koch and U. Koren, *IEEE J. Quantum Electronics*, **QE-27**, 641-653 (1991).
[9] Y.A. Akulova, G.A. Fish, H. Xu, E. Hall, M.C. Larson, P. Abraham, H. Marchand, et al, *Proc. IPRA*, paper IWF4, San Diego (2005).
[10] R. Nagarajan, C.H. Joyner, R.P. Schneider, et al, *IEEE J. Selected Topics in Quantum Electronics (JSTQE)*, **11** (1) 50-65 (2005).
[11] E.J. Skogen, J.W. Raring, G.B. Morrison, C.S. Wang, V. Lal, M.L. Masanovic, and L.A. Coldren, *IEEE JSTQE*, **11** (2) 343-355 (2005).
[12] J. W. Raring and L. A. Coldren, *IEEE Journal of Selected Topics in Quantum Electronics*, **13** (1) 3-14 (2007).
[13] A. Tauke-Pedretti, M. Dummer, M.N. Sysak, J.S. Barton, J.W. Raring, J. Klamkin, L.A. Coldren, *Proc. OFC*, Anaheim, PDP-36 (2007).

Widely Tunable 40 Gbps Transmitter Utilizing a High-Impedance Traveling-Wave EAM and SG-DBR Laser

Matthew M. Dummer, Jonathan Klamkin, John P. Mack, and
Larry A. Coldren
Univ. of California, ECE Department, Santa Barbara, CA 93106
TEL:(805)893-7163, FAX:(805)893-4500, email:dummer@engr.ucsb.edu

Abstract: A tunable transmitter featuring an SG-DBR laser is integrated with an undercut-etched, high impedance traveling-wave EAM. This device demonstrates 40 Gbps operation with >8.5 dB extinction over 25 nm tuning with 2.1 V drive.

OCIS codes: (140.3600) Tunable lasers; (230.4110) Modulators; (230.4205) MQW modulators; (230.7020) Traveling-wave devices

1. Introduction

Electroabsorption modulators (EAMs) are advantageous optical components for transmission of digital data due to their low drive voltage and high bandwidth. Traveling-wave (TW) designs which utilize transmission line electrodes have shown to significantly enhance the bandwidth of EAMs compared with the RC response of typical lumped element devices. However, one major limitation of most TW-EAMs is the low characteristic impedance of the capacitively-loaded electrode which creates a large mismatch between the device and 50 Ω electronic drivers. Two techniques for reducing the capacitance per unit length of the EAM which have been demonstrated are selective undercutting of the modulator core [1], and periodic loading by distributing the EAM along high-impedance interconnects [2]. Recently, we have implemented both of these methods in the same device to effectively double the characteristic impedance from 20 Ω to 40 Ω as well as achieve velocity matching of the electrical and optical signals [3]. In this work, for the first time, we present a high-impedance TW-EAM monolithically integrated with a sampled grating (SG)-DBR laser and output optical amplifier to form a widely-tunable transmitter. This device demonstrates greater than 15 dB/V DC modulation efficiency and greater than 8 dB extinction at 40 Gb/s over 25 nm of optical bandwidth.

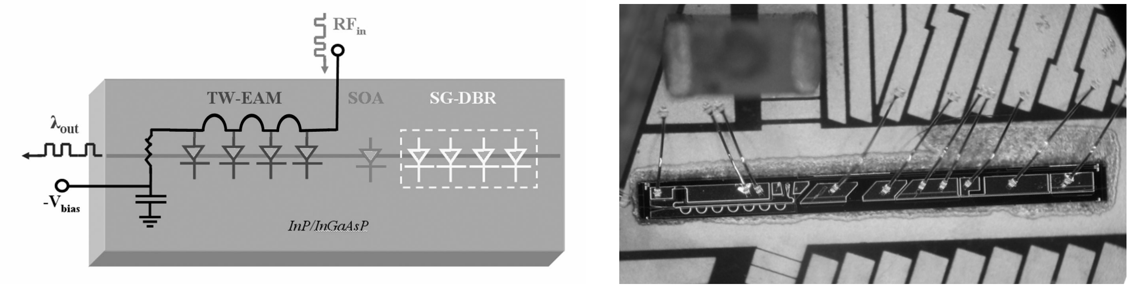

(a) Circuit diagram of integrated transmitter

(b) Photograph of fabricated transmitter on carrier

Fig. 1.

2. Design and Fabrication

The transmitter consists of a five stage SG-DBR laser followed by an output semiconductor optical amplifier (SOA) and TW-EAM which all share a common waveguide. A circuit diagram of the full device is shown in Fig. 1(a). The epitaxial layer structure for this device utilized a dual quantum well waveguide (DQW) [4] with 10 QWs centered in the InGaAsP core for modulation efficiency and 7 offset QWs above the core to provide gain. The photoluminescence peaks corresponding to the band edges of the two QW regions were 1470 nm and 1540 nm, respectively. The offset quantum wells were selectively etched from all but the laser gain and SOA regions before regrowth of the p-type InP cladding. The laser and SOA were designed with a surface ridge waveguide structure which tapered into an undercut waveguide for the modulator region. To achieve the undercut, first a deeply etched ridge was defined by reactive ion etching down into the n-cladding. Then a selective wet etch of sulfuric acid and peroxide mixed with water (1:1:10) was performed for 30 minutes to laterally reduce the width of the InGaAsP core from 3 μm to approximately 1.15 μm. A cross section of the modulator waveguide is shown in Figure 2. For this amount of undercut, simulations of the mode profile as a function of the waveguide core width show less than 2 percent decrease in the modal overlap with the centered quantum wells. Therefore the modulation efficiency is not significantly affected when the diode junction capacitance is reduced.

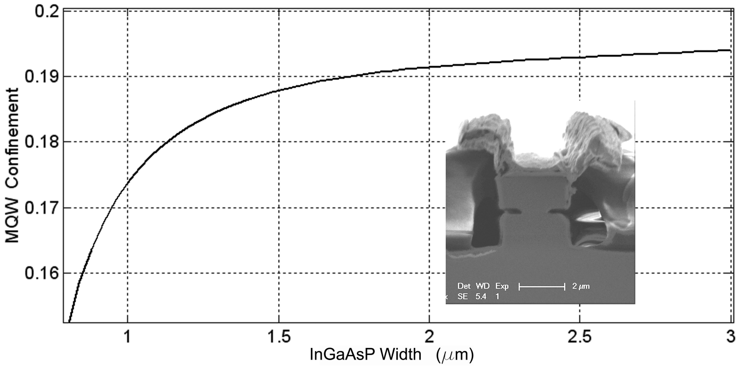

Fig. 2. Overlap of the optical mode with the EAM quantum wells for varying amount of undercut. Inset: cross section of the EAM waveguide.

Following the undercut etch, the EAM structure was buried with photo-defined benzocyclobutene (BCB) as a low-k dielectric. The BCB was etched to expose the modulator ridge top before metal contacts were formed. The modulator electrode was designed as a segmented microstrip line which alternated between passive and EAM-loaded sections. Over the 1600 μm of total length, the microstrip electrode contacted the ridge in eight separate 50 μm sections, yielding an effective modulator length of 400 μm. The optical path length between modulator sections was designed to match the phase of the electrical line to maintain coherent interaction of the two traveling waves along the entire length. A coplanar waveguide (CPW) was implemented at the input of the EAM electrode for directly contacting with a high-speed probe. At the opposite end of the EAM, a thin-film 35 Ω thin film NiCr resistor was deposited by e-beam evaporation. The resistor was followed by on-chip, and off-chip capacitors in parallel to provide an RF ground as shown in the device photograph. (Fig. 1(b))

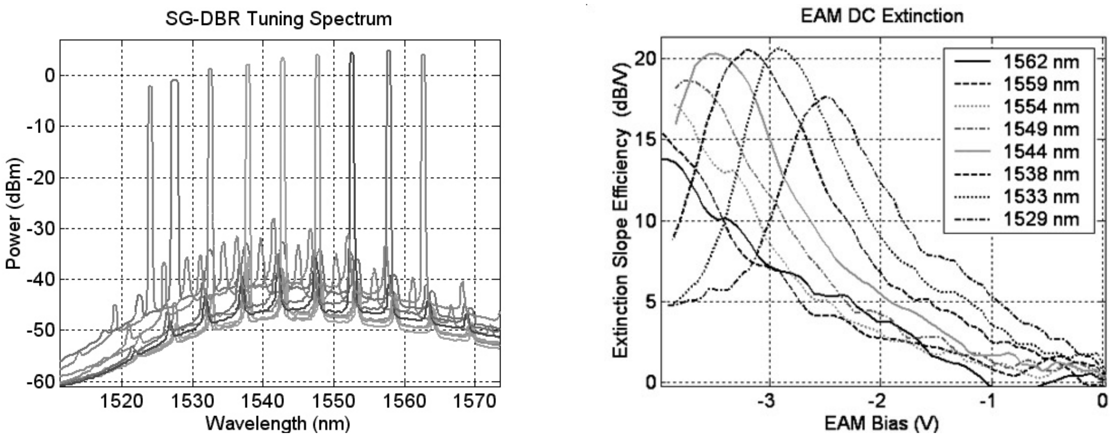

(a) Supermode tuning spectrum of SG-DBR laser

(b) DC modulation efficiency of the periodically loaded, undercut TW-EAM over the SG-DBR tuning range.

Fig. 3.

3. Transmitter Results

The fabricated SG-DBR laser is continuously tunable over the range of 1524 nm to 1563 nm. Figure 3(a) shows the tuning over 9 supermodes achieved by vernier tuning of the front and rear mirrors with laser and SOA bias currents of 125 mA and 75 mA, respectively. The side mode suppression ratio is greater than 30 dB in all cases. The variation in the output power from -2 dBm to 4 dBm is caused by both the gain spectrum of the offset QWs and the wavelength-dependent loss of the centered wells. The DC extinction characteristics of the TW-EAM were measured for reverse biases of 0 to 4 V over the wavelength range of the SG-DBR. As shown in Figure 3, the bias point of the modulator can be optimized to achieve greater than 15 dB/V peak extinction efficiency for more than 30 nm of output tuning. The efficiency of the modulator begins to decrease at the longer wavelengths because of the larger detuning between the optical energy and the band edge of the quantum well.

Dynamic, large signal modulation experiments have been performed at 40 Gb/s non-return-to-zero (NRZ) to demonstrate the high bandwidth of this device. Figure 4 shows the observed optical eye diagrams of for wavelengths of 1533, 1543, 1549, and 1559 nm with 2.1 V peak-to-peak drive. The EAM bias was -1.9, -2.5, -3.0 and -3.4 V, respectively. For all wavelengths, the eyes are clearly open with extinction ratios ranging from 8.5 to 9.8 dB.

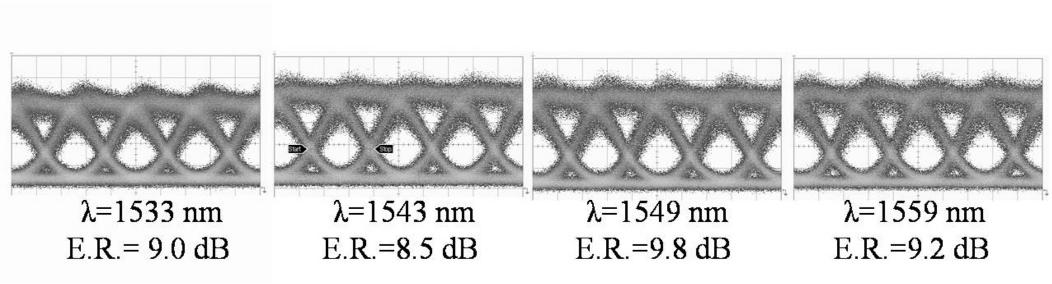

Fig. 4. 40 Gb/s NRZ eye diagrams

4. Conclusion

We have successfully developed a fabrication process for an integrated transmitter which combines a SG-DBR laser and high impedance TW-EAM. The 400 μm long modulator utilizes periodically loaded electrodes as well as an undercut waveguide to achieve very low capacitance per unit length. For over 25 nm of tuning, this device demonstrates greater than 15 dB/V peak efficiency and efficient modulation at 40 Gb/s NRZ with a 2.1 V electrical drive.

References

1. Y.-J. Chiu, T.-H. Wu, W.-C. Cheng, F. Lin, and J. Bowers, “Enhanced performance in traveling-wave electroabsorption modulators based on undercut-etching the active-region,” *Photonics Technology Letters, IEEE*, vol. 17, no. 10, pp. 2065–2067, 2005.
2. R. Lewen, S. Irmscher, U. Westergren, L. Thylen, and U. Eriksson, “Segmented transmission-line electroabsorption modulators,” *Lightwave Technology, Journal of*, vol. 22, no. 1, pp. 172–179, 2004.
3. M. M. Dummer, J. Klamkin, E. J. Norberg, J. W. Raring, A. Tauki-Pedretti, and L. A. Coldren, “Periodic loading and selective undercut etching for high-impedance traveling-wave electroabsorption modulators,” in *Optical Fiber Communication Conference, 2008. OFC 2008*.
4. M. Sysak, J. Raring, J. Barton, M. Dummer, D. Blumenthal, and L. Coldren, “A single regrowth integration platform for photonic circuits incorporating tunable sgdbr lasers and quantum-well eams,” *Photonics Technology Letters, IEEE*, vol. 18, no. 15, pp. 1630–1632, 2006.

Highly Polarized Single-Chip ELED Sources Using Oppositely Strained MQW Emitters and Absorbers

Steven C. Nicholes, James W. Raring, *Member, IEEE*, Erik J. Norberg, Chad S. Wang, *Member, IEEE*,
Matthew M. Dummer, *Student Member, IEEE*, Steven P. DenBaars, *Fellow, IEEE*, and Larry A. Coldren, *Fellow, IEEE*

***Abstract*—Integrated polarizer components with polarization extinctions >40 dB are desirable for state-of-the-art photonic integrated circuits. We demonstrate >60-dB polarization extinction from a single-chip InGaAsP–InP broadband source by combining an edge light-emitting diode consisting of compressively strained quantum wells (QWs) with an absorber consisting of tensile strained QWs. A 600-μm polarizer exhibits only 5 dB of insertion loss.**

***Index Terms*—Edge light-emitting diode (ELED), photonic integrated circuits (PICs), polarization, strained quantum well (QW).**

I. INTRODUCTION

PHOTONIC integrated circuits (PICs) with dynamic functionality are attractive alternatives to optical systems based on discrete components. However, the fabrication of complex PICs with extreme polarization control of the optical signal is quite difficult. This is due to the mixed emission and absorption of the transverse-electric (TE) and transverse-magnetic (TM) polarization modes in semiconductor materials such as InGaAsP–InP. Adding strain to these materials can greatly increase or decrease the TE/TM ratio, but this alone provides limited polarization extinction levels. Furthermore, integrated polarizer components have not demonstrated polarization extinctions between TE and TM modes in excess of about 20 dB in InGaAsP–InP [1], [2]. Devices such as fiber-optic gyroscopes demand polarization extinctions of at least 40 dB to achieve only moderate sensitivity levels [3]. Thus, to realize a highly sensitive, single-chip gyroscope, there is a clear need for novel approaches to polarization control.

We previously reported polarization extinctions of 40 dB by optimizing only the light source [4]. Our approach utilized compressively strained high-gain multiple quantum wells (MQW) as the active region in an edge light-emitting diode (ELED). To achieve even greater extinction, we have designed an on-chip polarizer that functions in conjunction with our highly polarized ELEDs to demonstrate a TE polarized device with >60-dB polarization extinction.

II. DEVICE DESIGN

Our polarizer approach uses strained MQW active regions. When strain is induced in the MQW, the degeneracy between the light hole (LH) and heavy hole (HH) bands at $k = 0$ splits. Compressive strain pushes the light hole band to higher energies than the heavy hole band so that conduction band (CB)-HH transitions, which provide gain/absorption to TE polarized light at $k = 0$, dominate. Tensile strain results in the opposite behavior so that CB-LH transitions, which are mostly TM polarized (and to a lesser extent TE polarized), dominate [5]. By combining a compressively strained (TE dominant) source with a tensile strained (TM dominant) MQW absorber that functions as a polarizer, the TM light generated by the ELED will be selectively absorbed, and very high polarization extinctions can be achieved (Fig. 1).

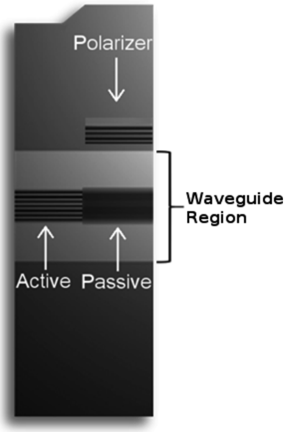

Fig. 1. Side-view schematic of MQWs used for integrated ELED/polarizer device. The active QW region is centered in the waveguide to maximize the confinement factor at 13%, while the polarizer QW region is placed above the waveguide to reduce the confinement factor to 2.3%.

The combined ELED/absorber devices were grown via metal–organic chemical vapor deposition (MOCVD) on a sulfur-doped InP substrate. The ELED MQW region of this device consisted of ten 6.5-nm InGaAsP QWs and eleven 8.0-nm InGaAsP barriers. The QW composition was chosen to create compressive strain (+0.9%) in the wells for TE dominant light output at 1550 nm and the barriers were grown with a small degree of tensile strain (−0.2%) for strain compensation. In the ELED region, the MQW was centered between symmetrical waveguides for a maximized optical confinement (Γ) of $\sim$13%. Active and passive waveguide regions were obtained by selectively shifting the active ELED bandedge from a photoluminescence peak (λ_{PL}) of 1540–1430 nm using quantum-well (QW) intermixing as described in [6].

Two different polarizer designs with the same QW compositions were examined (Table I). The QW width in Design 1

Manuscript received November 14, 2007; revised March 18, 2008. This work was supported in part by Defense Advanced Research Projects Agency CS-WDM.

The authors are with the Department of Materials and Department of Electrical Engineering, University of California Santa Barbara, Santa Barbara, CA 93116 USA (e-mail: snicholes@engineering.ucsb.edu).

Digital Object Identifier 10.1109/LPT.2008.926545

TABLE I
POLARIZER EPITAXIAL STRUCTURE

	Number of QWs	QW Thickness (Å)	PL Wavelength (nm)
Design 1	2	130	1548
Design 2	3	95	1515

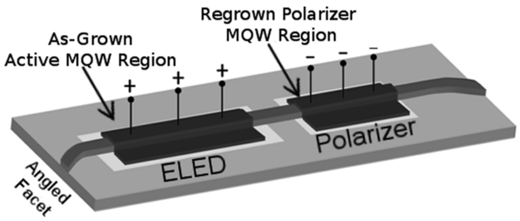

Fig. 2. Schematic of ELED device illustrating the integrated polarizer and angled/flared output facet.

was selected to align the polarizer absorption peak ($\lambda_{\rm PL} = 1548$ nm) with the gain peak of the ELED ($\lambda_{\rm PL} = 1540$ nm) to absorb TM light generated at any wavelength below the ELED $\lambda_{\rm PL}$. But, since CB-LH transitions also permit some TE absorption, a second design was explored with narrower QWs to blue-shift the polarizer absorption peak ($\lambda_{\rm PL} = 1515$ nm) relative to the ELED $\lambda_{\rm PL}$ to reduce undesirable TE absorption.

The polarizer MQW regions were realized via an MOCVD regrowth. An InP spacer layer on top of the waveguide offset the polarizer region MQW from the peak of the optical mode, reducing Γ to only 2.3%. The thickness of this spacer layer was chosen to keep Γ constant between the two designs. The polarizers employed tensile strained InGaAs wells (-1%) and 8.0-nm compressively strained InGaAsP barriers (0.3%). The polarizer region was defined using wet etching techniques. A subsequent regrowth defined the p-type cladding. This high-functionality PIC fabrication approach is described in [6].

The completed 3-μm-wide surface ridge waveguide devices consisted of a 1000-μm ELED, followed by a short passive section, a 300- to 1000-μm integrated polarizer, and a curved/flared output waveguide to reduce reflections (Fig. 2).

III. EXPERIMENTS AND DISCUSSION

Using a Glan Thompson polarizer to resolve the output polarization as in [4], the polarization extinction was measured for devices with and without an on-chip MQW polarizer. Fig. 3(a) shows the TE and TM polarization-resolved amplified spontaneous emissiong (ASE) spectrum from an ELED at 8.3 kA/cm^2 and the total output spectrum with no external polarizer. The TM-dominant CB-LH transition occurs at a higher energy than that of the TE-dominant CB-HH transition, and thus the peak wavelength of the TM spectrum ($\sim$1478 nm) is blue shifted from the peak wavelength of the TE spectrum (1545 nm). The peak at 1545 nm in the TM-resolved spectrum corresponds to TE light that our polarizing prism, which provided only $\sim$27 dB of polarization extinction, could not filter out [4]. When the Glan Thompson polarizer is removed from the system, both peaks are evident in the spectrum. With a TM peak power of -66 dBm and a TE peak power of -22 dBm, the native polarization extinction between the TE and TM peak powers of the 1000-μm ELED is $\sim$44 dB.

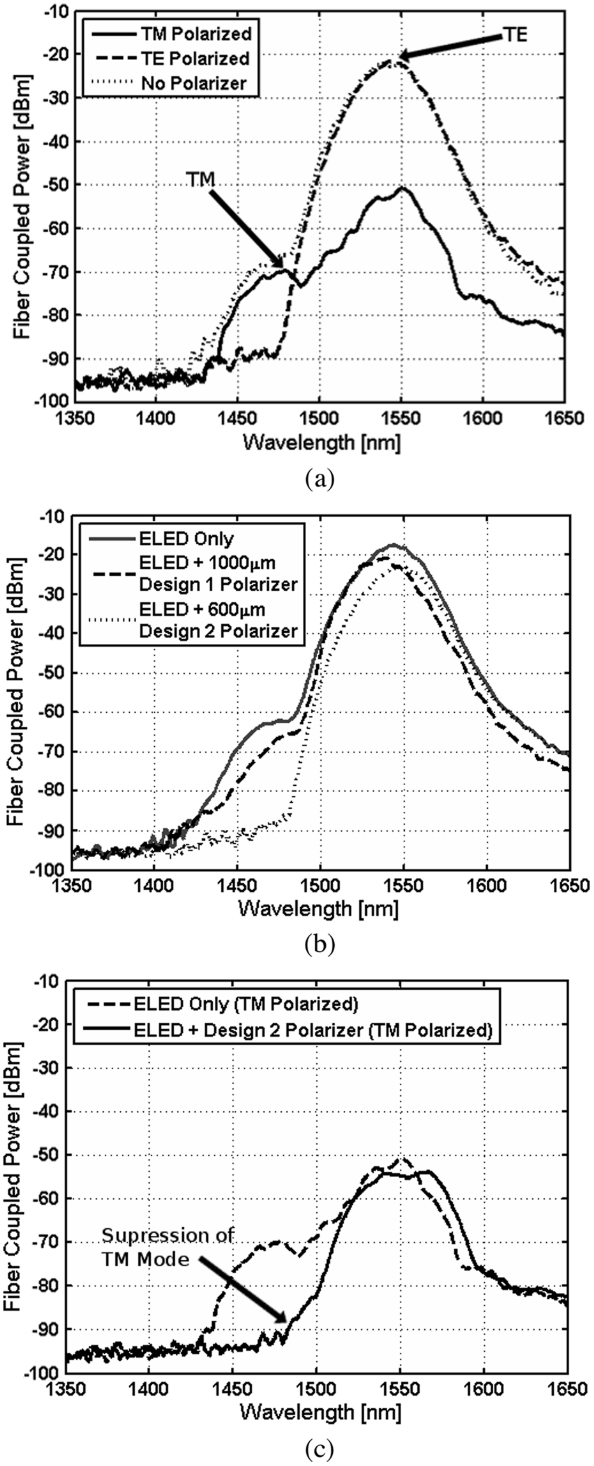

Fig. 3. Output ASE spectra from (a) 1000-μm-long ELED with no on-chip polarizer (resolved for polarization); (b) an ELED only versus an ELED followed by an integrated polarizer; (c) an ELED only versus an ELED and a 600-μm polarizer (Design 2) resolved for TM polarization.

Fig. 3(b) compares the ASE output spectrum of our standard ELED device with those incorporating an integrated polarizer. Clearly, a polarizer using Design 1 does not improve the polarization extinction of the device, which remains at about 44 dB. In contrast, when the ELED is paired with a polarizer of Design 2, the TM peak at 1478 nm is significantly suppressed. The TM-resolved spectra [Fig. 3(c)] for these two devices demonstrate that a polarizer employing Design 2 begins absorbing wavelengths around 1525 nm, and demonstrates a 20-dB improvement in polarization extinction at the TM peak power (1478 nm). Therefore, the polarization extinction between the TE and TM peak powers approaches 63 dB, with a TM peak power of about -87 dBm and a TE peak power of -24 dBm. Additionally, we experimented with applied biases on the polarizers to enhance the selective TM absorption, but found no improvement in polarization extinction levels with either design. It is apparently sufficient to simply probe the polarizer to provide a path for generated carriers to escape.

The difference in polarization extinction between the two polarizer designs is explained in terms of the placement of their respective PL peaks relative to the peak emission wavelength of the ELED. Because λ_{PL} of Design 1 occurred at the same wavelength as the peak emission of the ELED, the lowest energy CB states (near $k = 0$) of the polarizer were likely filled due to the high quantity of incident photons. This band filling effect would increase the dominant absorption energy of the polarizer (i.e., to states with $k > 0$). As shown in [7], when the k-vector corresponding to absorption/emission in tensile wells increases, the TM matrix element (which is related to the transition strength) is reduced. In fact, for high enough k values, the TM matrix element can fall to the same level as the TE matrix element, creating a situation in which TE absorption is just as likely as TM absorption. This scenario agrees with the data in Fig. 3(b) for Design 1, as a nearly equivalent reduction in power is seen at the major TE (1550 nm) and TM (1478 nm) emission peaks of the ELED. In the case of Design 2, λ_{PL} was shifted to 1515 nm, where the ELED output power is more than 10 dB below the peak power at 1550 nm, suggesting that the degree of band filling in this polarizer would be substantially lower than that of Design 1. With fewer filled states, the TM matrix element would remain larger than the TE matrix element and more TM absorption would occur. As further evidence of this phenomenon, we compared the absorbed photocurrent from the ELED into a 600-μm polarizer (no applied bias). Design 1 absorbs almost 13X as much photocurrent as Design 2 (4.7–0.37 mA), which can be explained if it exhibits significantly greater TE absorption than Design 2.

Fig. 4 shows the effect of polarizer length on the polarization extinction for Design 2. Although the TM peak power does tend to decrease with increased polarizer length, so does the TE peak power. For example, the peak TE power with a 600-μm polarizer falls from -22 to -29 dBm for a 1000-μm polarizer. Because there is no significant improvement in polarization extinction, the polarizer length should be kept below 600 μm to avoid excessive insertion loss. Fig. 4 also shows that the TE peak power for an ELED is about 5 dB higher than that of a device with a 600-μm polarizer. Because the matrix elements for CB-LH transitions permit some TE absorption, a reduction in output power is expected. However, some of this loss can be attributed to the difficulty of coupling output light through our setup and into an optical spectrum analyzer. Since our ELEDs are capable of generating 16 dBm of continuous-wave output power at higher biases [4], this loss is still acceptable for device applications.

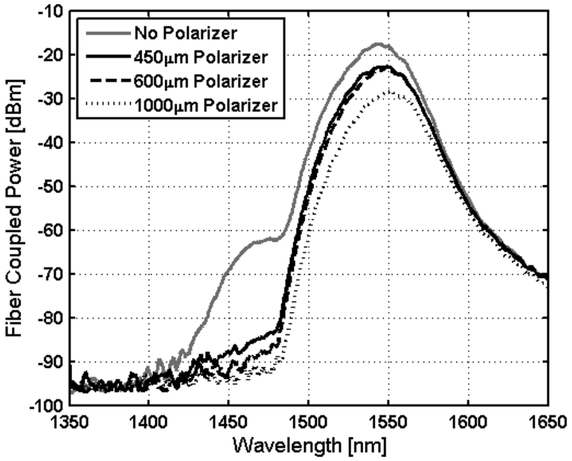

Fig. 4. ASE spectra for a 1000-μm ELED without an on-chip polarizer and with on-chip polarizers (Design 2) of various lengths.

IV. CONCLUSION

By pairing a compressively strained ELED with a tensile strained polarizer, we have demonstrated the highest reported polarization extinctions from a single-chip InGaAsP–InP broadband emitter. This configuration yields polarization extinctions >60 dB with insertion losses less than 5 dB. This technology is extendable to a variety of PIC applications, including single-chip high-sensitivity fiber-optic gyroscopes.

REFERENCES

[1] J. J. G. M. Van der Tol, J. W. Pedersen, E. G. Metaal, Y. S. Oei, H. van Brug, and I. Moreman, “Mode evolution type polarization splitter on InGaAsP–InP,” *IEEE Photon. Technol. Lett.*, vol. 5, no. 12, pp. 1412–1414, Dec. 1993.

[2] J. J. G. M. Van der Tol, J. W. Pedersen, E. G. Metaal, J. J.-W. Van Gaalen, Y. S. Oei, and F. H. Groen, “A short polarization splitter without metal overlays on InGaAsP–InP,” *IEEE Photon. Technol. Lett.*, vol. 9, no. 2, pp. 209–211, Feb. 1997.

[3] R. Bergh, H. Lefevre, and H. Shaw, “An overview of fiber-optic gyroscopes,” *J. Lightw. Technol.*, vol. LT-2, no. 2, pp. 91–107, Apr. 1984.

[4] S. C. Nicholes, J. W. Raring, M. Dummer, A. Tauke-Pedretti, and L. A. Coldren, “High-confinement strained MQW for highly polarized high-power broadband light source,” *IEEE Photon. Technol. Lett.*, vol. 19, no. 10, pp. 771–773, May 15, 2007.

[5] J. Burger, W. Steier, and S. Dubovitsky, “The energy-limiting characteristics of a polarization-maintaining Sagnac interferometer with an intraloop compressively strained quantum-well saturable absorber,” *J. Lightw. Technol.*, vol. 20, no. 8, pp. 1382–1387, Aug. 2002.

[6] J. Raring *et al.*, “Advanced integration schemes for high-functionality/high-performance photonic integrated circuits,” *Proc. SPIE*, vol. 6126, pp. 61260H1–H20, 2006.

[7] S. Seki, T. Yamanaka, W. Lui, Y. Yoshikuni, and K. Yokoyama, “Theoretical analysis of pure effects of strain and quantum confinement on differential gain in InGaAsP/InP strained-layer quantum-well lasers,” *IEEE J. Quantum Electron.*, vol. 30, no. 2, pp. 500–510, Feb. 1994.

Transmission Line Characterization of Undercut-Ridge Traveling-Wave Electroabsorption Modulators

Matthew M. Dummer, Jonathan Klamkin, Erik J. Norberg, Anna Tauke-Pedretti, James W. Raring, and Larry A. Coldren

***Abstract*—An experimental analysis of the electrical properties of traveling-wave electroabsorption modulators with undercut waveguides is presented. Modulators of varying ridge widths and amounts of undercut are fabricated and tested to compare characteristic impedance, effective index, microwave loss, and optical bandwidth. We demonstrate effective velocity matching and $>$40-GHz 3-dB bandwidth for a 400-μm-long device.**

***Index Terms*—Electroabsorption, traveling-wave devices, undercut etching.**

I. INTRODUCTION

ELECTROABSORPTION modulators (EAMs) have proven to be important devices for modulation of optical signals due to their compact size, high speed, low drive voltage, and ease of integration with semiconductor lasers. For traveling-wave modulators (TW-EAMs), transmission line electrodes are utilized such that the electrical drive signal interacts coherently with the propagating light thereby surpassing the traditional resistance–capacitance (*RC*) bandwidth limitation. However, the modulator capacitance still plays an important role in the frequency response. Traveling-wave devices are limited by impedance mismatch, velocity mismatch, and microwave loss, all of which are affected by the capacitance per length of the EAM. Recently, improved bandwidth of TW-EAMs has been demonstrated by undercutting of the waveguide core with selective wet etching [1], [2]. This technique allows for significant reduction of the diode junction capacitance while still maintaining a wide cladding for low series resistance [3]. Undercut etching has also been shown to lower the optical scattering loss by reducing the overlap between the mode and the outer sidewalls of the cladding layers [1].

In this work, we have developed a fabrication process for integrating undercut waveguide TW-EAMs with sampled grating DBR lasers for high-speed tunable transmitters [4]. As an optimization study, we have fabricated several discrete TW-EAMs with varied core and cladding dimensions in order to characterize their transmission line properties. Here, we present the experimental results of this study which demonstrate the dependence of the characteristic impedance, electrical effective index, and microwave loss on the modulator geometry over a wide design space. This study demonstrates improved velocity matching, increased impedance, and reduced loss for undercut waveguides with core dimensions as narrow as 1.4 μm.

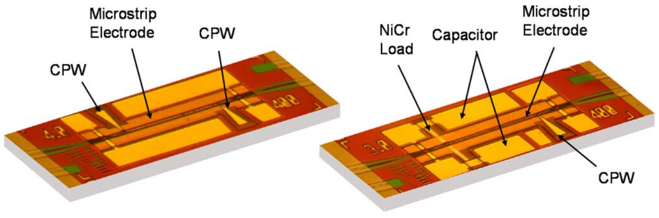

(a) (b)

Fig. 1. Fabricated TW-EAMs with (a) two-port CPW pad design and (b) integrated termination.

II. DESIGN AND FABRICATION

We have designed modulators with two different electrode configurations for these characterization experiments. As shown in Fig. 1, the first was designed with both input and output coplanar waveguide pads for two-port electrical characterization. The second was designed with an integrated matched termination to reduce electrical reflections [5]. The modulator microstrip electrodes were 400 μm long, 6 μm wide, and the width of the underlying ridges were varied on the mask from 2.5 to 5.0 μm. Laterally flared, curved waveguides were used at both facets to reduce optical reflections. The epitaxial layer structure for these modulators consisted of a 350-nm InGaAsP core surrounded by 1.8 μm each of InP for the upper and lower n- and p-doped cladding. The core contained a stack of ten quantum wells with a band edge corresponding to photoluminescence emission wavelength of 1465 nm. A sulfur-doped substrate was used to allow for backside n-contacts while 150 nm of highly doped p-InGaAs above the upper cladding provided an ohmic contact layer on the p-side. The optical waveguides for this device consisted of surface ridges at the facets which were tapered to deeply etched ridges for the modulation region of the TW-EAM. The ridges were patterned and defined using a combination of wet and dry etching before performing a selective wet etch to reduce the width of the InGaAsP core. Three pieces of the same wafer were processed, one with no undercut etching, and the other two with undercut etch times of 22 and 40 min in $H_2SO_4 : H_2O_2 : H_2O$ solution $(1:1:10)$. The total reduction in the active width of the two samples was measured to be 0.9

Manuscript received February 16, 2008; revised March 28, 2008. This work was supported by Defense Advanced Research Projects Agency (DARPA) MTO-LASOR Grant W911NF-04-9-0001.

The authors are with the Department of Electrical and Computer Engineering and the Department of Materials, University of California Santa Barbara, Santa Barbara, CA 93106 USA (e-mail: dummer@engineering.ucsb.edu).

Color versions of one or more of the figures in this letter are available online at http://ieeexplore.ieee.org.

Digital Object Identifier 10.1109/LPT.2008.926908

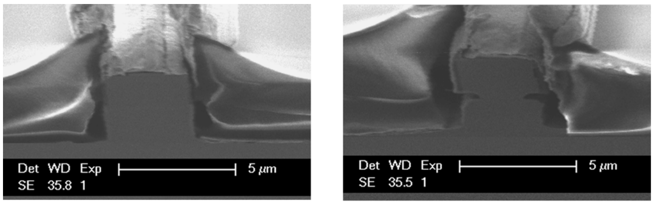

(a) (b)

Fig. 2. Scanning electron microscope cross section of (a) deep-etched and (b) undercut-ridge waveguide structures designed for a ridge width of 3.0 μm.

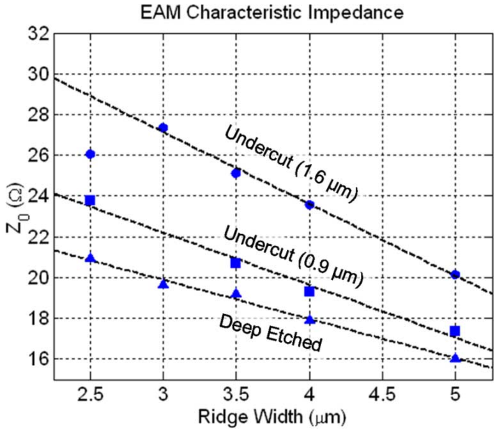

Fig. 3. Measured characteristic impedance versus ridge width for varied amount of undercut.

and 1.6 μm, respectively. The waveguides were then buried with photodefined benzocyclobutene (BCB) as a low-k dielectric. A via was etched through the BCB to expose the ridge-top before the final metallizations to form the p-side contact and thin-film NiCr resistor. An electron micrograph of the cross sections of the deeply etched (no undercut) and 40-min undercut-etched devices are shown in Fig. 2.

III. CHARACTERIZATION EXPERIMENTS

The TW-EAM transmission line structures were measured and analyzed using a two-port scattering parameter method [6]. For these experiments, all of the modulators tested were the two-terminal implementation shown in Fig. 1(a). The devices were directly probed with 50-Ω ground–signal–ground coplanar probes on both sides of the EAM and measurements were taken with an HP 3910C network analyzer. The measurement setup was calibrated to the ends of the probes using a calibration substrate, to accurately isolate the response of the device under test. All four electrical S-parameters were measured over a range of DC reverse biases; however, no change in response was observed beyond -2 V. For simplicity, no optical input power was present during the measurements. The characteristic impedance, effective index, and microwave loss were then extracted from the S-parameters using the ABCD matrix method [6].

All devices tested exhibited well behaved transmission line characteristics over the range of 130 MHz to 20 GHz. Fig. 3 shows the variation in characteristic impedance (Z_0) of 14 TW-EAMs with different ridge widths and levels of undercut. Only the impedance measured at 20 GHz (-3-V bias) is shown since there was little variation over the frequency range. The measured values range from 15 to 27 Ω with smaller diode areas exhibiting higher characteristic impedances. The EAMs with the most undercut exhibited the greatest increase in impedance with the exception of the 2.5-μm-wide ridge. In this device, the selective wet etch reduced the active region width to less than 0.9 μm which was not structurally sufficient to support the upper cladding during the rest of the fabrication process. This device also suffered from high series resistance and high optical loss which confirmed that the ridge structure was damaged.

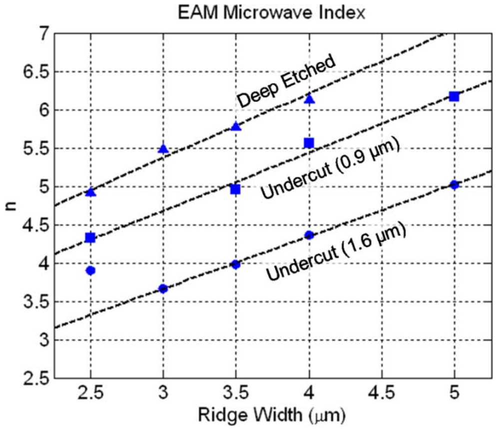

Fig. 4. Measured electrical effective index versus ridge width and undercut.

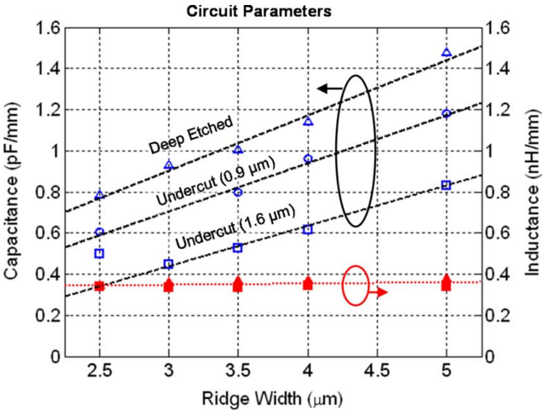

Fig. 5. TW-EAM capacitance and inductance per length.

For InGaAsP–InP-based modulators, the optical group index is approximately 4, whereas the electrical index is typically much higher due to the slow-wave propagation which arises from the diode capacitance, resulting in a velocity mismatch limitation [7]. The measured electrical effective index for the same set of EAMs is shown in Fig. 4. The results show that the reduced capacitance of the narrowed ridge and undercut waveguide significantly lowers the electrical index. In the case of the 3.0-μm ridge, the index is reduced from 5.5 to 3.7 after the undercut etch, demonstrating that the electrical velocity can be designed to exceed the optical velocity.

From the impedance and index measurements, we have also extracted the capacitance and inductance per length of each of the structures (Fig. 5). As expected, the inductance is nearly constant for all of the devices since the metal electrodes are identical but the capacitance becomes significantly lower as the core width is reduced. The minimum capacitance achieved in these devices was 0.45 pF/mm corresponding to a InGaAsP width of 1.4 μm.

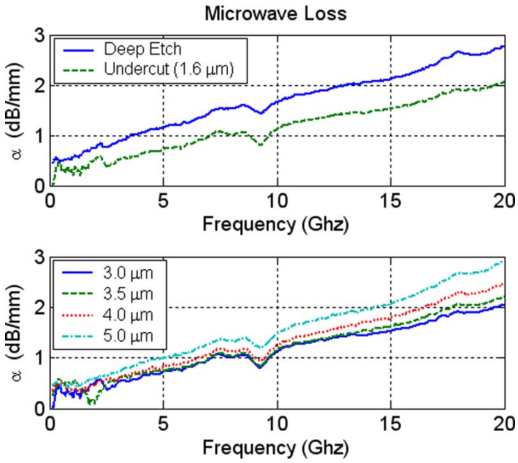

Fig. 6. Microwave loss parameter (α) (upper) comparing deep etched and undercut (1.6 μm) waveguides with for ridge width of 3.0 μm and (lower) comparing ridge width for undercut (1.6 μm) waveguides.

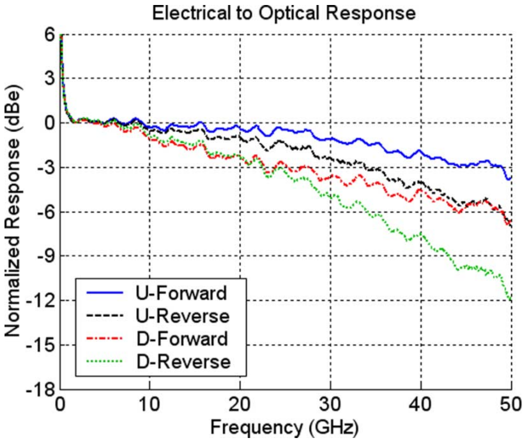

Fig. 7. Small signal E-O response for 3.0-μm deeply etched (D) and undercut (U) (1.6 μm) EAMs. “Forward” denotes copropagation and “Reverse” denotes counterpropagation of electrical and optical waves.

The TW-EAM structure is inherently lossy due to the diode resistance in series with the junction capacitance. However, extraction of the resistance values requires knowing the ratio of internal to external capacitance within the device [8]. Here, we have instead extracted the total microwave loss for both deep etched and undercut EAMs with 3.0-μm cladding and also for the undercut EAMs of varying ridge width (Fig. 6). In both cases, the loss decreases as the active region width is reduced. It is especially worth noting the reduced loss with decreasing ridge width, even though in this case the series diode resistance is higher. This is because α is proportional to $C^{3/2}$ but only linearly proportional to R and is, therefore, dominated by the junction capacitance [3].

IV. ELECTRICAL-TO-OPTICAL (E-O) RESPONSE

To demonstrate that the undercut waveguide is beneficial to the EAM performance, the E-O responses have been compared. The response was measured on devices with a 26-Ω integrated termination to be closely matched to the EAM impedance. The measurement was performed with an Agilent 8364A 50-GHz network analyzer and high-speed photodetector with a known frequency response. Light from an external laser source at 1.55 μm was coupled through the devices both forward and backward to compare the traveling-wave enhanced response. Fig. 7 shows the result of the E-O measurements for the 3.0-μm-wide modulators at -2.0-V reverse bias. In both devices, the increased response below 1 GHz is caused by the low-frequency limit of the on-chip capacitor. The undercut device 3-dB bandwidth is approximately 45 GHz compared with 25 GHz for the deeply etched device. Furthermore, the undercut modulator shows a 10-GHz enhancement in the forward traveling response compared with the reverse measurement, demonstrating the significance of the traveling-wave design.

V. CONCLUSION

We have presented an analysis of the microwave properties of TW-EAMs with selectively undercut active regions. We have shown that reducing the width of the waveguide core raises the characteristic impedance of the electrode by up to 35% and significantly lowers the microwave loss. Furthermore, the selective undercut can be used to reduce the junction capacitance sufficiently to achieve true velocity matching of the electrical and optical traveling waves. Using this fabrication technique, we have increased the 3-dB bandwidth of a 400-μm-long device from 25 to 45 GHz. These improved modulator designs can be incorporated with tunable lasers in future work on high-speed transmitters and monolithic wavelength converters.

REFERENCES

[1] Y.-J. Chiu, T.-H. Wu, W.-C. Cheng, F. Lin, and J. Bowers, “Enhanced performance in traveling-wave electroabsorption modulators based on undercut-etching the active-region,” *IEEE Photon. Technol. Lett.*, vol. 17, no. 10, pp. 2065–2067, Oct. 2005.
[2] H. Fukano, T. Yamanaka, M. Tamura, Y. Kondo, and T. Saitoh, “Very low driving-voltage InGaAlAs/InAlAs electroabsorption modulators operating at 40 Gbit/s,” *Electron. Lett.*, vol. 41, no. 4, pp. 211–212, Feb. 2005.
[3] F.-Z. Lin, Y.-J. Chiu, and T.-H. Wu, “Cladding layer impedance reduction to improve microwave propagation properties in p-i-n waveguides,” *IEEE Photon. Technol. Lett.*, vol. 19, no. 5, pp. 276–278, Mar. 1, 2007.
[4] M. Dummer, M. Sysak, J. Raring, A. Tauke-Pedretti, and L. Coldren, “Integration of a traveling-wave electro-absorption modulator with a widely tunable SG-DBR laser,” in *2007 Int. Conf. Indium Phosphide Related Mater.*, Matsue, May 2007, pp. 602–605.
[5] S. Irmscher, S. Irmscher, R. Lewen, and U. Eriksson, “InP–InGaAsP high-speed traveling-wave electroabsorption modulators with integrated termination resistors,” *IEEE Photon. Technol. Lett.*, vol. 14, no. 7, pp. 923–925, Jul. 2002.
[6] R. Spickermann and N. Dagli, “Experimental analysis of millimeter wave coplanar waveguide slow wave structures on GaAs,” *IEEE Trans. Microw. Theory Tech.*, vol. 42, no. 10, pp. 1918–1924, Oct. 1994.
[7] R. Walker, “High-speed III–V semiconductor intensity modulators,” *IEEE J. Quantum Electron.*, vol. 27, no. 3, pp. 654–667, Mar. 1991.
[8] R. Lewen, S. Irmscher, and U. Eriksson, “Microwave CAD circuit modeling of a traveling-wave electroabsorption modulator,” *IEEE Trans. Microw. Theory Tech.*, vol. 51, no. 4, pp. 1117–1128, Apr. 2003.

Multi-function Integrated InP-Based Photonic Circuits

Larry A. Coldren
ECE and Materials Departments
University of California, Santa Barbara, CA 93106
coldren@ece.ucsb.edu

The recent commercial success of viable multi-funtion InP-based Photonic ICs (PICs)[1,2] has altered the perception of many in the field that such components would continue to be products for the future, products that could not compete with hybrid approaches that could optimally incorporate known-good-die to give superior performance and reliability. Now there would appear to be fairly wide-spread acceptance of some monolithic integration technologies for at least some applications. Reductions in size and weight have not been too surprising, but improvements in cost, power dissipation, reliability, and even performance are the real reasons for these successes. The buzz seems to be that many component vendors are now trying to develop such PICs for a variety of applications.

At the core of most PICs is a basic active-passive waveguide integration technique, and this largely determines the viability of the resulting integration platform. Much of the basic work occurred more than a decade ago[3-5], and this led to a few successes, such as the integration of an electro-absorption modulator (EAM) with a DFB laser (the so-called EML), but until recently there have not been many PICs in production, certainly not 'multi-functional' ones.

In this tutorial a number of integration platforms will be reviewed and discussed[4-6]. Commercial examples as well as some newer proof-of-principle multi-functional PICs will be introduced to evaluate the viability of some of these integration approaches. The pro and cons of each approach will be identified. Some discussion of alternative hybrid integration approaches will also be given.

Figure 1 is an example of a single-chip, widely-tunable, data-format-transparent all-photonic transceiver that incorporates an SOA-PIN receiver with an SGDBR-EAM transmitter[7]. In the example given, the stages are internally connected to provide seemless wavelength conversion with only DC biases applied to the chip. Overall chip gain with some degree of regeneration has been demonstrated with this kind of configuration [8].

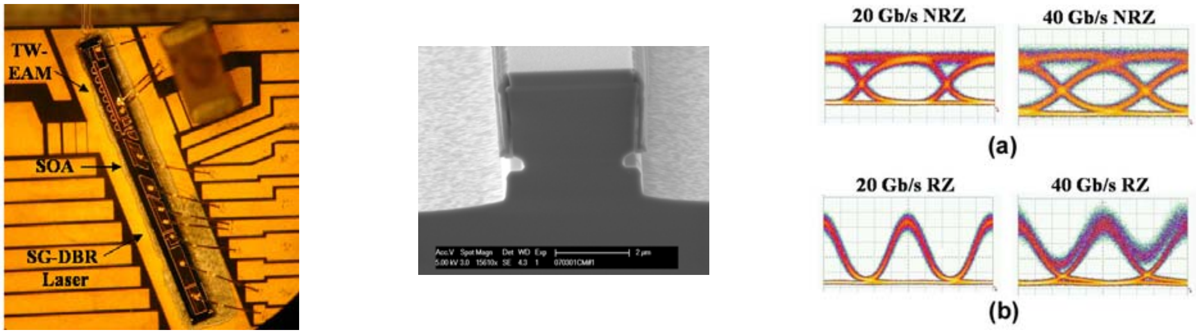

Figure 1. (Left): 5-40Gb/s NRZ or RZ wavelength converter tunable over 40 nm about 1550 nm. (Center): Cross section of a periodically-loaded, traveling-wave EAM with an undercut waveguide. (Right): Converted outputs at 20 and 40 Gb/s for (a) NRZ or (b) RZ.

I would like to acknowledge the inputs from my students and many other colleagues in the field, especially Chris Doerr at Alcatel-Lucent.

References:

[1] Y.A. Akulova, G.A. Fish, H. Xu, E. Hall, M.C. Larson, P. Abraham, H. Marchand, et al, *Proc. IPRA*, paper IWF4, San Diego (2005).
[2] R. Nagarajan, C.H. Joyner, R.P. Schneider, et al, *IEEE J. Selected Topics in Quantum Electronics (JSTQE)*, **11** (1) 50-65 (2005).
[3] M. Suzuki, Y. Noda, H. Tanaka, S. Akiba, Y. Kushiro, and H. Isshiki, *IEEE J. Lightwave Tech.*, **LT-5**, 1277-1285 (1987)
[4] W.C. Dautremont-Smith, R. J. McCoy, R.H. Burton, and A.G. Baca, *AT&T Tech. J.*, **68**, 64-82 (1989).
[5] T. L. Koch and U. Koren, *IEEE J. Quantum Electronics*, **QE-27**, 641-653 (1991).
[6] J. W. Raring and L. A. Coldren, *IEEE Journal of Selected Topics in Quantum Electronics*, **13** (1) 3-14 (2007).
[7] M.M. Dummer, M.N. Sysak, A. Tauke-Pedretti, J.W. Raring, J. Klamkin, and L.A. Coldren, *J. Lightwave Tech*., **26**, (8) 938-944 (2008).
[8] M.N. Sysak, J. W. Raring, J.S. Barton, H.N. Poulsen, D.J.Blumenthal, and L.A. Coldren, *J. Lightwave Tech*., **25** (12) 3748-37-59 (2007).

Multi-function Integrated InP-Based Photonic Circuits

ECOC'08 Tutorial

Larry A. Coldren
ECE and Materials Departments
University of California, Santa Barbara, CA 93106
coldren@ece.ucsb.edu

Acknowledgements: Chris Doerr, Alcatel-Lucent; Chuck Joyner, Infinera; UCSB colleagues

---

Outline/Contents

- Integration Platforms/Technology
- Transmitters
- Receivers
- Transceivers/Wavelength Converters
- Conclusions

Indium phosphide

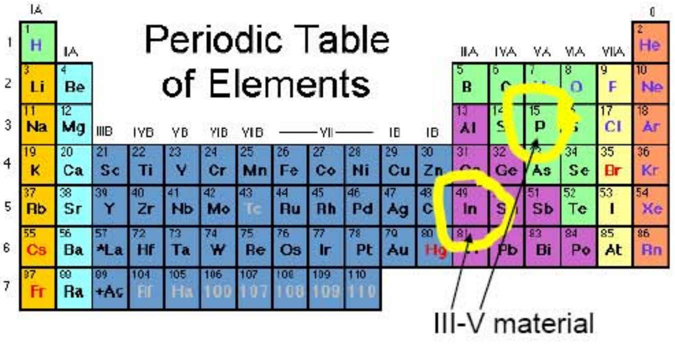

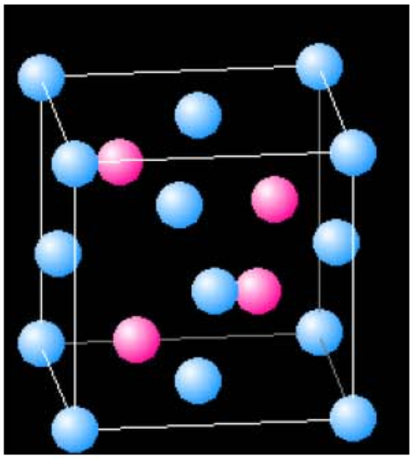

Zincblende structure

(two intersecting FCC lattices, one for In and one for P)

Lattice constant = 5.87 A at 300K

InGaAsP/InP lattice-matched alloys

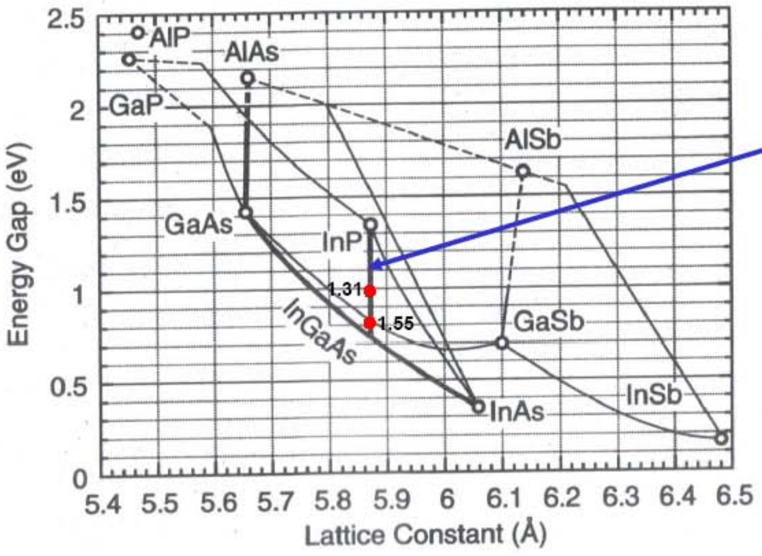

InGaAsP lattice-matched to InP

$\lambda_g(\mu\text{m}) = 1.24 / E_g(\text{eV})$

Lateral waveguides/couplers

Waveguide cross sections

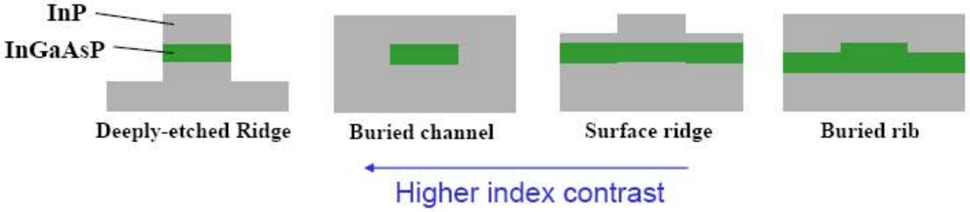

MMI coupler

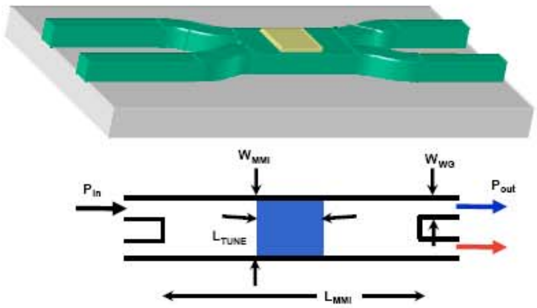

Modulators

Electro-absorption modulator (EAM)

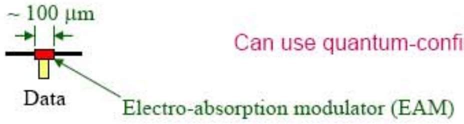

Can use quantum-confined Stark effect for large Δα

Mach-Zehnder modulator (MZM) lumped

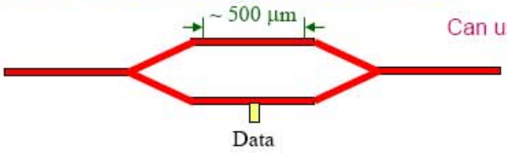

Can use quantum-confined Stark effect with larger Δλ

Traveling-wave linear phase modulator

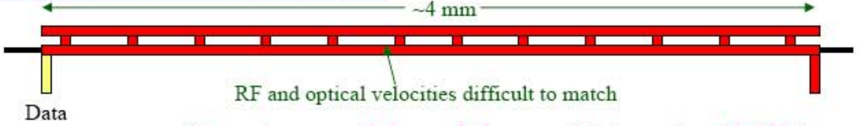

(Can get away with lumped phase modulator up to ~10 GHz)
(Also, current injection for < 1 GHz)

Active-Passive (axial) Integration

Desire lossless, reflectionless transitions between sections

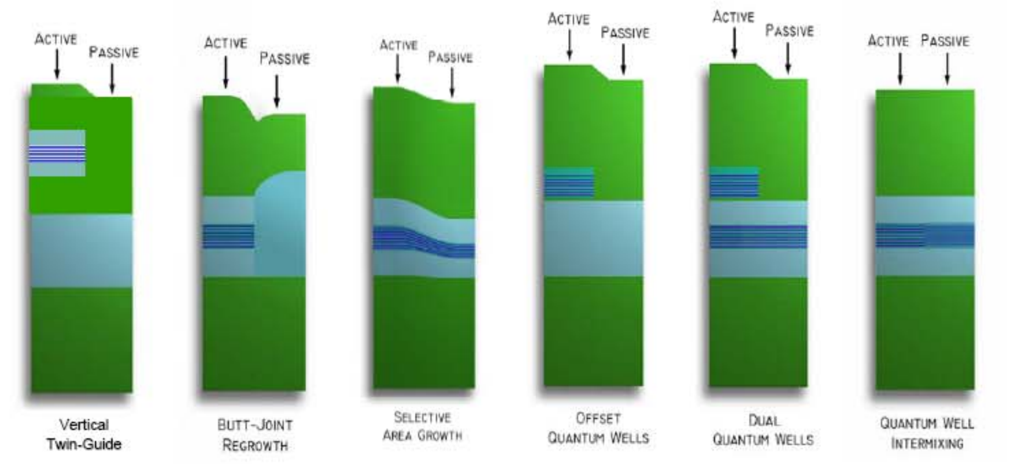

Partially transmissive mirrors

- **Coupling mirrors between integrated active and passive sections**

→ Etched grooves

- **Tunable single frequency**
- **Laser-modulator**
- **Laser-detector**

L.A. Coldren, B.I. Miller, K. Iga, and J.A. Rentschler, "Monolithic two-section GaInAsP/InP active-optical-resonator devices formed by RIE," *Appl. Phys. Letts.*, **38** (5) 315-7 (March, 1981).

→ DBR gratings and vertical couplers

- **Tunable single frequency**
- **Combined integration technologies**

Y. Tohmori, Y. Suematsu, Y. Tushima, and S. Arai, "Wavelength tuning of GaInAsP/InP integrated laser with butt-jointed built-in DBR," *Electron. Lett.*, **19** (17) 656-7 (1983).

First integrated InP (laser – X) devices

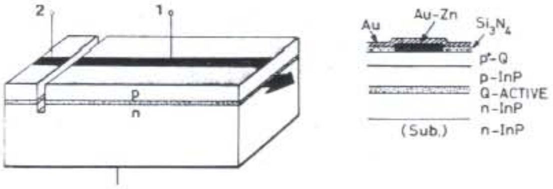

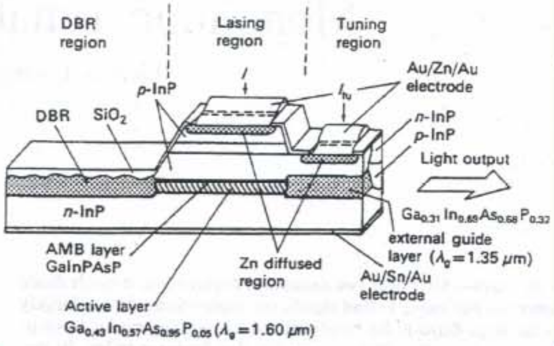

QWI For Multiple-Band Edges/Single Growth

- Simple/robust QWI process
  - Ability to achieve multiple band edges with a single implant

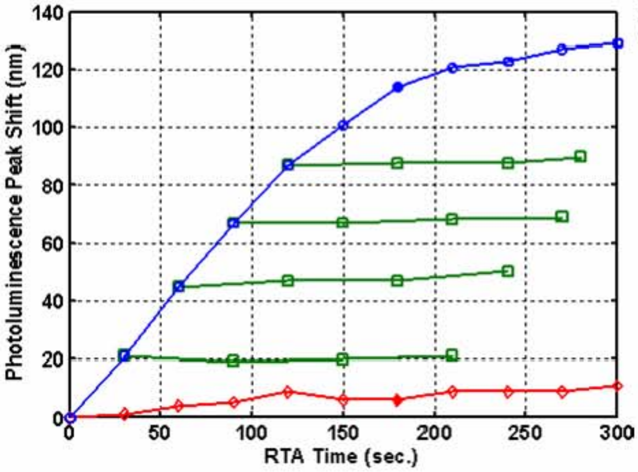

E. Skogen et al, "Post-Growth Control of the Quantum-Well Band Edge for the Monolithic Integration of Widely-Tunable Lasers and Electroabsorption Modulators," *IEEE J. Sel. Top. Quantum Electron.*

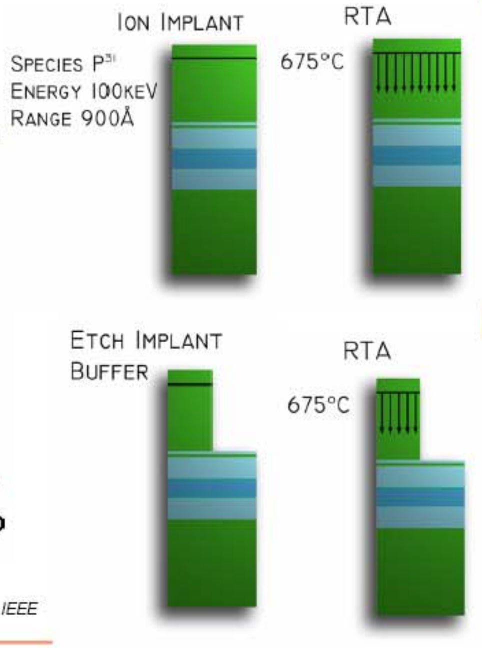

PIC Transmitters

Early PIC transmitter: EML

EML = electroabsorption-modulated laser

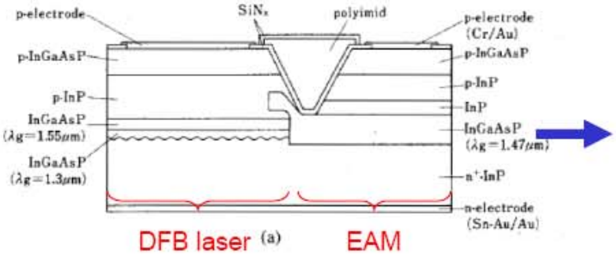

M. Suzuki, et al., *J. Lightwave Technol.*, **LT-5**, pp. 1277-1285, 1987.

Early PIC with wavelength-selectable laser and EAM

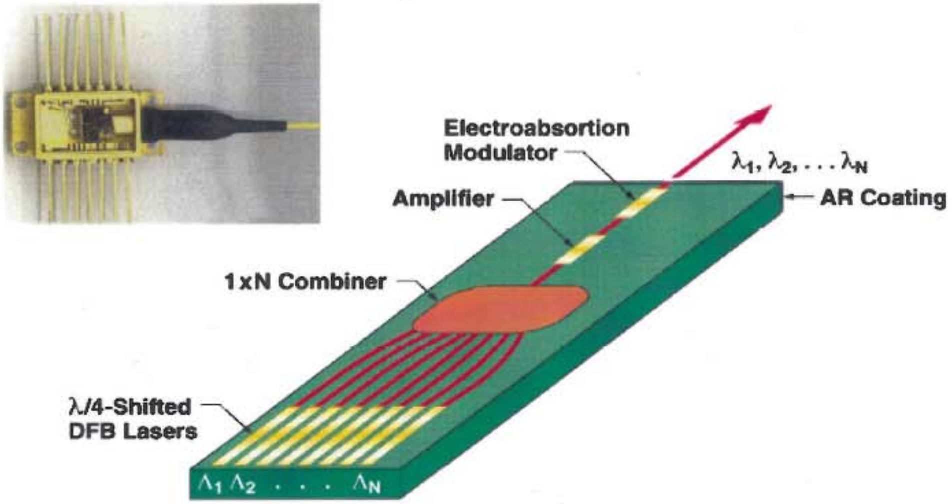

M. G. Young, et al., *Electron. Lett.*, **31**, pp. 1835-1836, 1995.

Early PIC with widely-tunable laser and EA or MZ-modulator

SGDBR+X: (UCSB'91-'08 → Agility'99-'05 → JDSU'05→)

- Vernier sampled DBRs and phase set wavelength
- External SOA controls amplitude

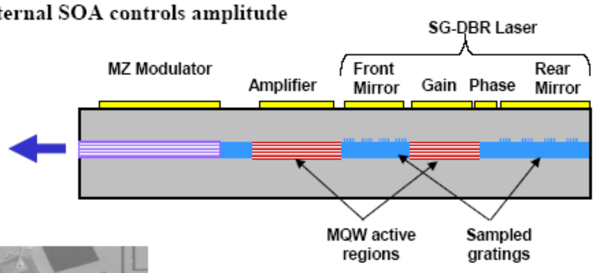

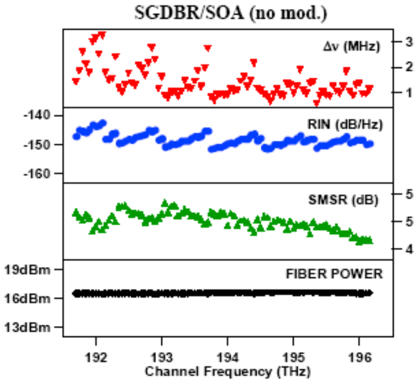

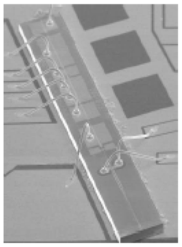

10 Gb/s Optical Duobinary Transmission

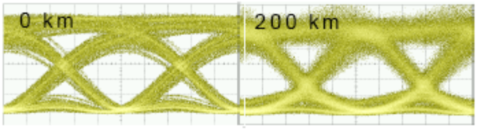

Courtesy of JDSU
+
UCSB

L.A. Johansson, L.A. Coldren, P.C. Koh, Y.A. Akulova, and G.A. Fish, "Transmission of 10 Gbps Duobinary Signals Using an Integrated Laser-Mach Zehnder Modulator" *Optical Fiber Commmication* (*OFC*), paper no. OThC4, San Diego, CA, MARCH, 2008

SGDBR- Mach-Zehnder transmitter stage of transceiver (wavelength converter)

Series-push-pull SGDBR-MZ transmitter

- Integrated load R and bypass C
- 30 GHz Bandwidth
- 40 Gb/s error free operation
- Low/negative chirp

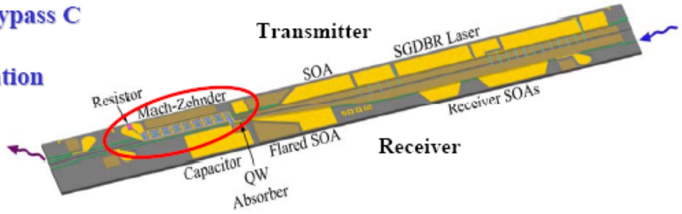

DQW

MZ small-signal bandwidth

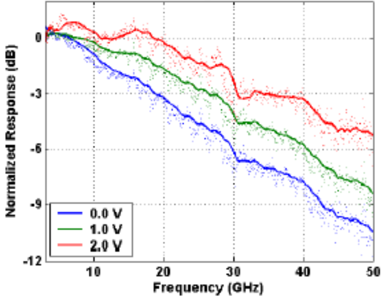

40 Gb/s eyes

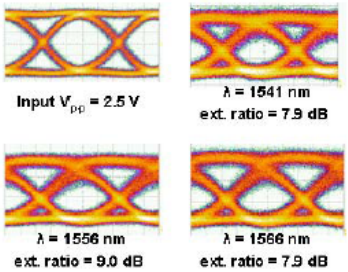

Negative chirp result

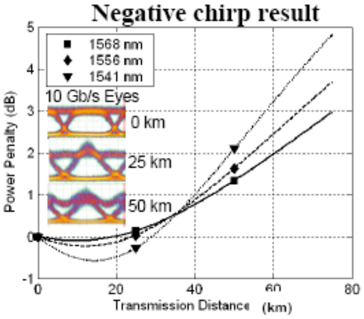

A. Tauke-Pedretti, M.N. Sysak, J.S. Barton, L.A. Johansson, J.W.Raring, and L.A. Coldren, "40 Gbps series-push-pull Mach-Zehnder Transmitter on a dual-QW integration platform," *Photon. Tech. Lett.*, **18** (18) 1922-4 (2006).

40 Gb/s SGDBR/TW-EAM

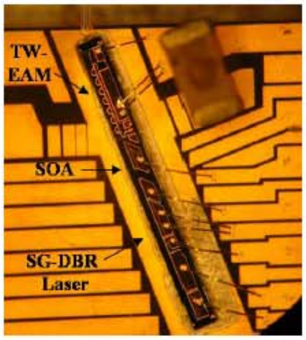

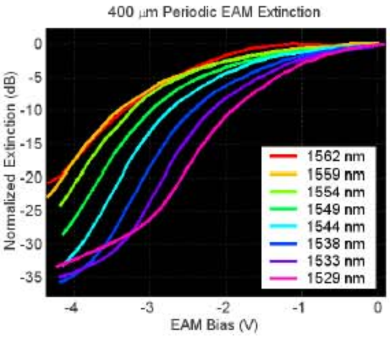

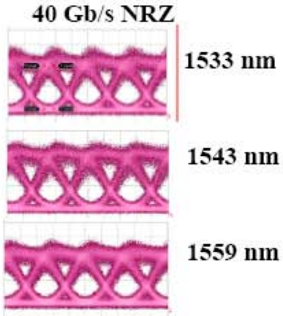

- Integration of traveling-wave EAM designs with SG-DBR laser
- Modulation efficiency 15 – 20 dB/V over the tuning range
- Open eyes at 40 Gb/s for all wavelengths
  - 6 – 10 dB extinction with 2.1V

M. M. Dummer, J.Klamkin, E. J. Norberg, J. W. Raring, A. Tauke-Pedretti, and L A. Coldren, " Periodic Loading and Selective Undercut Etching for High-Impedance Traveling-Wave Electroabsorption Modulators", *OFC'08*, March, 2008.

Recent multi-channel transmitter PIC

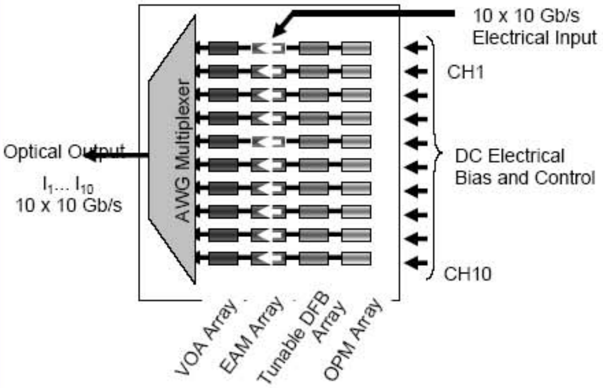

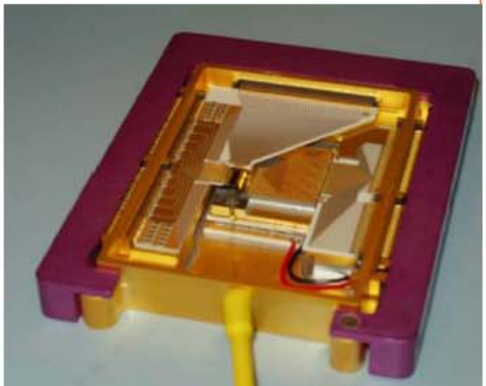

R. Nagarajan, et al., *Sel. Top. Quant. Electron.,* **11**, pp. 50-65, 2005.

Slide courtesy of C. Joyner

Multi-channel transmitter results

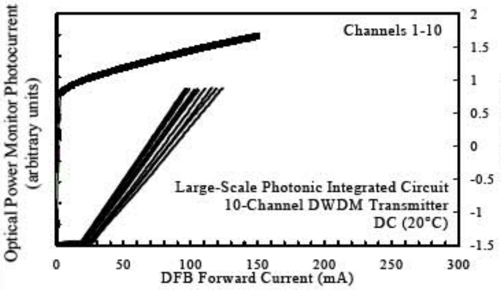

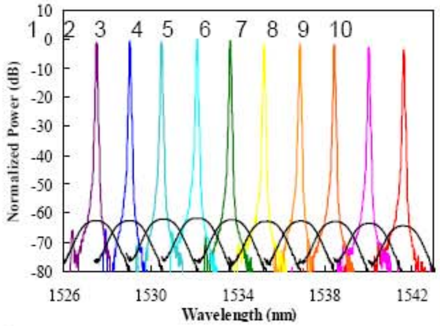

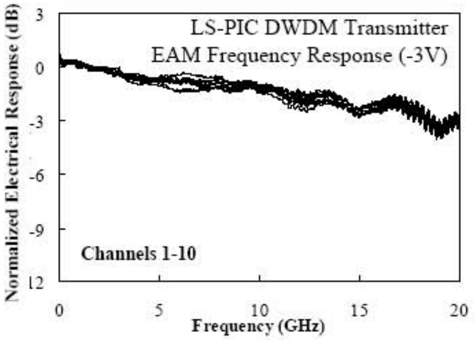

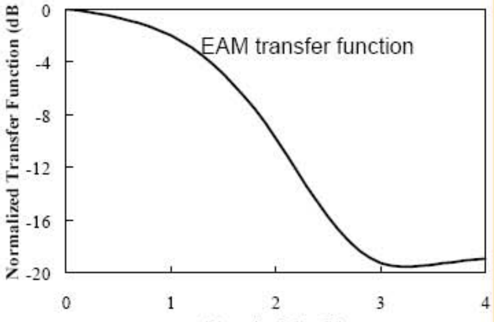

Slide courtesy of C. Joyner

Infinera

Traveling-wave MZM DQPSK PIC

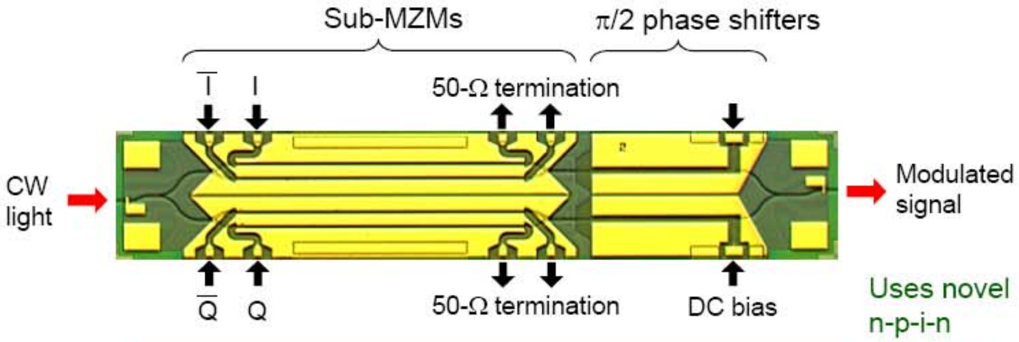

Uses novel n-p-i-n structure

Wavelength range: L-band (λ_{PL} = 1.47 μm)
RF input: Differential
EO interaction length: 3 mm (Sub-MZMs),
1.5 mm (π/2-phase shifter)
Chip size: **7.5 mm x 1.3 mm**

Courtesy of N. Kikuchi NTT

N. Kikuchi, *ECOC*, 10.3.1, 2007.

TW-MZM DQPSK Results

Driving voltage: 3 V_{pp} (V_{π}) for each

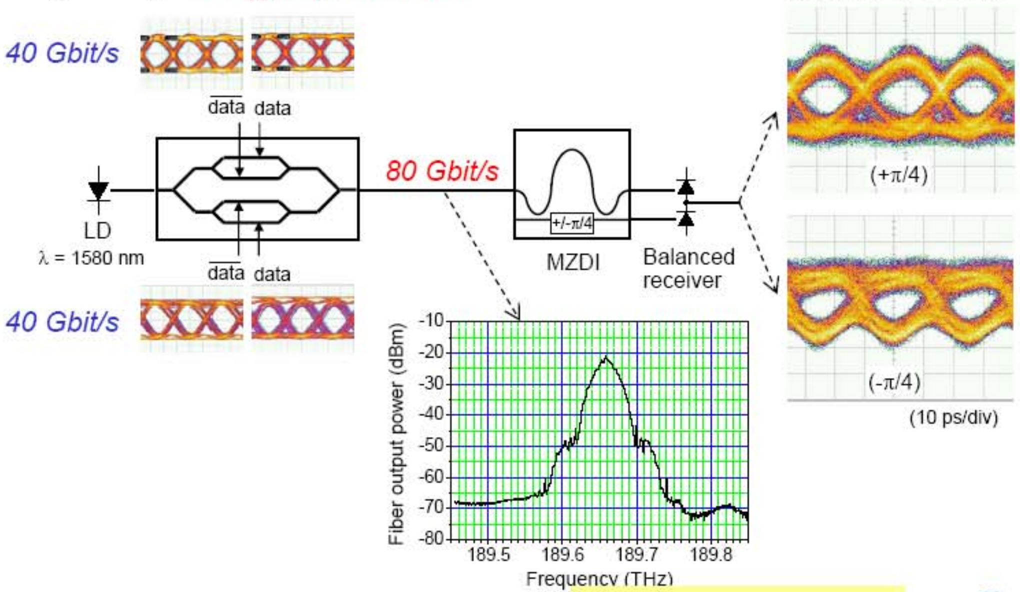

Slide courtesy of N. Kikuchi **NTT**

Recent InP DQPSK modulator PIC

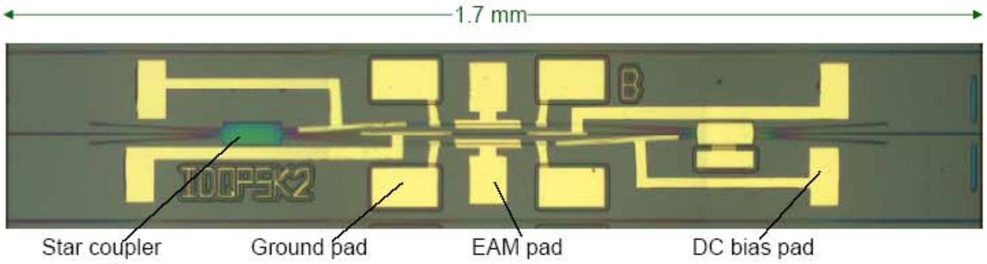

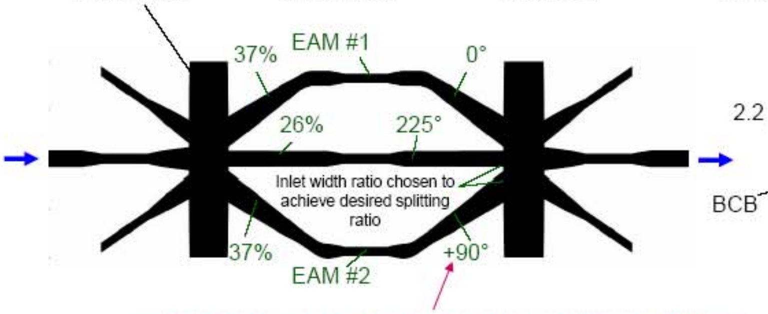

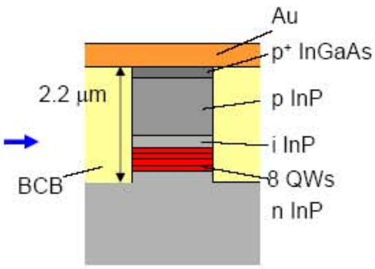

Set to 90° bias by design (using extra path length in one arm)

C. R. Doerr, et al., *OFC*, PDP33, 2007.

DQPSK modulator results

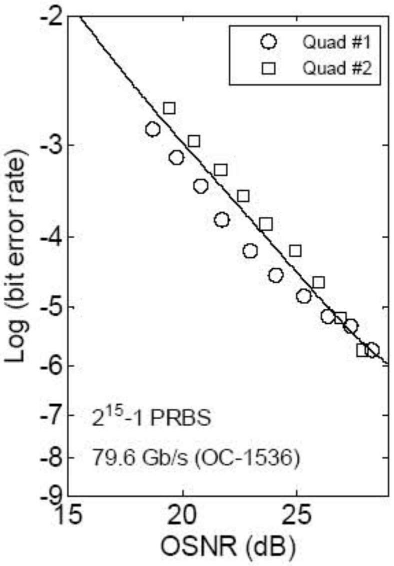

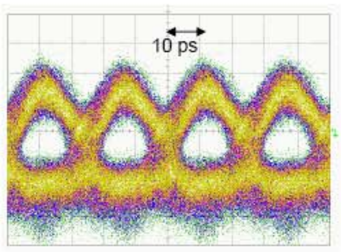

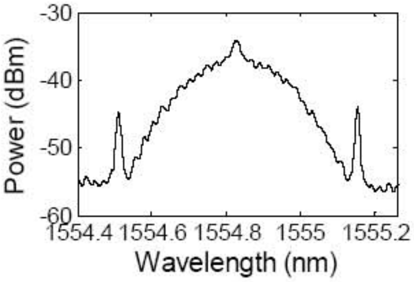

C. R. Doerr, et al., *OFC,* PDP33, 2007.

Receivers

Early PIC multi-wavelength receiver

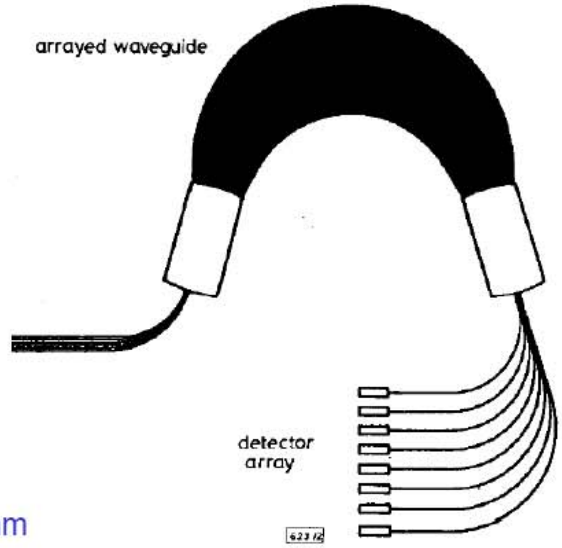

8 × 2 nm

J. B. D. Soole, et. al., *Electron. Lett.*, pp. 1289-1290, 1995.

Recent multi-channel receiver PIC

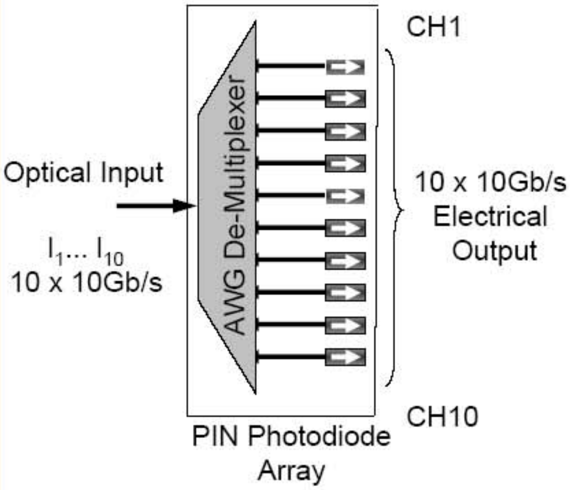
CH1

Optical Input

$l_1 \ldots l_{10}$
10 x 10Gb/s

AWG De-Multiplexer

10 x 10Gb/s
Electrical
Output

CH10

PIN Photodiode
Array

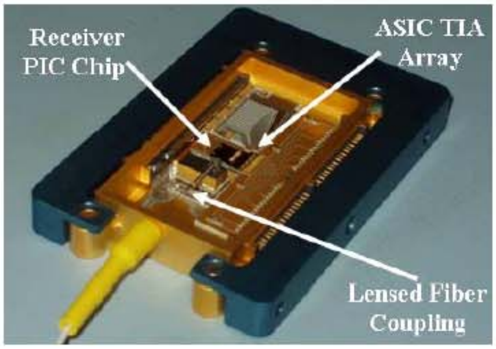

Slide courtesy of C. Joyner

R. Nagarajan, et al., *Sel. Top. Quant. Electron.*, **11**, pp. 50-65, 2005.

Multi-channel receiver results

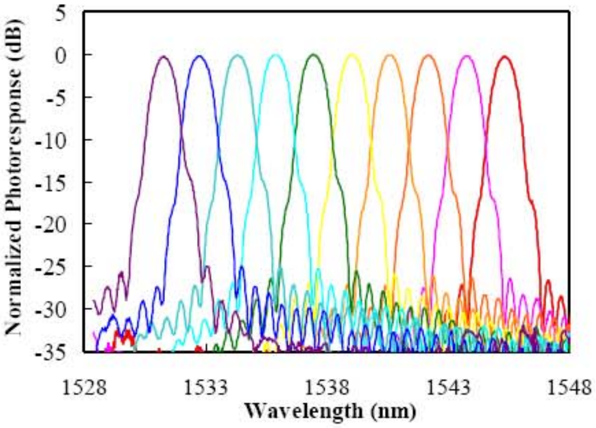

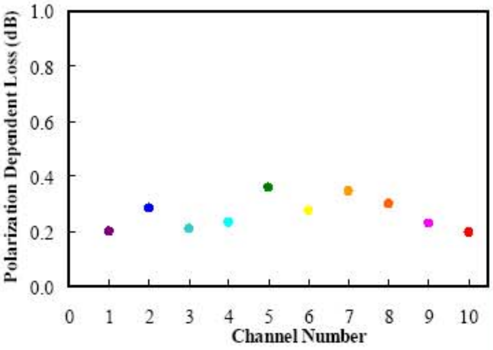

Slide courtesy of C. Joyner

Early heterodyne receiver PIC

Heterodyne receiver
for coherent

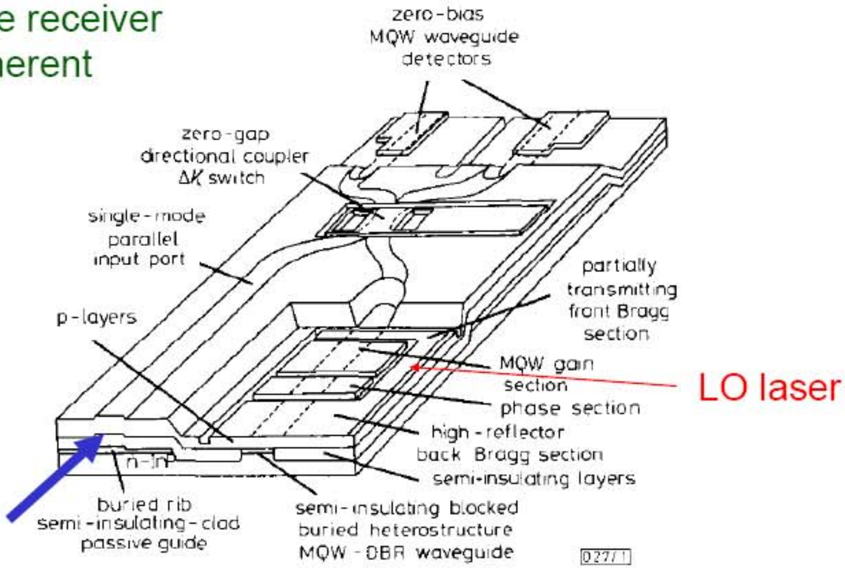

T. L. Koch, et al., *Electron. Lett.,* **25**, pp. 1621-1622, 1989.

Also, H. Takeuchi, et al., *IEEE Photon. Tech. Lett.,* **1**, pp. 398-400, 1989.

Balanced receiver for phase modulated signals

with feedback—NEED for OEICs!!

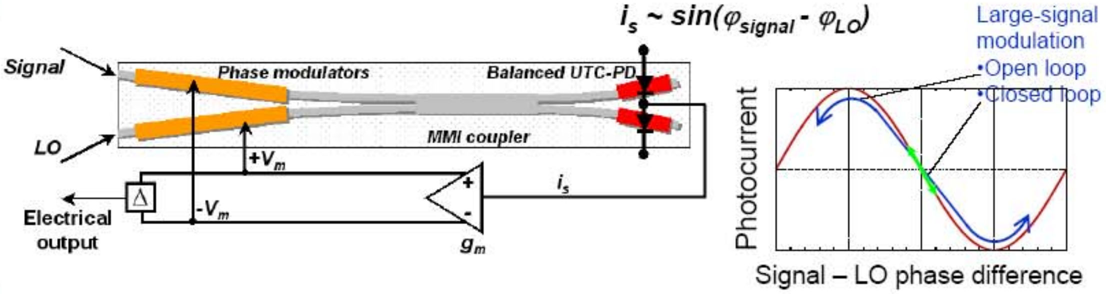

- Signal mixed with local oscillator to demodulate optical phase
  - Detected differential photocurrent represents signal-LO phase difference
  - Response of interferometer based demodulator is sinusoidal
- With feedback the differential photocurrent is reduced by the loop gain: $1/(1+T)$
  - Hybrid integrated EIC* provides transconductance amplification
  - Closely track received optical phase to operate within linear regime
  - NEED VERY SHORT FEEDBACK PATH

L.A. Johansson, H.F. Chou, A. Ramaswamy, L. A. Coldren, and J.E. Bowers, "Coherent optical receiver for linear optical phase demodulation," *Proc. MTT-S Microwave Sym.*, Tu3D-01 (June, 2007).

QWI/offset absorber PIC PM receiver

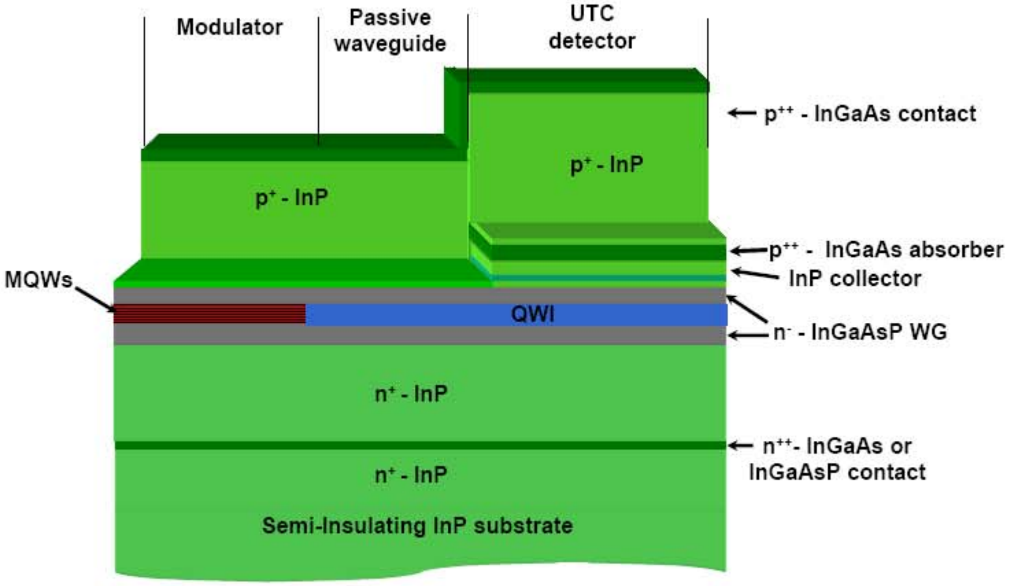

Balanced UTC-PD design

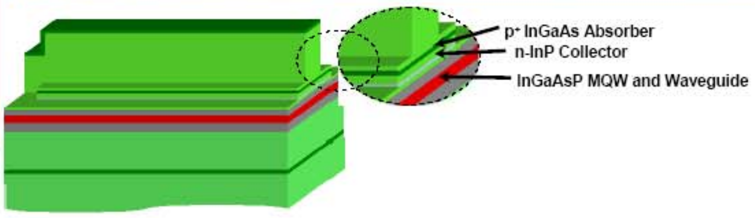

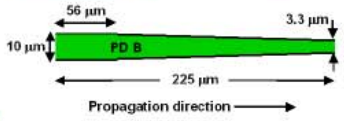

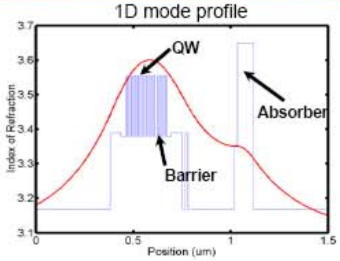

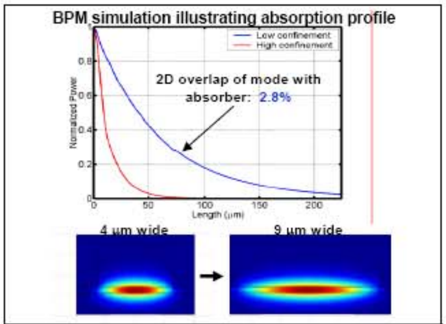

Long absorption profile and wide input reduce front end saturation

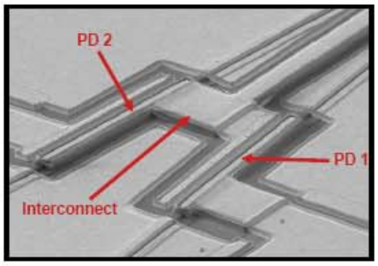

J. Klamkin, A. Ramaswamy, L. A. Johansson, H-F Chou, M.N. Sysak, J. W. Raring, N. Parthasarathy, S.P. DenBaars, J.E. Bowers, and L. A. Coldren, "High-output-saturation and high-linearity uni-traveling-carrier waveguide photodiodes," *Photonics Tech. Letts.* **19** (3) 149-151 (Feb. 2007).

Linearity Results

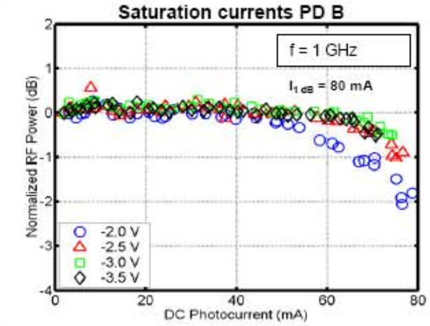

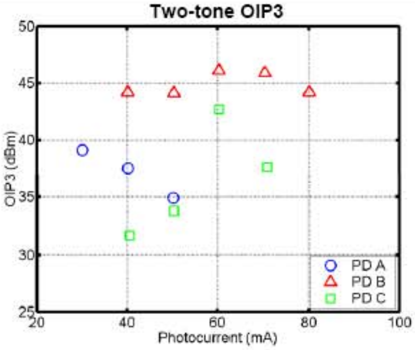

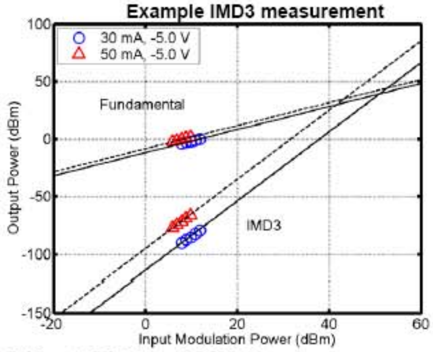

PD B: OIP3 = 46.1 dBm at 60 mA
44.2 dBm at 80 mA

*Record OIP3 for a WG PD

Phase modulator design

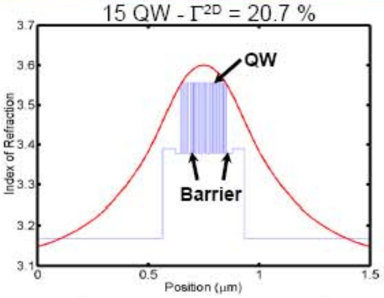

V_π^{DC} = 2.1 V•mm

Push-pull modulation

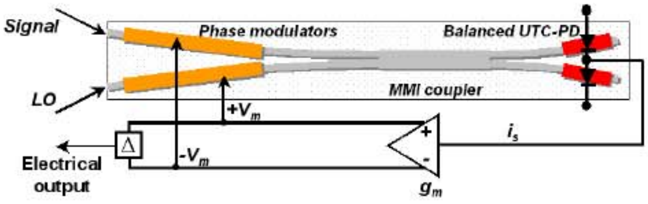

- **Linear term doubled, even order terms cancelled**
- **Third order distortion suppressed with bias optimization**

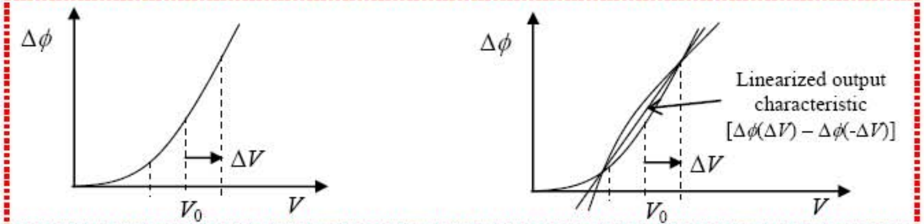

Tranceivers/wavelength converters

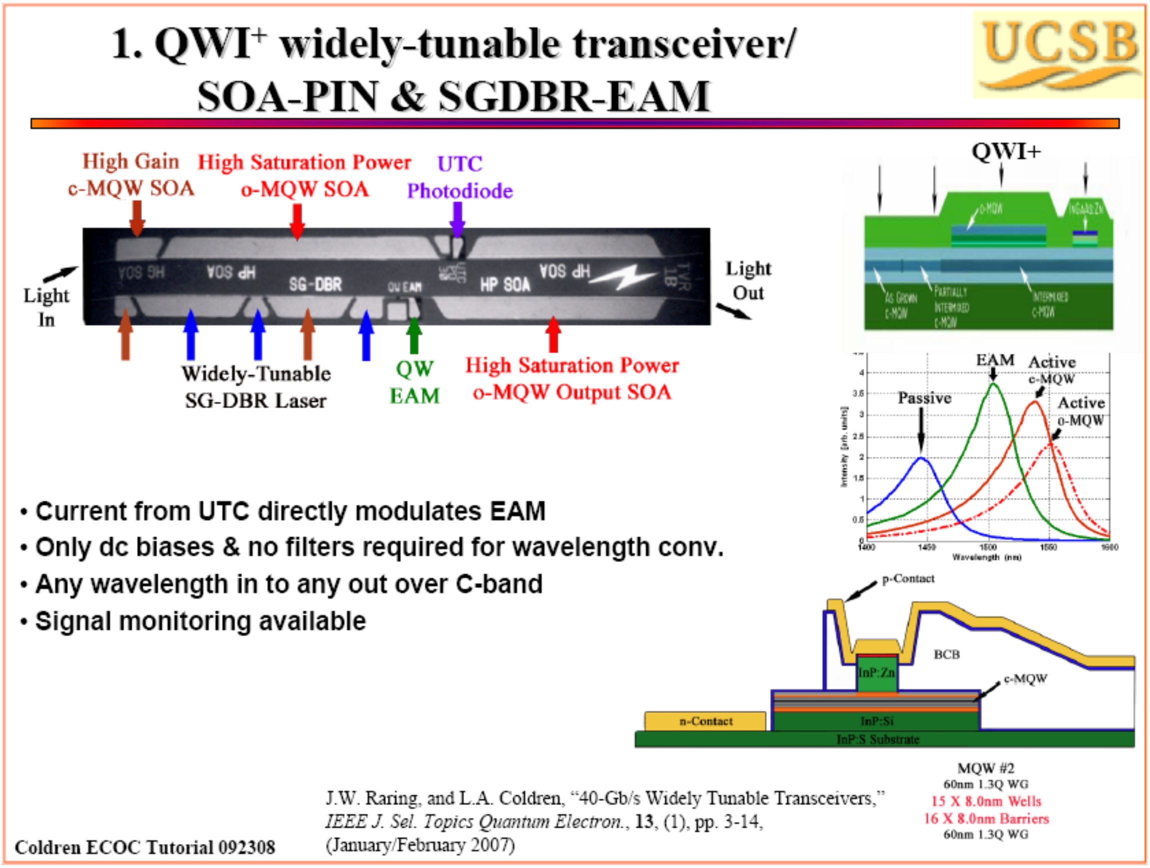

1. QWI+ widely-tunable transceiver/ SOA-PIN & SGDBR-EAM

- Current from UTC directly modulates EAM
- Only dc biases & no filters required for wavelength conv.
- Any wavelength in to any out over C-band
- Signal monitoring available

J.W. Raring, and L.A. Coldren, "40-Gb/s Widely Tunable Transceivers," *IEEE J. Sel. Topics Quantum Electron.*, **13**, (1), pp. 3-14, (January/February 2007)

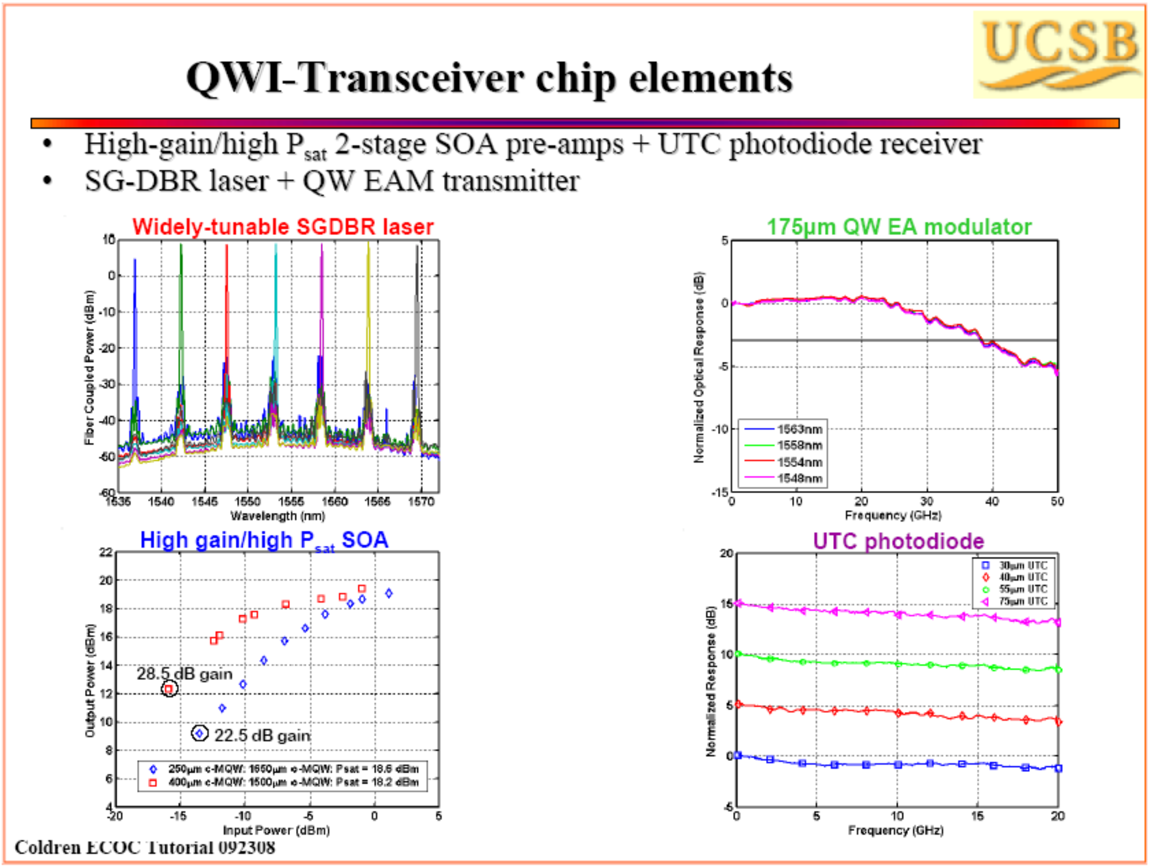

QWI-Transceiver chip elements

- High-gain/high P_{sat} 2-stage SOA pre-amps + UTC photodiode receiver
- SG-DBR laser + QW EAM transmitter

QWI$^+$ transceiver 40 Gb/s transmit and receive functionality

- Transmitter: 175µm EAM
- DC = 2.5-4.5V: V_{PtoP} = 2.5
- Receiver: 400 µm high-gain SOA with 40µm UTC

40 Gb/s TRANSMITTER EYES:

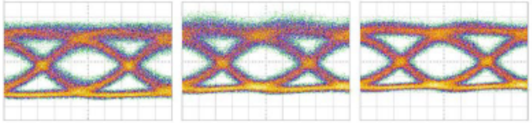

1547nm: E.R.=10.3 1554nm: E.R.=12.0 1565nm: E.R.=10.5

40 Gb/s RECEIVER EYES:

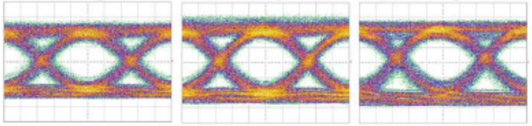

1550nm: Amp =300mV 1550nm: Amp =350mV 1550nm: Amp =500mV

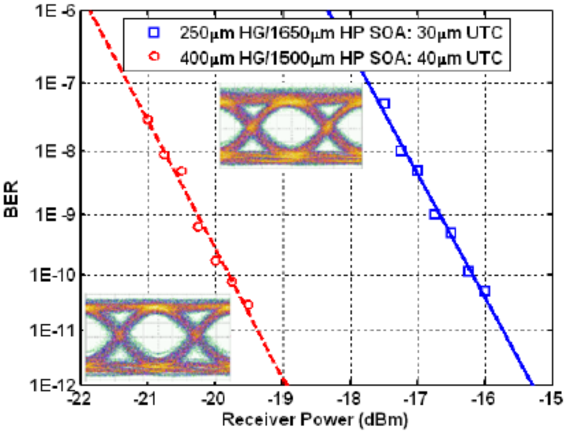

---

2. Wavelength converter/SOA-PIN receiver & SGDBR-Mach Zehnder transmitter

- **Photocurrent driven**
- **35 µm QW absorption region in receiver**
  - **Tapered for reduced capacitance**
- **300 µm traveling-wave Mach-Zehnder modulation region**
  - **Series-push-pull design to maximize bandwidth**
- **Data format and rate transparent**
- **No optical filter required**
- **Integrated termination resistor and bypass Capacitor**
  - **No external bias tees used**

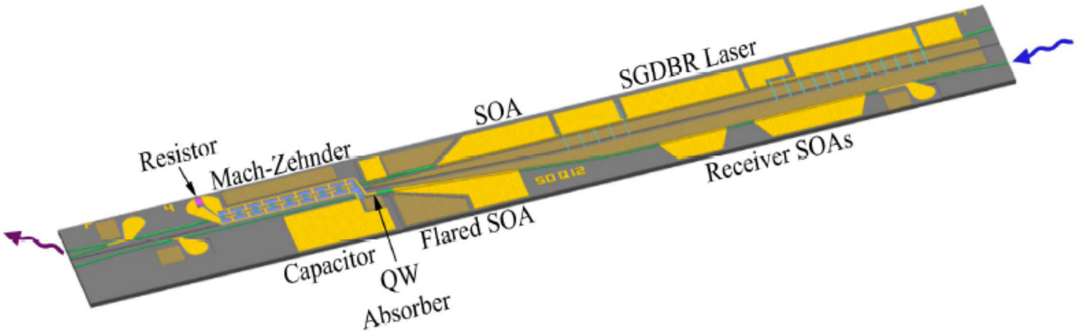

Simple offset QW integration platform

Use simplest integration platform to do the job

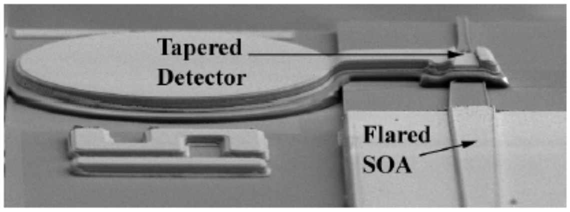

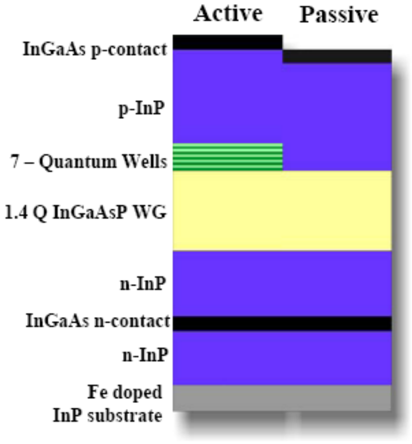

- **Receiver SOA**
  - **Offset quantum wells provide gain (23 dB achieved)**
  - **Linearly flared waveguide (16 dBm P_{sat})**
  - **13 dBm (20mW) → 1 V rms (2.8 V_{pp}) over 50 Ω**
- **Quantum-well PIN detector**
  - **Reverse biased laser QW provide high absorption coefficient**
  - **Wide front end prevents saturation**
  - **Tapering reduces capacitance**

A. Tauke-Pedretti, M.M. Dummer, M.N. Sysak, J.S. Barton, J.W. Raring, J. Klamkin, and L.A. Coldren, "Monolithic 40 Gbps Separate Absorption and Modulation Mach-Zehnder Wavelength Converter," *Proc. OFC*, paper no. PDP36, Anaheim, CA (March 25-29, 2007)

Mach-Zehnder Wavelength Converter

Current from absorber drives SPP-MZM

WC Performance

- **40 Gb/s NRZ operation**
- **<2.5 power penalty for varying input and output wavelengths**

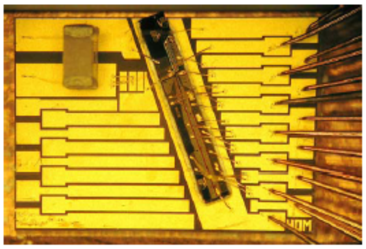

DQW

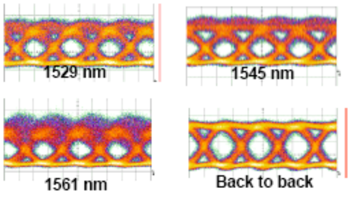

Constant input to varying output

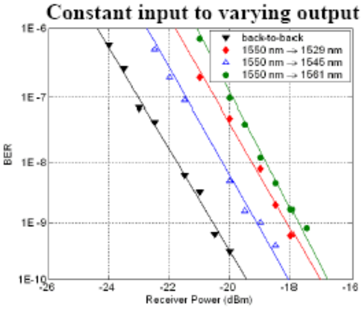

Varying input to constant output

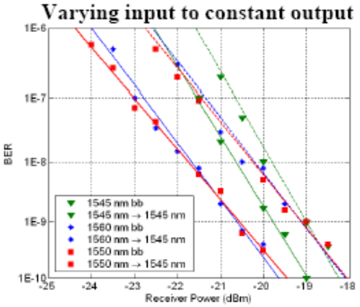

A. Tauke-Pedretti, M.M. Dummer, M.N. Sysak, J.S. Barton, J. Klamkin, J.W. Raring and L.A. Coldren, "Separate Absorption and Modulation Mach-Zender Wavelength Converter," *J. Lightwave Tech.*, **26**, (1), 91-98 (Jan. 2008)

4. SOA-PIN & SGDBR-TW/EAM wavelength converter

- Data format and rate transparent 5-40Gb/s
- No filters required (same λ in and out possible)
- On-chip signal monitor
- Two-stage SOA pre-amp for high sensitivity, efficiency and linearity
- Traveling-wave EAM with on chip loads
- Only DC biases applied to chip
- 40 nm wavelength tuning range

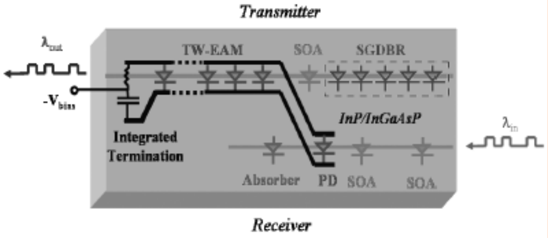

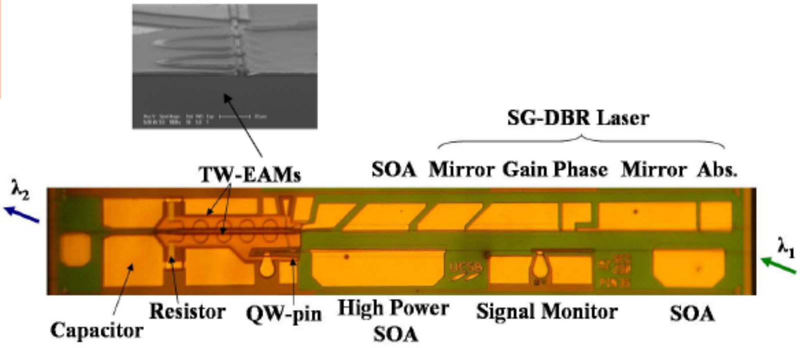

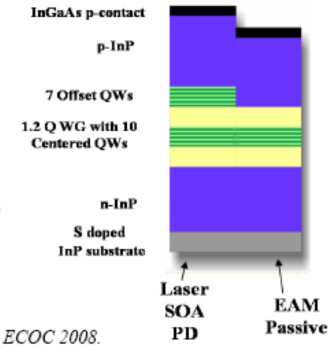

M. Dummer et al. *OFC 2008* OThC6 (2008), and Invited paper, *ECOC 2008*.

SGDBR/TW-EAM WC RF/DATA Characteristics

Eye Diagrams

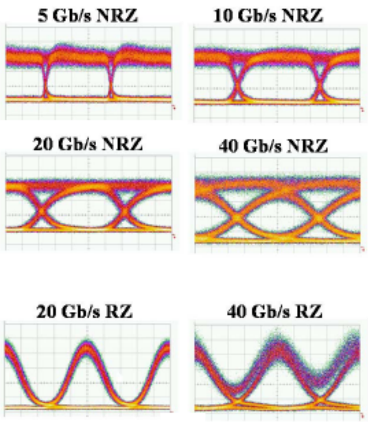

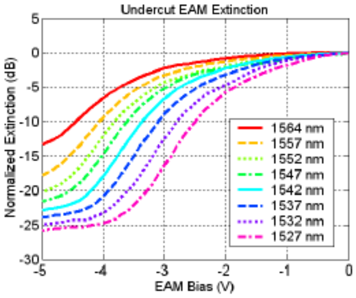

Bit-Error-Rate

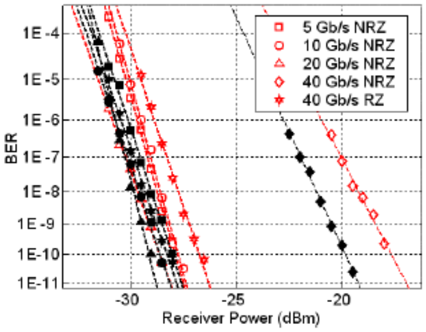

Wavelength converted (1560 to 1548 nm) bit error ratio (open symbols) compared with back-to-back transmission (solid symbols) (1548 nm) for PRBS 2^{31}-1 data at various bit rates

5. SOA-MZI Wavelength Converter PICs: 40 Gb/s Packet Forwarding Chip

- **Fast Tunable SGDBR Laser**
- **Differential Mach-Zehnder Interferometer SOA Wavelength Converter (‘all-optical’)**
- **Preamplifier SOAs**
- **Integrated delay**

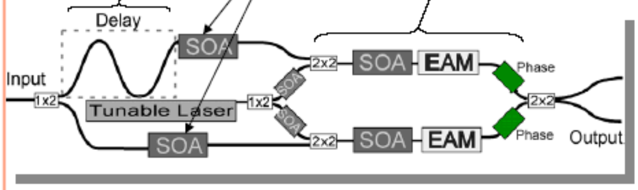

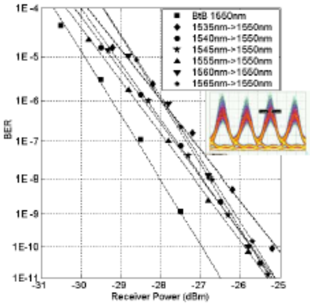

OQW & Butt-joint regrowth

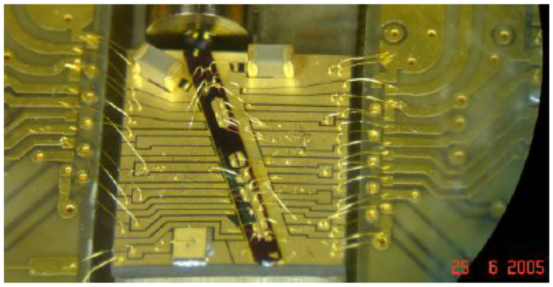

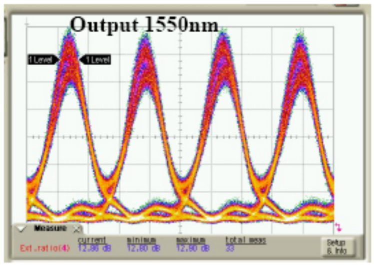

V. Lal, M. L. Masanovic, J. A. Summers, G. Fish, and D. J. Blumenthal, "Monolithic Wavelength Converters for High-Speed Packet-Switched Optical Networks," *JSTQE*, **13**, pp. 49-57, 2007.

---

6. Tunable wavelength converter using AWG-laser + SOA + filter

- Fast-tunable 40G wavelength converter
  - – 8-channel multi-frequency laser (MFL)
  - – λ-conversion via <u>nonlinear SOA</u> and delay filter

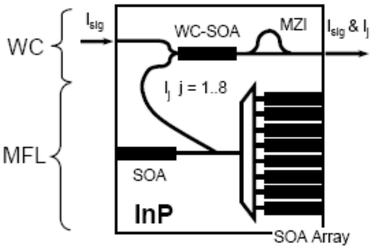

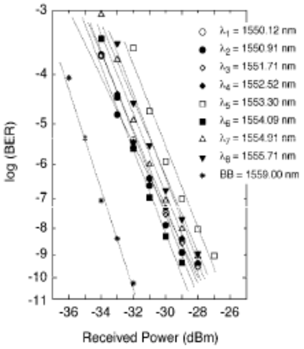

Converted optical eye diagram at 40 Gb/s

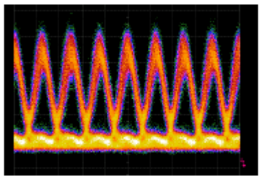

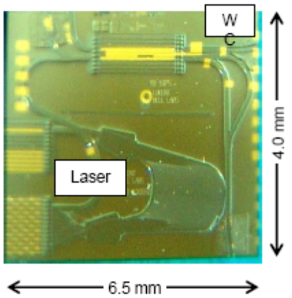

P. Bernasconi, et al., PDP16, *OFC* 2005.

Slide courtesy of P. Bernasconi
Alcatel-Lucent—IRIS Project

Packet Switching Technology

2-Stage Tunable Wavelength Converters

- **First stage generates known out of band wavelength to avoid need for filters and provide known input wavelength to output stage for improved efficiency**

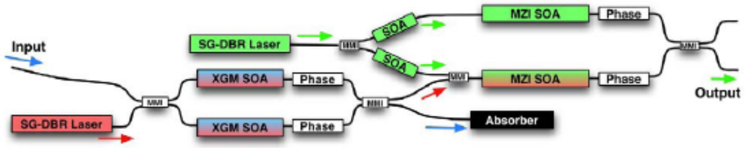

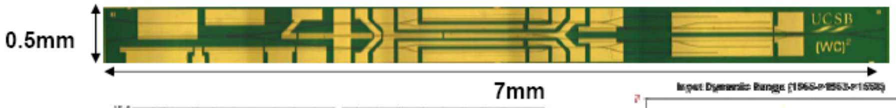

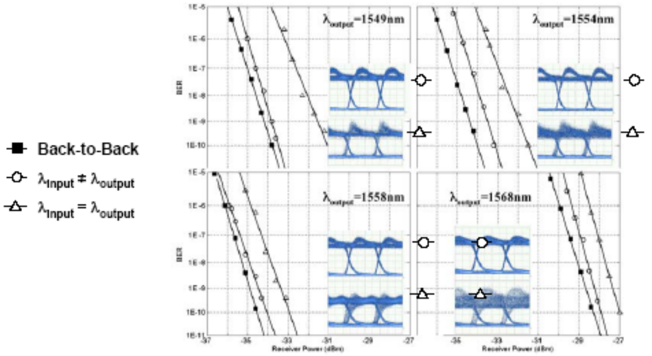

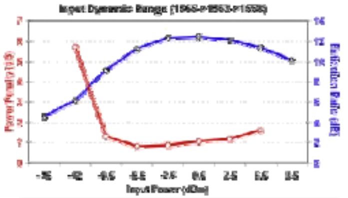

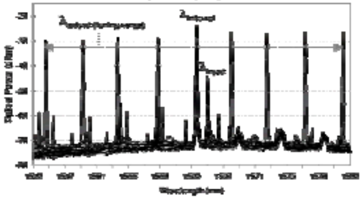

OFC 2007: OThT2: Monolithically Integrated Multi-Stage All-Optical 10Gbps Push-Pull Wavelength Converter, *Joseph A. Summers, Milan L. Masanovic, Vikrant Lal, Daniel J. Blumenthal*

Packet Forwarding Chip (PFC) - Packet λ-Conversion and Optical Label Re-Write

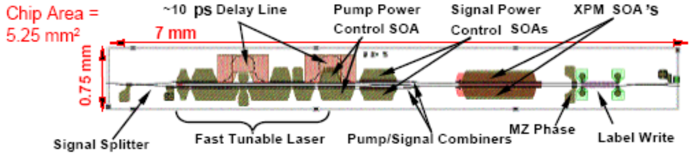

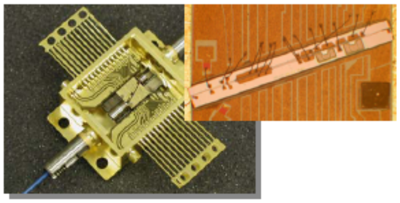

Variable Length Packets and Dynamic Forwarding

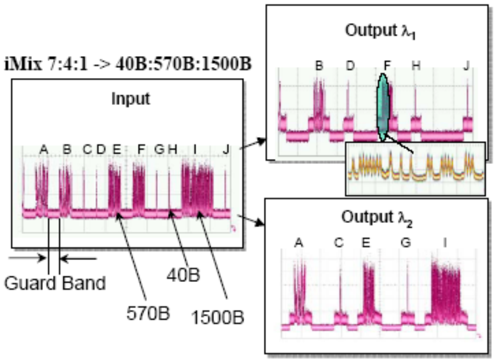

10G Optical Header Re-Write

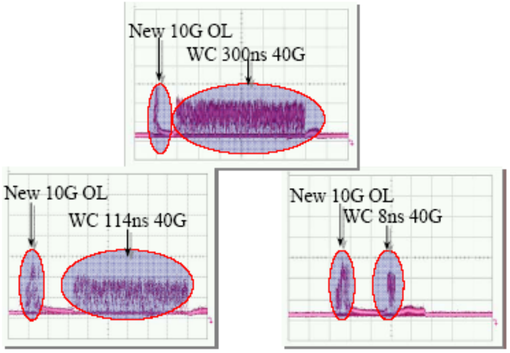

"Monolithic Widely Tunable Optical Packet Forwarding Chip in InP for All-Optical Label Switching with 40 Gbps Payloads and 10 Gbps Labels," V. Lal, M. Mašanović, D. Wolfson, G. Fish, C. Coldren, and D. J. Blumenthal, Postdeadline Paper, ECOC 2005 Glasgow, Scotland.

InP/Silicon Ring MLL and All-Optical Clock Recovery

- Mode locked laser with III-V quantum wells wafer bonded to silicon waveguides
- All-optical clock recovery with significant retiming and reshaping
  - 30 Gb/s 2^{31}-1 PRBS data input, 30 GHz clock output
  - Input wavelength insensitive
  - 14 ps input jitter, 1.7 ps output jitter
  - 4 dB input ER, >10 dB output ER

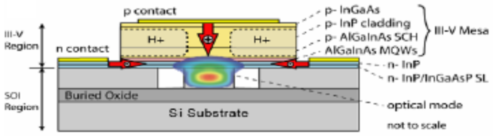

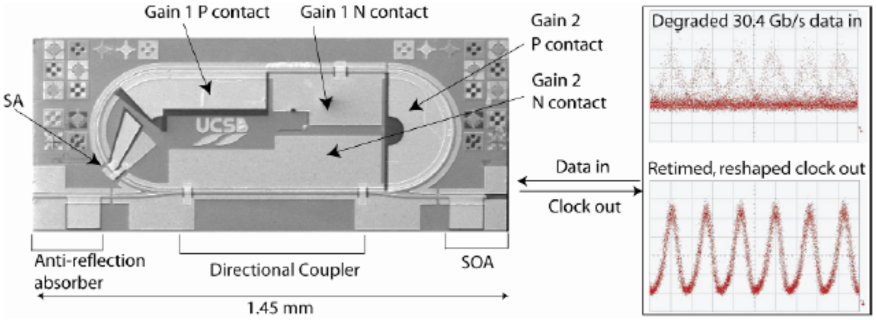

"A Racetrack Mode-Locked Silicon Evanescent Laser," A. Feng, et. al., Optics Express, http://www.opticsexpress.org/abstract.cfm?id=149007

"All-Optical Clock Recovery with Retiming and Reshaping Using a Silicon Evanescent Mode Locked Ring Laser," OFC 2008, Brian R. Koch1, Alexander W. Fang1, Henrik N. Poulsen1, Hyundai Park1, Daniel J. Blumenthal1, John E. Bowers1, Richard Jones2, Mario J. Paniccia2, Oded Cohen3; 1Univ. of California at Santa Barbara, USA, 2Intel Corp., USA, 3Intel Corp., Israel.

Hybrid InP/Si Switch & Photonic Chip Buffer

- InP Chip Insertion loss
  - Fiber-to-fiber gain : 2 dB
- Extinction ratio > 38 dB
- Switching time (longest SOA)
  - Rise time < 750 ps
  - Fall time < 1ns

- Silica on silicon chip
  - 0.04 dB/cm loss
  - Butt-coupled to switch
  - 450 cm (23ns)
  - PDL : 1 dB
  - CD : 130ps/nm-km

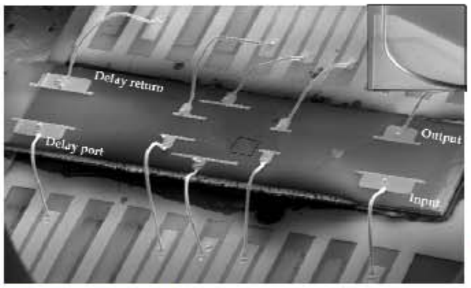

Switch: InP

Delay loop: SiO_2

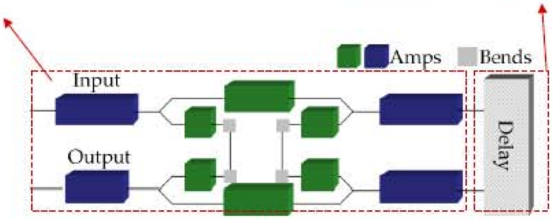

Burmeister, Bowers, PTL 18(1).

---

40 Gb/s Switch & Buffer Performance

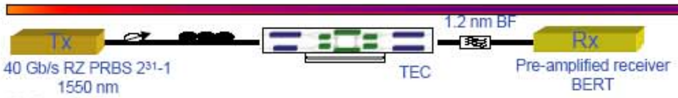

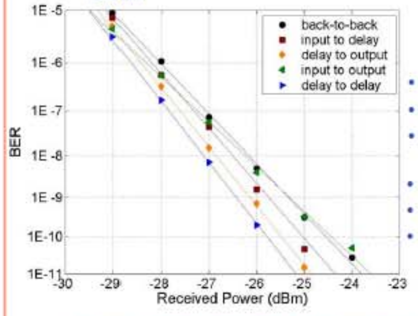

SWITCH

- Negative power penalty
- Gain from the amplifiers
- ASE reduced by filter

- Power penalty at 1e-9 BER
- Dynamic range : 15dB
- With <2 dB power penalty

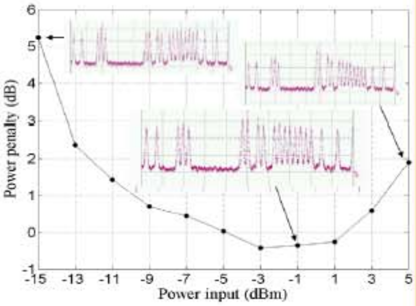

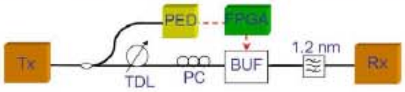

- Packets contain 64 bit identifier strings
- 5 circulations, or 64 ns of delay with 98% packet recovery
- More circulations possible with less loop loss, lower noise figure

BUFFER

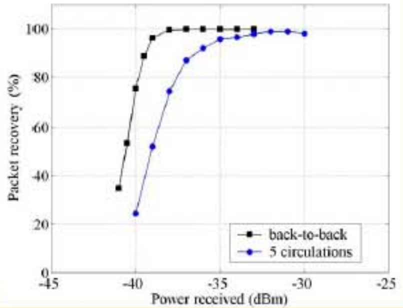

Burmeister et al. Optics Express (2008)

Conclusions

- Multi-functionality InP-based Photonic ICs can now be made with state-of-the-art performance and reductions in power dissipation, size, and <u>perhaps</u> cost in sufficient numbers.
- Multi-channel WDM transmitters, receivers, and wavelength converters demonstrated
- Many future PICs now on the 'drawing board'

Selectively-undercut traveling-wave electroabsorption modulators incorporating a p-InGaAs contact layer

Matthew M. Dummer, James R. Raring, Jonathan Klamkin, Anna Tauke-Pedretti, and Larry A. Coldren

University of California Santa Barbara, ECE Department, Santa Barbara, CA 93106 USA

dummer@engineering.ucsb.edu

Abstract: A novel fabrication process has been developed for fabricating undercut-etched electroabsorption modulators that are compatible with tunable lasers. This process allows for the incorporation of highly doped p-type InGaAs above the upper cladding as an ohmic contact layer. The EAM demonstrates significant improvement in the microwave performance with little effect on modulation efficiency due to the undercut etching. This device uses a traveling wave electrode design with an integrated, matched termination resistor to demonstrate a 34 GHz 3-dB bandwidth for a 600 μm long modulator.

OCIS codes: (230.4110) Modulators; (230.4205) MQW modulators; (230.7020) Traveling-wave devices

---

References and links

1. H. Kawanishi, H. Kawanishi, Y. Yamauchi, N. Mineo, Y. Shibuya, H. Mural, K. Yamada, and H. Wada, "EAM-integrated DFB laser modules with more than 40-ghz bandwidth," IEEE Photon. Technol. Lett. **13**, 954–956 (2001).
2. T. Knodl, C. Hanke, B. Saravanan, M. Peschke, R. Macaluso, and B. Stegmuller, "40 GHz monolithic integrated 1.3 μm InGaAlAs-InP laser-modulator with double-stack MQW layer structure," in *in Proceedings IEEE LEOS 17*, vol. 2, 2004, pp. 675–676 Vol.2.
3. J. Raring, L. Johansson, E. Skogen, M. Sysak, H. Poulsen, S. DenBaars, and L. Coldren, "40-Gb/s widely tunable low-drive-voltage electroabsorption-modulated transmitters," J. Lightwave Technol. **25**, 239–248 (2007).
4. H. Fukano, T. Yamanaka, M. Tamura, and Y. Kondo, "Very-low-driving-voltage electroabsorption modulators operating at 40 Gb/s," J. Lightwave Technol. **24**, 2219–2224 (2006).
5. T.-H. Wu, W.-C. Cheng, and D. Lee, "High-speed undercut-wet-etching-active-region traveling-wave electro-absorption modulator," in *in Proceedings IEEE LEOS 18*, 2005, pp. 426–427.
6. Y.-J. Chiu, T.-H. Wu, W.-C. Cheng, F. Lin, and J. Bowers, "Enhanced performance in traveling-wave electro-absorption modulators based on undercut-etching the active-region," IEEE Photon. Technol. Lett. **17**, 2065–2067 (2005).
7. M. Sysak, J. Raring, J. Barton, M. Dummer, D. Blumenthal, and L. Coldren, "A single regrowth integration platform for photonic circuits incorporating tunable SGDBR lasers and quantum-well EAMs," IEEE Photon. Technol. Lett. **18**, 1630–1632 (2006).
8. D. Pasquariello, E. Bjorlin, D. Lasaosa, Y.-J. Chiu, J. Piprek, and J. Bowers, "Selective undercut etching of InGaAs and InGaAsP quantum wells for improved performance of long-wavelength optoelectronic devices," J. Lightwave Technol. **24**, 1470–1477 (2006).
9. R. Lewen, S. Irmscher, U. Westergren, L. Thylen, and U. Eriksson, "Segmented transmission-line electroabsorption modulators," J. Lightwave Technol. **22**, 172–179 (2004).
10. R. Spickermann and N. Dagli, "Experimental analysis of millimeter wave coplanar waveguide slow wave structures on GaAs," IEEE Trans. Microwave Theory Tech. **42**, 1918–1924 (1994).
11. L. A. Coldren and S. W. Corzine, *Diode Lasers and Photonic Integrated Circuits*, K. Chang, Ed. (John Wiley and Sons, Inc. 1995).

#96794 - $15.00 USD Received 10 Jul 2008; revised 24 Sep 2008; accepted 24 Sep 2008; published 25 Nov 2008

12. F.-Z. Lin, Y.-J. Chiu, and T.-H. Wu, “Cladding layer impedance reduction to improve microwave propagation properties in p-i-n waveguides,” IEEE Photon. Technol. Lett. **19**, pp. 276–278 (2007).

---

1. Introduction

Traveling-wave electroabsorption modulators (EAMs) in InP-based materials are attractive devices for optical fiber communications due to their compact size, high speed, and low drive voltage. These devices are also very well suited for monolithic integration with semiconductor lasers, allowing for minimal coupling loss and simple packaging of single-chip transmitters [1, 2, 3]. Recently, selective wet-etching of the waveguide core has been demonstrated to significantly increase the bandwidth of EAMs as well as to reduce the optical propagation loss. There have been several reports of such devices with bandwidths as high as 50 GHz in both InP/InAlGaAs [4] and InP/InGaAsP [5] [6] material systems. Typically, InP-based devices make use of lattice-matched indium gallium arsenide as an intermediate semiconductor layer, because the lower band-gap allows for good ohmic contacts. However, since InGaAs is susceptible to the same wet etch chemistries as InAlGaAs and InGaAsP, undercut EAMs have previously been limited to using highly doped p-InP instead as the upper metallization interface. This type of contact scheme is not ideal for integration with forward biased devices such as semiconductor lasers, because high-resistance contacts can lead to excess heat generation and lower optical output power.

In this work, we present the first undercut InGaAsP-region modulator which allows the incorporation of a p^+-InGaAs contact layer. For these devices, we have developed a novel partial-sidewall mask process to protect the contact layer while leaving the waveguide core exposed to the selective wet etch. The material structure and fabrication process are compatible with those used for widely tunable sampled-grating (SG)DBR lasers. These EAMs show significantly improved performance due to the selective undercut as well as considerable bandwidth enhancement when operating in a traveling wave regime. We demonstrate EAMs up to 600 μm long EAM with a 3-dB bandwidth in excess of 30 GHz and open eyes at 40 Gb/s. The dynamic extinction ratio for this device is 6.0 dB with a 1.6 V drive.

2. Material structure

Efficient EAMs have previously been integrated with SGDBR lasers using either a dual quantum well integration platform (DQW), where separate sets of QWs define the gain and modulation regions [7], or a quantum well intermixing platform (QWI), where the band edge of single set of QWs is shifted to achieve the desired functionality in each region [3]. The epitaxial layer structure for this device, grown by metal organic chemical vapor deposition (MOCVD), was designed to be compatible with either of these integration techniques (Fig 1(a)). The multi-quantum well (MQW) stack centered in the waveguide consists of ten 90 $\AA$ wells separated by nine 50 $\AA$ barriers with a band edge corresponding to a photoluminescence peak (λ_{PL}) of 1465 nm. Although only a single growth is required for the EAM, the p-doped cladding was regrown separately to be consistent with laser fabrication.

3. Undercut fabrication

Fabricating the undercut waveguide requires deeply etching a ridge to expose the InGaAsP MQW material, followed by a selective wet-etch to reduce the core of the waveguide. We have chosen sulfuric acid, hydrogen peroxide, and DI water, mixed 1:1:10, as the undercut etchant, because of the high selectivity between InGaAsP and InP, and process repeatability. However, the lateral etch rate for InGaAs is more than 3 times faster than for InGaAsP [8], leading to the undesired removal of the contact layer during the undercut process. Fig. 1 shows a cross section

#96794 - $15.00 USD Received 10 Jul 2008; revised 24 Sep 2008; accepted 24 Sep 2008; published 25 Nov 2008

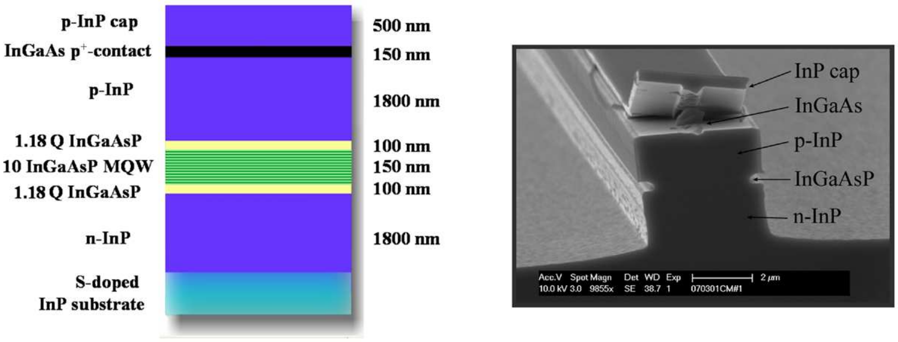

(a) (b)

Fig. 1. (a) Epitaxial layer structure of undercut TW-EAM. (b) Cross section of ridge structure after 15 min. selective wet etch. The narrow InGaAs layer was broken during cleaving.

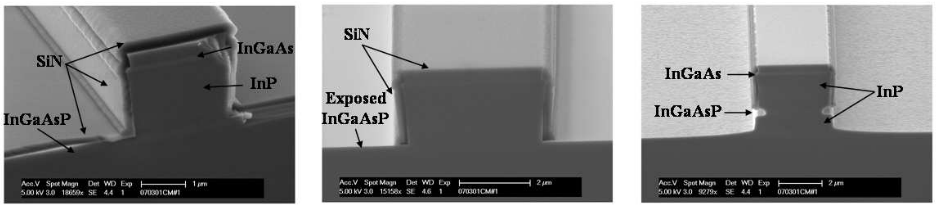

(a) (b) (c)

Fig. 2. Fabrication process for undercut EAM. (a) Surface ridge after 400 nm SiN deposition. (b) SiN nitride sidewall mask formation by vertical RIE. (c) Final cross-section after deeply etching ridge and 15 minute selective wet etching.

of a 3 μm wide ridge after 15 minutes of selective wet etching. In this case, the InGaAsP was etched only 0.5 μm, while the InGaAs layer was almost entirely removed.

During the modulator fabrication, it was therefore necessary to protect the InGaAs from the lateral etch before undercutting the waveguide core. This was accomplished by forming a partial sidewall mask, detailed in Fig. 2. First, the modulator ridge of the device was patterned using a 100 nm thick silicon nitride hard mask. The upper cladding was etched by methane-hydrogen-argon (MHA) reactive ion etching (RIE) followed by a hydrochloric/phosphoric acid (1:3) wet etch to stop exactly above the InGaAsP. A 400 nm-thick layer of SiN was then deposited by plasma enhanced chemical vapor deposition (PECVD). The SiN was subsequently etched by RIE using CF_4. Due to the anisotropy of the RIE, the SiN was preserved on the sidewalls of the ridges, while being completely removed from the horizontal surfaces. Active laser monitoring of the RIE prevented removal of the original 100 nm of SiN from the top of the ridge. This remaining SiN was then used as an in situ mask to deeply etch through the waveguide and lower cladding with MHA. Finally, a timed selective sulfuric-peroxide wet-etch was used to undercut the waveguide core. Figure 2(c) shows the final modulator geometry after etching for 15 minutes with the contact layer clearly intact.

Simulations of the optical mode profile have been performed to determine how the undercut etch effects the optical waveguide properties and modulation efficiency. Figure 3 shows the calculated overlap of the optical mode with the quantum wells as the core width is varied. For

#96794 - $15.00 USD Received 10 Jul 2008; revised 24 Sep 2008; accepted 24 Sep 2008; published 25 Nov 2008

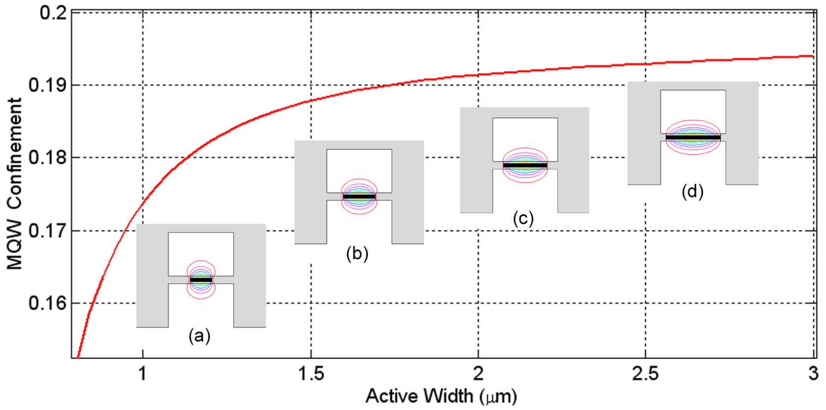

Fig. 3. Modal confinement in MQW active region vs quaternary waveguide width for 3 μm wide cladding. Insets (a)-(d) depict mode profile for 1.0, 1.5, 2.0, and 2.5 μm wide.

a waveguide core reduced from 3 μm to 1.25 μm, the difference in confinement is only 1% (0.194 to 0.184). However, for core widths less than 1 μm, the modal overlap declines rapidly. This is evident from the mode profile contours which show more of the optical power leaking out into the cladding as the core becomes narrower.

4. Modulator design

A photograph of the fabricated modulator is shown in Fig. 4(a). The device consisted of a surface ridge waveguide at the facets which tapered into undercut waveguide for the active modulator length. Using the fabrication technique described above, the core of the 3 μm ridge was selectively wet-etched for 40 minutes to reduce the width to 1.4 μm. A AuGe ground plane was defined on both sides of the ridge before the ridge was buried in benzocylcobutene (BCB) as a low-k dielectric. A via was etched through the BCB and the sacrificial InP cap layer was removed to expose the p-InGaAs prior to final Ti/Pt/Au metallization. The metal electrode was designed as a 600 μm microstrip line such that the electrical and optical signals co-propagate along the length of the device. A coplanar waveguide (CPW) allowed for directly probing on one side of the transmission line while the opposite side was terminated with a integrated NiCr thin-film resistor. A metal-insulator-semiconductor (MIS) capacitor was also added to eliminate the DC power dissipation in the resistor [9]. A schematic depicting the competed device cross section is shown in Fig. 4(b).

5. Electrical characterization

The TW-EAM has been characterized by electrical scattering parameter measurements. For these experiments, modulator test structures with CPW pads on both sides were fabricated to allow for 2-port electrical characterization with a vector network analyzer. We have compared the magnitudes of the S_{21} and S_{11} measurements for 600 μm long EAMs with and and without the selective undercut. The response of both devices is shown in Fig. 5 for -2.5 V DC bias. The undercut device clearly exhibits better microwave performance with greater bandwidth and much lower return loss. From the S-parameter data, the transmission line characteristics of the TW-EAM have been extracted using the ABCD matrix method [10]. As shown in Fig 6(a), the characteristic impedance is raised from 20 Ω to 28 Ω due to the capacitance reduction of the undercut etch.

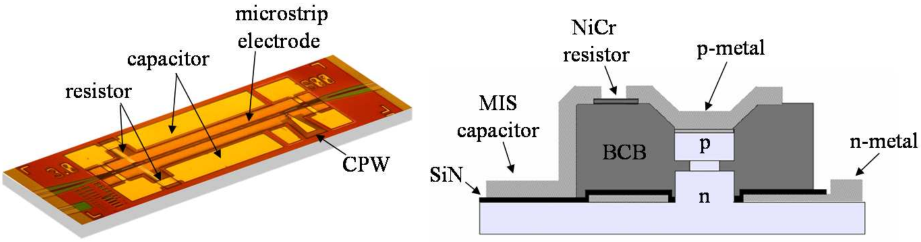

(a) (b)

Fig. 4. (a) Fabricated TW-EAM with integrated resistor and capacitor termination. (b) Schematic cross-section of device and metallization layers.

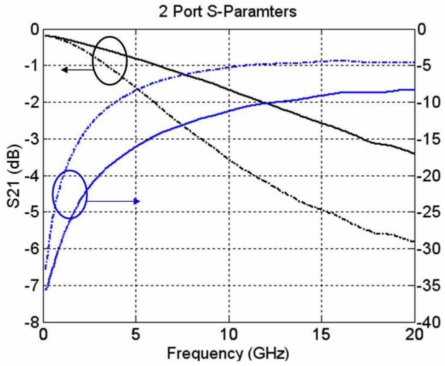

Fig. 5. Comparison of 2-port electrical S-parameters for TW-EAM with (solid) and without (dotted) undercut etching. DC bias is -2.5 V.

The electrical velocity in InP-based TW-EAMs is typically much lower than the optical velocity due to the slow-wave mode propagation induced by the diode capacitance. For long EAMs, this velocity mismatch can be a limiting factor for the bandwidth of the device. In InP/InGaAsP waveguides the optical group index is typically about 4 [11]. Fig 6 shows that with the undercut waveguide, the electrical index has been reduced from around 6 to 4, thereby achieving better velocity matching to the optical wave. The microwave loss has also been extracted for both devices as a function of frequency. Because the electrical attenuation coefficient (α) is dominated by the junction capacitance [12], the undercut is beneficial as well for improving the microwave loss.

6. Optical measurements

We have compared the modulation efficiency for the TW-EAM with and without the undercut etch. Figure 7(a) shows the DC extinction characteristics for both devices. For TE polarized light, the devices exhibit comparable extinction as predicted from the simulation, demonstrating that the undercut narrower waveguide does not effect the efficiency of the TW-EAM. Small signal electrical to optical (EO) responses have been measured for the undercut TW-EAM, shown in Fig. 7(b). A continuous wave optical signal was coupled through each facet to compare the forward and backward traveling-wave response. For a termination resistance of 26 Ω, the forward traveling 3-dB bandwidth is 34 GHz. In this case the device is well impedance matched and well velocity matched, so the bandwidth is limited almost entirely by the microwave loss. If

Received 10 Jul 2008; revised 24 Sep 2008; accepted 24 Sep 2008; published 25 Nov 2008

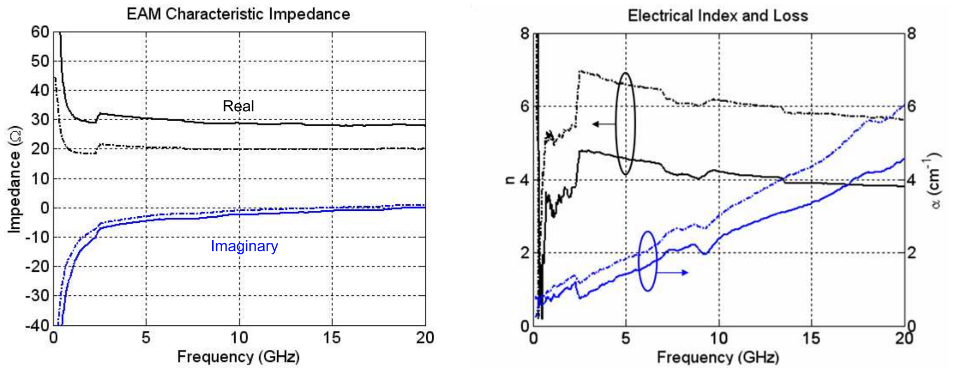

(a) (b)

Fig. 6. (a) Characteristic impedance, and (b), microwave index and attenuation extracted from S-parameters. Solid lines and dotted lines denote devices with and without undercut etching, respectively.

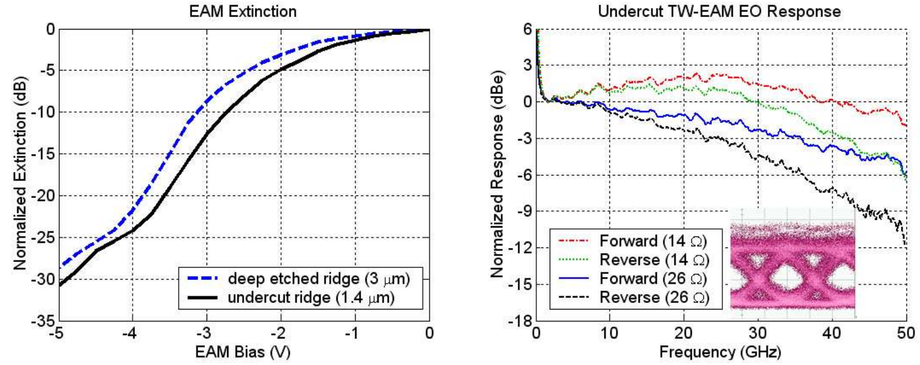

(a) **(b)**

Fig. 7. (a) DC extinction characteristics of EAM with and without undercut for $\lambda = 1550nm$. (b) Traveling-wave frequency response for the 600 μm long undercut EAM. The inset shows the 40 Gb/s (PRBS $2^{31}-1$) eye for the forward traveling 26 Ω case.

the EAM is terminated with a resistance lower than the characteristic impedance, the reflected RF power adds constructively to the forward traveling power to generate an enhancement in the response. With a 14 Ω termination, the resonance peak is 2 dB higher than the initial value and the 3-dB bandwidth is increased to greater than 50 GHz. The low frequency rise in the response is caused by the limit of the on-chip capacitor. For data transmission with long word lengths, it is necessary to add a larger capacitor in parallel off chip to extend the low-frequency range. We have performed large signal modulation of digital data at 40 Gb/s non-return-to-zero (NRZ). The inset in Fig. 7 shows the observed modulated output for the device with 26 Ω operating in the forward traveling regime. The dynamic extinction ratio was 6 dB for a drive voltage of 1.6 V peak-to-peak

7. Conclusion

We have demonstrated a novel fabrication method for incorporating a p-InGaAs ohmic contact layer with an undercut-etched EAM. This device exhibits no reduction in efficiency due to the

narrowed waveguide after reducing the core width from 3 to 1.4 μm. For a 600 μm long device with matched termination, the 3-dB bandwidth was 34 GHz. To our knowledge, this is the longest InP-based EAM ever reported which is capable of modulation rates up to 40 Gb/s. The material structure and fabrication process used for this device allow for monolithic integration with SGDBR lasers for future generations of very high bandwidth widely tunable transmitters.

#96794 - $15.00 USD Received 10 Jul 2008; revised 24 Sep 2008; accepted 24 Sep 2008; published 25 Nov 2008

I. Photonic IC Technology and Devices

B. Wavelength Converter and Packet Switching PICs

Separate Absorption and Modulation Mach-Zehnder Wavelength Converter

Anna Tauke-Pedretti, *Student Member, IEEE,* Matthew M. Dummer, *Student Member, IEEE,*
Matthew N. Sysak, *Member, IEEE,* Jonathon S. Barton, *Member, IEEE,* Jonathan Klamkin, *Student Member, IEEE,*
James W. Raring, *Member, IEEE,* and Larry A. Coldren, *Fellow, IEEE.*

***Abstract*— A monolithic separate absorption and moduation region (SAM) wavelength converter is demonstrated. The transmitter consists of a sampled-grating DBR (SGDBR) laser and a series-push-pull Mach-Zehnder modulator. The pre-amplified receiver is composed of a flared semiconductor optical amplifier and a quantum well pin photodetector. Integrated resistors and capacitors are used to minimize microwave losses and remove the need for external bias tees. The design, fabrication and operation of this photonic integrated circuit is presented. Small signal response measurements show a device bandwidth in excess of 20 GHz. Operation at 40 Gbps with NRZ data shows less than a 2.5-dB power penalty across the 32 nm laser tuning range with no additional power penalty for conversion to the input wavelength.**

***Index Terms*— tunable lasers, optical modulation, photonic integrated circuits (PICs), Mach-Zehnder modulator, semiconductor optical amplifier (SOA), sampled-grating DBR laser (SGDBR), offset quantum wells, wavelength converter.**

I. INTRODUCTION

WAVELENGTH conversion will be an important part of the next generation of optical networks, allowing for dynamic wavelength management and enabling all-optical routers. These characteristics reduce wavelength blocking, where signal contention is an issue allowing the network to operate with lower latency and at bandwidths closer to capacity. Devices demonstrating bit-rate transparency, small form factors and low power consumption will best meet the demands of these networks. [1]

Monolithic approaches to wavelength conversion are particularly attractive due to their low packaging costs and increased scalability. High functionality photonic integrated circuits (PICs) have been achieved using straightforward integration platforms requiring only a single blanket regrowth and simple fabrication. These PICs remove the need for optical fiber coupling between individual components, which simplifies packaging and reduces power consumption. The small footprint of PICs make device arrays realizable.

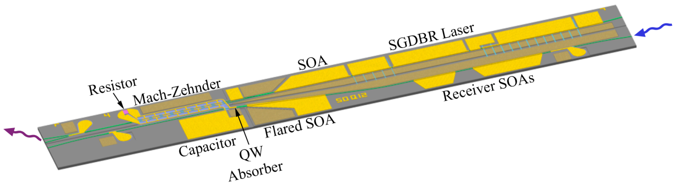

Fig. 1. Diagram of the SAM Mach-Zehnder wavelength converter

One of the most extensively studied approaches to wavelength conversion is the use of semiconductor optical amplifiers (SOAs). These devices use cross gain modulation (XGM) or cross phase modulation (XPM) in a saturated SOA to convert the input signal to a new wavelength [2]. Filterless operation has been reported for SOA-based wavelength converters at 10 Gbps using Sagnac interferometers [3] and advanced Mach-Zehnder interferometers [4]. The bandwidth of SOA-based wavelength converters is inherently limited by carrier lifetime effects; however, there has been efforts using delayed interference techniques for return-to-zero data formats. Monolithically integrated devices including an on-chip laser and implementing delayed interferometers have been successfully reported at bit rates of 40 Gbps with return-to-zero data formats [5], [6].

Recently there has been success with the separate absorption and modulation (SAM) approach to wavelength conversion. In this method, a transmitter and receiver are monolithically integrated on a single chip. The photodiode is directly connected to the modulator allowing the photocurrent from an absorbed input signal to directly drive an optical electro-absorption modulator (EAM) [7]. Since the photodiode produces enough photocurrent to drive the optical modulator there is no need for any electrical amplification. Due to the spatial separation of the receiver and transmitter waveguides, SAM wavelength converters have no optical filtering requirements and are capable of conversion to the input wavelength. These devices also have the advantage of lower power consumption and smaller footprints than comparable SOA-based devices. Devices utilizing an external light source have demonstrated bit rates up to 500 Gbps [8]. Monolithic devices with regenerative capabilities at 10 Gbps have also been achieved [9]. It has also been shown that the integration of resistors and capacitors simplify the device operation by removing the need for external biasing and high-speed probes [7].

The work in this paper utilizes the SAM approach to wavelength conversion with Mach-Zehnder modulators (MZMs), instead of EAMs. Optical gates utilizing integrated photodetectors and MZMs with gate opening times as short as 5 ps

---

This work was supported by Defense Advanced Research Projects Agency (DARPA) MTO-LASOR Grant W911NF-04-9-0001 and MTO-CS-WDM Grant N66001-02-C-8026.

A. Tauke-Pedretti, M. Dummer, J. Barton, J. Klampkin and L. Coldren are with the Department of Electrical and Computer Engineering and the Department of Materials, University of California Santa Barbara, Santa Barbara, CA 93106 USA (telephone: 805-893-5955, email: atauke@engineering.ucsb.edu).

J.W. Raring is with Sandia National Laboratories, Albuquerque, NM USA

M.N. Sysak is with Intel Corporation, San Jose, CA USA

have been reported [10]. The use of MZMs are attractive for their ability to achieve zero or slightly negative chirp and high extinction ratios. Widely-tunable series-push-pull Mach-Zehnder modulator transmitters have demonstrated efficient operation at 40 Gbps [11] and negative chirp making them an important building block in this work. A widely tunable sampled-grating DBR (SGDBR) laser is used as the integrated light source allowing for tuning across 32 nm. The receiver is composed of a high saturation power SOA and an efficient quantum well photodetector. Wavelength conversion at 40 Gbps is achieved by taking advantage of the bandwidth benefits of traveling-wave device design. Microwave losses associated with high-speed probes and external bias tees are minimized by using a bias scheme requiring only DC probes and integrating a bypass capacitor and load resistor on-chip. Similar devices demonstrating error-free operation at 10 Gbps have been previously reported [12].

This paper is organized as follows; the Mach-Zehnder SAM wavelength converter is introduced in Section I. In Section II the material platform and fabrication of the device is discussed. Sections III and IV cover the design and performance of the transmitter and receiver sections respectively. Finally, Section V presents the biasing and operation of the fully integrated wavelength converter at 40 Gbps with an non-return-to-zero (NRZ) data stream. This is followed by a conclusion and summary of work.

II. INTEGRATION PLATFORM AND FABRICATION

The epitaxial material structure is grown by MOCVD on a semi-insulating substrate to allow for isolation between the transmitter and receiver ridges, as well as to reduce the capacitance of high speed pads. The wavelength converter's dual quantum well (DQW) integration platform is comprised of two sets of quantum wells (Fig. 2) [13]. A set of offset quantum wells (λ_{PL} = 1550 nm) are used in the gain section of the SGDBR and the SOAs. These wells are also reverse biased for use in the absorbing region. A separate set of seven quantum wells (λ_{PL} = 1465 nm) are centered in the 1.2-Q InGaAsP waveguide and aid the modulator efficiency by the utilization of the quantum confined Stark effect [14]. These centered wells are present throughout the device and therefore must be detuned from the operating wavelength to maintain low optical passive loss. An additional benefit of the centered quantum wells is the lower waveguide doping needed compared to bulk modulator regions. This means lower biases are necessary to fully deplete the waveguide, as well as more of the waveguide depleting thus reducing the ridge capacitance.

Initially, the offset quantum wells are removed with a wet etch from all passive areas (everywhere but the laser gain sections, the SOAs and the absorber), this is followed by dry etching of the holographically defined gratings in the grating burst regions. At this point, the single blanket regrowth of the InP cladding and InGaAs p-contact layer is performed. Following the regrowth, the ridges are are defined using a dry etch and a wet cleanup etch to insure smooth sidewalls. The device junction capacitance is reduced by etching into the top 1000 $\mathring{A}$ of the waveguide, which became p-doped due to diffusion during the regrowth. The n-InGaAs contact layer is then exposed and the Ni/AuGe/Ni/Au n-contacts are deposited. The receiver and transmitter ridges are isolated by etching a 100 μm wide strip down to the Fe-doped substrate between the two ridges, at this time the semiconductor resistor is also isolated from the rest of the n-contact layer. Photo-bis-benzocyclobutene (BCB) deposited under the high speed pads reduces the device capacitance. The p-contacts are evaporated following BCB deposition and exposure of the ridge tops. A proton implant was used to electrically isolate the pads and to reduce optical losses.

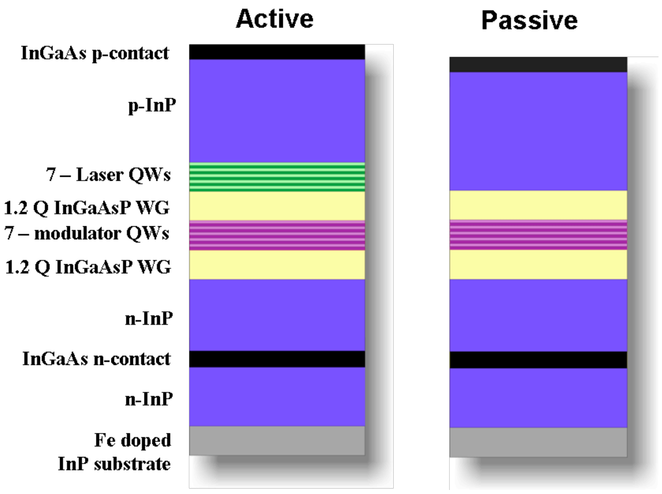

Fig. 2. Material structure of device. Epitaxial structure in the active regions is shown on the left and the passive regions is shown on the right.

The devices were then thinned, cleaved and a multi-layer antireflection (AR) coating was applied to the facets. In addition to the AR coating, curved and flared ridges were used to reduce facet reflections. The devices were mounted on aluminum nitride carriers for testing and the contacts were wirebonded to the carrier. All biases were applied with a DC probe card. The fabricated wavelength converter has a footprint of 3.3 mm × 0.46 mm.

III. TRANSMITTER

The five section widely tunable SGDBR laser used for the integrated light source consists of: a rear absorber, rear mirror, phase section, gain section and front mirror. These lasers are capable of achieving a quasi-continuous tuning range greater than 40 nm. Coarse tuning is achieved with a vernier based tuning mechanism controlled through current injection into the front and rear mirrors, while a phase sections allows for finer wavelength adjustment [15] [16]. A 500 μm long SOA follows the SGDBR allowing for power adjustments without effecting the lasing wavelength and blocking of the laser signal during wavelength tuning.

The Mach-Zehnder interferometer is composed of a 1×2 multimode interferometer (MMI) to split the light from the SGDBR and a 2×2 MMI to combine the light at the output. A forward-biased phase electrode within the Mach-Zehnder interferometer is used to insure the interferometer is biased

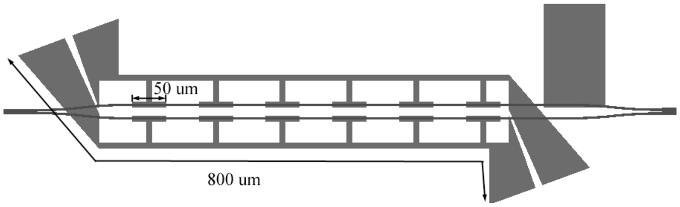

Fig. 3. Diagram of the test modulator transmission lines.

for maximum extinction ratios. The Mach-Zehnder modulator is operated in a series-push-pull fashion with the microwave signal from the photodiode applied across the tops of the two modulator arms. This configuration puts the two arms of the Mach-Zehnder in series along the microwave signal path. Therefore, the capacitance associated with the diodes is in series, effectively halving the device's capacitance. The reduction in device capacitance translates into higher bandwidths [17], [18]. Additionally, similar transmitters with series push-pull Mach-Zehnder modulators have been shown to produce output signals with negative chirp, which is important to maximize transmission distances [11]. It is expected these chirp characteristics will translate to the wavelength converted signal. Semiconductor resistors are integrated for on-chip terminations and to minimize the microwave loss.

The series-push-pull Mach-Zehnder modulator has been designed as a traveling wave structure with a characteristic impedance matched to 50 Ω. In order to reduce the transmission line capacitance thus increasing the transmission line characteristic impedance, the ridge width is reduced from 3 μm in the laser and SOA regions to 2 μm within the modulators. Additionally, the coplanar stripline (CPS) is capacitively loaded with periodic 50 μm long T-structures contacting the ridge. This configuration distributes the capacitance and increases CPS gap, which increases the characteristic impedance of the device. Unloaded, the transmission line impedance is 125 Ω. The Mach-Zehnder ridges add significant capacitance to the transmission line thus reducing the characteristic impedance to 50 Ω. Using s-parameter measurements as described in [19], the CPS transmission line parameters were extracted. All transmission lines measured were 800 μm long; however the number of T-structures was varied to change the amount of loading (Fig.3). The characteristic impedances for devices of lengths 300 μm (6 T-structures), 400 μm (8 T-structures) and 500 μm (10 T-structures) and loading of 38%, 50% and 63% respectively are shown in Fig. 4. The characteristic impedances for identical transmission line structures without loading are also shown in Fig. 4. The index of the transmission lines was also extracted yielding an index of 6, which although mismatched from the optical group index of 4 does not have a significant impact on the device bandwidth.

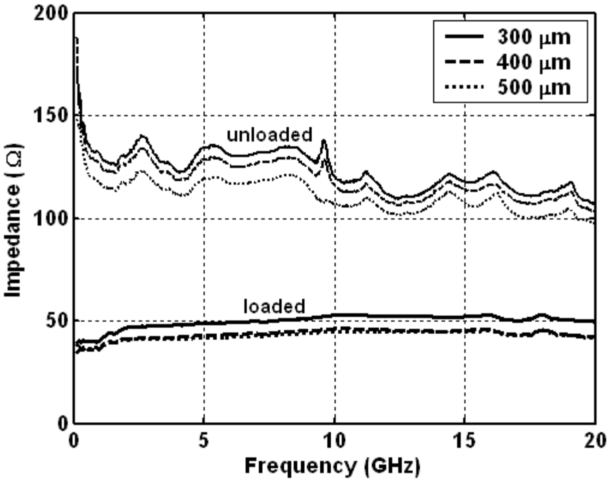

Fig. 4. Characteristic impedance of capacitively loaded transmission lines used in Mach-Zehnder modulator for unloaded lines and the loaded lines including the MZM ridge (V_{MZ1} = V_{MZ2} = -2 V).

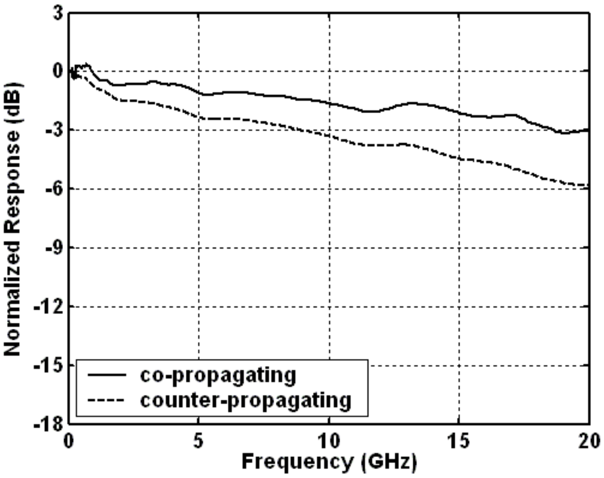

Fig. 5. Traveling wave bandwidth for 300 μm long Mach-Zehnder (V_{MZ1} = V_{MZ2} = -2 V and R_{load} = 50 Ω).

The wavelength converter utilizes a 300 μm long Mach-Zehender modulator with six 50 μm long T-structures. Transmitter bandwidth measurements for a 300 μm long Mach-Zehnder modulator for co-propagating and counter-propagating electrical and optical waves were taken to confirm the traveling wave operation of the modulator (Fig. 5). These measurements show an 10 GHz improvement with co-propagation when the termination is matched to the transmission line impedance verifying the traveling wave operation of the device.

IV. RECEIVER

The receiver ridge is composed of linearly flared SOA and a 35 μm long taped quantum well photodetector [20]. The receiver section must generate enough photocurrent to drive the modulator while avoiding saturation effects. Quantum well detectors are quite attractive for their ease of integration with gain regions and their high absorption coefficient [21]. Saturating the photodetector will cause field screening problems due to trapped carriers thus reducing the device bandwidth. While the deep offset quantum wells are advantageous for providing carrier confinement in the gain regions of the wavelength converter, these same wells allow for poor carrier escape

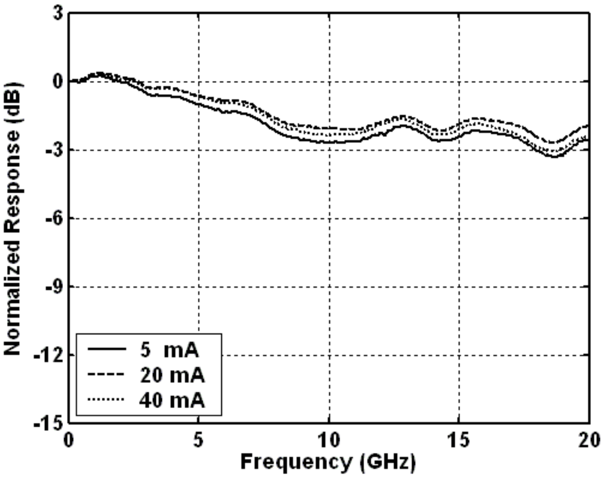

Fig. 6. Small signal measurements for a 50 μm long quantum well photodiode tapered from 9 μm to 2 μm (V_{PD} = -4 V, R_{load} = 25 Ω and P_{in} was varied).

causing field screening which is detrimental when used as absorbing region. This is why it is necessary to provide a significant reverse bias (-4 V to -6 V) on the detectors to prevent saturation. Additionally, the detectors start off quite wide in the front end (9 μm) and taper off to 2 μm as more power is absorbed. This design allows for lower photocurrent densities at the front of the device, while still keeping area and capacitance to a minimum. The saturation characteristics of a 50 μm long photodetector have been measured by comparing the small signal response for various input photocurrents (Fig. 6), and no saturation effects have been observed for photocurrents up to 40 mA which is sufficient to drive the modulator. The small signal response measurements for this photodetector terminated in 25 Ω shows a bandwidth of 20 GHz.

The carrier density within an SOA will vary with significant input powers. The response time associated with a saturated SOA will induce pattern effects significantly degrading the converted signal. The saturation power of an SOA is governed by Equation 1 which shows the saturation power of the SOA can be increased by reducing any of the following parameters: carrier lifetime (τ), active region power density ($\Gamma_{xy}/(wd)$) or differential gain (a).

$$G = G_o exp\left[-\frac{G-1}{G}\frac{P_o}{P_s} \right], P_s = \frac{wdh\nu}{a\Gamma_{xy}\tau} \quad (1)$$

The most straightforward way of increasing the saturation power is through the carrier lifetime which is inversely dependent on current density. Therefore, it is beneficial to operate the SOAs at the highest currents possible without the gain rolling over from heating. Further enhancements in the saturation power can be achieved by altering the geometry of the SOA to reduce the active region power density. In this work, the power density has been reduced by laterally flaring the SOA to provide a significant improvement in the device saturation power [20]. However, careful calculation of the flare length and widths are necessary as wider SOAs will require more current adding to device power consumption and heating. Ideally the SOA will flare at the same rate as device gain staying just below saturation the whole way. These effects have been modeled and the results are shown in Fig. 7 [22].

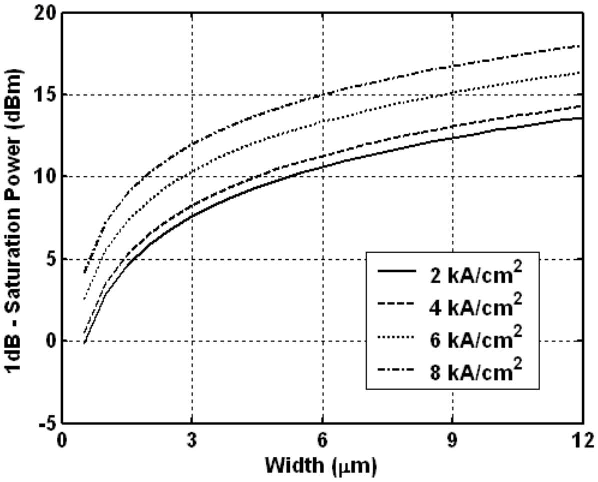

Fig. 7. Simulation of the effects of ridge width and current density on output saturation power.

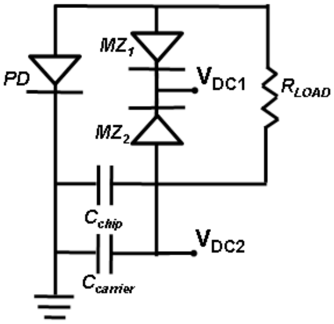

Fig. 8. Schematic of wavelength converter biasing.

The amplifiers in the wavelength converter were designed based upon the modeling. A 3 μm wide and 500 μm long straight SOA was implemented to boost the initial input power. This is followed by a 550 μm long SOA flared laterally from 3 μm to 12 μm wide to achieve high saturation powers. These amplifiers were coupled with 35 μm long tapered quantum well photodiodes. These receivers are polarization dependent due to the compressive strain in the quantum wells; therefore the input signal polarization was adjusted to TE to allow for maximum gain during all measurements. This dependence is typical of devices implementing strained quantum wells and could be eliminated through the redesign of the SOA and photodetector quantum wells [23].

V. WAVELENGTH CONVERTER

A. Biasing

It is beneficial to design a biasing scheme that allows for most of the electrical passive components to be integrated

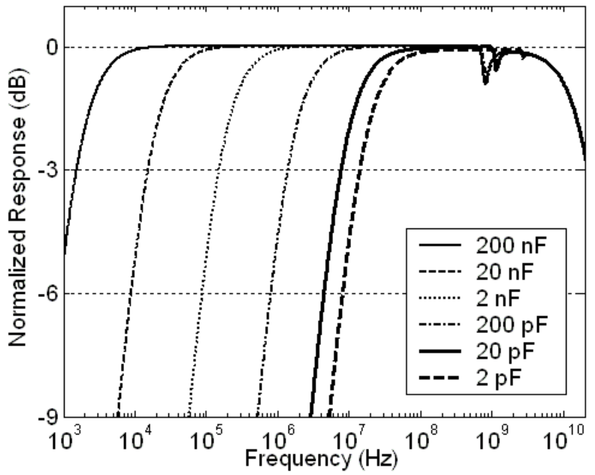

Fig. 9. Simulated effect of capacitor value on the low frequency cutoff value of the wavelength converter. The dip seen at 1 GHz is due to a LC resonance between the on-chip capacitor and the wirebonds to the on-carrier capacitor.

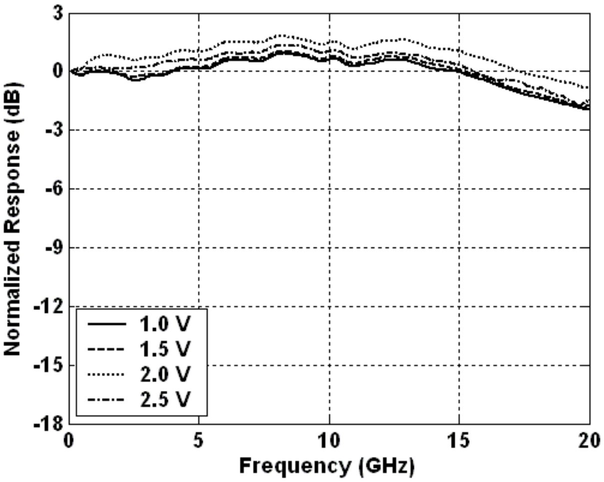

Fig. 10. Small signal response of wavelength converter. (R_{load} = 25 Ω; V_{DC2} = -5 V and varying values of V_{DC2}-V_{DC1}.)

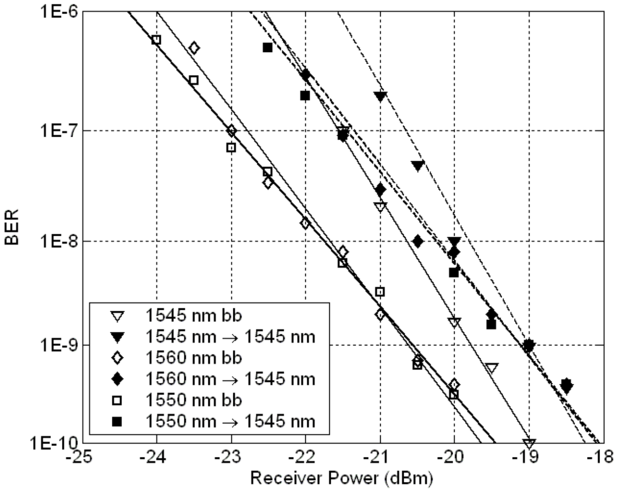

Fig. 11. BER measurements for conversion at 40 Gbps for varying input wavelengths to an output wavelength of 1545 nm. Back to back measurements are plotted with solid lines and converted measurements are plotted with dashed lines. (P_{in} = 0.4 mW; I_{gain} = 100 mA; I_{TxSOA} = 120 mA; I_{RxSOA1} = 185 mA; I_{RxSOA2} = 250 mA, V_{DC2}-V_{DC1}= -2 V and V_{DC2} = -5.6 V)

onto the monolithic chip for the minimization of microwave losses, ease of testing and scalability of devices into arrays. The integration of resistors and capacitors insures that external bias tees are not needed for operation. The result of these efforts is the biasing scheme shown in Fig. 8. This biasing scheme allows direct bias control of one arm of the MZM. The other MZM arm and the photodiode are biased through the resistor; therefore, their exact bias point will vary based on the DC photocurrent level.

The on-chip termination resistor was fabricated from the InGaAs n-contact layer of the epitaxial material. In order to achieve the desired resistance value it is important to obtain an accurate measurement of the n-InGaAs sheet resistance. The sheet resistance was extracted using circular transfer length measurements (TLMs) [24] and the resistor dimensions were designed accordingly. This allowed the resulting resistors to be within 94 % of the desired value. The fabrication of these resistors require the material surrounding the resistor to be etched to the semi-insulating substrate thus providing proper electrical isolation from the rest of the device. The power handling capabilities of the resistor are quite good, as over 6 V can be applied across it without damage. Therefore, the resistors should not fail within the typical operating conditions of the wavelength converters.

An on-chip capacitor was used as a RF bypass capacitor for biasing. This parallel plate capacitor was formed from the InGaAs n-contact layer and the p-metal with 3000 $\AA$ of SiN_x as the dielectric. The resulting capacitor has an area of 0.111 mm^2 and a capacitance of 19 pF. Since this on-chip capacitor is too small to provide a path for the signals low frequency components, an additional 220 nF on-carrier capacitor has been wirebonded in parallel with the integrated capacitor. The effect of the capacitor size on the low frequency cutoff of the wavelength converter can be seen in Fig. 9. Additionally, a small resistor (2 Ω) is used in series with the carrier capacitor to dampen any LC resonances caused by the inductance of the wirebonds.

B. Experiments

The bandwidth of the device was measured using a HP3705A network analyzer. The wavelength converter demonstrated greater than 20 GHz bandwidth as shown in Fig. 10. The slight bandwidth enhancement seen at 10 GHz is due to the impedance mismatch between the 50 Ω transmission line of the Mach-Zehnder modulator and the 25 Ω integrated termination resistor. The improvement in bandwidth with reverse bias is due to a capacitance reduction from an increase in the depletion region of the device.

Bit error rate (BER) measurements with a NRZ 2^7-1 pseudorandom bit stream were taken with a 40 Gbps SHF bit-error-rate-tester (BERT). The word length was limited by the setup noise floor. The output of the BERT was amplified

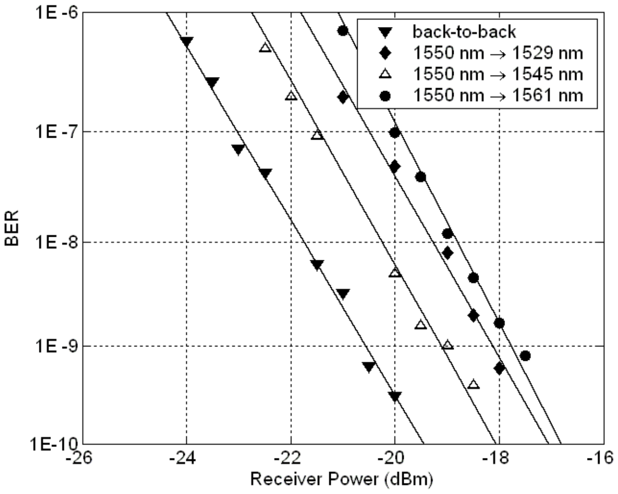

Fig. 12. 40 Gbps BER measurement for conversion from an input wavelength of 1550 nm to varying output wavelengths. (P_{in} = 0.4 mW; I_{gain} = 130 mA; I_{TxSOA} = 110 mA; I_{RxSOA1} = 185 mA; I_{RxSOA2} = 250 mA; V_{DC2}-V_{DC1}=-2 V and V_{DC2} = -5.6 V)

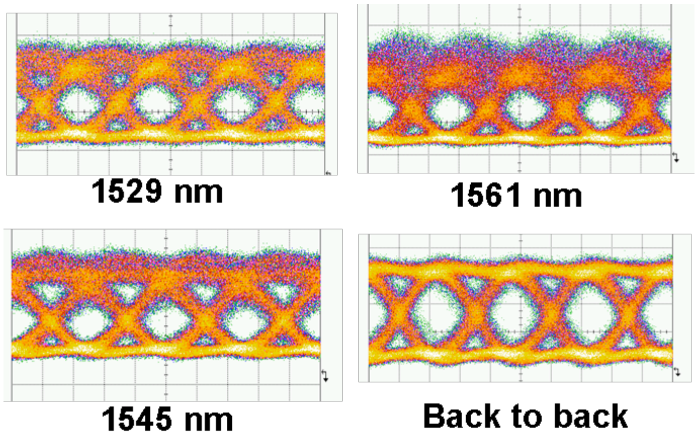
1529 nm **1561 nm**

1545 nm **Back to back**

Fig. 13. 40 Gbps eye diagrams for conversion from 1550 nm to varying output wavelengths across the SGDBR tuning range.

by a high power eribum doped amplifier (EDFA), followed by a polarization controller before being coupled into the wavelength converter using a conically tipped lensed fiber. The output of the wavelength converter was coupled into a conically tipped lensed fiber and connected directly to the commercial pre-amplified optical receiver.

In order to achieve the bandwidth necessary for error-free operation at 40 Gbps, a high-speed ground-signal probe terminated in 50 Ω was placed in parallel with the integrated 25 Ω termination resistor. This configuration makes the effective termination 17 Ω. In future device fabrication runs, the resistor can be designed for a smaller value and no high-speed probes would be necessary. The input power was 0.4 mW, which generated 28 mA of photocurrent in the photodetector. These power levels allow the SOA to be operated below the output saturation power. All measurements were taken at a temperature of 19^o C. The DC bias points on the MZM and photodiode were -2 V and -5.6 V respectively.

Error free operation was achieved for conversion between varying input wavelengths and an output wavelength of 1545 nm. The BER measurements showed power penalties less than 2 dB (Fig. 11). One of the advantages of the SAM wavelength converters is the ability to convert to the input wavelength and the BER measurements confirm this with no additional power penalty for input wavelength conversion. The change in slope of the back-to-back and converted BER measurements for an input power of 1545 nm is due to the wavelength dependance of the commercial transmitter used in the test setup. Bit-error-rate measurements were also taken for conversion from 1550 nm to wavelengths across the SGDBR tuning range (1528 nm-1561 nm) resulting in power penalties less than 2.5 dB (Fig. 12). The open eye diagrams for this conversion experiment are seen in Fig. 13. The increased power penalty for conversion to 1561 nm is due to the decreased efficiency of the modulator at longer wavelengths. The coupling loss between the chip and fiber were approximated to be 3 dB for both the input and output facets. The wavelength converter was operated with an input power of -4 dBm and output powers of -7 dBm; therefore, the device facet-to-facet conversion efficiency was -3 dB.

VI. CONCLUSION

A monolithic separate absorption and moduation region (SAM) wavelength converter has been fabricated with an integrated resistor and capacitor. This device presents a realizable solution for wavelength conversion with a small footprint and low-power dissipation. The transmitter ridge consists of a widely tunable SGDBR and a traveling-wave series-push-pull Mach-Zehnder modulator. The receiver ridge utilizes a high-saturation power flared SOA and a tapered quantum well absorber. This device requires no external bias tees due to the integration of a parallel plate capacitor and semiconductor resistor. The spatial separation of the input and output wavelengths allows for no optical filtering requirement.

The wavelength converter's small signal response measurements showed a bandwidth in excess of 20 GHz. This Mach-Zehnder SAM wavelength converter is the first monolithic wavelength converter reported to operate at 40 Gbps using NRZ data. Characterization at 40 Gbps demonstrated power penalties of less than 2.5 dB across the laser tuning range of 32 nm. Additionally, there was no additional power penalty observed for conversion to the input wavelength.

ACKNOWLEDGMENTS

The authors would like to thank Henrik Poulson and John Mack for their help with testing equipment.

REFERENCES

[1] M. Borella, J. Jue, D. Banerjee, B. Ramamurthy, and B. Mukherjee, "Optical components for WDM lightwave networks," *Proceedings of the IEEE*, vol. 85, no. 8, pp. 1274–1307, 1997.

[2] T. Hatta, T. Miyahara, Y. Miyazaki, K. Takagi, K. Matsumoto, T. Aoyagi, K. Motoshima, K. Mishina, A. Maruta, and K. Kitayama, "Polarization-Insensitive Monolithic 40-Gbps SOA MZI Wavelength Converter With Narrow Active Waveguides," *IEEE Journal of Selected Topics in Quantum Electronics*, vol. 13, no. 1, pp. 32–39, 2007.

[3] Y. Shibata, N. Kikuchi, S. Oku, I. Ito, H. Okamoto, Y. Kawaguchi, Y. Kondo, Y. Suzuki, and Y. Tohmori, “Filter-free all-optical wavelength conversion using sagnac interferometer integrated with parallel-amplifier structure (sipas),” *Electronics Letters*, vol. 38, no. 21, pp. 1273–1275, 2002.

[4] D. Wolfson, T. Fjelde, A. Kloch, C. Janz, F. Poingt, F. Pommereau, I. Guillemot, F. Gaborit, and M. Renaud, “Detailed experimental investigation of all-active dual-order mode Mach-Zehnder wavelength converter,” *Electronics Letters*, vol. 36, no. 15, pp. 1296–1297, 2000.

[5] V. Lal, M. L. Masanovic, J. A. Summers, G. Fish, and D. J. Blumenthal, “Monolithic Wavelength Converters for High-Speed Packet-Switched Optical Networks,” *Selected Topics in Quantum Electronics, IEEE Journal of*, vol. 13, no. 1, pp. 49–57, 2007.

[6] P. Bernasconi, L. Zhang, W. Yang, N. Sauer, L. L. Buhl, J. H. Sinsky, I. Kang, S. Chandrasekhar, and D. T. Neilson, “Monolithically Integrated 40-Gb/s Switchable Wavelength Converter,” *Journal of Lightwave Technology*, vol. 24, no. 1, pp. 71–76, January 2006.

[7] M. Dummer, M. Sysak, J. Raring, A. Tauke-Pedretti, and L. Coldren, “Widely Tunable Single-Chip Transceiver for 10 Gb/s Wavelength Conversion,” in *Device Research Conference (DRC)*, no. II.A-3, University Park, PA, June 2006.

[8] S. Kodama, T. Yoshimatsu, and H. Ito, “500 Gbit/s optical gate monolithically integrating photodiode and electroabsorption modulator,” *Electronics Letters*, vol. 40, no. 9, pp. 555–556, 2004.

[9] M. Sysak, J. Raring, J. Barton, H. Poulsen, D. Blumenthal, and L. Coldren, “Extinction ratio regeneration, signal re-amplification (2R), and broadband wavelength switching using a monolithically integrated photocurrent driven wavelength converter,” *Optics Express*, vol. 14, no. 23, pp. 11 348–11 353, November 2006.

[10] T. Yoshimatsu, S. Kodama, and H. Ito, “InP-based ultrafast optical gate monolithically integrating uni-travelling-carrier photodiode and Mach-Zehnder modulator,” *Electronics Letters*, vol. 41, no. 22, pp. 1243–1244, 2005.

[11] A. Tauke-Pedretti, M. Sysak, J. Barton, J. Raring, L. Johansson, and L. Coldren, “40-Gb/s Series-Push-Pull Mach-Zehnder Transmitter on a Dual-Quantum-Well Integration Platform,” *IEEE Photonics Technology Letters*, vol. 18, no. 18, pp. 1922–1924, September 15 2006.

[12] A. Tauke-Pedretti, M. Dummer, J. S. Barton, M. N. Sysak, J. W. Raring, J. Klamkin, and L. A. Coldren, “Widely tunable 10 Gbit/s separate absorption and modulation Mach-Zehnder wavelength converter,” *Electronics Letters*, vol. 43, no. 10, pp. 584–585, 2007.

[13] M. Sysak, J. Raring, J. Barton, M. Dummer, D. Blumenthal, and L. Coldren, “A single regrowth integration platform for photonic circuits incorporating tunable SGDBR lasers and quantum-well EAMs,” *IEEE Photonics Technology Letters*, vol. 18, no. 15, pp. 1630–1632, August 2006.

[14] J. S. Weiner, D. A. B. Miller, and D. S. Chemla, “Quadratic electro-optic effect due to the quantum-confined Stark effect in quantum wells,” *Applied Physics Letters*, vol. 50, no. 13, pp. 842–844, 1987.

[15] L. C. V. Jayaraman, Z.M. Chuang, “Theory, design, and performance of extended tuning range semiconductor lasers with sampled gratings,” *IEEE Journal of Quantum Electronics*, vol. 29, no. 6, pp. 1824–1834, June 1993.

[16] L. A. Coldren, “Monolithic tunable diode lasers,” *Selected Topics in Quantum Electronics, IEEE Journal of*, vol. 6, no. 6, pp. 988–999, 2000.

[17] J. S. Barton, M. L. Masanovic, A. Tauke-Pedretti, E. J. Skogen, and L. A. Coldren, “Monolithically-integrated 40 Gbit/s widely-tunable transmitter using series push-pull Mach-Zehnder modulator SOA and Sampled-Grating DBR laser,” in *Optical Fiber Communication Conference and Exposition and The National Fiber Optic Engineers Conference*, Anaheim, CA USA, March 2005, paper OTuM3.

[18] R. G. Walker, “High-speed III-V semiconductor intensity modulators,” *IEEE J. Quantum Electron.*, vol. 27, pp. 654–667, Mar. 1991.

[19] R. Spickermann and N. Dagli, “Experimental analysis of millimeter wave coplanar waveguide slow wave structures on GaAs,” *IEEE Transactions on Microwave Theory and Techniques*, vol. 42, no. 10, pp. 1918–1924, October 1994.

[20] A. Tauke-Pedretti, M. Dummer, J. S. Barton, M. N. Sysak, J. W. Raring, and L. A. Coldren, “High Saturation Power and High Gain Integrated Photoreceivers,” *IEEE Photon. Technol. Lett.*, vol. 17, no. 10, pp. 2167–2169, Oct. 2005.

[21] B. Mason, S. Chandrasekhar, A. Ougazzaden, C. Lentz, J. Geary, L. Buhl, L. Peticolas, K. Glogovsky, J. Freund, L. Reynolds, G. Przybylek, F. Walters, A. Sirenko, J. Boardman, T. Kercher, M. Rader, J. Grenko, D. Monroe, and L. Ketelsen, “Photonic integrated receiver for 40 Gbit/s transmission,” *Electronic Letters*, vol. 38, no. 20, pp. 1196–10 097, September 2002.

[22] V. Lal, W. Donat, A. T. Pedretti, L. Coldren, D. Blumenthal, and J. Piprek, “Broadband Rate-Equation Model including Many-Body Gain for WDM Traveling-Wave SOAs,” in *5th International Conference Numerical Simulation of Optoelectronic Devices*, Berlin, Germany, September 2005, pp. 125–126.

[23] D. Wake, S. Judge, T. Spooner, M. Harlow, W. Duncan, I. Henning, and M. O’Mahony, “Monolithic integration of 1.5 um optical preamplifier and PIN photodetector with a gain of 20 dB and a bandwidth of 35 GHz,” *Electronic Letters*, vol. 26, no. 15, pp. 1166–1168, July 19 1990.

[24] J. Klootwijk and C. Timmering, “Merits and Limitations of Circular TLM structures for contact resistance determination for novel III-V HBTs,” in *Proceeding of IEEE 2004 Conference on Microelectronic Test Structures*, vol. 17, March 2004, pp. 247–252.

Anna Tauke-Pedretti received the B.S. degree in Physics and Electrical Engineering from the University of Iowa, Iowa City, in 2001, and the M.S. and Ph.D. degrees in Electrical and Computer Engineering from the University of California, Santa Barbara, in 2002 and 2007 respectively. Her current research interests focus on InP-based photonic integrated circuits for high-speed wavelength conversion. She has also developed monolithic high-speed transmitters and high-saturation power pre-amplified receivers.

Matthew M. Dummer received the B.S. degree in Electrical Engineering from the University of Minnesota in 2002, and the M.S. from the University of California, Santa Barbara in 2004. He is currently at UCSB pursuing the Ph.D. His research focuses on high functionality photonic integrated circuits for wavelength conversion. He also specializes in the fabrication of high power semiconductor optical amplifiers and photodiodes, as well as traveling wave circuit design for electroabsorption modulators.

Matthew N. Sysak received his B.S. degree in Chemical Engineering from the Pennsylvania State University in 1998, and his M.S. and Ph.D. degrees from the University of California Santa Barbara in 2002 and 2005, respectively. His PhD thesis focused on material design as well as device design, fabrication, and testing of monolithically integrated, widely tunable, optoelectronic wavelength converters and signal regenerators. Following his PhD, Dr. Sysak joined Prof. John Bowers’ research group as a Post-Doctoral Scholar where he worked on novel photonic circuit design and fabrication for analog, phase modulated links. In 2007 he joined Intel Corporation in Santa Clara, CA, where he is working on silicon photonic integrated circuits. Dr. Sysak has authored and coauthored over 50 conference and journal papers, has been an invited speaker at several technical meetings, and is a member of OSA, IEEE, and SPIE.

Jonathon S. Barton was born in Sacramento, CA, in 1975. He earned the B.S. degree in Electrical Engineering and Material Science Engineering, at the University of California, Davis in 1998. He was an Intel fellow in 2004 and completed the Ph.D. degree in Electronic Materials at the University of California, Santa Barbara in 2004. At the University of California, Santa Barbara, he pioneered work on C-band 40 Gbps tunable monolithically integrated Mach-Zehnder transmitters. Furthermore, he has coauthored over seventy papers, invited and contributed talks on tunable lasers and photonic integrated circuits, at various international conferences.

Jonathan Klamkin received the B.S. degree in Electrical and Computer Engineering from Cornell University in 2002, the M.S. degree in Electrical and Computer Engineering from the University of California, Santa Barbara (UCSB) in 2004, and is now working toward the Ph.D. degree in Materials at UCSB. His research interests include the design, growth, fabrication, and characterization of widely-tunable semiconductor lasers, photodetectors, optical intensity and phase modulators, and semiconductor optical amplifiers for InP based photonic integrated circuits. Currently his efforts are focused on novel coherent integrated receivers for highly linear fiber-optic links.

James W. Raring earned the B.S. degree from the materials engineering department at California Polytechnic State University, San Luis Obispo in 2001 and the Ph.D. in materials science from the University of California, Santa Barbara in 2006. His research focused on the design, growth, and fabrication of high-functionality wavelength-agile InGaAsP based photonic integrated circuits (PIC). By coupling quantum well intermixing with MOCVD regrowth, he combined widely-tunable sampled grating DBR lasers, 40 Gb/s electroabsorption modulators, low-confinement high-saturation power semiconductor optical amplifiers, and 40 Gb/s uni-traveling carrier photodiodes to demonstrate the first single-chip 40 Gb/s optical transceiver. In 2006, James joined the RF/optoelectronic group at Sandia National Laboratories where he continues to work on leading edge PICs. He has authored or co-authored over 70 technical papers and is a member of IEEE LEOS, OSA and SPIE.

Larry A. Coldren received the Ph.D. degree in electrical engineering from Stanford University, Stanford, CA in 1972. After 13 years in the research area at Bell Laboratories, he joined the University of California, Santa Barbara (UCSB), in 1984, where he is now the Fred Kavli Professor of optoelectronics and sensors, and the Director of the Optoelectronics Technology Center. In 1990, he cofounded Optical Concepts, later acquired as Gore Photonics, to develop novel vertical cavity surface-emitting laser (VCSEL) technology and in 1998 he cofounded Agility Communications to develop widely tunable integrated transmitters. At Bell Laboratories, he initially worked on waveguided surface-acoustic wave signal processing devices and coupled-resonator filters. He later developed tunable coupled-cavity lasers using novel reactive-ion etching (RIE) technology that he created for the then new InP-based materials. At UCSB he continued work on multiple-section tunable lasers, inventing, in 1988, the widely tunable multi-element mirror concept. During the late 1980s, he also developed efficient vertical-cavity multiple-quantum-well modulators, which led to novel VCSEL designs that provided unparalleled levels of performance.

His current research interests include developing new photonic integrated circuit (PIC) and VCSEL technology, including the underlying materials growth and fabrication techniques, creation of vertical and in-plane GaN-based emitters, efficient all-epitaxial InP-based VCSELs, and a variety of PICs incorporating numerous optical elements for widely tunable integrated transmitters, receivers, and wavelength converters. He has authored or coauthored over 700 papers, five book chapters, one textbook, and is a holder of 36 patents. Prof. Coldren has presented dozens of invited and plenary talks at major conferences. He is a Fellow of the Optical Society of America and Institute of Electrical Engineers, and a member of the National Academy of Engineering. He was the recipient of the 2004 John Tyndall Award.

SOA Gate Array Recirculating Buffer for Optical Packet Switching

Emily F. Burmeister, John P. Mack, Henrik N. Poulsen, Jonathan Klamkin, Larry A. Coldren,
Daniel J. Blumenthal, John E. Bowers
Electrical and Computer Engineering Department, University of California at Santa Barbara, Santa Barbara, California 93106-9560
emily@ece.ucsb.edu

Abstract: A compact recirculating buffer using an InP-based 2x2 switch with gain and a fiber delay line is demonstrated at 40 Gb/s. Packet throughput of 98% is measured for up to 8 circulations, or 0.18 µs.

OCIS codes: (060.1810) Buffers, couplers, routers, switches, and multiplexers; (250.3140) Photonic integrated circuits

1. Introduction

Optical buffering is one of the major challenges in realizing the benefits of optical packet switching. However, a compact, scalable, high bit-rate solution has yet to be demonstrated [1]. The majority of optical buffering approaches can be generalized as either feedback or feed-forward buffers, many of which implement two-by-two and one-by-two switches [2, 3]. Although reasonable storage times have been demonstrated, there have not been any practical compact solutions. The buffer presented here is demonstrated without any additional components in the delay loop and can be easily integrated with an on-chip silicon or silica delay. To the authors' knowledge, this device has the best performance for a buffer approach amenable to integration.

2. Buffer design

A recirculating buffer approach is chosen to provide dynamic control of storage times with the granularity of the delay line length. Recirculating buffers have been pursued with success in the past using fiber loops [4, 5] and therefore show promise for a practical buffer if they can be designed to be amenable to integration while not sacrificing performance. The buffer combines a 2x2 InP-based switch with 450 centimeters of fiber or silica delay line (Fig. 1a). The delay line length is chosen to be slightly longer than the length of a packet and its guard bands; thus allowing the greatest resolution in possible delay times.

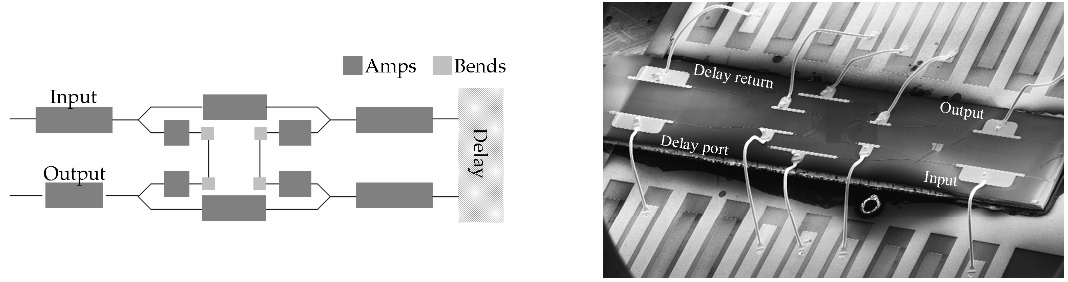

Fig. 1. a) Schematic of 2x2 switch with amplifiers. b) SEM image of the switch affixed and wire-bonded to a submount.

Recirculating buffers place significant performance requirements on the 2x2 switch. To be competitive, the switch must be bit-rate scalable up to 40 Gb/s, have low crosstalk (< -40 dB) and high extinction ratios (>40 dB) for cascadability [6], and be able to switch within packet guard bands. The semiconductor optical amplifier (SOA) gate matrix switch is the most promising switch choice for recirculating buffers because it is fast, meets the crosstalk requirement, and has low insertion loss. During operation, the signal is split toward the two possible ports and the switching amplifier is turned on for the desired path while the other path's amplifier is left off to absorb the remainder. A fabricated switch was previously characterized with good performance up to 40 Gb/s and switching times less than 2 ns [7]. A second generation for integration was fabricated and is shown in Fig. 1b.

The InGaAsP/InP SOA gate matrix switch presented here has an improved integrated amplifier layout and waveguide routing. The switch uses an offset quantum well platform in which the quantum wells are grown above a bulk waveguide layer. This results in an offset between the peak of the mode and the gain region and thereby lowers the confinement factor. The benefits of this platform include ease of fabrication, the possibility of future integration with other standard photonic integrated circuits, and linear performance at higher output powers due to the lower confinement factor [8]. Many-body gain simulations were performed to optimize the placement and lengths of the amplifiers in order to distribute the gain and minimize saturation. The total gain is designed to exceed the loss by only several dB. Therefore, during the first several circulations there is slight gain until the amplified spontaneous emission (ASE) builds up and detracts slightly from signal gain. The amplifier lengths range from 200 μm long for the switching amplifiers in the shortest path up to 650 μm long for the input amplifier and the amplifiers on both ends of the delay. In addition, the amplifier directly before the delay is flared as it will see the most power. An additional component is the tightly confining, deeply etched bend to avoid crossing waveguides while allowing the input and output ports to be positioned on the side opposite to the delay ports.

3. Measurements

3.1 Measurement setup

The experiments were performed on devices that were soldered and wirebonded to aluminum nitride submounts and subsequently affixed with thermal compound to a copper mount. The submounts were cooled to approximately 18˚C. Lensed fibers were used at each of the four ports to couple light on and off the chip. The optical signal (1550 nm) was modulated using an SHF 50 Gb/s BERT with RZ 2^{31}-1 pseudo-random bit sequence (PRBS) data at 40 Gb/s. Packet measurements were made using 40-byte packets which contained identifier strings for characterization. A variable attenuator and a polarization controller were placed in the setup before the device to maintain a TE-polarized input since the quantum well amplifiers are polarization dependent. A 1.2-nm bandpass filter was placed before the receiver to reduce the ASE.

3.2 InP switch

Static measurements and bit error rate testing were performed using continuous data at 40 Gb/s to characterize the performance of the switch. The chip gain from the input port fiber to the delay fiber was approximately 2 dB. The sensitivity degradation for the four port configurations at 40 Gb/s is shown in Fig. 2a. The back-to-back measurement is taken as a reference for the system by bypassing only the device under test with a fiber patch cord. As can be seen in Fig. 2a, the measurements show negative power penalty. This is due to reshaping from the amplifiers and the bandpass filter used to reduce the accumulated ASE. The primary limitation of sensitivity is the ASE that builds up in the amplifiers. The dynamic range of the input power is shown below in Fig. 2b and is greater than 15 dB.

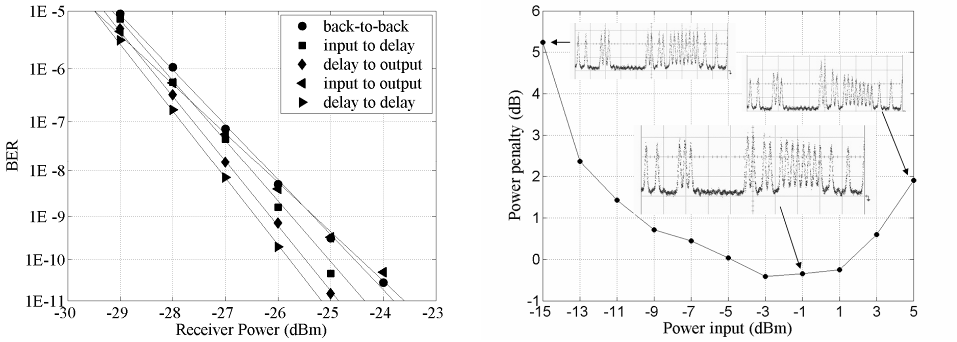

Fig. 2. a) BER vs. optical power at 40 Gb/s RZ 2^{31}-1. b) Operable range of input powers for the path from the input port to the delay port.

3.3 Buffering

The InP-based switch was combined with a fiber delay loop to demonstrate successful optical buffering of packets. The fiber delay was chosen to be 23 ns, which is therefore also the resolution of the storage time. Optical signal-to-noise ratios (OSNR) were measured by taking the difference of the power of the signal and the noise at a wavelength 1 nm away. These calculations were done for a range of the input power to the device for all storage times from 1 to 10 circulations. The back-to-back OSNR was 53 dBm.

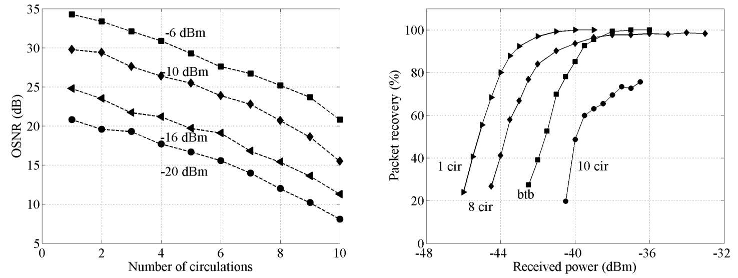

Fig. 3. a) Optical signal-to-noise ratios as a function of number of circulations for a range of input powers. b) Packet recovery percentage as a function of received power for back-to-back and 1, 8, and 10 circulations.

Packet recovery data was then taken to demonstrate that the data was preserved. Due to the size and spacing of the packets, the BERT can not synchronize to the data; therefore bit error rate measurements are not possible. Packet recovery is used as a Layer 2 metric that can predict the buffer's ultimate success in an all-optical router. Forty-byte packets were stored for up to 184 ns with recovery greater than 98%, as shown in Fig. 3b. In addition, the dynamic range of the buffer was tested for 4 circulations and shown to be error-free over an 8 dB range of input power (Fig. 4a). Lastly, a 5-nm bandpass filter was used in the recirculation loop to reduce the ASE buildup. Figure 4b shows the improvement provided by the filter, which increases the maximum storage time to 230 ns.

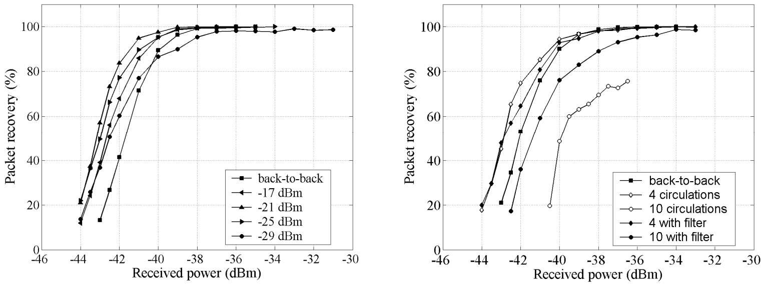

Fig. 4. a) Packet recovery measurements for varying input power for a delay of 4 circulations.
b) Improvement shown in packet recovery by using a bandpass filter in the delay line.

4. Conclusions

The buffer demonstrated here uses an SOA gate array switch that has excellent extinction (40 dB), low crosstalk (-40 dB) and sufficient gain to balance the recirculating losses. The buffer is randomly accessible in time increments of 23 ns and can store packets for up to 184 ns with greater than 98% packet recovery. This approach provides a practical solution to meet the predicted memory needs in future optical routers [9]. The buffer presented offers a compact solution for optical memory that can be easily integrated with a chip delay.

This work is supported by DARPA and the Army under contract #W911NF-04-9-0001.

5. References

[1] E. F. Burmeister, D. J. Blumenthal, and J. E. Bowers, "A comparison of optical buffering technologies," *Optical Switching and Networking*, in press doi:10.1016/j.osn.2007.07.001 (2007).

[2] W. Vanderbauwhede and H. Novella, "A multi-exit recirculating optical packet buffer," *IEEE Photon. Technol. Lett.*, vol. 17, pp. 1749-1751, Aug. 2005.

[3] D. K. Hunter, D. Cotter, R. B. Ahmad, W. D. Corwell, T. H. Gilfedder, P. J. Legg, and I. Andonovic, "Buffered switch fabrics for traffic routing, merging, and shaping in photonic cell networks," *IEEE J. Lightwave Technol.*, vol.15, pp.86-101, Jan. 1997.

[4] K. L. Hall and K. A. Rauschenbach, "All-optical buffering of 40-Gb/s data packets," *IEEE Photon. Technol. Lett.*, vol. 10, Mar. 1998.

[5] N. Chi, Z. Wang, and S. Yu , "A large variable delay, fast reconfigurable optical buffer based on multi-loop configuration and an optical crosspoint switch matrix," *Optical Fiber Communication Conference*, OFC, Anaheim, CA, OFO7, 2006.

[6] C. P. Larsen, and M. Gustavsson, "Linear crosstalk in 4x4 semiconductor optical amplifier gate switch matrix," *IEEE J. Lightwave Technol.*, vol. 15, pp. 1865-1870, Oct. 1997.

[7] E. F. Burmeister, J. E. Bowers, "Integrated gate matrix switch for optical packet buffering," *IEEE Photon. Technol. Lett.*, vol. 18, no. 1, pp. 103-106, Jan. 2006.

[8] B. Mason, J. S. Barton, G. A. Fish, L. A. Coldren, and S. P. Denbaars, "Design of sampled grating DBR lasers with integrated semiconductor optical amplifiers," *IEEE Photon. Technol. Lett.*, vol. 12, pp. 762-764, 2000.

[9] N. Beheshti, Y. Ganjali, R. Rajaduray, D. Blumenthal, and N. McKeown, "Buffer sizing in all-optical packet switches," *Optical Fiber Communication Conference*, OFC, Anaheim, CA, OThF8, 2006.

Widely Tunable Separate Absorption and Modulation Wavelength Converter With Integrated Microwave Termination

Matthew M. Dummer, *Student Member, IEEE*, Matthew N. Sysak, *Member, IEEE, Member, OSA*,
Anna Tauke-Pedretti, *Student Member, IEEE*, James W. Raring, *Member, IEEE, Member, OSA*,
Jonathan Klamkin, *Student Member, IEEE*, and Larry A. Coldren, *Fellow, IEEE, Fellow, OSA*

***Abstract*—A widely tunable wavelength converter utilizing a separate absorption and modulation configuration and only dc bias connections is demonstrated. The device integrates an SG-DBR laser with a traveling-wave electroabsorption modulator and an optically pre-amplified receiver and introduces a simplified bias scheme by the inclusion of passive resistor and capacitor circuit elements. We discuss a the design of these passive elements and their compatibility with fabrication of photonic integrated circuits. The device demonstrates over 12 GHz optical bandwidth and error free 10 Gb/s wavelength conversion is achieved with less than 2.5 dB power penalty over 25 nm of output tuning.**

***Index Terms*—Electroabsorption, optical receivers, optical transmitters, p-i-n photodiodes, sampled grating distributed Bragg reflector (SG-DBR), semiconductor optical amplifiers (SOAs), traveling wave devices, wavelength conversion (WC), wavelength division multiplexing (WDM).**

I. INTRODUCTION

As CURRENT optical fiber communications continue to push the limits of bandwidth utilization, wavelength conversion is becoming an increasingly important function in wavelength division multiplexed (WDM) networks. Wavelength conversion in high traffic networks reduces blocking probabilities, when signal contention is problematic, and has applications in optical routing, switching and add/drop multiplexing [1]. Monolithically integrated wavelength converters (WC), in which a tunable laser source can be incorporated on-chip, are particularly interesting devices due to their small footprint, low-cost packaging, and potential for scalability.

Although many technologies for wavelength conversion have been employed, there are two main approaches which lend themselves to monolithically integrated devices. The first of these is a carrier-modulated all-optical approach, in which an input signal is combined with a tunable laser source in the same semiconductor optical amplifier (SOA). If operated in the saturation regime, the inherent non-linearity of the SOA provides cross gain (XGM) and cross phase modulation (XPM) to transfer the information from the input wavelength to the wavelength from the tunable source. The bandwidth of SOA-based WCs is limited by the carrier recovery lifetime of the SOAs, and operation has typically been limited to data rates up to 10 Gb/s [2], although faster operation has also been demonstrated with very high power penalties [3]. Recently, delayed interferometric techniques have been employed to surpass the carrier recovery lifetime limit and 40 Gb/s operation has been achieved in a monolithic device [4], [5].

The other approach to monolithic wavelength conversion, pursued in this work, is based on separate absorption and modulation (SAM) of the optical signals. In this approach, a tunable transmitter and optical receiver are monolithically integrated on a single-chip. The photodiode of the receiver is interconnected to the modulator of the transmitter, which can be either a Mach-Zehnder (MZ) or electroabsorption modulator (EAM). The input signal into the receiver is optically pre-amplified using an SOA such that sufficient photocurrent is generated in the photodiode to directly drive the modulator without any electronic driver circuitry. With this configuration, the input data can be transcribed onto any output wavelength within the range of the tunable source. SAM-WCs have demonstrated wavelength conversion up 10 Gb/s [6] and have potential for higher bit rate scaling, as similar configurations used in optical gates have already demonstrated functionality up to 500 Gb/s [7]. Other advantages of SAM-WCs include lower power dissipation and smaller footprint than their SOA-based counterparts, reshaping and re-amplification (2R) of the input data signal [8], and the elimination of any output optical filtering requirement, since the two optical signals are spatially separated throughout the entire device. The potential for 3R regeneration has also been demonstrated by including clock recovery circuitry for retiming [8]. However, previous demonstrations of SAM-WCs have been complicated by the transport of microwave signals off of the chip requiring high speed probes, bias-Ts [6], and complex bias circuitry [9]. In this paper, we demonstrate an EAM based SAM-WC in which a termination resistor and dc-blocking capacitor are integrated onto the chip, such that only a common dc bias is required for the both EAM and photodiode and no additional RF components are necessary. By keeping all high frequency components confined to the chip, this advancement greatly simplifies the packaging requirements and allows for operation and scalability of SAM-WCs which is

Manuscript received April 18, 2007; revised November 16, 2007. This work was supported by the Defense Advanced Research Projects Agency (DARPA) under MTO-LASOR Grant W911NF-04-9-0001 and MTO-CS-WDM Grant N66001-02-C-8026.

The authors are with the Department of Electrical and Computer Engineering and the Department of Materials, University of California Santa Barbara, Santa Barbara, CA 93106 USA (e-mail: dummer@engineering.ucsb.edu).

Color versions of one or more of the figures in this paper are available online at http://ieeexplore.ieee.org.

Digital Object Identifier 10.1109/JLT.2007.915202

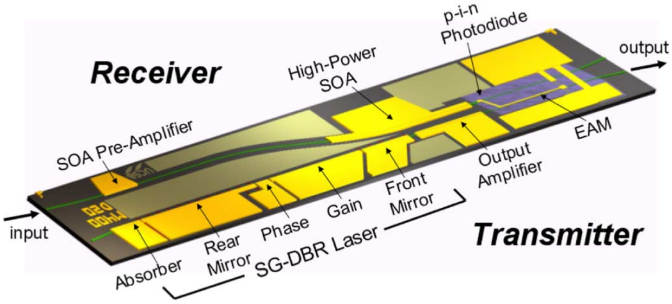

Fig. 1. Schematic of the monolithically integrated wavelength converter with separate receiver and tunable transmitter. The total device footprint is 3.1 mm by 0.5 mm.

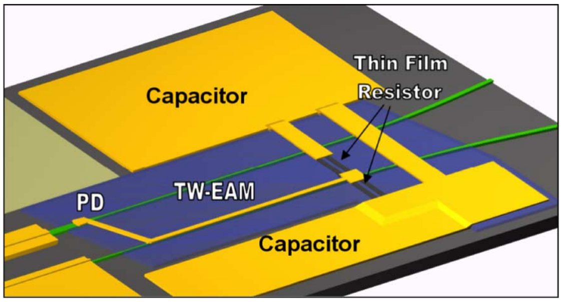

Fig. 2. Schematic of integrated photodiode and EAM with on chip load resistor and dc-blocking capacitor.

analogous to SOA-based implementations while maintaining all the benefits of a separate absorption and modulation device.

II. Wavelength Converter Design

This device is fabricated using the dual quantum well (DQW) integration platform described in [10], which incorporates a 350 nm quaternary (InGaAsP) waveguide layer between p- and n-type InP cladding layers above and below, respectively. The DQW consists of a set of seven offset quantum wells (QWs) with a photoluminescence peak wavelength (λ_{PL}) of 1542 nm above the waveguide layer and eight detuned quantum wells $(\lambda_{PL} = 1455 \text{ nm})$ centered in the waveguide. The offset wells provide the optical gain for the laser and SOA components and are selectively etched from passive and modulation regions before blanket regrowth of the p-type InP cladding. The centered wells are present throughout the device and are used for EAM efficiency under reverse bias but are detuned from the operating wavelength to maintain low optical loss throughout the unbiased passive regions.

Fig. 1 depicts the full the SAM-WC consisting of two spatially separated surface-ridge waveguides which function as the receiver and transmitter. The receiver consists of two SOAs followed by a quantum well p-i-n photodiode (PIN-PD). The first SOA is 200 μm long and 3 μm wide and the second SOA is 800 μm long and with a ridge that flares linearly to 9 μm over the last half of the length. The flared ridge design has been shown to improve the saturation power of the SOA by reducing optical power density within the waveguide [11]. An S-bend between the two receiver SOAs was designed to minimize the interconnect distance between the PIN-PD and the EAM. The PIN-PD is 20 μm long and utilizes the offset QW stack as the absorbing layer for generating photocurrent. The ridge width is tapered from 9–6.5 μm to prevent saturation from excess space charge while minimizing the total capacitance.

The transmitter consists of a widely tunable sampled grating distributed Bragg reflector (SG-DBR) laser followed by an output 400 μm long SOA and 400 μm long EAM. The SG-DBR and SOA ridge width is 3.5 μm and tapers to a 2.5μm in the EAM. Photo-BCB (Benzo-cyclobutene) is defined around the EAM and PIN-PD as a low-k dielectric to reduce parasitic capacitance. A 75 μm long electrical interconnect above the BCB connects the PIN-PD to the EAM (Fig. 2). The interconnect and PIN-PD and EAM electrodes are designed as microstrip transmission lines and configured such that the optical and electrical signals propagate in the same direction to take advantage of traveling wave effects. The EAM electrode is terminated by an on-chip resistor and dc blocking capacitor described in detail in Section III.

III. Passive Components

The resistor and capacitor elements function to terminate the generated microwave signals after being transported from the absorbtion to modulation regions. The load resistance directly determines the magnitude of the electric field in the EAM, and hence the conversion efficiency, as well as the total operating bandwidth of the device. Power handling is also important, as the resistor must be capable sinking all the photocurrent generated in both the PIN-PD and EAM. For this work, NiCr thin film resistors were chosen because of their ease of fabrication and patterning with standard liftoff techniques. It is well known that electron beam evaporation of NiCr alloyed sources produces varying sheet resistance, and poor repeatability due to the differing vapor pressures of nickel and chrome during deposition [12]. To ensure controllable composition and repeatability we have instead developed a digital layer deposition technique where nickel and chrome sources are evaporated separately and then alloyed by annealing. For the initial run of devices, four layers totaling 720Å were deposited with a composition of 70:30 Nickel-Chrome followed by an anneal at 390 C. These resistors were patterned as either 1.25 or 2.5 squares with stripe lengths of 40 μm. This first run exhibited a low sheet resistance of 10 $\Omega/\square$ and poor power handling capability with breakdown occurring for dc biases greater than 1 V. On subsequent fabrication runs the resistor pattern dimensions were increased by 2.5 times to improve power handling and an eight layer deposition process was used to improve the uniformity of the alloy composition. For the same thickness, NiCr composition, and anneal temperature, the resistivity was increased to 14 $\Omega/\square$ as shown in Fig. 3. The eight-layer resistors also demonstrated better ohmic behavior and sustained biases greater than 2 V dc. These results have been repeated in three further fabrications.

As shown in Fig. 2 the resistor is followed by two metal-insulator-metal (MIM) capacitors on either sides of the ridges that provide a low impedance ground path for the microwave signal and allow for biasing of the EAM and PIN-PD. A 3500Å thick n-contacting AuGe ground plane extends from below the BCB to form the lower plate of the capacitor. The dielectric material consists of 2500Å of silicon nitride deposited by physical evaporation chemical vapor deposition (PECVD). A 2.5 μm thick

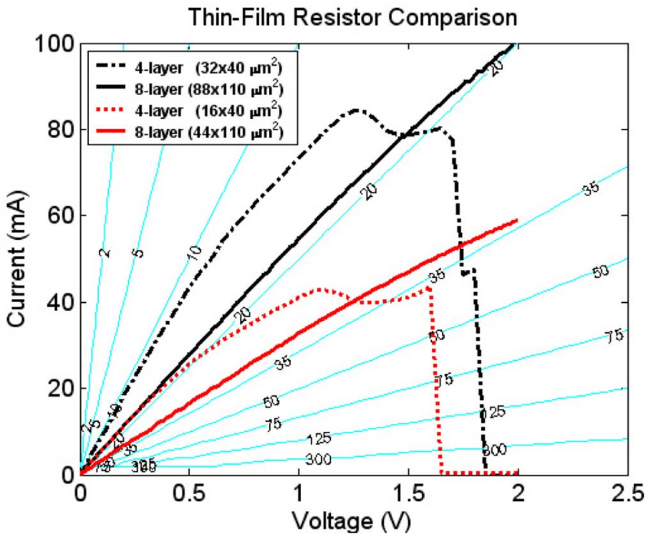

Fig. 3. Comparison of resistance and power handling for two NiCr resistor fabrications. Run 1 and 2 are denoted four layer and eight layer, respectively. Physical resistor dimensions are listed in parenthesis. Constant resistance contours are shown for reference.

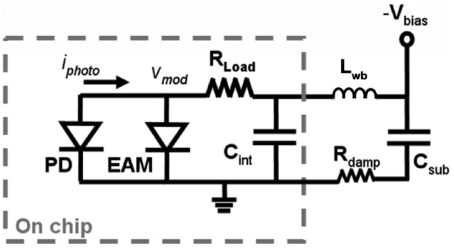

Fig. 4. Equivalent circuit diagram of wavelength converter.

gold layer forms the top plate of the capacitor and the interconnect to the NiCr resistor. The total area of the two on-chip capacitors is 0.14 mm^2 with a capacitance that has been measured to be 30 pF.

IV. BIASING

A circuit diagram depicting the bias configuration for the wavelength converter is shown in Fig. 4. Only a single reverse bias, applied through wirebonds to the two plates of the capacitor, is needed for biasing both the EAM and PIN-PD. Since both plates are equivalently "RF ground," this bias scheme eliminates any parasitic capacitance typically associated with bonding pads and the need for any transmission lines or bias-Ts off chip. Also, placing the resistor in series with the two diodes ensures no dc power dissipation in the load resistor under normal reverse bias operation, aside from the dc photocurrent generated in the EAM. Though simplistic, this bias circuit also has two issues which need to be addressed. First, the 30 pF on chip capacitor (C_{int}) is a sufficient ground for frequencies above 600 MHz. However typically a larger capacitor $(C_{\mathrm{sub}} = 220\ \mathrm{nF})$ is added to the carrier to extend the low frequency response. This is especially important for achieving minimal pattern dependance for pseudo random bit streams with long word lengths. Second, the wirebonds from the carrier to the on-chip capacitor induce an LC resonance in the frequency response. Fig. 5 shows a simulation of the small signal response for different values of wirebond inductance (L_{wb}). By minimizing the wirebond length and adding a small amount of series resistance to dampen the inductive peak (R_{damp}), the resonance can be effectively eliminated. Typically R_{damp} values used range from 3 to 5 Ω for wirebonds less than 2 mm. Larger resistance values are avoided since they create a non-uniform response by effectively increasing the termination resistance for low frequency components.

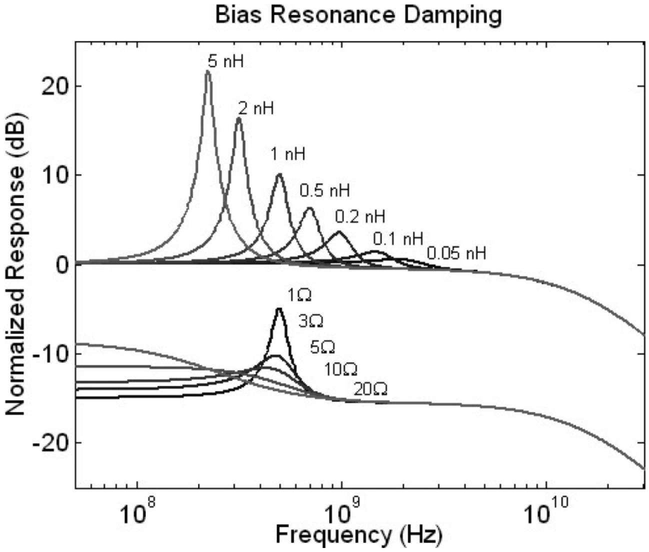

Fig. 5. Simulated effects of wirebond resonance on wavelength converter frequency response for various wirebond inductances (top) and damping resistor values (bottom).

V. RECEIVER PERFORMANCE

The receiver and transmitter have been extensively characterized separately to determine their individual contributions to wavelength converter performance. Due to the use of compressively strained QWs, the SOAs and PIN-PD are highly polarization sensitive and the input signal must be optimized to the transverse electric (TE) orientation to achieve the best performance. Both high gain and saturation power of the receiver SOAs are key attributes for achieving conversion gain and high extinction ratios. Fig. 6 shows the optical output power (P_{out}) versus input power (P_{in}) of the receiver for both SOAs biased at a current density of 6 $\mathrm{kA/cm}^2$. The continuous wave (CW) measurements show the receiver optical gain to be 19 dB when operating in the linear regime. The 1-dB output compression power of the receiver is 14 dBm, which translates into 25 mA of dc photocurrent generation. The modal absorption coefficient of the offset QWs under reverse bias has been measured by photocurrent spectroscopy to be 450 cm^{-1}, yielding an a internal quantum efficiency of 60% for the 20 μm long PIN-PD. Small signal frequency response measurements demonstrate a 3-dB bandwidth in excess of 20 GHz for the PIN-PD with 25 Ω termination. With sufficient bias, the tapered ridge PIN-PD design exhibits excellent power handling capabilities [11]. As shown in Fig. 7, with 14 mA average photocurrent the device shows no bandwidth degradation due to saturation effects for reverse biases greater than 2.5 V.

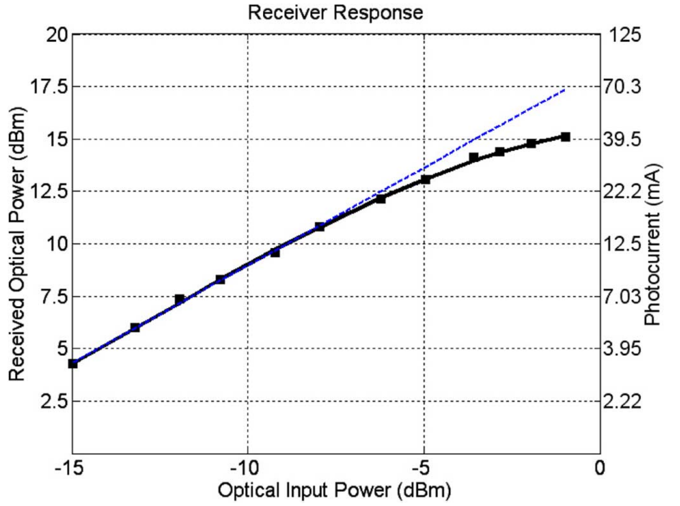

Fig. 6. Optical output power (P_{out}) vs optical input power (P_{in}) for biases of 40 mA and 290 mA on 200 $\mu\mathrm{m}$ and 800 $\mu\mathrm{m}$ SOAs, respectively. The measured photocurrent level from the PIN-PD is shown on the right axis. PIN-PD bias was $-3.0\ \mathrm{V}$.

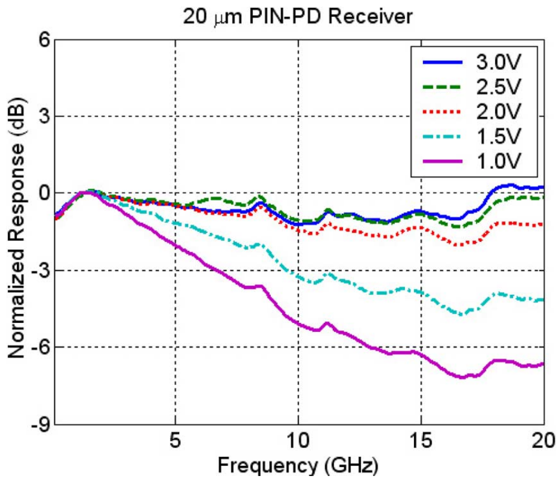

Fig. 7. Frequency response of 20 $\mu\mathrm{m}$ long PIN-PD photodetector for varying reverse bias with 25 Ω termination. The input power into the receiver was $-6.7\ \mathrm{dBm}$ and average detected photocurrent was 14 mA.

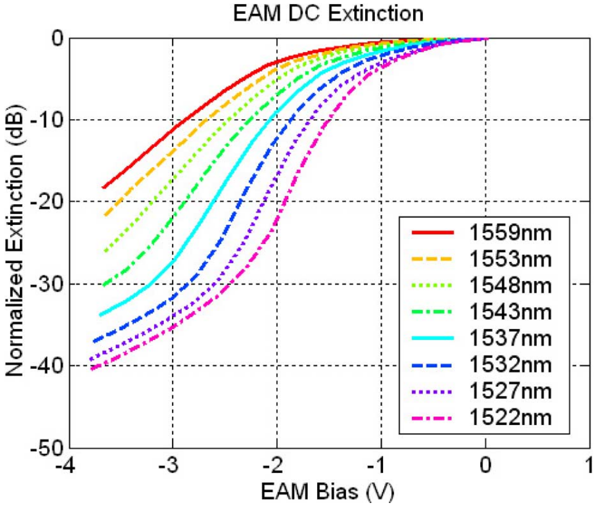

Fig. 8. DC extinction curves taken from 400 $\mu\mathrm{m}$ EAM over the tuning range of the SG-DBR.

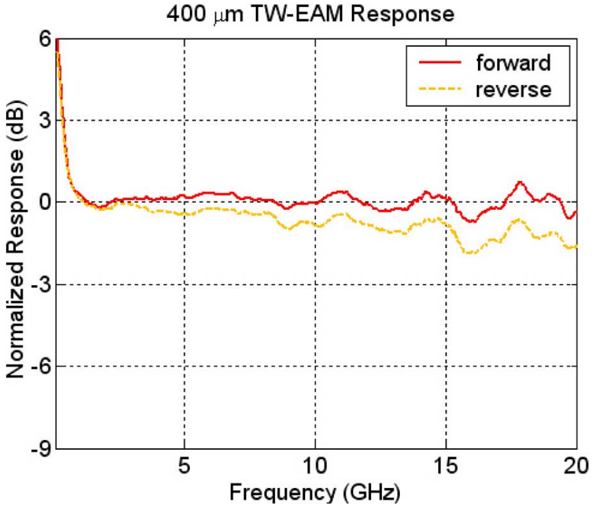

Fig. 9. Forward and reverse EO traveling wave response for the discrete 400 $\mu\mathrm{m}$ EAM. On-chip termination is 20 Ω. The dc bias is $-2\ \mathrm{V}$.

VI. TRANSMITTER PERFORMANCE

The SG-DBR laser utilizes vernier tuning of the front and rear mirrors to achieve continuous tuning of the emission wavelength from 1522–1565 nm. The maximum fiber coupled output power is 6.2–9.8 dBm over the wavelength range of the SG-DBR for bias currents of 150 mA applied to both the gain section of the laser and the output SOA. dc extinction curves for the 400 $\mu\mathrm{m}$ long EAM are shown in Fig. 8 for wavelength between 1522 nm and 1559 nm. The detuned band edge of the centered quantum wells creates a strong wavelength dependence with peak slope efficiencies that range from 25 dB/V for the shortest wavelength down to 10 dB/V for longest wavelength.

Since the positions of the laser source and electrical termination in the wavelength converter are fixed, it is impossible to determine the amount of traveling wave (TW) benefit in the EAM directly. Instead, discrete TW-EAMs were fabricated on the same wafer as the integrated wavelength converter to measure the electrical-to-optical (EO) response. These EAMs were directly driven by probing a coplanar waveguide (CPW) and terminated by the same on-chip resistor and capacitor. EO small signal measurements were performed using an external 1550 nm laser source coupled into either facet to compare co- and counter-propagating TW bandwidth. The characteristic impedance of the EAM transmission line was measured as 24 Ω and the NiCr resistor value used was 20 Ω to minimize electrical reflections in the device. These low impedances are typical of such capacitively loaded electrode structures [13], [14]. Fig. 9 shows results of the EO measurements comparing the "forward" response, when the optical signal propagates in the same direction as the electrical drive, and "reverse," when the two signals counter-propagate. Although the 3-dB bandwidth is greater than 20 GHz in both cases, the forward measurement exhibits virtually no roll-off over the measurement range, which demonstrates the significance of the traveling wave design. The dc bias for both of these measurements was $-2.0\ \mathrm{V}$, although other experiments show that the response is independent of

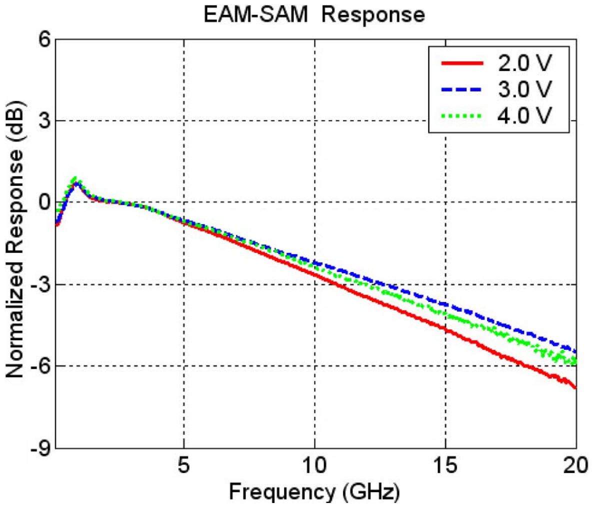

Fig. 10. Optical-to-optical small signal frequency response for SAM-WC for various reverse biases of EAM and PIN-PD. Load resistor is 35 Ω.

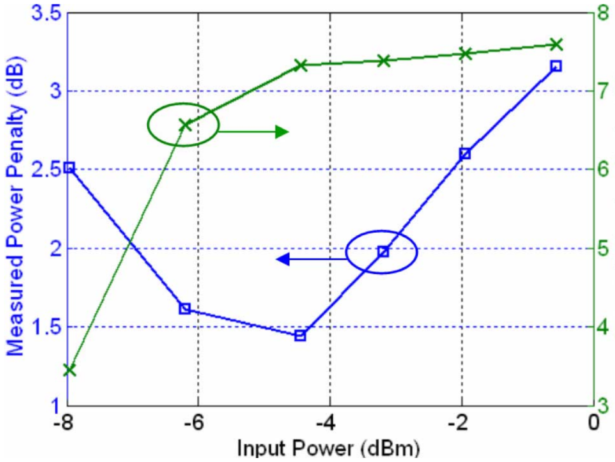

Fig. 11. Wavelength converted power penalty (at $\mathrm{BER} = 10^{-9}$) and output extinction ratio for varied input signal powers. The input wavelength is 1548 nm and the output wavelength is 1537 nm. The EAM and PIN-PD bias is -2.5 V.

bias for typical operating points between −1.5 and 3.5 V. The sharp rise in the response below 1 GHz shows the limit of the integrated capacitor, since no external capacitor was used during this experiment.

VII. WAVELENGTH CONVERTER EXPERIMENTS

A series of experiments have been performed to evaluate wavelength conversion performance. For these experiments, the device under test was mounted and wirebonded to an aluminum nitride carrier. The carrier was place on a copper stage with a temperature actively maintained at 16° C. A dc probe card contacting the carrier was used to apply all biases and optical signals were coupled to and from the chip using conically tipped lensed fibers. In all experiments, the input signal was amplified by an erbium doped fiber amplifier (EDFA) followed by an optical filter to reduce amplified spontaneous emission (ASE) noise and a polarization controller to optimize the receiver gain.

Testing of the wavelength converter consisted of both small and large signal characterization. First, small signal measurements were taken to determine the total optical-to-optical (OO) bandwidth of the device. The results of the small signal frequency response measurement are shown in Fig. 10 for varying bias. For −3 V bias and 35 Ω on-chip termination, the 3-dB optical bandwidth of the wavelength converter is 12.6 GHz.

Large signal experiments consisted of measuring the bit error rate (BER) of the device for wavelength conversion of digital data at 10 Gb/s with non-return-to-zero (NRZ) format. The BER test setup was similar to the one described in [15] and utilized a $2^{31}-1$ pseudo-random bit stream (PRBS) as the input signal. Bit error rate curves were generated by attenuating the output of the device and measuring the BER for various powers into a commercial optical receiver.

A. *Dynamic Range Experiments*

The dynamic range of the SAM-WC receiver greatly affects the wavelength converter performance. Low input powers result in insufficient photocurrent levels for driving the EAM causing poor output extinction ratios (ER). Conversely, high input powers result in output pattern dependence due to saturation of the receiver SOA. Because of this, it was necessary to find the optimum input power for the device by measuring the BER at several input power levels. The bias currents for this experiment were fixed at 40 and 240 mA for the receiver SOAs, and 100 and 40 mA for the laser gain section and transmitter SOA, respectively. For fixed input and output wavelengths of 1548 and 1537 nm, the BER of the wavelength converted signal was compared with the BER for back-to-back transmission and the difference was calculated as a power penalty.

Fig. 11 shows the results of varying the optical input power into the wavelength converter. The measured power penalty at a BER of 10^{-9} along with the associated output extinction ratio is plotted for each input power. The power penalty reaches a minimum of 1.4 dB at the input power of −4.5 dBm. The explanation for this is best seen in the output eye diagrams in Fig. 12. Each eye, (a)–(f), is the wavelength converted output corresponding to the data points in Fig. 11 from left to right. For low input powers, (a) and (b), the BER is limited by the reduced output extinction ratio. For higher input powers, (d)–(f), the power penalty increases even though the output ER continues to improve. In this case, signal distortion due to the receiver SOA saturation becomes the limiting factor. The effect of the pattern dependence in the eye diagrams is apparent in the rising crossover point, and increased jitter and fall time that can be attributed to gain recovery time in the saturated receiver SOA.

The results of this experiment show that the optimum input power into the wavelength converter, −4.5 dBm, matches the 1-dB compression point of the receiver SOA from Fig. 6. The eye labeled (c) represents the optimum output with 7.3 dB extinction and 0.3 mW output amplitude. This value corresponds to unity conversion gain after accounting for 4 dB fiber coupling losses. Higher conversion efficiency is possible by increasing the bias current in the transmitter SOA to boost the output power. However, this comes at the expense of increased thermal crosstalk between the transmitter and receiver SOAs which reduces the maximum achievable receiver power.

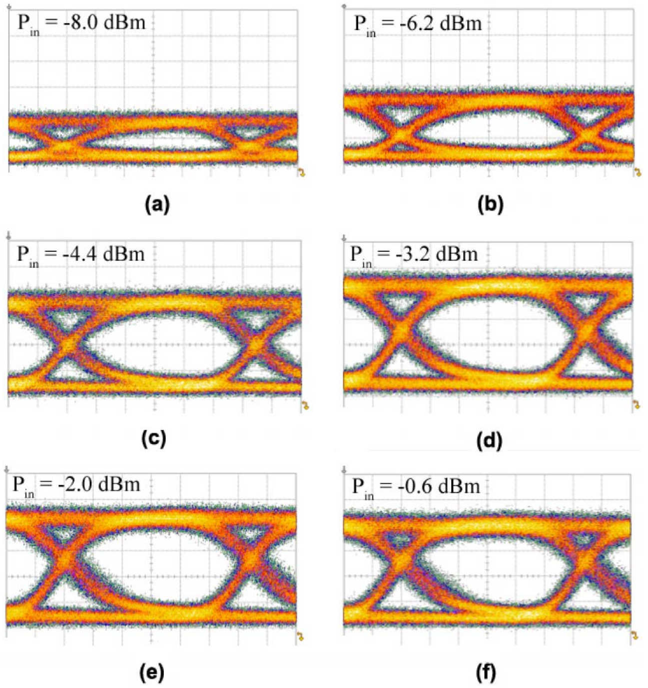

Fig. 12. 10 Gb/s wavelength converted (1548–1537 nm) eye diagrams corresponding to the input powers (P_{in}) in Fig. 11. The scales of the two axes are 16.3 ps/div and $95\ \mu\mathrm{W/div}$.

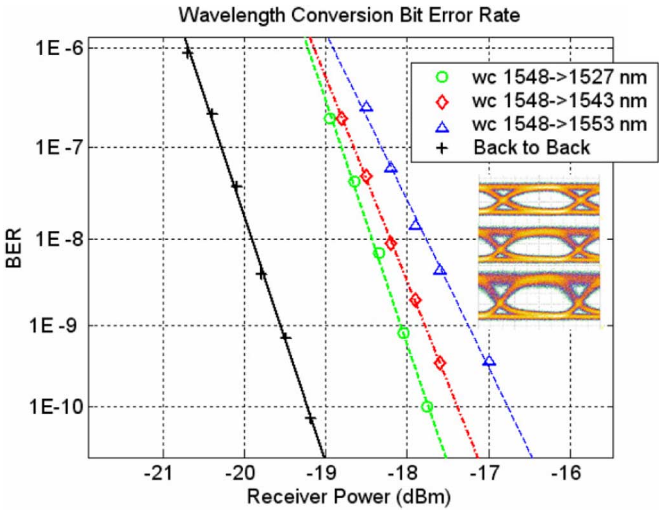

Fig. 13. Wavelength conversion BER measurements for constant input and varying output wavelength compared with back-to-back transmission. The corresponding eye diagrams are shown for 1527, 1543, and 1553 nm from top to bottom with extinction ratios of 8.0, 7.4, and 6.6 dB, respectively.

B. Wavelength Conversion Performance

After an optimal input power was determined, wavelength conversion was performed from the same fixed wavelength (1548 nm) to multiple output wavelengths across the tuning range of the SGDBR. The bias for the EAM and PIN-PD was adjusted to take advantage of the steepest slope efficiency of the modulator at each wavelength (Fig. 8). BER curves were generated at multiple wavelengths and again compared to back-to-back transmission to compute the conversion power penalty. The results of these wavelength conversion experiments are shown in Fig. 13. The dc bias was to $-2.2\ \mathrm{V}$, $-2.9\ \mathrm{V}$, and $-3.2\ \mathrm{V}$ for the wavelengths of 1527, 1543, and 1553 nm, respectively. The input power in to the device was $-4.5\ \mathrm{dBm}$ and the output powers were -6.0, -5.2, and $-4.0\ \mathrm{dBm}$, respectively, after subtracting 4 dB fiber coupling losses from both facets. The extinction ratio of the wavelength converted signal ranges from 8.0–6.6 dB. Using a 2 s gating period, error-free operation was observed for all wavelengths with less than 2.5 dB power penalty compared with back-to-back transmission. The decrease in power penalty with shorter output wavelengths in this device is attributed to the increase in output extinction ratio [16]. Therefore, the digital performance could be improved by optimizing the design and band-edge detuning of the modulator quantum wells to achieve higher slope efficiency at the longer wavelengths.

VIII. CONCLUSION

SAM-WCs offer a low-power, small-footprint, bit rate scalable solution for wavelength conversion in WDM networks. We have presented the design, fabrication, and characterization of the first EAM-based widely tunable separate absorption and modulation wavelength converter with integrated passive circuit elements for terminations and biasing. This monolithically integrated device requires only dc connections to the InP chip, greatly reducing biasing and packaging complexity. Wavelength conversion at 10 Gbps demonstrated error free performance with power penalties of less than 2.5 dB over 25 nm of output wavelength tuning. The device performance can be further optimized by improving the linearity of the receiver SOAs, as well as increasing the efficiency of both the photodiode and EAM. These improvements in conjunction with an optimized traveling wave architecture should provide bit rate scaling to accommodate much higher data rates in the future.

REFERENCES

[1] S. Yoo, “Wavelength conversion technologies for WDM network applications,” *J. Lightwave Technol.*, vol. 14, no. 6, pp. 955–966, 1996.

[2] M. Masanovic, V. Lal, J. Summers, J. Barton, E. Skogen, L. Rau, L. Coldren, and D. Blumenthal, “Widely tunable monolithically integrated all-optical wavelength converters in inp,” *J. Lightwave Technol.*, vol. 23, no. 3, pp. 1350–1362, 2005.

[3] T. Hatta, T. Miyahara, Y. Miyazaki, K. Takagi, K. Matsumoto, T. Aoyagi, K. Motoshima, K. Mishina, A. Maruta, and K. Kitayama, “Polarization-insensitive monolithic 40-Gbps SOA MZI wavelength converter with narrow active waveguides,” *IEEE J. Sel. Topics Quantum Electron.*, vol. 13, pp. 32–39, 2007.

[4] V. Lal, M. Masanovic, J. Summers, L. Coldren, and D. Blumenthal, “Performance optimization of an InP-based widely tunable all-optical wavelength converter operating at 40 Gb/s,” *IEEE Photon. Technol. Lett.*, vol. 18, no. 4, pp. 577–579, 2006.

[5] P. Bernasconi, W. Yang, L. Zhang, N. Sauer, L. Buhl, I. Kang, S. Chandrasekhar, and D. Neilson, “40 Gbit/s RZ wavelength converter in a monolithically integrated chip with a tunable laser,” *Electron. Lett.*, vol. 41, no. 12, pp. 701–702, 2005.

[6] M. Sysak, J. Raring, J. Barton, M. Dummer, A. Tauke-Pedretti, H. Poulsen, D. Blumenthal, and L. Coldren, “Single-chip, widely-tunable 10 Gbit/s photocurrent-driven wavelength converter incorporating a monolithically integrated laser transmitter and optical receiver,” *Electron. Lett.*, vol. 42, no. 11, pp. 657–658, 2006.

[7] S. Kodama, T. Yoshimatsu, and H. Ito, “500 Gbit/s optical gate monolithically integrating photodiode and electroabsorption modulator,” *Electron. Lett.*, vol. 40, no. 9, pp. 555–556, 2004.

[8] M. Sysak, J. Raring, L. Johansson, H. Poulsen, J. Barton, D. Blumenthal, and L. Coldren, “Optical 2R and 3R signal regeneration in combination with dynamic wavelength switching using a monolithically integrated, widely tunable photocurrent driven wavelength converter,” in *Proc. Eur. Conf. Optical Communication (ECOC)*, Cannes, France, Sep. 2006, p. Th3.4.1.

[9] J. S. Barton, M. N. Sysak, A. Tauke-Pedretti, M. Dummer, J. Raring, L. A. Johansson, M. L. Masanovic, D. J. Blumenthal, and L. A. Coldren, *Field Modulated Wavelength Converters*, L. A. Eldada and E. Lee, Eds. : SPIE, 2006, vol. 6124, pp. 612417–612417.

[10] M. Sysak, J. Raring, J. Barton, M. Dummer, D. Blumenthal, and L. Coldren, "A single regrowth integration platform for photonic circuits incorporating tunable SGDBR lasers and quantum-well EAMS," *IEEE Photon. Technol. Lett.*, vol. 18, no. 15, pp. 1630–1632, 2006.

[11] A. Tauke-Pedretti, M. Dummer, J. Barton, M. Sysak, J. Raring, and L. Coldren, "High saturation power and high gain integrated photoreceivers," *IEEE Photon. Technol. Lett.*, vol. 17, no. 10, pp. 2167–2169, 2005.

[12] R. F. Kopf, R. Melendes, D. C. Jacobson, A. Tate, M. A. Melendes, R. R. Reyes, R. A. Hamm, Y. Yang, J. Frackoviak, N. G. Weimann, H. L. Maynard, and C. T. Liu, "Thin-film resistor fabrication for InP technology applications," *J. Vacuum Sci. Technol. B: Microelectron. Nanometer Structures*, vol. 20, no. 3, pp. 871–875, 2002.

[13] G. Li, S. Pappert, P. Mages, C. Sun, W. Chang, and P. Yu, "High-saturation high-speed traveling-wave InGaAsP-InP electroabsorption modulator," *IEEE Photon. Technol. Lett.*, vol. 13, no. 10, pp. 1076–1078, 2001.

[14] R. Lewen, S. Irmscher, and U. Eriksson, "Microwave cad circuit modeling of a traveling-wave electroabsorption modulator," *IEEE Trans. Microw. Theory Tech.*, vol. 51, no. 4, pp. 1117–1128, 2003.

[15] M. Sysak, J. Barton, L. Johansson, J. Raring, E. Skogen, M. Masanovic, D. Blumenthal, and L. Coldren, "Single-chip wavelength conversion using a photocurrent-driven EAM integrated with a widely tunable sampled-grating DBR laser," *IEEE Photon. Technol. Lett.*, vol. 16, no. 9, pp. 2093–2095, 2004.

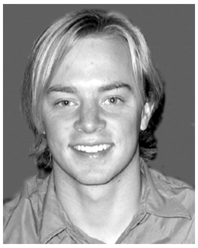

Matthew M. Dummer (S'06) received the B.S. degree in electrical engineering from the University of Minnesota, Twin Cities, in 2002, and M.S. degree from the University of California, Santa Barbara, in 2004, where he is current working toward the Ph.D. degree.

His research focuses on high functionality photonic integrated circuits for wavelength conversion. He also specializes in the fabrication of high power semiconductor optical amplifiers and photodiodes, as well as traveling wave circuit design for electroabsorption modulators.

Matthew N. Sysak (M'06) received the B.S. degree in chemical engineering from the Pennsylvania State University, University Park, in 1998, and the M.S. and Ph.D. degrees from the University of California, Santa Barbara, in 2002 and 2005, respectively. His Ph.D. dissertation focused on material design as well as device design, fabrication, and testing of monolithically integrated, widely tunable, optoelectronic wavelength converters and signal regenerators.

He is currently working on novel photonic circuit design and fabrication for analog, phase modulated links. He has authored and coauthored over 30 conference and journal papers.

Dr. Sysak is a member of the Optical Society of America (OSA), Washington, DC, and the International Society for Optical Engineering (SPIE), Bellingham, WA.

Anna Tauke-Pedretti (S'02) received the B.S. degree in physics and electrical engineering from the University of Iowa, Iowa City, in 2001 and the M.S. degree from the University of California, Santa Barbara, in 2002, where she is currently working toward the Ph.D. degree.

Her current research interests focus on InP-based photonic integrated circuits for high-speed wavelength conversion. She has also developed monolithic high-speed transmitters and high-saturation power pre-amplified receivers.

James W. Raring (M'03) received the B.S. degree from California Polytechnic State University, San Luis Obispo, in 2001 and the Ph.D. degree in materials science from the University of California, Santa Barbara, in 2006. His dissertation focused on the design, growth, and fabrication of high-functionality wavelength agile photonic integrated circuits operating at 10 and 40 Gb/s. The photonic circuits were based on sampled grating DBR lasers, electroabsorption modulators, semiconductor optical amplifiers, and photodiodes.

His work explores novel integration methods coupling quantum-well intermixing with straightforward MOCVD regrowth steps. He has authored or coauthored over 70 technical papers.

Dr. Raring is a member of the Optical Society of America (OSA), Washington, DC, and the International Society for Optical Engineering (SPIE), Bellingham, WA.

Jonathan Klamkin (S'04) received the B.S. degree in electrical and computer engineering from Cornell University, Ithaca, NY, in 2002 and the M.S. degree in electrical and computer engineering from the University of California, Santa Barbara (UCSB), in 2004, where he is currently working toward the Ph.D. degree.

His research interests include the design, growth, fabrication, and characterization of widely-tunable semiconductor lasers, photodetectors, optical intensity and phase modulators, and semiconductor optical amplifiers for InP based photonic integrated circuits. Currently his efforts are focused on novel coherent integrated receivers for highly linear fiber-optic links.

Larry A. Coldren (F'82) received the Ph.D. degree in electrical engineering from Stanford University, Stanford, CA, in 1972.

After 13 years in the research area at Bell Laboratories, he joined the University of California, Santa Barbara (UCSB), in 1984, where he is now the Fred Kavli Professor of Optoelectronics and Sensors, and the Director of the Optoelectronics Technology Center. In 1990, he cofounded Optical Concepts, later acquired as Gore Photonics, to develop novel vertical cavity surface-emitting laser (VCSEL) technology and in 1998 he cofounded Agility Communications to develop widely tunable integrated transmitters. At Bell Laboratories, he initially worked on waveguided surface-acoustic wave signal processing devices and coupled-resonator filters. He later developed tunable coupled-cavity lasers using novel reactive-ion etching (RIE) technology that he created for the then new InP-based materials. At UCSB he continued work on multiple-section tunable lasers, inventing, in 1988, the widely tunable multielement mirror concept. During the late 1980s, he also developed efficient vertical-cavity multiple-quantum-well modulators, which led to novel VCSEL designs that provided unparalleled levels of performance. His current research interests include developing new photonic integrated circuit (PIC) and VCSEL technology, including the underlying materials growth and fabrication techniques, creation of vertical and in-plane GaN-based emitters, efficient all-epitaxial InP-based VCSELs, and a variety of PICs incorporating numerous optical elements for widely tunable integrated transmitters, receivers, and wavelength converters. He has authored or coauthored over 700 papers, five book chapters, one textbook, and is a holder of 36 patents.

Prof. Coldren is a Fellow of the Optical Society of America (OSA), Washington, DC, and the Institution of Engineering and Technology (IET), London, U.K., and a member of the National Academy of Engineering. He was the recipient of the 2004 John Tyndall Award. He has presented dozens of invited and plenary talks at major conferences.

Photonic Integrated Circuits for Optical Routing and Switching Applications

Milan L. Mašanović, Emily F. Burmeister, Anna Tauke-Pedretti, Brian R. Koch, Matthew M. Dummer, Joseph A. Summers, Jonathon S. Barton, Larry A. Coldren, John E. Bowers, Daniel J. Blumenthal
Electrical and Computer Engineering Department, University of California at Santa Barbara, Santa Barbara, California 93106-9560
mashan@ece.ucsb.edu

Abstract: We report on the latest advances in implementation of integrated photonic components required for optical routing: wavelength converters, optical buffers, and mode-locked lasers.

OCIS codes: (060.1810) Buffers, couplers, routers, switches, and multiplexers; (250.3140) Photonic integrated circuits

1. Introduction

The increasing demand for Internet capacity poses significant challenges to commercial electrical router design and deployment due to the increased power and space requirements of using pure electronic solutions and the problems posed (e.g. the power spreading problem). All-optical packet switching and routing technologies [1,2] hold promise to provide more efficient power and footprint scaling with increased router capacity. In this paper we cover the latest advances in photonic integrated circuit (PIC) optical packet switching and routing technologies investigated under the DARPA/MTO DOD-N program sponsored LASOR project [1]. In the LASOR architecture, 40 Gbps optical packets are routed based on the packet's wavelength and 10 Gbps optical labels. Integration of the switching and routing function onto PICs allows for advanced routing functions to be realized in the optical domain while offering advantages of integration including reduced footprint and power requirements.

The key components in the LASOR optical router [1] are a packet switching fabric, an optical buffer, a wavelength sensitive routing element, and a data regenerative element. The packet switch converts optical packets to new wavelengths based on information stored in a lookup table. The optical buffer is used to mitigate the contention between different packets directed to the same switch output port. A wavelength sensitive routing element is used in conjuction with an all-optical wavelength converter to forward packets from input buffers to output ports. The optical packets are regenerated at the router output (retiming, reshaping and reamplification (3R)).

In this paper, we report on the latest advances in implementation of the photonic integrated circuits (PICs) required for optical routing. These components include high-speed, high-performance integrated tunable wavelength converters and packet forwarding chips, integrated optical buffers, and integrated mode-locked lasers.

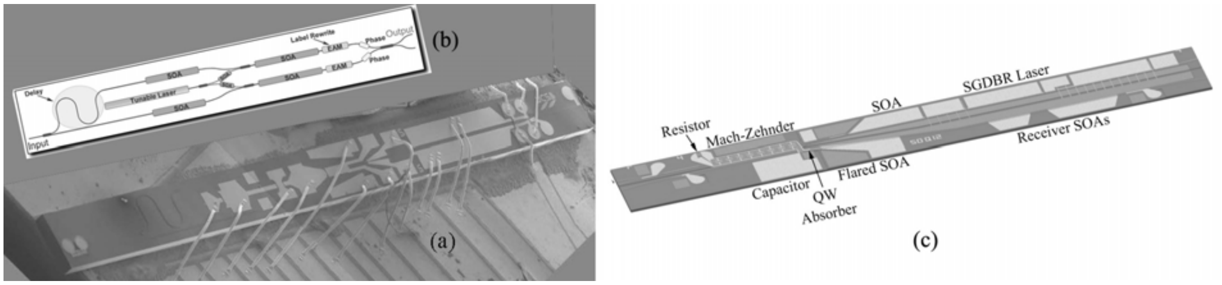

Figure 1 – (a) 40 Gbps packet forwarding chip (PFC) electron micrograph (b) PFC schematic (c) 40 Gbps separate absorption and modulation (SAM) tunable wavelength converter

2. Widely Tunable Optical Wavelength Converters and Packet Forwarding Chips

Packet forwarding in an optical router is performed through fast wavelength tuning, wavelength conversion of the payload, and encoding of a label for the outgoing packet. At the core of this functionality is a fast switching, widely tunable wavelength converter PIC. There are two main mechanisms exploited for monolithically integrated wavelength converters – non-linear effects in a semiconductor optical amplifier (SOA) caused by the pump-probe signal interaction [3], and traveling wave effects of signal detection and remodulation in a photodiode-modulator based system [6].

Significant advances have been made in SOA-based tunable wavelength converters, utilizing both sampled grating DBR lasers [3] and Arrayed Waveguide Grating (AWG) based discretely tunable lasers [4]. Wavelength conversion with both device types at bit rates of 40 Gbps RZ has been reported. In addition, a fully integrated packet forwarding chip (PFC), operating with 40 Gbps payloads and 10 Gbps labels has been successfully demonstrated and used in an optical switch demonstration [1,3]. Finally, multistage tunable wavelength converter MZI-SOA based implementations with on chip signal filtering have been demonstrated as well [5].

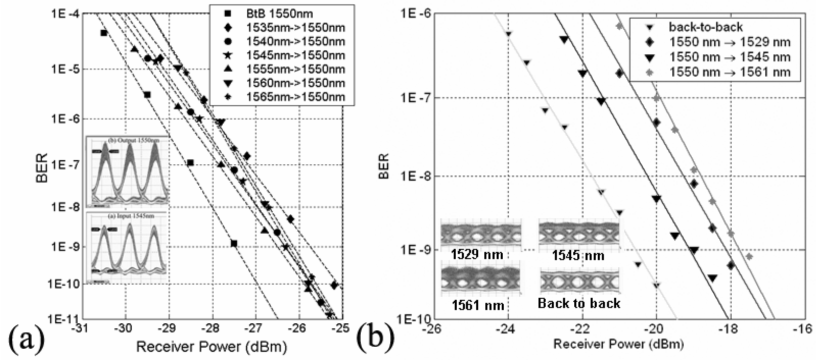

Figure 2 – (a) PFC - Bit error rate results for 40 Gbps RZ operation (b) SAM - Bit error rate results for 40 Gbps NRZ operation

Recently, successful demonstration of the separate absorption and modulation (SAM) approach to wavelength conversion has been accomplished for bit rates up to 40 Gbps [6]. In this method, a transmitter and receiver are monolithically integrated on a single chip. The photodiode is directly connected to the modulator through an on-chip terminated traveling wave electrode, allowing the photocurrent from an absorbed input signal to directly drive an optical modulator. Since the photodiode produces enough photocurrent to drive the optical modulator there is no need for any electrical amplification. Due to the spatial separation of the receiver and transmitter waveguides, SAM wavelength converters have no optical filtering requirements. These devices also have the advantage of lower power consumption and smaller footprints than comparable SOA-based devices. Operation at 40 Gbps with NRZ data shows less than a 2.5 dB power penalty across the 32 nm laser tuning range with no additional power penalty for conversion to the input wavelength. Both Mach-Zehnder and EAM based devices are being investigated [6,7].

3. Integrated Optical Buffers

The realization of practical optical memory elements to resolve packet contention is necessary before optical routers can become viable. The most successful optical buffering demonstrations have used either feedback or feed-forward buffers, many of which implement two-by-two or one-by-two switches [8]. Although practical storage times have been demonstrated, there have not been any integrated solutions.

Recently, a simple recirculating buffer that operates without additional control components in the delay loop was presented [9]. This recirculating buffer was based on an InP SOA gate array two-by-two switch and an optical fiber delay loop, 450 centimeters, or 23 ns, in length. The buffer exhibited greater than 40 dB extinction, sub-nanosecond switching, and fiber-to-fiber gain. Up to 184 ns of storage was demonstrated with greater than 98% packet recovery for 40 Gb/s, 40-byte packets, Figure 3. To the authors' knowledge, this device has the best performance for a buffer approach amenable to integration. Further work on all photonic chip based buffers is underway.

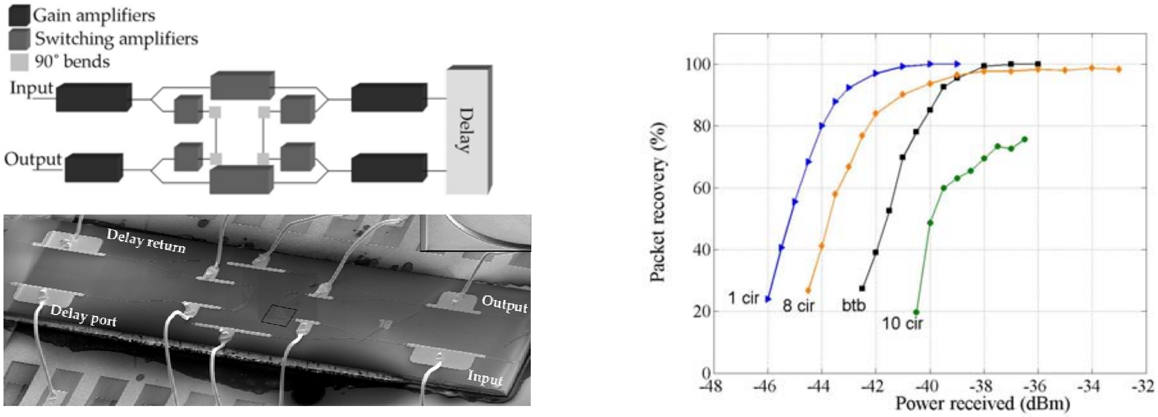

Figure 3 (top-left) Schematic of 2x2 switch with amplifiers (bottom left) SEM image of the switch affixed and wire-bonded to a submount (right) Packet recovery of 98% for up to 8 circulations (184 ns delay).

4. Monolithic Mode-Locked Laser and Optical Amplifier

Mode locked lasers (MLLs) are key components for 3R regeneration applications in optical routers. Some qualities of MLLs utilized in optical clock recovery are their ability to perform jitter reduction, pulse reshaping, and amplification. Since the frequency of mode locking is determined by the cavity length, traditional MLLs with cleaved facets are not reproducible at a specific frequency. This, special MLL designs, compatible with further integration into complex 3R PICs, are of particular interest.

Recently, we have experimentally demonstrated optical clock recovery using a novel mode-locked laser (MLL) [10, 11] monolithically integrated with an output semiconductor optical amplifier. The laser's distributed Bragg reflector (DBR) mirror positions are determined using lithography, allowing for mode locking and clock recovery at the exact frequency of the design (35.00 GHz), which is easily scalable to 40 GHz or higher. The laser design and fabrication platform are compatible with other photonic integrated circuit components, enabling integrated signal processing using these MLLs in the future.

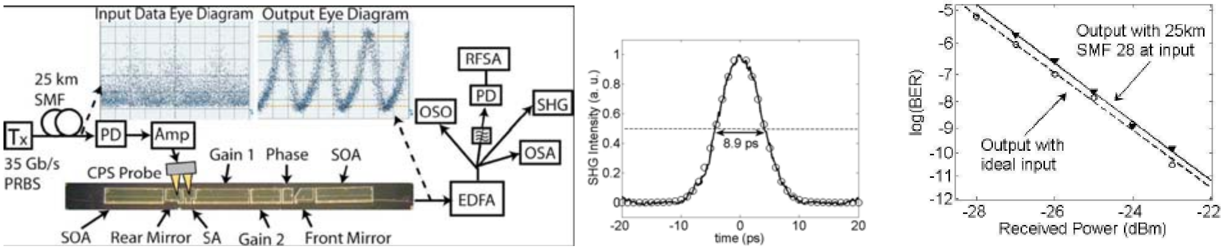

Figure 4 – (left) Experimental setup for hybrid clock recovery, with eye diagrams of the input and output signals and photograph of the device. The recovered clock appears to have high jitter because of poor OSO triggering. The actual jitter is 1.14 ps (middle) SHG trace of the output pulses. The solid line is the data and the open circles are a Gaussian fit (right) Bit error rates of the output clock that has been gated by the input data and sent to the receiver with a normal input and with input signal degradation

The device was shown to generate nearly transform limited pulses at 35.0-GHz repetition rate with pulse widths tunable between 3.5 and 8.5 ps, over 12 dB extinction ratio (ER), and 8.3 dBm average output power. Both all-optical [10] and hybrid [11] clock recovery were tested for this device. Among other regenerative capabilities, the device performed optical clock recovery with 50% jitter reduction from a degraded input signal with low ER. By combining this type of MLL with a nonlinear optical gate such as a Mach Zehnder SOA structure or SAM device, a fully integrated 3R regenerator can be created.

This work is supported by DARPA and the Army under contract #W911NF-04-9-0001.

5. References

[1] D. Wolfson et al., "All-optical asynchronous variable-length optically labeled 40 Gbps packet switch," presented at the ECOC'05, Eur. Conf. Opt. Commun., Glasgow, Scotland, 2005.
[2] J. Gripp et al., "IRIS optical packet router", Journal of Optical Networking, v 5, n 8, Aug. 2006, p 589-97
[3] V. Lal et al., "Monolithic Wavelength Converters for High-Speed Packet-Switched Optical Networks," Selected Topics in Quantum Electronics, IEEE Journal of, vol. 13, no. 1, pp. 49–57, 2007.
[4] P. Bernasconi et al., "Monolithically integrated 40-gb/s switchable wavelength converter", Journal of Lightwave Technology, v 24, n 1, Jan. 2006, 71-6
[5] J. Summers et al., "Design and operation of a monolithically integrated two-stage tunable all-optical wavelength converter", IEEE Photonics Technology Letters, v 19, n 21, Nov. 2007, p 1768-1770
[6] A. Tauke-Pedretti et al., "Monolithic 40 Gbps Separate Absorption and Modulation Wavelength Converter", OFC post deadline paper, 2007.
[7] A. Tauke-Pedretti et al., "Separate Absorption and Modulation Mach-Zehnder Wavelength Converter", IEEE Journal of Lightwave Technology, v 26, n 1, Jan. 2008
[8] E. F. Burmeister et al., "A comparison of optical buffering technologies," Optical Switching and Networking, vol. 5, pp. 10-18, Jan. 2008.
[9] E. F. Burmeister et al., "SOA Gate Array Recirculating Buffer for Optical Packet Switching," *Optical Fiber Communication Conference, OFC*, San Diego, CA, OWe4 (2008).
[10] B. R. Koch et al., "35 Gb/s monolithic all-optical clock recovery pulse source," in *OFC 2007*, Anaheim, CA, Paper OWP2.
[11] B. R. Koch et al., "Monolithic Mode-Locked Laser and Optical Amplifier for Regenerative Pulse Optical Clock Recovery," IEEE Photonics Technology Letters, v 19, n 9, May 2007

Recent Progress on LASOR Optical Router and Related Integrated Technologies

Jonathon S. Barton[1], Milan L. Mašanović[1], Matthew M. Dummer[1], Anna Tauke-Pedretti [1], Emily F. Burmeister[3], Brian R. Koch[4], Joseph A. Summers[1], Larry A. Coldren[1], John E. Bowers[1], Daniel J. Blumenthal[1]

1: University of California Santa Barbara, Harold Frank Hall Santa Barbara 93117
2: Sandia National Laboratories, Alburquerque, New Mexico
3: Ciena Corp. Linthicum, Maryland 21090
4: Intel Corp. Santa Clara, CA

Abstract: In this talk we review the latest progress on the DOD-N LASOR optical router project. Architectural studies including design and buffering will be discussed as well as prototype node performance. Recent results in integration in InP and Si/InP platforms will be described.

Keywords: Buffers, couplers, routers, switches, Photonic integrated circuits

Introduction

All-optical packet switching and routing technologies [1,2] hold promise to provide more efficient power and footprint scaling with increased router capacity. In this paper we cover the latest advances in photonic integrated circuit (PIC) optical packet switching and routing technologies investigated under the DARPA/MTO DOD-N program sponsored LASOR project [1]. In the LASOR architecture, 40 Gbps optical packets are routed based on the packet's wavelength and 10 Gbps optical labels. Integration of the switching and routing function onto PICs allows for advanced routing functions to be realized in the optical domain while offering advantages of integration including reduced footprint and power requirements.

The key components in the LASOR optical router [1] are a packet switching fabric, an optical buffer, a wavelength sensitive routing element, and a data regenerative element.

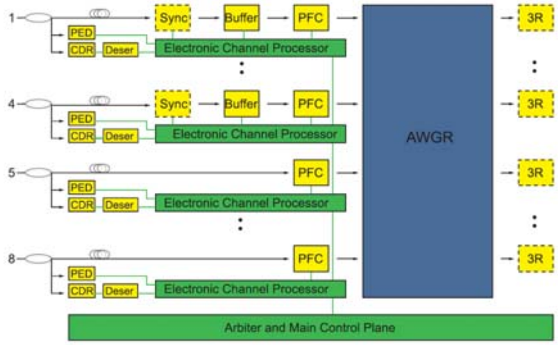

Figure 1 - LASOR Architecture with PFC, Buffers, Routing and 3R elements

The packet switch converts optical packets to new wavelengths based on information stored in a lookup table. The optical buffer is used to mitigate the contention between different packets directed to the same switch output port. A wavelength sensitive routing element is used in conjuction with an all-optical wavelength converter to forward packets from input buffers to output ports. These components include high-speed, high-performance integrated tunable wavelength converters and packet forwarding chips, integrated optical buffers, and integrated mode-locked lasers for 3R regeneration.

Widely Tunable Optical Wavelength Converters and Packet Forwarding Chips

Packet forwarding in an optical router is performed through fast wavelength tuning, wavelength conversion of the payload, and encoding of a label for the outgoing packet. A SEM of a typical device is shown in Figure 1. At the core of this functionality is a fast switching, widely tunable wavelength converter PIC. There are two main mechanisms exploited for monolithically integrated wavelength converters – non-linear effects in a semiconductor optical amplifier (SOA) caused by the pump-probe signal interaction [3], and traveling wave effects of signal detection and re-modulation in a photodiode-modulator based system [6].

Significant advances have been made in SOA-based tunable wavelength converters, utilizing both sampled grating DBR lasers [3] and Arrayed Waveguide Grating (AWG) based discretely tunable lasers [4]. Wavelength conversion with both device types at bit rates of 40 Gbps RZ has been reported. In addition, a fully integrated packet forwarding chip (PFC), operating with 40 Gbps payloads and 10 Gbps labels has been successfully demonstrated and used in an optical switch demonstration [1,3]. Finally, multistage tunable wavelength converter MZI-SOA based implementations with on chip signal filtering have been demonstrated as well [5].

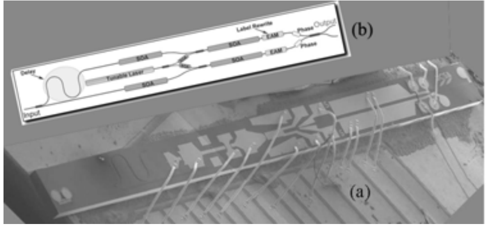

Figure 1 – (a) Packet Forwarding Chip SEM and device diagram

Recently, successful demonstration of the separate absorption and modulation (SAM) approach to wavelength conversion has been accomplished for bit rates up to 40 Gbps [6]. In this method, a transmitter and receiver are monolithically integrated on a single chip.

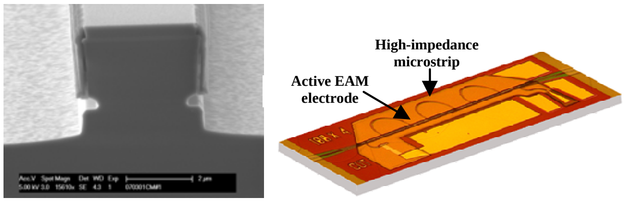

Figure 2 – (a) SEM of Undercut modulators b) Traveling wave electrode modulator used in wavelength converter

Figure 2 shows a SEM of undercut modulators employed in the latest generation of SAM devices which reduces the capacitance and enable 40G RZ wavelength conversion.

In a SAM device, the photodiode is directly connected to the modulator through an on-chip terminated traveling wave electrode, allowing the photocurrent from an absorbed input signal to directly drive an optical modulator. Due to the spatial separation of the receiver and transmitter waveguides, SAM wavelength converters have no optical filtering requirements. These devices also have the advantage of lower power consumption, and smaller footprints, with respect to comparable SOA-based devices. Operation at 40 Gbps with NRZ data shows less than a 2.5 dB power penalty across the 32 nm laser tuning range with no additional power penalty for conversion to the input wavelength. Both Mach-Zehnder and EAM based devices are being investigated [6,7].

Integrated Optical Buffers

In order to become viable, practical optical memory elements must resolve packet contention. The most successful optical buffering demonstrations have used either feedback or feed-forward buffers, many of which implement two-by-two or one-by-two switches [8]. Although practical storage times have been demonstrated, integrated solutions are not currently available.

Recently a simple re-circulating buffer was demonstrated based on an InP SOA gate array two-by-two switch and an optical fiber delay loop, 450 centimeters, or 23 ns, in length.

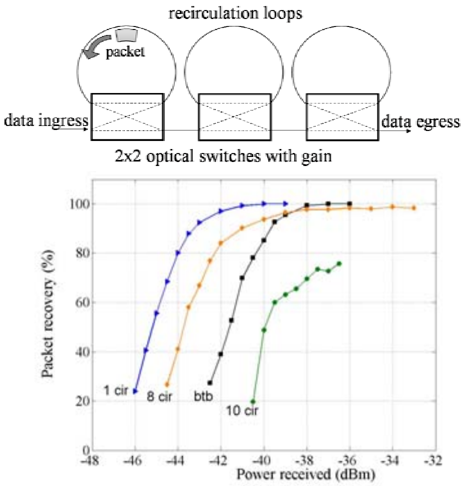

Figure 3 (top) Schematic of 3 element recirculating buffer 2x2 switch with amplifiers (bottom) Packet recovery of 98% for up to 8 circulations (184 ns delay).

The buffer exhibited greater than 40 dB extinction, sub-nanosecond switching, and fiber-to-fiber gain. Up to 184 ns of storage was demonstrated with greater than 98% packet recovery for 40 Gb/s, 40-byte packets, as shown in Figure 3.

Monolithic Mode-Locked Laser and Optical Amplifier

Mode locked lasers (MLLs) are key components for 3R regeneration applications in optical routers by providing jitter reduction, pulse reshaping, and amplification.

Recently, we have experimentally demonstrated optical clock recovery using a novel mode-locked laser (MLL) [10, 11] monolithically integrated with an output semiconductor optical amplifier. The laser design and fabrication platform are compatible with other photonic integrated circuit components, enabling integrated signal processing using these MLLs in the future.

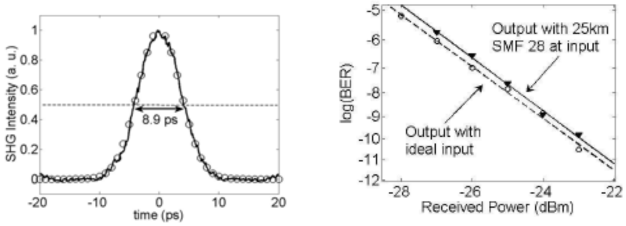

Figure 4 – (a) MLL pulseshape and (b) BER

The device was shown to generate nearly transform limited pulses at 35.0-GHz repetition rate with pulse widths tunable between 3.5 and 8.5 ps, over 12 dB extinction ratio (ER), and 8.3 dBm average output power.

6. Acknowledgment

This work is supported by DARPA and the Army under contract #W911NF-04-9-0001.

7. References

[1] D. Wolfson et al., "All-optical asynchronous variable-length optically labeled 40 Gbps packet switch," presented at the ECOC'05, Eur. Conf. Opt. Commun., Glasgow, Scotland, 2005.

[2] J. Gripp et al., "IRIS optical packet router", Journal of Optical Networking, v 5, n 8, Aug. 2006, p 589-97

[3] V. Lal et al., "Monolithic Wavelength Converters for High-Speed Packet-Switched Optical Networks," Selected Topics in Quantum Electronics, IEEE Journal of, vol. 13, no. 1, pp. 49–57, 2007.

[4] P. Bernasconi et al., "Monolithically integrated 40-gb/s switchable wavelength converter", Journal of Lightwave Technology, v 24, n 1, Jan. 2006, 71-6

[5] J. Summers et al., "Design and operation of a monolithically integrated two-stage tunable all-optical wavelength converter", IEEE Photonics Technology Letters, v 19, n 21, Nov. 2007, p 1768-1770

[6] A. Tauke-Pedretti et al., "Separate Absorption and Modulation Mach-Zehnder Wavelength Converter", IEEE Journal of Lightwave Technology, v 26, n 1, Jan. 2008

[7] E. F. Burmeister et al., "A comparison of optical buffering technologies," Optical Switching and Networking, vol. 5, pp. 10-18, Jan. 2008.

[8] B. R. Koch et al., "Monolithic Mode-Locked Laser and Optical Amplifier for Regenerative Pulse Optical Clock Recovery," IEEE Photonics Technology Letters, v 19, n 9, May 2007

40 Gb/s Widely Tunable Wavelength Converter with a Photocurrent-Driven High-Impedance TW-EAM and SGDBR Laser

Matthew M. Dummer, Jonathan Klamkin, Anna Tauke-Pedretti, and Larry A. Coldren
Univ. of California, ECE Department, Santa Barbara, CA 93106 USA
TEL:(805) 893-7163, FAX:(805) 893-4500, email:dummer@engr.ucsb.edu

Abstract— **We demonstrate a monolithic transceiver which integrates pre-amplified QW-pin receiver with a tunable SGDBR laser and high-impedance EAM. This device performs wavelength conversion at 40 Gb/s over 22 nm of optical bandwidth.**

I. INTRODUCTION

Widely-tunable lasers, like the sampled-grating (SG)DBR, have recently begun to dominate WDM systems. However, such systems still suffer from the cost, size, and power dissipation inherent within OEO approaches, which require discrete components such as receivers and modulators to be coupled to these lasers. Continued advancements in high-functionality photonic integration offer solutions to these shortfalls, delivering a level of performance that now rivals state-of-the-art discrete devices. In this work we present a fully-monolithic transceiver which integrates a high-power pre-amplified receiver and traveling-wave electroabsorption modulator with a widely tunable SGDBR laser. This single chip has been designed to perform wavelength conversion without any additional electronics at data rates up to 40 Gb/s.

II. DEVICE DESIGN AND FABRICATION

The schematic shown in Fig. 1 depicts the full wavelength converter device, designed for separate absorption and modulation (SAM) of optical signals [1], [2]. The receiver side consists of a two-stage SOA followed by a 35 μm long quantum well p-i-n (QW-pin) photodiode. The transmitter side is comprised of an SGDBR laser followed by an SOA and two parallel electroabsorption modulators (EAMs). One EAM is photocurrent driven by the QW-pin to perform wavelength conversion while the other can be electrically modulated with an external driver. The epitaxial layer structure for this device utilizes a dual quantum well platform for achieving the necessary high performance of each of the optical components [2]. Seven offset quantum wells (OQW) grown above the waveguide core provide gain for the laser and SOAs as well as absorption in QW-pin. Ten QWs centered in the waveguide core (CQW) provide high modulation efficiency but are detuned from the lasing wavelength in able to maintain low-loss passive waveguides.

The transmitter and receiver each employ very different geometries to optimize their individual performance (Fig. 2).

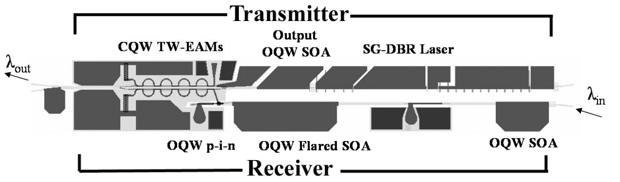

Fig. 1. Schematic of integrated wavelength converter device

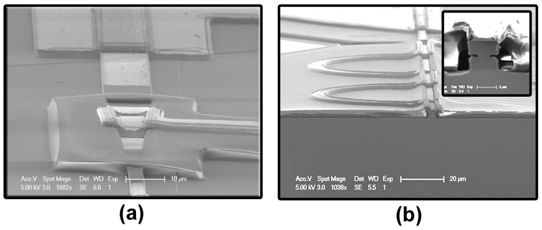

Fig. 2. SEM images of (a) the tapered-ridge photodiode and (b) the periodic TW-EAM electrode. Inset shows the undercut EAM waveguide cross section.

The SOA and QW-pin make use of laterally flared and tapered ridge waveguides, respectively, to improve the saturation power and linearity of the input optical signal [1]. The 250 μm long modulator was designed with a high-impedance traveling wave (TW) configuration to achieve very high bandwidth. The TW-EAM design incorporates a selective undercut etch [3] to reduce the core of the waveguide from 3.0 μm to 1.15 μm wide and is periodically distributed in five 50-μm sections along a high impedance microstrip line [4]. Together these two implementations significantly reduce the capacitance per length and improve velocity matching between the optical and electrical signals. The EAM transmission line is terminated with a 25 Ω NiCr resistor and DC blocking capacitor for low RF loss and simple biasing.

III. CW CHARACTERIZATION

The SGDBR laser achieves continuous tuning over the range of 1524 to 1564 nm. Figure 3 shows the overlayed supermode spectra demonstrating greater than 30 dB side mode suppression across the tuning range. The DC modulator extinction from 0 V to -5 V has been measured across the tuning range of the SGDBR (Fig. 4) with maximum slope efficiency ranging from 13 dB/V up to 19 dB/V. The extinction

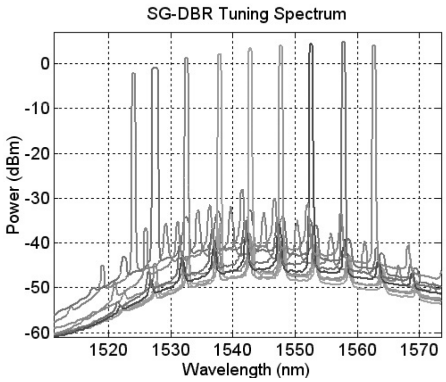

Fig. 3. Supermode tuning spectra of the SGDBR laser

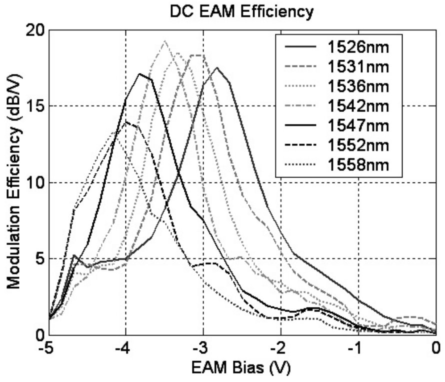

Fig. 4. Extinction efficiency of the 250 μm long EAM

variation observed is a consequence of the amount of detuning between the lasing wavelength and the modulator band edge. The CW response of the receiver is shown in Figure 5 for an input wavelength of 1550 nm. For DC biases of 70 mA and 310 mA on the two SOAs, and -3.0 V on the QW-pin, the unsaturated gain of the receiver was greater than 20 dB. Although over 60 mA of photocurrent is possible, the 1-dB gain compression of the receiver occurs at an input power of -5.4 dBm, corresponding to 32 mA of linear photocurrent for driving the EAM.

IV. HIGH SPEED PERFORMANCE

Wavelength conversion at 40 Gb/s has been performed using $2^{31}-1$ PRBS data generated from an SHF bit error rate tester. For these experiments, the receiver SOAs were highly pumped (9.0 kA/cm^2) to maximize the saturation power, while the laser and output SOA were biased low (5.8 and 2.5 kA/cm^2) to limit the EAM photocurrent and reduce thermal crosstalk. The common-voltage configuration of the EAM and QW-pin creates a biasing tradeoff between input power and output wavelength. For each output wavelength, the bias voltage was chosen to maximize the output extinction while maintaining sufficient field in the photodiode to prevent bandwidth degradation from space charge effects. Figure 6 shows the clearly open eye diagrams converted from 1560 nm to 1537, 1548, and 1559 nm for both RZ and NRZ data formats with extinction ratios ranging from 7.3 to 11.7 dB. The optical input power was -6.2 dBm and -5.5 dBm for the RZ and NRZ signals, respectively. In all cases, the output extinction is significantly higher for the RZ data format because the lower average power of the return-to-zero bit stream yields better receiver saturation characteristics and higher photocurrent swing.

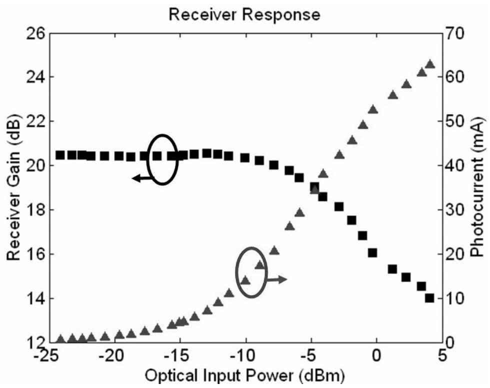

Fig. 5. CW response of the optically pre-amplified receiver

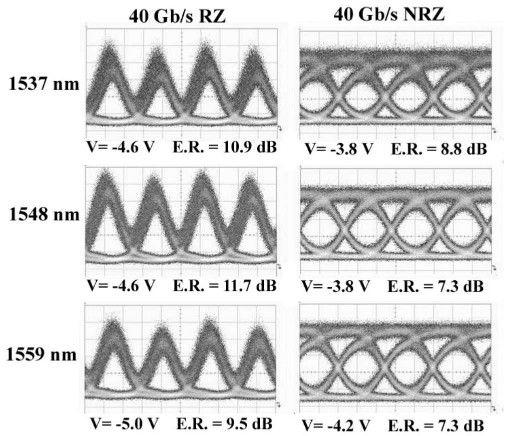

Fig. 6. 40 Gb/s RZ and NRZ wavelength converted eye diagrams with output extinction ratio for corresponding bias voltage

V. CONCLUSION

We have presented a monolithic wavelength converter which utilizes a tunable SGDBR laser, a pre-amplified QW-pin photodiode, and high-impedance TW-EAM. This devices demonstrates 40 Gb/s wavelength conversion with greater than 7 dB output extinction over 22 nm of optical bandwidth.

ACKNOWLEDGMENT

This work was supported by DARPA MTO-LASOR Grant W911NF-04-9-0001.

REFERENCES

[1] A. Tauke-Pedretti, et al. *J. of Light. Tech.*, vol. 26, no. 1, pp. 91–98, 2008.
[2] M. Dummer, et al. *J. of Light. Tech.*, vol. 26, no. 8, pp. 938–944, 2008.
[3] Y.-J. Chiu, et al. *IEEE PTL*, vol. 17, no. 10, pp. 2065–2067, 2005.
[4] R. Lewen, et al *J. of Light. Tech.*, vol. 22, no. 1, pp. 172–179, 2004.

A Bit-Rate-Transparent Monolithically Integrated Wavelength Converter

Matthew M. Dummer, Jonathan Klamkin, Anna Tauke-Pedretti and Larry A. Coldren
Univ. of California, ECE Department, Santa Barbara, CA 93106 USA
dummer@engr.ucsb.edu

Abstract

We demonstrate monolithic wavelength converters based on a PD-EAM optical gate and tunable SG-DBR laser operating at any bit rate up to 40 Gb/s in both NRZ and RZ formats.

Introduction:

Monolithic wavelength converters (WCs) are important devices for future WDM networks as they enable dynamic wavelength management and all-optical signal routing while reducing optical loss, power consumption, and packaging complexity. A common implementation of monolithic WC is based on non-linear SOAs to achieve cross-gain or cross-phase modulation between an input data signal and CW signal from an on-chip tunable light source. However, due to the slow gain recovery time of the integrated amplifiers, these devices typically rely on delayed interferometry to achieve high data rates and are therefore limited to single a bit rate and data format [1,2].

In this work we demonstrate the first broadband, widely-tunable monolithic wavelength converter that operates at any data rate up to 40 Gb/s in both return-to-zero (RZ) and non-return-to-zero (NRZ) data formats. The bit-rate transparency of this device, which is based on a separate absorption and modulation (SAM) architecture, makes it very well suited for future use in highly flexible WDM networks.

Device Design:

The SAM device is based on an integrated transceiver design with separate transmitter and receiver waveguides similar to [3]. A photograph of the device is shown in Fig. 1. The transmitter consists of a widely tunable sampled grating (SG)-DBR laser followed by an output SOA and two parallel high-impedance traveling-wave electro-absorption modulators (TW-EAM) [4]. One of the EAMs can be electrically driven to function as a transmitter while the other is used to perform wavelength conversion. The receiver is designed with two SOAs followed by a quantum-well p-i-n (QW-pin) photodiode (PD). A microstrip transmission line connects the QW-pin to one of the TW-EAM electrodes such that the photocurrent generated in the receiver directly modulates the output of the SG-DBR laser to produce wavelength conversion. This type of traveling-wave optical gate enables very high bandwidths, as similar configurations have demonstrated switching times as fast as 2 ps [5]. The TW-EAM electrode is followed by a thin-film resistor (25 Ω) and capacitor which serve to terminate the photocurrent signal and allow for DC biasing.

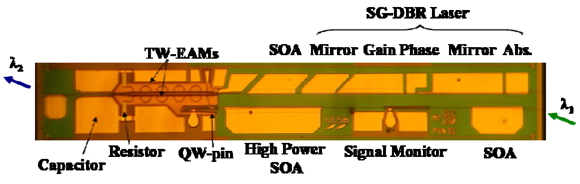

Figure 1: Photograph of integrated wavelength converter. The total footprint of the device is 4.0 mm x 0.45 mm.

Receiver and Transmitter Measurements:

The performance of the wavelength converter is entirely determined by the efficiency of both the receiver and the EAM. For the receiver, achieving high saturation power in both the SOAs and the photodiode is important for maintaining high extinction ratios and limiting pattern dependence. To characterize the receiver linearity we have measured the CW response as shown in Figure 2. The optical input and output powers were obtained by reverse biasing the first SOA to measure the input photocurrent and then forward biasing both SOAs to measure the photocurrent in the QW-pin. For these measurements, the biases were 70 mA, 310 mA, and -3 V for the 400 μm and 800 μm SOAs, and 35 μm photodiode, respectively. The gain of the receiver is greater than 20 dB and it is capable of generating up to 30 mA of linear DC photocurrent before saturation begins to occur.

The SG-DBR laser is tunable from 1524 nm to 1564 nm with fiber-coupled output powers from -2 to 4 dBm over the wavelength range. Figure 3 shows the DC extinction characteristics of the 250 μm EAM over the laser tuning range, demonstrating 20-30 dB extinction from 0 to 5 volts. The observed wavelength dependence is typical of QW EAMs, which require greater amount of Stark shift as the lasing wavelength becomes further detuned from the QW band edge.

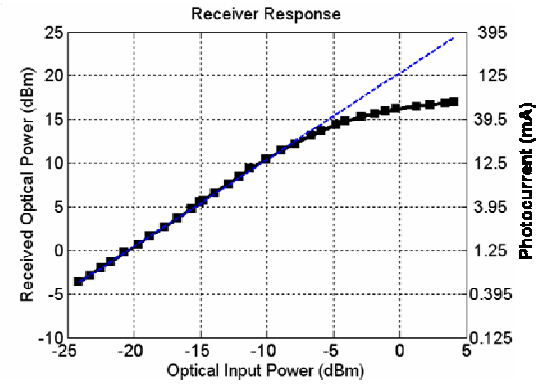

Figure 2: Response of the SOA pre-amplified QW-pin receiver

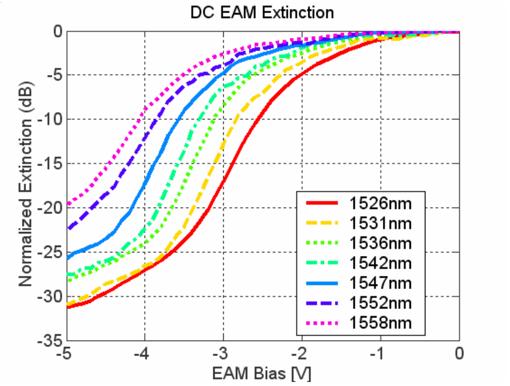

Figure 3: Extinction characteristics of the TW-EAM over the tuning range of the SG-DBR laser

Wavelength Conversion:

To demonstrate the high bandwidth and bit-rate transparency of the device, wavelength conversion has been performed at various bit rates for both RZ and NRZ formats. Using an SHF bit error rate tester, optical PRBS data $(2^{31}-1)$ was generated and coupled to and from the WC with lensed fibers. The bias conditions for the two receiver SOAs were 110 mA and 310 mA, and the laser gain section and the transmitter SOA, were biased at 95 mA and 30 mA, respectively. The SG-DBR mirrors were tuned by current injection to the desired output wavelength. The bias across the photodiode and EAM was adjusted to achieve the maximum amplitude of the output signal. Figure 4(a) shows the wavelength converted eye diagrams (1560 nm to 1548 nm) for NRZ input data signals at 5, 10, 20 and 40 Gb/s. The input power in all cases was -5.5 dBm and the output power was -12 dBm accounting for 4 dB fiber coupling losses. With a bias of -3.8 V, the output extinction ratio was 8.9, 9.4, 9.5 and 8.1 for the four data rates respectively.

To evaluate the return-to-zero performance, input RZ signals were generated at both 20 Gb/s and 40 Gb/s using a 20 GHz clock signal and $LiNbO_3$ modulator with a V_π or $2V_\pi$ drive to carve the NRZ data. Figure 4(b) shows the wavelength converted output eye diagrams for both data rates. The lower average power of the RZ data format allows for greater signal swing and therefore greater output extinction. For an input power of -6.2 dBm and PD-EAM bias of -4.5, the output extinction ratios were 11.5 dB and 10.8 dB for 20 Gb/s and 40 Gb/s.

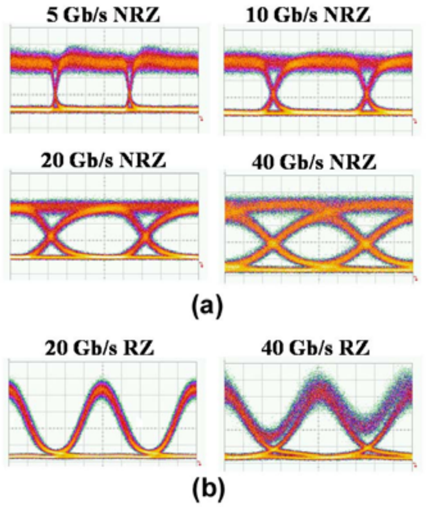

Figure 4: Wavelength converted (1560 nm to 1548 nm) eye diagrams in both (a) non-return-to-zero and (b) return-to-zero format

Conclusion:

We have demonstrated a monolithically integrated, widely tunable SAM wavelength converter for highly flexible WDM applications. This device demonstrates efficient wavelength conversion for data rates ranging from 5 Gb/s up to 40 Gb/s in both RZ and NRZ data formats with output extinction ratios exceeding 8 dB.

Acknowledgment

The authors acknowledge the support of DARPA under the MTO-LASOR Grant W911NF-04-9-0001.

References

[1] V. Lal et al. *Photon. Tech Lett.* vol. 18, no. 4 pp. 577-59 (2006)

[2] P. Bernasconi et al. *Electron. Lett.* Vol. 18, no 4 pp 701-702 (2005)

[3] M. Dummer et al. *J. Lightwave Tech.*. Vol. 26, no. 8 pp. 938-944 (2008)

[4] M. Dummer et al. *OFC 2008* OThC6 (2008)

[5] S. Kodama et al. *Electron Lett* vol. 40 no. 9 pp 555-556 (2004)

I. Photonic IC Technology and Devices

C. RF-Photonics, Filters and Analog PICs

Integrated Coherent Receivers for High-Linearity Microwave Photonic Links

Anand Ramaswamy, *Student Member, IEEE*, Leif A. Johansson, *Member, IEEE*, Jonathan Klamkin,
Hsu-Feng Chou, *Member, IEEE*, Colin Sheldon, Mark J. Rodwell, *Fellow, IEEE*,
Larry A. Coldren, *Fellow, IEEE, Fellow, OSA*, and John E. Bowers, *Fellow, IEEE, Fellow, OSA*

***Abstract*—In this paper, we present a coherent receiver based on an optical phase-locked loop (PLL) for linear phase demodulation. The receiver concept is demonstrated at low frequency. For high-frequency operation, monolithic and hybrid integrated versions of the receiver have been developed and experimentally verified in an analog link. The receiver has a bandwidth of 1.45 GHz. At 300 MHz, a spurious free dynamic range (SFDR) of 125 dB $\cdot$ Hz$^{2/3}$ is measured.**

***Index Terms*—Analog links, coherent communication, microwave photonics, phase-locked loop (PLL), phase modulation.**

I. INTRODUCTION

THE transport of analog signals over optical fiber allows for the placement of signal processing electronics away from the often exposed location of the antenna unit. The low-loss nature of fiber allows the signal to be transported over long distances with minimal signal loss. Since the transport is performed in the optical domain, the link itself is immune to electromagnetic interference. Original work on radio over fiber was considered for satellite communication applications [1]. More recent efforts have primarily focused on wireless mobile communication systems [2], where the relatively linear response of inexpensive directly modulated sources [3], [4] make moderate performance inexpensive links attractive for this application.

For higher dynamic range analog systems that require extreme linearity, radio over fiber does not currently meet the most stringent performance requirements. Direct modulation of laser diodes is a linear process, but the need for high speed modulation and very low noise at the signal frequency is difficult to meet with a single optical source. The two requirements can be decoupled if an external optical modulator is used. However, for intensity modulation the modulation depth is limited to 100% and it is difficult to fit a truly linear transfer function between zero and full transmission. In contrast, optical phase modulation can generate practically unlimited modulation depth. Many optical phase modulators also rely on the linear electrooptic effect, e.g., LiNbO$_3$ modulators. Unfortunately, there is currently a lack of techniques for linear phase demodulation. A standard optical mixing based phase detector has a sinusoidal response which then limits the link performance [5].

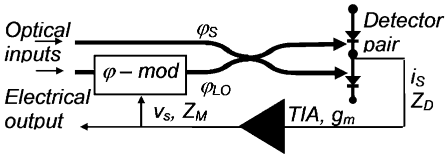

Fig. 1. Schematic outline of receiver architecture.

In this paper, we describe a technique for linear optical phase demodulation using an optical phase locked loop [6]. The paper is organized as follows. In Section II the operating principle of the phase detector is outlined and a basic analytical model is developed to reveal the limits of performance of the phase detector. The next section summarizes a proof-of-principle system demonstration built using discrete components at low frequency. Section IV introduces the development of a high-speed integrated optical phase receiver. The following section describes the performance of the subcomponents of the receiver, before the link results using the integrated receiver are shown in Sections VII and VIII.

II. THEORY

The base function of the proposed receiver is shown in the diagram of Fig. 1. The receiver is built around a standard optical mixing based phase detector with a differential output signal current given by

$$i_S = 2R\sqrt{P_S P_{\rm LO}}\sin(\varphi_S - \varphi_{\rm LO}) \tag{1}$$

Where P_S and $P_{\rm LO}$ are signal and LO optical power, φ_S and $\varphi_{\rm LO}$ are optical phase and R is the responsitivity of the detector. This signal is then amplified to form a driving voltage to a tracking optical phase modulator

$$v_S = Z_D \cdot g_m \cdot Z_M \cdot i_S \tag{2}$$

where Z_D, Z_M are detector and modulator impedances and g_m is the amplifier transimpedance. Finally, the feedback phase is given by

$$\varphi_{\rm LO}(t) = \frac{\pi}{V_{\pi,R}} \cdot v_s \tag{3}$$

Manuscript received June 29, 2007; revised September 21, 2007. This work was supported by the DARPA PHOR-FRONT program under the United States Air Force Contract FA8750-05-C-0265.

A. Ramaswamy, L. A. Johansson, C. Sheldon, M. J. Rodwell, L. A. Coldren, and J. E. Bowers are with the Department of Electrical and Computer Engineering, University of California, Santa Barbara, CA 93106 USA (e-mail: anand@ece.ucsb.edu).

J. Klamkin is with the Materials Department, University of California, Santa Barbara, CA 93106 USA (e-mail: klamkin@engineering.ucsb.edu).

H.-F. Chou was with the Department of Electrical and Computer Engineering, University of California, CA 93106 USA. He is now with Luminent OIC Inc., Chatsworth, CA 91311 USA (e-mail: Hsu-Feng.Chou@ieee.org).

Color versions of one or more figures are available at http://ieeexplore.ieee.org.

Digital Object Identifier 10.1109/JLT.2007.911899

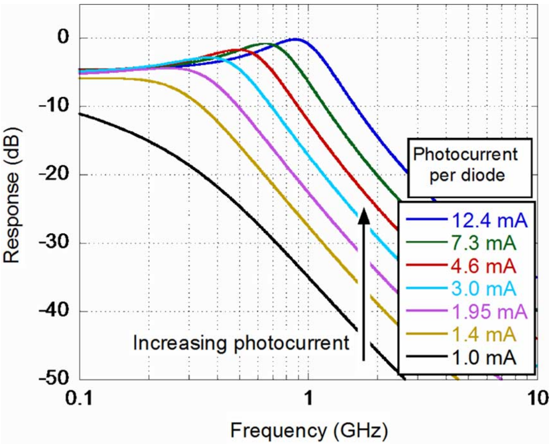

Fig. 2. Simulated close loop response of receiver.

where $V_{\pi,R}$ is the half wave voltage of the reference modulator. For a linear phase modulator and for close phase tracking, i.e., when the feedback gain is large and $\varphi_S \approx \varphi_{\mathrm{LO}}$, the reference modulator drive signal, v_S will be linearly related to the input phase and forms the linear output signal from the receiver.

The receiver forms a classic feedback system where the Laplace transform can be applied. The sine component in (3) can be linearized and the LO phase is given by

$$\begin{aligned}\varphi_{\mathrm{LO}} &= \frac{\pi}{V_{\pi,R}} Z_D(s) \cdot g_m(s)\\ &\quad \times \cdot Z_M(s) \cdot 2R\sqrt{P_S P_{\mathrm{LO}}} \cdot \mathrm{K}\\ &\quad \times \mathrm{K} \cdot e^{-s\tau}(\varphi_S - \varphi_{\mathrm{LO}})\\ &= T(s) \cdot (\varphi_S - \varphi_{\mathrm{LO}}) \qquad (4)\end{aligned}$$

where $s = 2\pi$ if is the Laplace variable, T is the open-loop gain and τ is the delay of the feedback path, now appearing in an exponential term. The delay will add a phase lag at higher frequencies and to prevent oscillation in the feedback loop, the feedback gain must be below unity at the frequency where the phase crosses -180°. This forms the basic bandwidth limitation in the loop such that to generate a fast feedback loop at microwave frequencies, picosecond feedback delay is required.

The closed-loop response given by $H = T/(1+T)$ can be calculated from the open-loop transfer function. The overall optical link response using the closed-loop receiver can now be calculated. Fig. 2 shows an example of such a calculation where an effort has been made to use measured data from Section VI to derive the component performance parameters that contribute to the open-loop transfer function.

This feedback loop differs from a typical optical phase-lock loop in that an optical modulator is used instead of a current controlled oscillator (CCO) in the form of a frequency tuned laser [7]. Here, the phase tracking range is limited by the available phase swing across the reference modulator. This limitation can be overcome by implementing an additional, slow loop to extend the tracking range, and/or having an LO input that is coherent in phase with the unmodulated signal input. The lack of a CCO removes an integration in the loop that needs to be compensated for. This can be implemented by tailoring the frequency dependence of the transimpedance amplifier to provide the right feedback response. A better solution is to rely on the detector and modulator impedances. By taking advantage of the detector and modulator capacitances, two integrations are automatically formed and the feedback amplifier now only needs to incorporate a lag-compensation network for stability in order to form a second-order phase-locked loop. This leads to greatly improved efficiency, in that no matching resistors need to be used to generate a flat detector and modulator frequency response. In fact, for sufficiently high photocurrent values, it becomes possible to not use any transimpedance amplification in the feedback path but to instead rely on a direct interconnect between modulator and detector to realize a first-order loop with a single pole formed by the detector in parallel with the modulator impedance.

III. PROOF OF CONCEPT DEMONSTRATION

In order to explore the feasibility of the proposed receiver and demonstrate that closure of the feedback path results in a significant enhancement of linearity without any penalty in SNR, a proof of principle experimental setup was built [8]–[10]. The operating frequency is limited to the 100 KHz range due to the relatively large loop delays introduced by the fiber patch cords of the discrete components used in the receiver.

The experimental arrangement for this approach is outlined in Fig. 3. The output from a continuous-wave (CW) optical source is split into a signal path and a reference path using a polarizing beam splitter (PBS) and polarization maintaining fiber. A two-tone RF probe signal (140 KHz and 160 KHz) is applied separately to the $\mathrm{LiNbO_3}$ phase modulators at the transmitter. In the receiver, the signals from the two paths are mixed and photodetected. The optical mixer is composed of a single-polarization optical coupler and a balanced photodetector. PM4 is the local phase modulator that provides feedback. The load of the balanced photodetector is 100 pf in parallel with the parallel combination of 2.96 kΩ and 20 kΩ. PM3 is driven by a slow feedback circuit that tracks large but slow variations in phase caused by the environment around the setup and uses it to maintain the bias of the demodulator at quadrature. A first-order RC filter is added to the output stage to suppress any noise generated by the stabilization electronics from entering the signal loop. A more detailed description of the experiment can be found in [11].

When the photocurrent from the balanced photodetector is large enough, say a few mA, several volts of voltage swing can be obtained with a high impedance load. This is sufficient to drive the $\mathrm{LiNbO_3}$ reference modulators on the LO branch and consequently eliminates the need for electrical loop amplifiers, forming an "all-optical" loop as described in the previous section. The frequency dependence of the load now determines the loop filter function. It is worth noting that the balanced modulator configuration described in Section V and implemented in the integrated version of the receiver is not realized in the discrete setup.

Fig. 4 plots the power of the detected fundamental and intermodulation terms as a function of the input link power. The stabilization loop remains closed for both open and closed loop operation. A SFDR of 104.5 $\mathrm{dB \cdot Hz^{2/3}}$ is obtained for open loop operation.

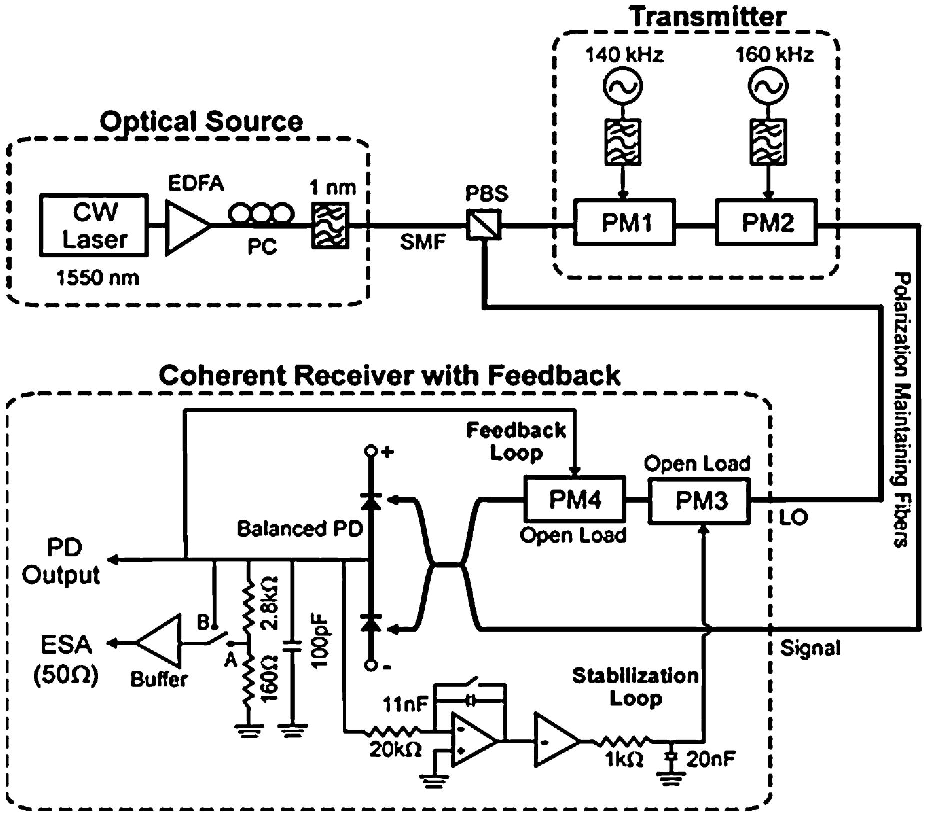

Fig. 3. Experimental setup of the all photonic version of the proposed coherent receiver. ESA: Electrical Spectrum Analyzer; PD: photodetector.

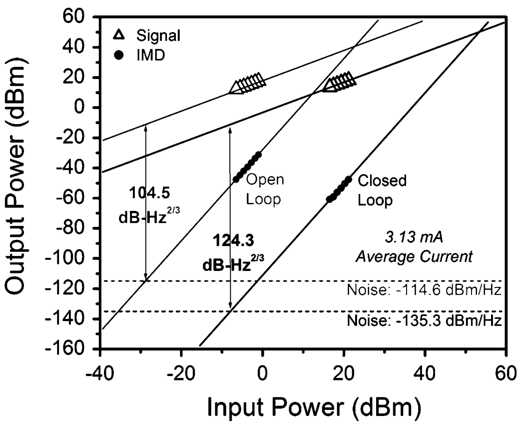

Fig. 4. SFDR measurement at 3.13 mA of average photocurrent per detector. Gray: open loop; Black: closed loop. IMD: third-order intermodulation distortion.

When the loop is closed a number of effects are observed. First, there is a significant decrease in the detected power on account of the reduced net phase swing across the demodulator. However, as predicted, this is not accompanied by any degradation in SNR as the noise floor too is suppressed by the same factor. The second effect is a drastic reduction of the intermodulation terms that appear at 120 and 180 KHz. This translates into an improvement in SFDR by about 20 to 124.3 dB $\cdot$ Hz$^{2/3}$. The calculation of shot noise power when the loop is closed is complicated by the feedback effect. Essentially, the shot noise current manifests itself as phase shot noise at the reference modulator. This in turn appears as voltage shot noise at the ouput of the balanced PD. With the buffer switch in position B (Fig. 3) the shot noise power is measured on a Electrical Spectrum Analyzer (ESA) that has a 50-Ω termination. It is observed that the measured noise levels are approximately 10 dB higher than the theoretical shot noise limit. As a consequence of operating at low frequencies, the difference can be attributed to the $1/f$ noise contributions from the optical source. The proof of concept demonstrations of the optoelectronic and all photonic feedback receivers is the first step towards realizing a receiver that has an operating bandwidth in the gigahertz range. Such a receiver requires low feedback delay ($<$ 10 ps) and consequently, hybrid or monolithic integration of electronics and photonics is necessary [12].

IV. INTEGRATED RECEIVER DEVELOPMENT

To reach microwave frequencies the latency in the loop needs to be small. In the proof-of-principle demonstration above using fiber optics, component length of several meters produced a loop operating frequency of $\sim$ 100 kHz. Using two orders of magnitude more compact LiNbO$_3$ waveguiding would produce a low operating frequency on the order of 10 MHz. To reach microwave frequencies of around 1 GHz, a waveguiding platform four orders of magnitude more compact than fiber optics must be used with component lengths in the 100s of microns region. This is being satisfied using an InP photonic integration platform.

Fig. 5 shows an SEM and block diagram of the low latency feedback receiver comprising of a photonic integrated circuit

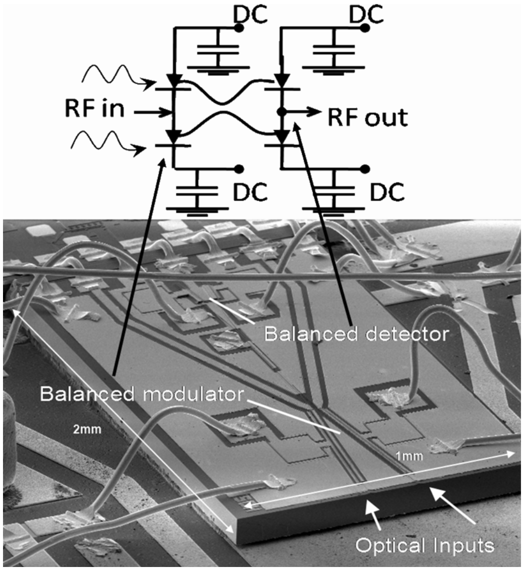

Fig. 5. SEM and block diagram of Integrated Optoelectronic Receiver: Wire bonds in upper part connect to Integrated Electronic IC (not shown).

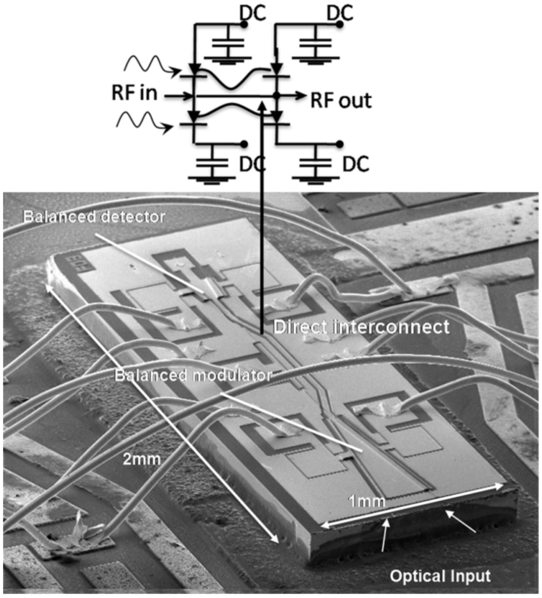

Fig. 6. SEM and block diagram of Integrated All-Photonic receiver.

and an electronic integrated circuit. The InP based photonic IC consists of a balanced UTC photodetector pair [13], a 2×2 waveguide multimode interference (MMI) coupler and tracking phase modulators in a balanced configuration. In quadrature, this type of balanced receiver discriminates against common-mode and second-order nonlinearities. The tracking optical phase modulators are *driven* differentially so as to add opposite-sign phase shifts to the incoming signal and LO resulting in a cancellation of even-order nonlinearities and common-mode noise. Additionally, driving the modulators in a differential fashion doubles the drive voltage presented to the modulator thereby doubling the available phase swing. The capacitances of the photodiodes and modulators are exploited as circuit elements rather than being parasitics that need to be eliminated. These now perform the desired loop integrations and can therefore be much larger. The electronic chip that interfaces with the PIC is primarily a transconductance amplifier that converts the voltage generated by photodiode integration into a modulator drive current. The modulator integrates this current to produce the required phase shift. The electronic IC also has a pair of buffer amplifier capable of driving 50 ohms. The electronic chip finally contains a lag compensation circuit to improve the phase margin and provide stability to the system.

Because the detector and modulator capacitances are implemented as lumped elements and best operate as ideal current mode integrators, a high-gain version of the receiver that requires no electronics in the feedback path is feasible. The detector photocurrent drives the sum of the photodiode and modulator capacitance, generating a voltage that is proportional to the photocurrent. As the received photocurrent increases, lower gain is required from the electronic amplifiers in the phased locked loop. Subsequently, for sufficiently high photocurrents the modulator impedance can be tailored to provide adequate filtering and stable phase feedback so that it can be driven directly by the detector photocurrent, similar to the proof-of concept demonstration in Section III. An SEM and block diagram of this all photonic receiver is shown in Fig. 6. Note that an electronic chip is still required to provide a buffered output.

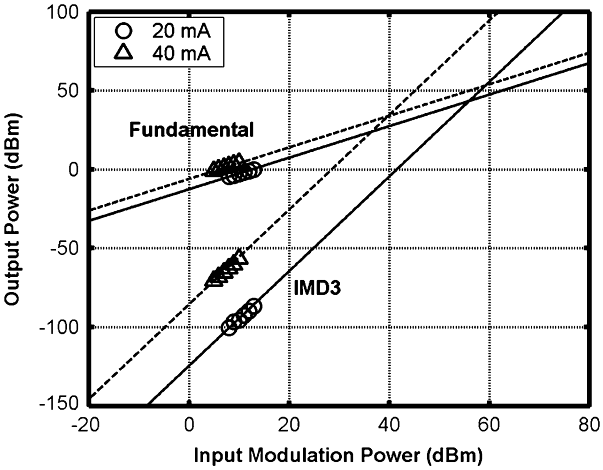

Fig. 7. IMD3 measurements for a 10 μm × 150 μm UTC-PD. At 20 mA the bias voltage is -8 V and at 40 mA the bias voltage is -5.8 V.

The practical challenge in taking full advantage of the linearity of a phase modulated link stems from stringent performance requirements on the detectors and modulators.

V. MODULATOR AND DETECTOR PERFORMANCE

In the low frequency, all photonic demonstrator, the SFDR obtained was limited by the maximum amount of photocurrent (3.13 mA per detector) and linear voltage swing that could be detected without degradation in linearity. It is predicted that if this number can be increased to 100 mA then 138–148 $\mathrm{dB} \cdot \mathrm{Hz}^{2/3}$ of SFDR can be realized. However, this means that highly linear photodiodes must be used with output IP3 performance on the order of 50 dBm at this photocurrent. Fig. 7 shows the OIP3 of the UTC photodiode used in the receiver. A 10 μm × 150 μm UTC-PD has a saturation current greater than 40 mA

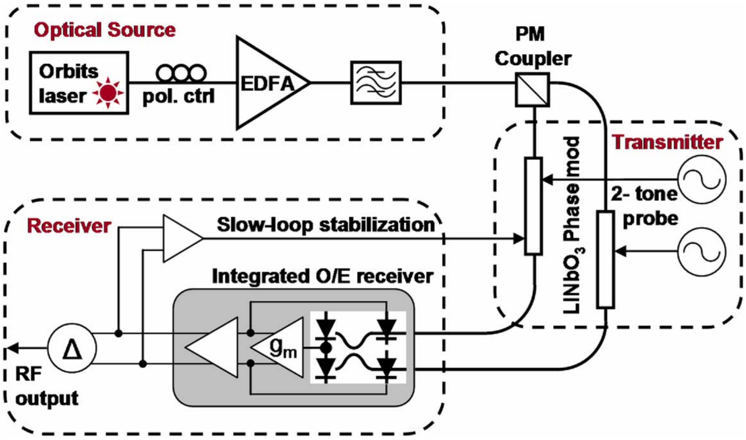

Fig. 8. Schematic of Experimental setup for Link Experiment.

and OIP3 values of 43 and 34 dBm at photocurrent levels of 20 and 40 mA, respectively [14].

A second critical performance requirement is the linearity of the phase modulators. While closed-loop operation suppresses nonlinearities from the optical interferometer as well as the amplifier, any nonlinear response of the phase modulator will remain. Since the feedback loop will force the reference phase to closely track the signal phase, a nonlinear phase modulator will consequently be modulated by a nonlinear drive signal. Using linear $LiNbO_3$ phase modulators, this is not a limiting problem. However, Stark effect InP phase modulators predominantly rely on the more efficient quadratic electrooptic effect. The high efficiency leads to very short modulator structures and low latency, but the linearity of a single modulator will limit the available receiver performance.

An improved modulator configuration is obtained by placing two phase modulators, one in the signal arm and one in the LO arm, in a push-pull configuration. These are now driven in antiphase. The compound response is now given by

$$\begin{aligned}\varphi_m &= \varphi_1(v_m) - \varphi_2(-v_m)\\ &= \sum_n a_n v_m^n - \sum_n a_n(-v_m)^n\\ &= \sum_{n'} 2a_{2n'+1} v_m^{2n'+1}\end{aligned} \tag{5}$$

Where φ_m and v_m are the modulation phase and drive voltage, respectively, and a_n is the Taylor expansion coefficient around the modulator bias point. It is seen that the quadratic term along with any higher even-order terms are cancelled using this configuration. A second beneficial effect is that the amplitude modulation from the phase modulators is to a first-order approximation cancelled [15].

VI. ANALOG LINK EXPERIMENT

The performance of both receivers was evaluated by placing them in an experimental test bed that simulates an analog link [14]. The setup, shown in Fig. 8, is similar to the configuration described earlier for the low-frequency demonstration. However, a few modifications have to be made in order for the system to handle the high optical powers (20–28 dBm) used in the link experiment. For instance, a 100-GHz DWDM drop filter rated to 5 W is used instead of an optical bandpass filter. Additionally, a 50/50 polarization maintaining (PM) coupler replaces the polarizing beam splitter (PBS).

At the transmitter, a two tone drive signal is applied separately to $LiNbO_3$ Phase modulators that have V_π's of 4.4 and 5.5 V respectively. This ensures the spectral purity of the drive signals as the closely spaced RF tones ($\Delta f = 2$ MHz) are combined in the optical domain.

At the output of the receivers the differential signal is tapped into a slow feedback loop which generates a low-frequency drive signal to one of the phase modulators. This stabilizes the system against environmental drifts and maintains the bias of the phase demodulator at quadrature. Ideally, the stabilization circuit should be located in the receiver module. However, for experimental convenience it is driving the phase modulator at the transmitter.

The box labeled ‘Integrated O/E receiver’ shows a schematic of the photonic integrated circuit coupled with the transimpedance amplifier and buffer of the electronic integrated circuit used in the optoelectronic (O/E) version of the receiver. The differential output from the amplifier drives the reference modulators on the PIC. The RF outputs sensed from the buffer constitute the receiver’s output. They are 180° out of phase and are combined differentially.

VII. FREQUENCY RESPONSE

A. *Optoelectronic Receiver*

The effect of the feedback architecture is to suppress the net phase swing across the detector by a factor of $(1/1+T)$ where T is the Loop Transmission Gain. Fig. 9 plots the closed loop frequency response of the receiver at different levels of detected photocurrent.

From theory we know that when the loop is locked and the reference modulator is closely tracking the incoming phase, the link gain is determined by the ratio of the drive signals to the source and reference modulator. This can be observed at low frequencies for a wide range of photocurrents. As the frequency

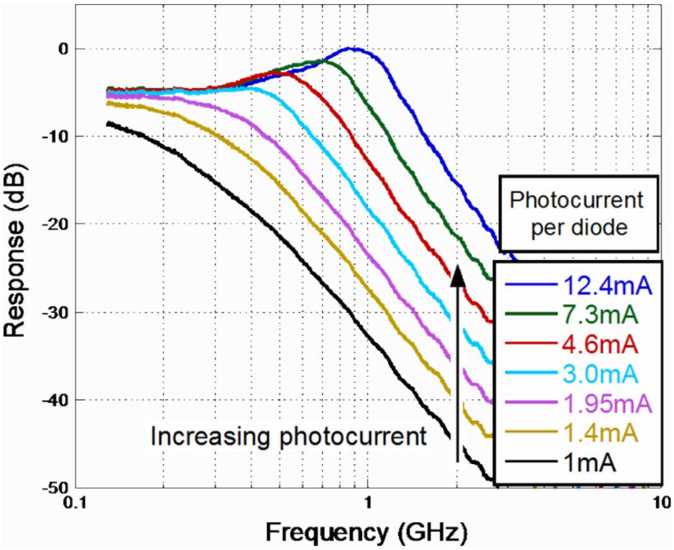

Fig. 9. Link gain of optoelectronic receiver at varying photocurrent levels.

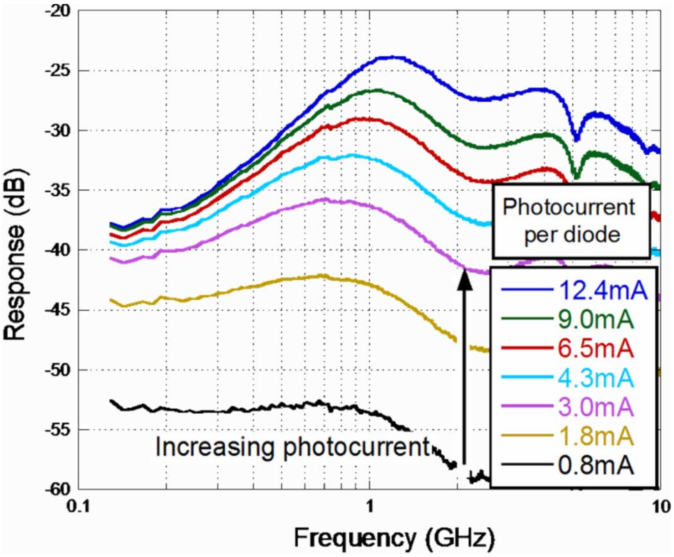

Fig. 10. Link gain of all-photonic receiver at varying photocurrent levels.

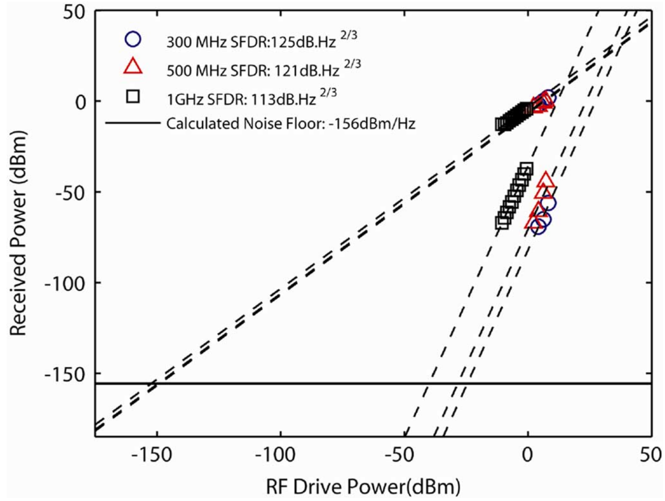

Fig. 11. SFDR of optoelectronic receiver at 300 MHz, 500 MHz and 1 GHz. Photocurrent set at 12 mA per detector.

increases, the feedback gain decreases and only at high photocurrent levels is the gain sufficient for phase tracking. Beyond a point, the loop transmission gain is too low for any tracking and consequently, the optical link gain becomes proportional to the photocurrent and loop filter transfer function. The loop bandwidth, here defined as the 3 dB frequency of the closed-loop link response, reaches 1.45 GHz at 12 mA of photocurrent. The delay limited bandwidth, within which the loop remains stable is approximately 4 GHz. Additionally, we note a peaking in the link gain for high photocurrent values at frequencies close to a GHz. This can be explained by the denominator in the closed-loop gain, $1 + T$. A second-order feedback loop contains two integrations with a -180° feedback phase. To provide stability at unity gain, the transimpedance amplifier contains a lag-compensating network to push the phase well above -180° at unity gain. This has been designed for delay-limited feedback gain and does therefore not provide optimum lag-compensation at around 1 GHz.

B. All Photonic Receiver

The operation of the all photonic receiver differs from the optoelectronic receiver in that the efficiency of the modulators is sufficiently high for them to be driven by the absorbed RF photocurrent alone. The modulators are operated under forward bias and have an I_π of approximately 10 mA below 100 MHz. Fig. 10 shows the measured link response using this receiver. In the optoelectronic receiver when the incoming phase is being tracked closely by the reference modulator, the response is flat and determined by the drive voltage ratio to the source and reference modulator. In the all photonic receiver the response when the loop is closed varies with frequency. This is observed in the plot in Fig. 10 and can be attributed to the frequency dependence of the I_π of the modulator. The link gain is still related to the ratio of V_π between source and reference modulator. For a forward biased modulator, the diode impedance is typically very low (10–15 Ω) and requires a very small drive voltage, overall resulting in a much lower link gain than when a reverse biased reference modulator is used.

VIII. SFDR MEASUREMENT

Using the Link Setup of Fig. 8, a two tone SFDR measurement is made on the optoelectronic receiver at three different frequencies with the same photocurrent (12 mA) in each detector. The results of this measurement are shown in Fig. 11. In Section VI we observed that the loop gain is higher at lower frequencies. Hence, the reference modulator can better track the incoming signal phase and consequently the SFDR is much higher at 300 MHz (125 dB $\cdot\text{Hz}^{2/3}$) than at 500 MHz or 1 GHz. As the loop gain decreases there is a diminishing reduction in the net received phase and at 1 GHz the reduction is negligible. Thus, the SFDR measured (113 dB $\cdot\text{Hz}^{2/3}$) corresponds closely to the open loop SFDR at that frequency. The noise floor shown is the

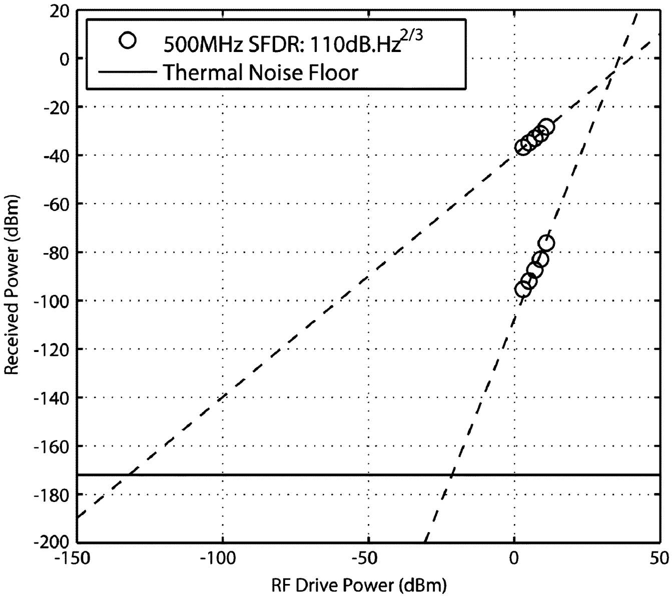

Fig. 12. SFDR of all photonic receiver at 500 MHz and 15 mA of photocurrent per detector.

calculated shot noise level. In practice, the noise floor is determined by the ASE of the high-power EDFA (30 dB gain, 5.5 dB NF) that was used to provide the required optical power. It is estimated that if a low-noise, high power laser is used, shot-noise limited operation should be available at this photocurrent level.

Fig. 12 shows a similar SFDR measurement made at 500 MHz on the all photonic receiver. The SFDR is considerably lower (110 $\mathrm{dB} \cdot \mathrm{Hz}^{2/3}$) when compared to the SFDR at 500 MHz (121 $\mathrm{dB} \cdot \mathrm{Hz}^{2/3}$) for the optoelectronic receiver. Shot-noise limited performance is also not available for this receiver configuration. Since the on chip reference modulators are forward biased their drive voltage is low and consequently, the buffer amplifer noise is higher than the drive signal to the modulator needed to suppress the shot noise of the receiver. In the receiver, thermal noise dominates over the shot noise at the received photocurrent (15 mA). An effort is being made to realize lower loss and hence, higher receiver photocurrent and loop gain for both the optoelectronic and all-photonic receiver architectures.

IX. CONCLUSION

In this paper, we have described and experimentally demonstrated a coherent integrated receiver that is based on a broadband optical phased locked loop. The delayed limited bandwidth of the loop is 4 GHz. In order to port the link to a much higher carrier frequency, we are exploring the idea of optical sampling [17]–[21]. Additionally, the PLL bandwidth of 1.45 GHz demonstrated here would be sufficiently large to track the phase noise of standard semiconductor lasers with low phase error.

ACKNOWLEDGMENT

The authors would like to thank helpful discussions with Larry Lembo, Darko Zibar, Steve Pappert, and Jim Hunter. Northrop Grumman Space Technologies are acknowledged for providing the electronic IC.

REFERENCES

[1] J. E. Bowers, A. C. Chipaloski, S. Boodaghians, and J. W. Carlin, "Long distance fiber-optic transmission of C-band microwave signals to and from a satellite antenna," *J. Lightw. Technol.*, vol. LT-5, pp. 1733–1741, 1987.

[2] D. Wake, M. Webster, G. Wimpenny, K. Beacham, and L. Crawford, "Radio over fiber for mobile communications," in *Proc. Microw. Photon. (MWP'04)*, Oct. 2004, pp. 157–160.

[3] A. Larsson, C. Carlsson, J. Gustavsson, A. Haglund, and P. Modh, "Broadband direct modulation of VCSELs and applications in fiber optic RF links," presented at the Proc. IEEE Int. Topical Meet. Microw. Photon., Oct. 2004, paper WA-1, unpublished.

[4] P. Hartmann *et al.*, "Demonstration of highly linear uncooled DFB lasers for next generation RF over fibre applications," in *Proc. 28th European Conf. Opt. Commun. (ECOC)*, 2002, vol. 2, pp. 1–2.

[5] F. Bucholtz, V. J. Urick, M. S. Rogge, and K. J. Williams, "Performance of analog photonic links employing phase modulation," presented at the Proc. OSA Topical Meet. Coherent Opt. Technol. Applicat. (COTA), 2006, Paper CFA6, unpublished.

[6] Y. Li *et al.*, "Receiver for a coherent fiber-optic link with high dynamic range and low noise figure," in *Proc. Int. Top. Meet. Microw. Photon. (MWP'05)*, Seoul, Korea, 2005.

[7] M. Ohtsu, *Highly Coherent Semiconductor Lasers*. Norwood, MA: Artech House, 1992.

[8] H. F. Chou, A. Ramaswamy, D. Zibar, L. A. Johansson, J. E. Bowers, M. Rodwell, and L. A. Coldren, "SFDR improvement of a coherent receiver using feedback," presented at the Proc. OSA Top. Meet. Coherent Opt. Techn. Applicat. (COTA), Whistler, BC, 2006, Paper CFA3, unpublished.

[9] H. F. Chou, L. A. Johansson, D. Zibar, A. Ramaswamy, M. Rodwell, and J. E. Bowers, "All-optical coherent receiver with feedback and sampling," in *Proc. Int. Top. Meet. Microw. Photon. (MWP'06)*, Grenoble, France, 2006.

[10] G. E. Betts, W. Krzewick, S. Wu, and P. K. L. Yu, "Experimental demonstration of linear phase detection," *IEEE Photon. Technol. Lett.*, vol. 19, no. 1 3, pp. 993–995, Jul. 2007.

[11] H. F. Chou, A. Ramaswamy, D. Zibar, L. A. Johansson, J. E. Bowers, M. Rodwell, and L. A. Coldren, "High-linearity coherent receiver with feedback," *IEEE Photon. Technol. Lett.*, vol. 19, no. 12, pp. 940–942, Jun. 2007.

[12] M. N. Sysak, J. W. Raring, J. S. Barton, M. Dummer, A. Tauke-Pedretti, H. N. Poulsen, D. J. Blumenthal, and L. A. Coldren, "Single-chip, widely-tunable 10 Gbit/s photocurrent-driven wavelength converter incorporating a monolithically integrated laser transmitter and optical receiver," *Electron. Lett.*, vol. 42, no. 11, pp. 657–658, May 2007.

[13] J. Klamkin *et al.*, "Monolithically integrated balanced uni-traveling-carrier photodiode with tunable MMI coupler for microwave photonic circuits," in *Proc. Conf. Optoelectron. Microelectron. Mater. Dev. (COMMAD)*, Perth, Australia, Dec. 2007.

[14] J. Klamkin *et al.*, "High output saturation and high-linearity uni-traveling-carrier waveguide photodiodes," *IEEE Photon. Technol. Lett.*, vol. 19, no. 3, pp. 149–151, Feb. 2007.

[15] L. A. Johansson, H. F. Chou, A. Ramaswamy, J. Klamkin, L. A. Coldren, M. J. Rodwell, and J. E. Bowers, "Coherent optical receiver for linear optical phase demodulation," in *Proc. IEEE MTT-S Int. Microw. Symp.*, Honolulu, Hawaii, Jun. 2007.

[16] A. Ramaswamy, L. A. Johansson, J. Klamkin, C. Sheldon, H.-F. Chou, M. J. Rodwell, L. A. Coldren, and J. E. Bowers, "Coherent receiver based on a broadband optical phase-lock loop," presented at the Optical Fiber Communications Conference (OFC) Postdeadline Technical Digest. Opt Soc., 2007, Paper PDP3, unpublished.

[17] P. W. Juodawlkis, J. C. Twichell, G. E. Betts, J. J. Hargreaves, R. D. Younger, J. L. Wasserman, F. J. O'Donnell, K. G. Ray, and R. C. Williamson, "Optically sampled analog-to-digital converters," *IEEE Trans. Microw. Theory Tech.*, vol. 49, pp. 1840–1852, 2001.

[18] P. W. Juodawlkis, J. J. Hargreaves, R. D. Younger, G. W. Titi, and J. C. Twichell, "Optical down sampling of wideband microwave signals," *J. Lightw. Technol.*, vol. 21, no. 12, pp. 3116–3124, Dec. 2003.

[19] D. Zibar, L. A. Johansson, H. F. Chou, A. Ramaswamy, M. Rodwell, and J. E. Bowers, "Novel optical phase demodulator based on a sampling phase-locked loop," *IEEE Photon. Technol. Lett.*, vol. 19, no. 9, pp. 686–688, May 2007.

[20] D. Zibar, L. A. Johansson, H. F. Chou, A. Ramaswamy, M. Rodwell, and J. E. Bowers, "Investigation of a novel optical phase demodulator based on a sampling phase-locked loop," in *Proc. Int. Top. Meet. Microw. Photon. (MWP'06)*, Grenoble, France, 2006.

[21] L. A. Johansson, D. Zibar, A. Ramaswamy, L. Coldren, M. Rodwell, and J. E. Bowers, "Analysis of sampled optical phase-lock loops," in *Proc. MWP'07*, submitted for publication.

Anand Ramaswamy (S'06) received the B.S. degree in electrical engineering with a minor in physics and the M.S. degree in electrical engineering from the University of Southern California, Los Angeles, and the University of California, Santa Barbara, in 2005 and 2007, respectively. He is currently working towards the Ph.D. degree under Professor John E. Bowers at the University of California, Santa Barbara.

His research interests are in coherent communication systems and nonlinear mechanisms in high-power photodetectors.

Leif A. Johansson received the Ph.D. degree in engineering from University College London, U.K., in 2002.

He accepted a Postdoctoral position at the University of California at Santa Barbara in 2002. His current research interests include design and characterization of integrated photonic devices for analog and digital applications. He is a member of the IEEE.

Jonathan Klamkin received the B.S. degree in electrical and computer engineering from Cornell University, Ithaca, NY, in 2002, the M.S. degree in electrical and computer engineering from the University of California, Santa Barbara (UCSB), in 2004, and is currently working toward the Ph.D. degree in materials at UCSB.

His research interests include the design, epitaxial growth, fabrication, and characterization of widely tunable semiconductor lasers, photodetectors, optical intensity and phase modulators, compact couplers, and semiconductor optical amplifiers for InP-based photonic integrated circuits. Currently, his efforts are focused on novel coherent integrated receivers for highly linear fiber microwave photonic links.

Hsu-Feng Chou (S'01–M'06) received the B.S. degree in physics and the M.S. degree in electrooptical engineering from the National Taiwan University (NTU), Taipei, Taiwan, R.O.C., in 1996 and 1998, respectively, and the Ph.D. degree in electrical and computer engineering from the University of California, Santa Barbara (UCSB) in 2005, where his research focused on high-speed optical communication systems.

From 1998 to 2000, he was an Engineering Officer in the R.O.C. Navy. From 2005 to 2006, he was a Postdoctoral Fellow at UCSB, with research interests in coherent RF photonic links and dynamically reconfigurable optical packet switching. He is currently with LuminentOIC Inc.,Chatsworth, CA. He has authored or coauthored over 50 papers published in various journals and conference proceedings.

Colin Sheldon received the Sc.B. degree in electrical engineering from Brown University, Providence, RI, in 2004 and the M.S. degree in electrical engineering from the University of California, Santa Barbara, in 2006. He is currently pursuing the Ph.D. degree in electrical engineering at the University of California, Santa Barbara, under the supervision of Prof. Mark Rodwell.

His research interests include high-speed circuit design, coherent optical communications, and wireless communication links.

Mark J. Rodwell (F'03) received the B.S. degree from the University of Tennessee, Knoxville, in 1980, the M.S.and Ph.D. degrees from Stanford University, Stanford, CA, in 1982 and 1988, respectively.

He is Professor and Director of the UCSB Nanofabrication Laboratory and the NSF Nanofabrication Infrastructure Network (NNIN) at the University of California, Santa Barbara. He was with AT&T Bell Laboratories, Whippany, NJ, from 1982 to 1984. His current research focuses on high-bandwidth InP bipolar transistors, compound semiconductor field-effect transistors for VLSI applications, and millimeter-wave integrated circuit design in both silicon VLSI and III–V processes.

Dr. Rodwell was the recipient of a 1989 National Science Foundation Presidential Young Investigator award and for his work on GaAs Schottky-diode ICs for subpicosecond/millimeter-wave instrumentation, he was awarded the 1997 IEEE Microwave Prize.

Larry A. Coldren (S'67–M'72–SM'77–F'82) received the Ph.D. degree in electrical engineering from Stanford University, Stanford, CA, in 1972.

He is the Fred Kavli Professor of Optoelectronics and Sensors at the University of California, Santa Barbara, CA. After 13 years in the research area at Bell Laboratories, he joined UC-Santa Barbara in 1984, where he now holds appointments in Materials and Electrical and Computer Engineering, and is Director of the Optoelectronics Technology Center. In 1990, he cofounded Optical Concepts, later acquired as Gore Photonics, to develop novel VCSEL technology; and in 1998 he cofounded Agility Communications, recently acquired by JDSU, to develop widely tunable integrated transmitters. He has authored or coauthored over 800 papers, five book chapters, one textbook, and has been issued 61 patents. He has presented dozens of invited and plenary talks at major conferences.

Prof. Coldren is a Fellow of the Institution of Electrical Engineers (IEE) and Fellow of the Optical Society of America (OSA). He is the recipient of the 2004 John Tyndall Award and a member of the National Academy of Engineering.

John E. Bowers (F'04) received the M.S. and Ph.D. degrees from Stanford University, Stanford, CA.

He is a Professor in the Department of Electrical Engineering, and in the Technology Management Program at the University of California, Santa Barbara. He is also CTO and cofounder of Calient Networks. His research interests are primarily concerned with silicon photonics, optoelectronic devices, optical switching, and transparent optical networks. He is cofounder of the Center for Entrepreneurship and Engineering Management, and founder of Terabit Technology. Previously, he had worked for AT&T Bell Laboratories and Honeywell before joining UCSB. He has published eight book chapters, 400 journal papers, 600 conference papers, and has received 49 patents.

Dr. Bowers is a Fellow of the Optical Society of America (OSA) and the American Physical Society, and a recipient of the IEEE LEOS William Streifer Award and the South Coast Business and Technology Entrepreneur of the Year Award. He was an elected member of the IEEE LEOS Board of Governors, a LEOS Distinguished Lecturer, and Vice President for Conferences for LEOS. He is a member of the National Academy of Engineering. He received the ACE Award for Most Promising Technology for the hybrid silicon laser in 2007.

Design and Implementation of Ultra-Compact Grating-Based 2x2 Beam Splitter for Miniature Photonic Integrated Circuits

Chin-Hui Chen, Jonathan Klamkin, Leif A. Johansson, and Larry. A. Coldren
Department of Electrical and Computer Engineering, University of California, Santa Barbara, CA 93106
Phone: 805.893.5955, Fax: 805.893.4500, Email: janet@ece.ucsb.edu

Abstract: We provide detailed experimental study of reflectivity, insertion loss, and interference extinction ratio for our recently proposed and demonstrated grating-based beam splitter. Both low-loss and high-extinction-ratio devices are demonstrated for reflectivities close to 50%.

OCIS codes: (130.3120) Integrated optics devices; (230.1360) Beam splitters

1. INTRODUCTION

As the Photonic Integrated Circuits (PICs) become more complex, a demand for smaller and more efficient optical devices increases. This is particularly true for integrated-optic beam splitters, which play an important role in reducing the size of our Coherent Optical Integrated Receiver (CHOIR) PIC [1], [2]. Here, a very compact size of the beam splitter is essential not only for reducing the physical dimension of the PIC, but also for enabling the stability of the PIC at higher frequencies via decreasing the delay in the optical feedback circuit [1]. The recently proposed grating-based beam splitter [2] has been demonstrated to have a superior ultra-short splitting length of only 10 μm. Although the grating-based beam splitter is considerably smaller than its conventional counterparts, it requires a comparable fabrication complexity. Also, it can achieve high throughput, while many other advanced technologies such as photonic crystal [3] and air trenches [4] cannot.

This work provides insights into the design and fabrication issues relating to the ultra-compact grating-based beam splitter. It reveals the necessary approach to be taken in optimizing the beam splitter for more efficient CHOIR PICs in terms of reflectivity, loss, and interference extinction ratio. To the best of our knowledge, this is the first work to demonstrate that both low insertion loss and high interference extinction ratio are achievable using a grating-based beam splitter.

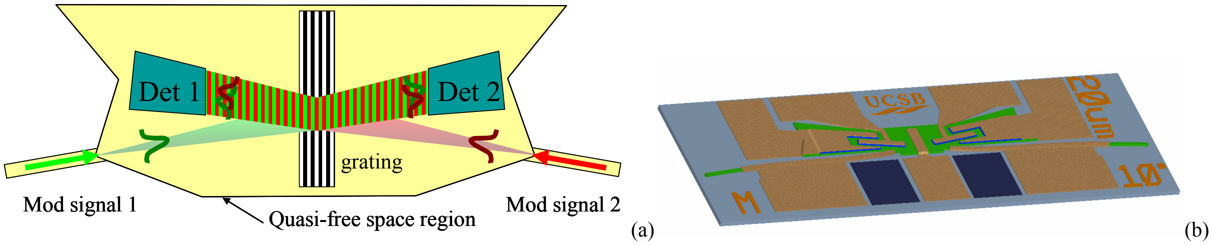

FIGURE 1. (a) Schematic diagram of grating-based beam splitter, integrated with two modulators and two photodetectors. Waveguide boundary is far away from the diverged beams in the quasi-free space region. Green and red colors represent input signals from the two modulators. (b) Fabricated grating-based beam splitter, including the modulators and photodetectors, shown to scale.

2. DESIGN AND FABRICATION

The design goal at hand is to realize an integrated beam splitter which has an equal splitting ratio, low insertion loss, short propagation length, as well as a high degree of interference between the output beams of two integrated multiple-quantum-well (MQW) phase modulators that are used in our CHOIR PICs, as shown in Fig. 1(a). Fig. 1(a) also shows the two integrated photodetectors used in the PIC, which are also used to obtain the measurements presented below. The simulations are based on 2-D, quasi-free space, two-wave interference method, as explained in [2]. One of the major issues with oblique incidence into a grating that is thick compared to the beam width is unequal mode distortion for the diffracted and undiffracted beams. This distortion comes from the continuous energy exchange in gratings [5]. In order to minimize degradation of interference due to this effect, two novel design techniques are used in this work: 1) the angle of incidence is made to be 10 degrees to the normal incidence, and 2) the gratings are etched deep through the slab waveguide layer, which allows the grating region to be ultra short. Consequently, severe mode distortions can be avoided. In addition, the quasi-free space region shown in Fig. 1(a) is designed to provide for rapid beam divergence and, thus, for large beam-width-to-grating-length ratio.

The grating-based beam splitters are implemented on an InGaAsP/InP integration platform as illustrated in Figure 1 (b). The gratings are patterned on a SiO_2 hard mask using holographic exposure and then transferred by methane/hydrogen/argon (MHA)-based reactive ion etching (RIE) with oxygen addition [6]. Due to the non-uniformity of the photoresist at the edge of the grating burst, the actual grating lengths are 5 μm shorter than expected. The largest index contrast in the grating is achieved when the slab waveguide layer is completely etched through. As shown in [2], the etch of the deep grating grooves is followed by a regrowth of an InP cladding layer without apparent air voids, which suggests low void-stimulated scattering losses in our devices. An array of PICs containing grating-based beam splitters of various lengths and detectors of various widths has been fabricated and measured in this study, as explained below.

3. RESULTS AND DISCUSSION

Figure 2 shows the reflectivity spectra, plotted versus wavelength detuning from the Bragg wavelength, for the beam splitter having three different grating lengths (*Lg*) of 5 μm, 10 μm, and 15 μm and integrated with three different detectors having widths of 7 μm (*S*), 12 μm (*M*), and 23 μm (*L*). The middle grating length (*Lg*=10 μm) is designed to match the width of the optical beam incident on it, and the middle detector width (12 μm) is designed to match the width of its incident beam incident on it. The three detectors have the same length of 100 μm, which is long enough to absorb most of the light.

***Reflection**:* In the cases when *Lg* = 5 μm and *Lg* = 10 μm, the peak reflectivities for all three detector widths are typical of those for thin gratings and small incident angles. As the grating length gets larger than the interacting beam width, as is the case for *Lg* = 15 μm, the mode profiles of the reflected and transmitted waves experience unequal distortions [5], which also explains the difference in the data for the three detectors. The same data can be fitted to the well known *tanh*-relation [7] between reflectivity and $\kappa * Lg$, with some reasonable assumptions, as shown in Fig. 3 (a). We assume that the κ value is 85% of the ideal case where a rectangular grating profile and a completely-etched-through slab waveguide are used. In our devices, because of the practical fabrication issues, we observe a certain degree of inevitable round up in the grating profile that results from the regrowth step, as shown in [2], and we also observe that the slab waveguide layers are not completely etched through. In addition, the reflectivity is assumed to saturate at 72%, as the overlap between the grating thickness and the mode profile in the transverse plane is not unity and some parts of the incident wave are transmitted through the deep grating region without experiencing any interference [8].

***Loss**:* The insertion loss data shown in Fig. 3 (b) provides information about: 1) propagation losses between the modulators and detectors, 2) scattering losses of the gratings, and 3) detector coupling losses, which are due to mismatches between the mode shapes and detector input areas. The propagation loss should be identical in all the cases studied since the waveguide geometry is kept the same. The coupling loss for the detector *L* can be assumed to be independent of the mode profile, since most of the incident light can be collected. Consequently, the insertion loss data obtained for the widest detector in Fig. 3(b) indicate that there is a small dependence of the scattering loss on the grating length. For the detector *M*, most of the incident light is still collected for all gratings lengths, except for some marginal loss due to the mode distortion in longer gratings. The material propagation loss can be estimated

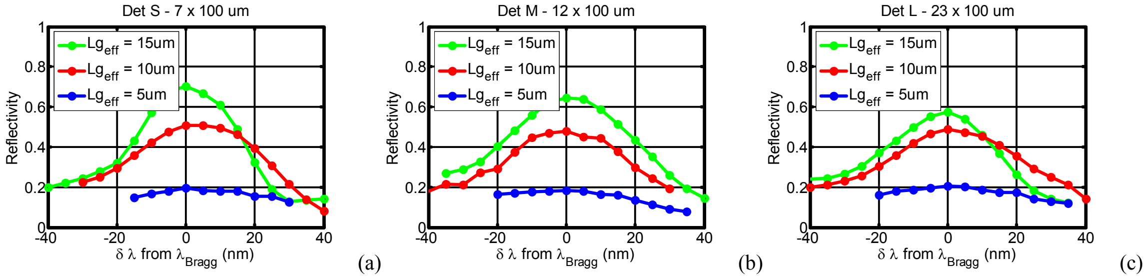

FIGURE 2. Reflectivity data with different grating lengths and detector widths. (a) Detector *S* width = 7 μm (b) Detector *M* width = 12 μm (c) Detector *L* width = 23 μm.

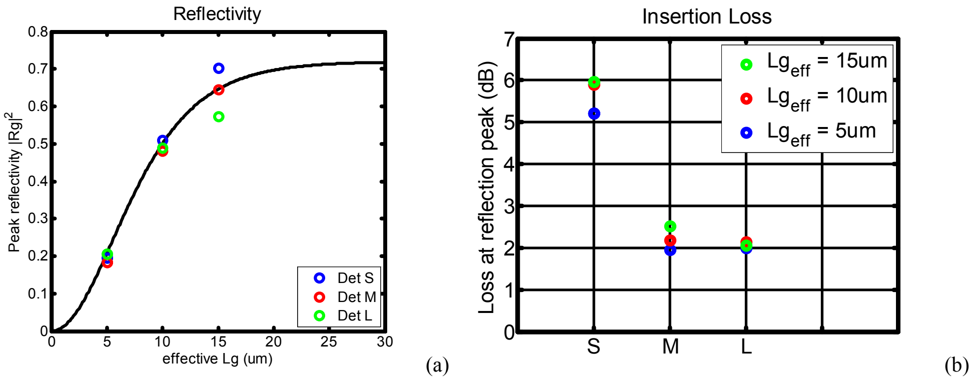

FIGURE 3. Bragg condition data. (a) Peak reflectivity. Circles are data from Figure 2 with different grating lengths and detector widths. Solid line represents the reflectivity *tanh* relation [7]. (b) Insertion loss for different detector widths: Detector *S* (7 μm), Detector *M* (12 μm), and Detector *L* (23 μm).

to be 0.5 dB.If we also take waveguide scattering losses into account, the grating scattering loss alone can be estimated to be less than 1.5 dB. For the detector *S*, excess coupling losses of about 3 to 4 dB for different grating lengths are measured, as expected, because only a portion of the incident light is captured due to the small detector width.

***Extinction Ratio**:* The interference behavior of the two beams coming from the two nominally identical MQW phase modulators is characterized by the extinction ratio between their constructive and destructive interferences. The extinction ratios are obtained by measuring the photocurrents of the detectors at their optimal operation points. The highest measured extinction ratios for the detector *L*, *M* and *S* are 6.5 dB, 13.5 dB and over 16 dB, respectively. Because the grating distorts the reflected and transmitted modes differently, the narrowest detector has the best extinction ratio as it mostly captures the parts of the modes that interfere most effectively. Therefore, with a proper choice of the detector width, both low insertion loss and high extinction ratio in our PICs can be achieved with deeply etched grating-based beam splitters. For example, for the 10-μm long grating and 12-μm wide photodetector, both 50% reflectivity (see Fig. 3(a)) and 2 dB insertion loss (see Fig. 3(b)) can be achieved for an extinction ratio as large as 13.5 dB.

4. CONCLUSION

In this paper, we have presented a comprehensive study of the ultra-compact grating-based beam splitter, where we were able to experimentally confirm our theoretical predictions. We have demonstrated beam splitters having 50% reflectivity and insertion loss as low as 2 dB. These ultra-short devices are only 10 μm long, and are invaluable for applications such as our CHOIR PICs, where they provide loop stability for high-frequencies, which cannot be easily achieved with competing technologies, in addition to larger than 13.5 dB extinction ratio. Moreover, the work provides design guidelines for future integrated grating-based beam splitters.

5. REFERENCES

[1] A. Ramaswamy, et al., “Coherent Receiver Based on a Broadband Optical Phase-Lock Loop,” *OFC Conference* post deadline paper, 2007.

[2] C. H. Chen, et al., “Ultra-compact Grating-based 2x2 Beam Splitter for Miniature Photonic Integrated Circuits,” The 20th Annual Meeting of IEEE *LEOS* 2007.

[3] S. Shi, et al., “Dispersion-based beam splitter in photonic crystals,” *Optics Letters*, Vol. 29, No. 6, March 2004.

[4] Y. Lin, et al., “Compact and high efficiency polymer air-trench waveguide bends and splitters,” *Proceedings of SPIE,* Vol. 6462, March 2007.

[5] M. R. Wang, “Analysis and observation of finite beam Bragg diffraction by a thick planar phase grating,” *Applied Optics*, Vol. 35, No. 4, pp. 582-592, Feb. 1996.

[6] J. E. Schramm, et al., “Fabrication of high-aspect-ratio InP-based vertical-cavity laser mirrors using $CH_4/H_2/O_2/Ar$ reactive ion etching,” *Journal of Vacuum Science & Technology B: Microelectronics and Nanometer Structures*, Vol. 15, No. 6, pp. 2031-2036, Nov. 1997.

[7] S. W. *Corzine*, et al., “A tanh substitution technique for the analysis of abrupt and graded interface multilayer dielectric stacks,” *Journal of Quantum Electronics*, Vol. 27, No. 9, pp. 2086-2090, Sep. 1991.

[8] J. Ctyroky, et al., “Analysis of a deep waveguide Bragg grating,” *Optical and Quantum Electronics*, Vol. 30, pp. 343-358, May 1998.

Output Saturation and Linearity of Waveguide Unitraveling-Carrier Photodiodes

Jonathan Klamkin, *Student Member, IEEE*, Yu-Chia Chang, Anand Ramaswamy, *Student Member, IEEE*,
Leif A. Johansson, *Member, IEEE*, John E. Bowers, *Fellow, IEEE*, Steven P. DenBaars, *Fellow, IEEE*, and
Larry A. Coldren, *Fellow, IEEE*

***Abstract*—Waveguide unitraveling-carrier photodiodes (UTC-PDs) with different absorber and collector layer doping levels have been fabricated and characterized. These photodiode (PD) structures are fabricated on a platform that allows for the monolithic integration of multiquantum-well optical phase modulators and couplers for realizing novel coherent receivers. Compared to PD A, PD B has a lower and more graded p-doping profile in the absorber layer and also a higher n-doping level in the collector layer. For PD B a larger field is induced in the absorber layer at high photocurrent levels. Also the higher n-doping in the collector layer is adequate for providing charge compensation. For PD B, there is an enhancement in the RF response as the photocurrent level is increased. At a frequency of 1 GHz, the saturation current for PD A is around 65 mA and that for PD B is around 63 mA. For PD B, the third-order output intercept point at photocurrent levels of 30 and 40 mA is 37.2 and 34.9 dBm, respectively. That for PD A is 35.8 and 30.4 dBm. PD B is, therefore, favorable for linear operation at high current levels.**

***Index Terms*—Coherent receiver, fiber-optic link, linearity, saturation current, third-order intermodulation distortion (IMD3), third-order output intercept point (OIP3), unitraveling-carrier photodiode (UTC-PD).**

I. INTRODUCTION

COHERENT fiber-optic links that utilize phase modulation can demonstrate high spur-free dynamic range and high signal-to-noise ratio. The challenge with phase modulation is building a coherent receiver that can linearly demodulate the phase of the received signal. To overcome this, we have demonstrated a novel coherent receiver architecture employing feedback for closely tracking the phase of the received signal [1], [2]. The incoming signal is mixed with a local oscillator signal and the detected photocurrent representing the phase difference is then fed back to a reference phase modulator. For high loop gain the signal phase is tracked closely. With a monolithically integrated approach, the delay of the feedback can be kept short enough for operation in the gigahertz (GHz) frequency range.

A very important requirement of this coherent receiver is the realization of photodiodes (PDs) that demonstrate both high output saturation current and high linearity at GHz frequencies and can be monolithically integrated with optical phase modulators and couplers. The unitraveling-carrier photodiode (UTC-PD) is designed for high speed and high current operation [3]. We have previously demonstrated a monolithic balanced UTC-PD with a tunable multimode interference coupler on a platform that allows for the integration of MQW phase modulators [4]. In a UTC-PD light is absorbed in an undepleted p-type narrow bandgap layer, referred to as the absorber, and photogenerated electrons subsequently diffuse to a wide bandgap drift layer, referred to as the collector. Electrons are the only active carriers and electrons have a higher drift velocity than holes, therefore space charge saturation effects are reduced when compared to a p-i-n PD.

Several techniques for improving the performance of UTC-PDs have been demonstrated. Charge compensation was used to improve the saturation current by intentionally n-doping the collector layer [5]. By doing so, the electric field is preconditioned to be higher in the presence of a large mobile space charge density. Others have reported an enhancement in the response of UTC-PDs that have a graded doping profile in the p-type absorber [6]. This grade results in a potential profile that can aid electron transport. This same effect was also observed for UTC-PDs with uniform but relatively lower absorber doping [7].

We previously reported waveguide UTC-PDs that demonstrated output saturation currents greater than 40 mA at 1 GHz and a third-order output intercept point (OIP3) of 43 dBm at 20 mA and 34 dBm at 40 mA [8]. We observed a significant improvement in the saturation characteristics for devices that had a wider input waveguide. Here we have closely investigated the effects of the doping profile in several layers of the UTC-PD structure on the output response, saturation current, and third-order intermodulation distortion (IMD3). In particular, two different waveguide UTC-PDs were fabricated and characterized. The most significant differences in these devices are the doping profiles in the absorber and collector layers. The devices are referred to as PD A and PD B. In PD A, the p-doping in the absorber layer is not only higher, but also more uniform. The n-doping in the collector layer of PD A is 7E15 cm^{-3} whereas that for PD B is 6E16 cm^{-3}. For PD B an enhancement in the output response is observed at high current. This is believed to be due to the combination of the lower and more graded absorber doping profile as well as the higher collector doping level. The lower and more graded doping level in the absorber results in a small field induced at high current levels, and the higher collector doping level provides charge compensation. Both PDs exhibit saturation current levels that, to the best of our knowledge, are some of the highest reported for waveguide PDs

---

Manuscript received July 24, 2007; revised October 9, 2007. This work was supported by the Defense Advanced Research Projects Agency (DARPA) PHOR-FRONT program under United States Air Force Contract FA8750-05-C-0265.

The authors are with the Materials Department and the Electrical and Computer Engineering Department at the University of California, Santa Barbara, CA 93106 USA (e-mail: klamkin@engineering.ucsb.edu).

Digital Object Identifier 10.1109/JQE.2007.914768

TABLE I
UTC-PD LAYER STRUCTURE

Layer	Thickness (nm)	Doping (cm^{-3})
p-InGaAs contact	150	2E19
p-InP cladding	2,000	1E18
p-InGaAs absorber	**75**	**P**
InGaAs	8	UID
InGaAsP	16	UID
InP	6	UID
n-InP	7	1E18
n-InP collector	**200**	**N**
n-InP field termination	25	2E18
n-InGaAsP stop etch	15	5E17
n-InP	15	5E16
InGaAsP MQW and waveguide		
n-InP	600	1E18
n-InGaAsP contact	100	3E18
n-InP	500	1E18
SI InP substrate	350,000	

at comparable frequencies. For PD B, the OIP3 increases with photocurrent more so than for PD A. PD B exhibits higher linearity at high photocurrent levels.

II. DEVICE DESIGN AND FABRICATION

The epitaxial structures are grown by metalorganic chemical vapor deposition (MOCVD) on semi-insulating InP substrates. The PD structures are grown directly above an InGaAsP optical waveguide. Passive regions are formed by selectively removing the PD layers using wet chemical etching. This step is followed by a blanket p-InP cladding and p-InGaAs contact layer regrowth. Surface ridges are formed, and metal contacts are deposited and annealed. Benzocyclobutene dielectric is used to reduce parasitic capacitance. The layer structure in a photodetection region following regrowth is shown in Table I. The p-doping level in the absorber and the n-doping level in the collector are denoted p and n, respectively. The doping levels for those layers, which are unintentionally doped are denoted UID. The n-InP field termination layer terminates the applied field across the collector layer of the PD in the photodetection regions and prevents depletion of the optical waveguide below. A cross section SEM image of a fabricated device is shown in Fig. 1. Light is coupled from a lensed fiber into the optical waveguide in a passive region and then absorbed as it propagates in a photodetection region. Because of the spatial separation of the absorber layer in the UTC-PD structure and the peak of the incoming optical mode, carrier generation is distributed more uniformly along the length of the device. This as well as a wide input waveguide help to reduce front-end saturation.

Of particular interest in understanding the device performance are the doping profiles in the absorber and collector layers. Zn is used for p-doping and Si is used for n-doping. The Zn and Si concentration in the structures were measured by secondary ion mass spectroscopy. The doping profiles are shown in Fig. 2. The absorber p-doping level was intended to be greater than 2E18 cm^{-3}. Because of the high diffusivity of Zn at growth temperatures, the grading in the doping profile can vary. For PD B, the peak Zn concentration in the absorber is 25% lower than that for PD A and the profile is more graded (high to low) toward the absorber/collector interface. These characteristics should result in a higher induced electric field in the absorber region of PD B and therefore a larger enhancement in the output response. The Si concentration in the collector of PD A is 7E15 cm^{-3} and that for PD B is 6E16 cm^{-3}, nearly an order of magnitude higher. The latter is adequate for providing charge compensation. Devices were fabricated with various geometries. The results that follow are for devices that are 10 μm wide and 150 μm long.

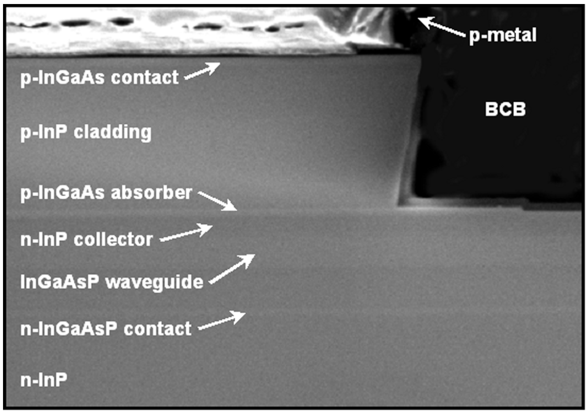

Fig. 1. Cross section SEM image of PD structure.

III. RESULTS AND DISCUSSION

The electrical frequency responses of the UTC-PDs were measured at various biases for photocurrent levels up to around 70 mA. Fig. 3 shows the RF power as a function of dc photocurrent at 1 GHz for both devices. The data is normalized to 0 dB. For these measurements the modulation depth was 50%. The saturation characteristics of PD B vary with bias more so than those of PD A. The saturation current, defined here as the photocurrent level where the RF response is compressed by 1 dB, is around 65 mA for PD A and around 63 mA for PD B for a bias of -3.5 V. Fig. 4 shows the RF power normalized to an ideal line with a slope of 20 dB/decade. For PD A, the response is fairly constant with increasing photocurrent until the onset of saturation. For PD B, there is a significant enhancement in the response with increasing photocurrent. This enhancement is due in part to a small field induced in the absorber at high photocurrent levels. The p-doping in the absorber of PD B is lower and more graded so this field should be greater in this device. The enhancement is also due to the higher n-doping in the collector of PD B. This doping provides some charge compensation and preconditions the electric field for operation at high photocurrent levels. Because the device areas are large, the 3-dB bandwidth is *RC*-limited. Therefore, any enhancement in the response should be attributed more so to improvements in the field distribution in the depletion region or the device capacitance rather than improvements in carrier transit time. For low biases the RF response of PD B saturates at much lower photocurrent levels than that of PD A. For example, at a bias of -2 V the saturation current of PD B is less than 20 mA whereas for PD A it is greater than 40 mA. This is due to the fact that the doping in the collector layer of PD B is significantly higher. As such a higher bias is required to deplete the collector layer and optimize the field profile.

The internal quantum efficiency (IQE) was also measured for both PDs and the results are shown in Fig. 5. The PD structures

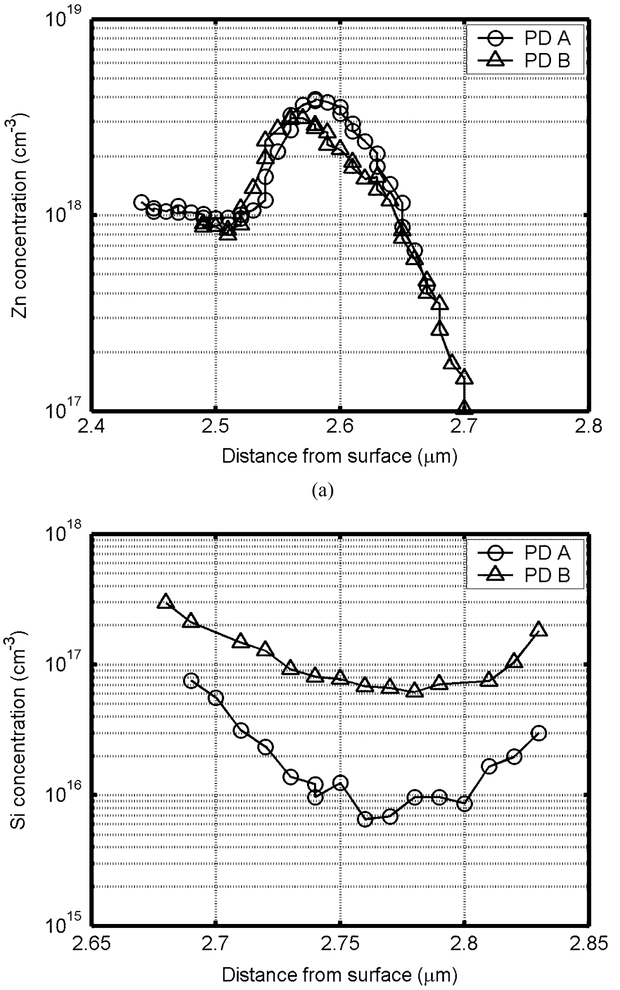

(a)

(b)

Fig. 2. (a) Zn doping profile in absorber and (b) Si doping profile in collector for both PDs.

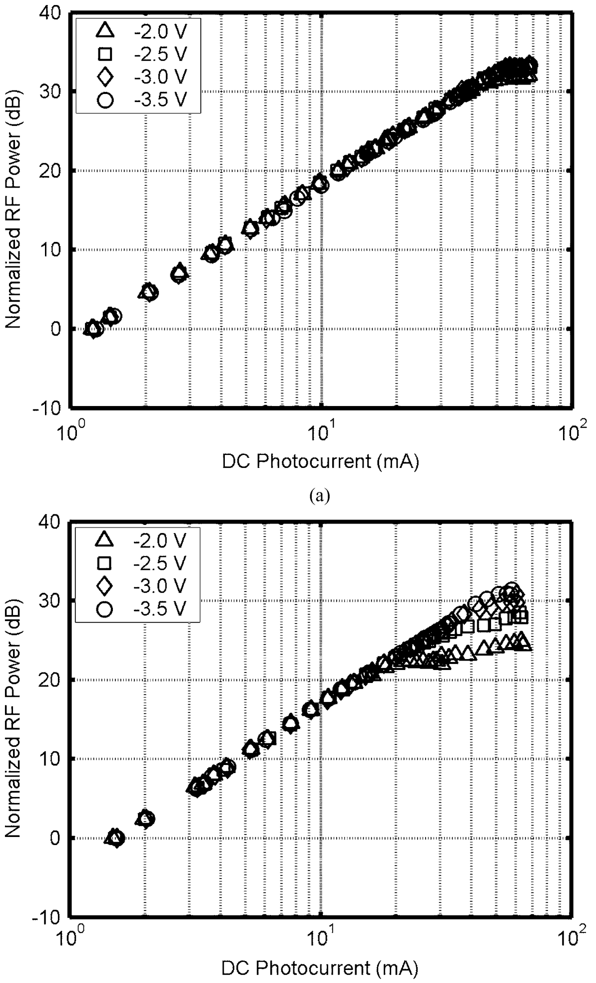

(a)

(b)

Fig. 3. Normalized RF power as a function of dc photocurrent at 1 GHz for (a) PD A and for (b) PD B.

are designed to be very efficient for the device length of 150 μm. The IQE for PD A is around 99% and that for PD B is around 96%. For PD A the IQE is fairly constant with photocurrent and bias. For PD B there is a slight increase in IQE with increasing photocurrent. The IQE also degrades slightly at high photocurrent levels for low biases. The change in 3-dB bandwidth as a function of dc photocurrent level is shown in Fig. 6 for both PDs. As expected, there is a larger enhancement with increasing photocurrent for PD B. For this PD the 3-dB bandwidth is enhanced by as much as 40%–50% whereas for PD A it is enhanced by at most around 30%. The saturation current was also extracted at 0.5 and 2 GHz. For PD A, the saturation current at these frequencies is 67 and 62, mA respectively. For PD B it is 60 and 62 mA.

To characterize the linearity of the PDs, a two-tone setup was used similar to that in [9]. Tones were generated at 1 and 0.8 GHz. The output fundamental and IMD3 power were measured as a function of input modulation power at various photocurrent levels and biases. Fig. 7 shows the IMD3 measurements for both devices at a photocurrent level of 30 mA and a bias of -5 V. The OIP3 at these conditions for PD A is 35.8 dBm and that for PD B is 37.2 dBm. The input modulation power levels applied correspond to a modulation index range of around 62%–82%. Fig. 8 shows the OIP3 as a function of dc photocurrent for both PDs. For these measurements the bias for both devices was -5 V and the input RF tones were 1 and 0.8 GHz as before. At 10-mA dc photocurrent, PD A demonstrates a significantly higher OIP3. However at higher photocurrent levels, the OIP3 for PD B is higher. This is consistent with the saturation characteristics observed. The enhancement in OIP3 with increasing photocurrent is typical of UTC-PDs. The authors in [10] attribute this to the electric field induced in the absorber layer, which improves the RF response. For PD B the increase in OIP3 in going from 10 to 20 mA of photocurrent is greater than that for PD A. It is possible that because the absorber layer doping profile in PD B is lower and more graded, the induced electric field is greater and therefore the enhancement in the RF response and in turn the OIP3 is greater. This does not however explain why the OIP3 of PD B is lower at the lower photocurrent level. The n-doping level of PD B is 6E16 cm^{-3} and that for PD A is 7E15 cm^{-3}. The doping level in PD B is sufficient for providing charge compensation, which preconditions the electric field for high photocurrent levels. This also contributes to the enhancement in OIP3 at higher photocurrent levels. Because of the

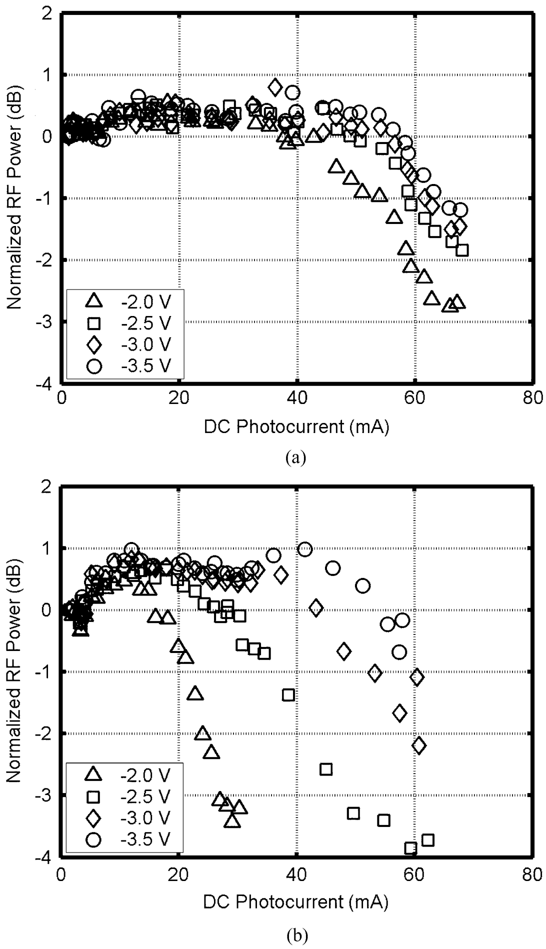

(a)

(b)

Fig. 4. Normalized RF power as a function of dc photocurrent at 1 GHz for (a) PD A and for (b) PD B.

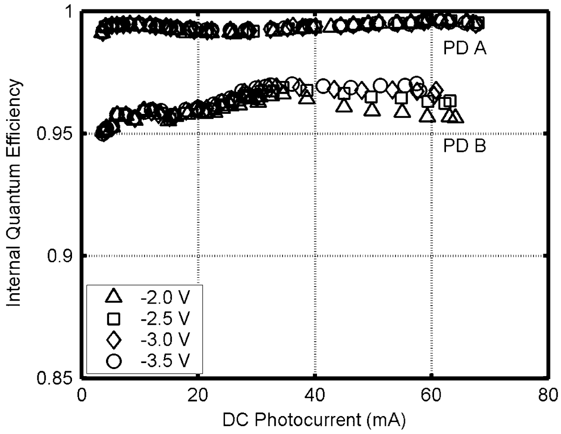

Fig. 5. Internal quantum efficiency as a function of dc photocurrent for PD A and PD B.

higher doping in PD B, at low photocurrent levels the collector layer may only be partially depleted and therefore the response is degraded when compared to PD A. In general increasing the bias reduces space charge saturation and enhances both the RF response and the OIP3 [4], [11]. For PD B a higher bias may therefore be required at low photocurrent levels in order to deplete the field layer and achieve higher OIP3.

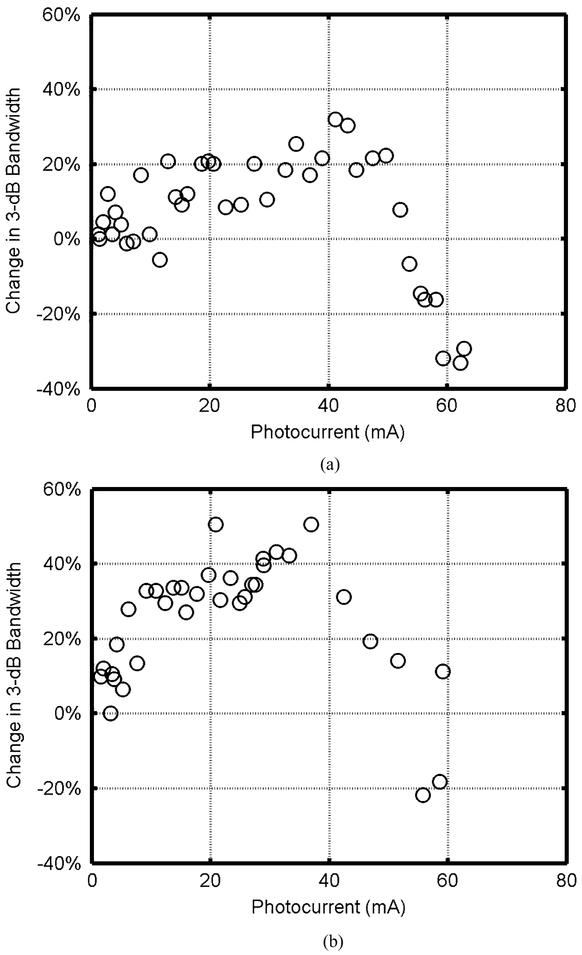

(a)

(b)

Fig. 6. Change in 3-dB bandwidth as a function of dc photocurrent for (a) PD A and for (b) PD B. The bias is −3.5 V for both devices.

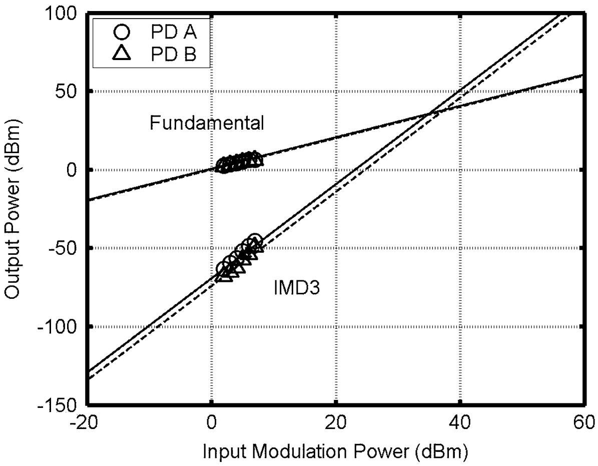

Fig. 7. IMD3 measurements at 30 mA for PD A and for PD B. The bias is −5 V for both devices.

The OIP3 was also measured for other frequency tones at a fixed photocurrent level of around 40 mA. Fig. 9 shows the OIP3 as a function of the higher frequency tone (f_2). For PD A, the OIP3 is fairly constant and begins to degrade slightly as f_2 approaches 1.0 GHz. For PD B, the OIP3 degrades with f_2

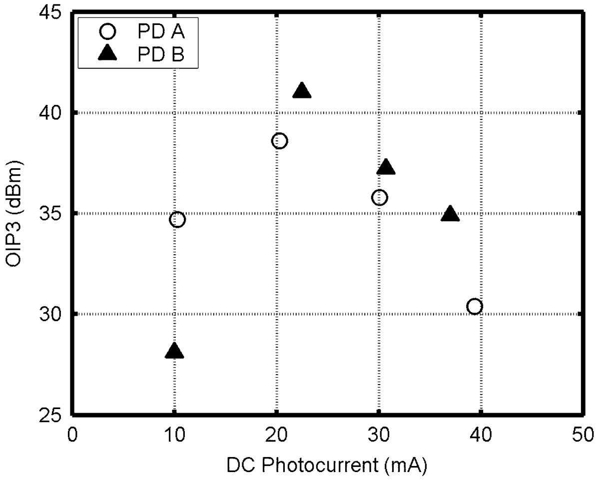

Fig. 8. OIP3 as a function of dc photocurrent for PD A and PD B. The bias is -5 V for all measurements.

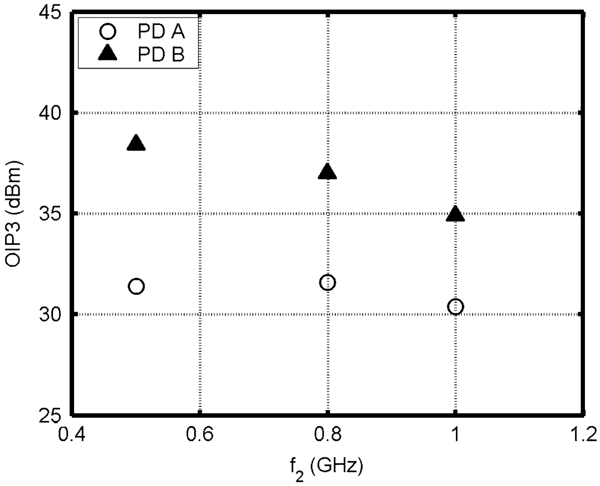

Fig. 9. OIP3 as a function of the higher frequency tone (f_2) for PD A and PD B. The photocurrent level is 40 mA and the bias is -5 V for all measurements.

however the OIP3 of PD B is higher than that of PD A at all of the measured values of f_2.

It appears that because of its enhanced response, PD B exhibits a higher OIP3 at high photocurrent levels. Overall PD B seems to perform better, however the design of the PD structure, namely the doping profiles in the absorber and collector layers, can be tailored for a specific region of operation. Recall that for the same bias, PD A exhibits a higher OIP3 at a photocurrent level of 10 mA. To reach the same OIP3 at this photocurrent level, PD B requires a higher bias. If heat dissipation is considered, PD A is favorable for operation at low photocurrent levels. However at all measured photocurrent levels above 10-mA PD B exhibits a higher OIP3 for the same bias, therefore PD B is favorable for high current operation.

IV. CONCLUSION

We have fabricated and tested UTC-PDs with different absorber and collector layer doping profiles. An enhancement in the response is observed for PD B, which has a lower and more graded absorber doping as well as a higher collector doping. These result in a higher induced field in the absorber layer and charge compensation respectively. Saturation currents of 65 mA for PD A and 63 mA for PD B are demonstrated. To the best of our knowledge these represent some of the highest saturation currents reported for waveguide PDs. IMD3 measurements were also performed to investigate the effects of the response enhancement of PD B on linearity. The OIP3 at a photocurrent level of 10 mA is 34.7 dBm for PD A and 28.1 dBm for PD B. However at higher photocurrent levels, the OIP3 for PD B is higher than that for PD A. At 40 mA for example, the OIP3 of PD B is 34.9 dBm whereas for PD A it is 30.4 dBm. PD B is therefore preferable for high current operation.

REFERENCES

[1] H.-F. Chou, A. Ramaswamy, D. Zibar, L. A. Johansson, J. E. Bowers, M. Rodwell, and L. Coldren, “SFDR improvement of a coherent receiver using feedback,” presented at the Coherent Optical Technol. Appl. Conf., 2006, Paper CFA3.

[2] A. Ramaswamy, L. A. Johansson, J. Klamkin, C. Sheldon, H.-F. Chou, M. J. Rodwell, L. A. Coldren, and J. E. Bowers, “Coherent receiver based on a broadband optical phase-lock loop,” presented at the OFC Postdeadline Papers, 2007, Paper PDP3.

[3] T. Ishibashi, T. Furuta, H. Fushimi, S. Kodama, H. Ito, T. Nagatsuma, N. Shimizu, and Y. Miyamoto, “InP/InGaAs uni-traveling-carrier photodiodes,” *IEICE Trans. Electron.*, vol. E83-C, no. 6, pp. 938–949, Jun. 2000.

[4] J. Klamkin, A. Ramaswamy, H.-F. Chou, M. N. Sysak, J. W. Raring, N. Parthasarathy, S. P. DenBaars, J. E. Bowers, and L. A. Coldren, “Monolithically integrated balanced uni-traveling-carrier photodiode with tunable MMI coupler for microwave photonic circuits,” in *Proc. Conf. Optoelectron. Microelectron. Materials Devices*, 2006, pp. 184–187.

[5] N. Li, X. Li, S. Demiguel, X. Zheng, J. C. Campbell, D. A. Tulchinsky, K. J. Williams, T. D. Isshiki, G. S. Kinsey, and R. Sudharsansan, “High-saturation-current charge-compensated InGaAs-InP uni-traveling-carrier photodiode,” *IEEE Photon. Technol. Lett.*, vol. 16, no. 3, pp. 864–866, Mar. 2004.

[6] N. Shimizu, N. Watanabe, T. Furuta, and T. Ishibashi, “InP-InGaAs uni-traveling-carrier photodiode with improved 3-db bandwidth of over 150 GHz,” *IEEE Photon. Technol. Lett.*, vol. 10, no. 3, pp. 412–414, Mar. 1998.

[7] N. Shimizu, N. Wantanabe, T. Furuta, and T. Ishibashi, “Improved response of uni-traveling-carrier photodiodes by carrier injection,” *Jpn. J. Appl. Phys.*, vol. 37, pp. 1424–1426, 1998.

[8] J. Klamkin, A. Ramaswamy, L. A. Johansson, H.-F. Chou, M. N. Sysak, J. W. Raring, N. Parthasarathy, S. P. DenBaars, J. E. Bowers, and L. A. Coldren, “High output saturation and high-linearity uni-traveling-carrier waveguide photodiodes,” *IEEE Photon. Technol. Lett.*, vol. 19, no. 3, pp. 149–151, Feb. 2007.

[9] H. Jiang, D. S. Shin, G. L. Li, T. A. Vang, D. C. Scott, and P. K. L. Yu, “The frequency behavior of the third-order-intercept point in a waveguide photodiode,” *IEEE Photon. Technol. Lett.*, vol. 12, no. 5, pp. 540–542, May 2000.

[10] T. Ohno, H. Fukano, Y. M. T. Ishibashi, T. Yoshimatsu, and Y. Doi, “Measurement of intermodulation distortion in a unitraveling-carrier refracting-facet photodiode and a p-i-n refracting-facet photodiode,” *IEEE Photon. Technol. Lett.*, vol. 14, no. 3, pp. 375–377, Mar. 2002.

[11] K. J. Williams and R. D. Esman, “Design considerations for high-current photodetectors,” *J. Lightw. Technol.*, vol. 17, no. 8, pp. 1443–1454, Aug. 1999.

Jonathan Klamkin (S'04) received the B.S. degree in electrical and computer engineering from Cornell University, Ithaca, NY, in 2002, and the M.S. degree in electrical and computer engineering from the University of California, Santa Barbara (UCSB) in 2004, where he is currently working toward the Ph.D. degree in materials.

His research interests include the design, epitaxial growth, fabrication, and characterization of widely-tunable semiconductor lasers, photodetectors, optical intensity and phase modulators, compact couplers, and semiconductor optical amplifiers for InP-based photonic integrated circuits. Currently his efforts are focused on novel coherent integrated receivers for highly linear microwave photonic links.

Yu-Chia Chang received the B.S. degree in electrical engineering and the M.S. degree in electrooptical engineering from National Taiwan University, Taipei, Taiwan, R.O.C., in 1997 and 1999, respectively. He is currently working toward the Ph.D. degree in electrical and computer engineering, University of California, Santa Barbara (UCSB).

He worked for BenQ Inc., Taiwan, R.O.C., in 1999–2001 and National Taiwan University in 2001–2002. His current research interests are the design, growth, and characterization of high-efficiency high-speed vertical-cavity surface-emitting lasers for optical interconnect applications.

Anand Ramaswamy (S'06) received the B.S. degree in electrical engineering with a minor in physics from the University of Southern California, Los Angeles, 2005 and the M.S. degree in electrical engineering from the University of California, Santa Barbara, in 2007, respectively, where he is currently working towards the Ph.D. degree under Professor John E. Bowers.

His research interests lie in coherent communication systems and non-linear mechanisms in high power photodetectors.

Leif. A Johansson received the Ph.D. degree in engineering from University College London, U.K., in 2002.

He took up a postdoctoral position at the University of California at Santa Barbara in 2002. His current research interests include design and characterization of integrated photonic devices for analog and digital applications.

John E. Bowers (F'93) received the M.S. and Ph.D. degrees from Stanford University, Stanford, CA.

He is a Professor in the Department of Electrical Engineering, and in the Technology Management Program at the University of California, Santa Barbara. He is also CTO and cofounder of Calient Networks. His research interests are primarily concerned with silicon photonics, optoelectronic devices, optical switching and transparent optical networks. He is cofounder of the Center for Entrepreneurship and Engineering Management, and founder of Terabit Technology. He worked for AT&T Bell Laboratories and Honeywell before joining UCSB. He has published eight book chapters, 400 journal papers, 600 conference papers and has received 49 patents.

Dr. Bowers is a Fellow of OSA and the American Physical Society, and a recipient of the IEEE LEOS William Streifer Award and the South Coast Business and Technology Entrepreneur of the Year Award. He was an elected member of the IEEE LEOS Board of Governors, a LEOS Distinguished Lecturer, and Vice President for Conferences for LEOS. He is a member of the National Academy of Engineering. He received the ACE Award for Most Promising Technology for the hybrid silicon laser in 2007.

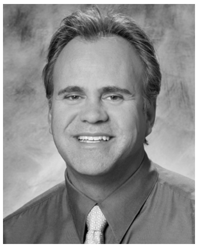

Steven P. DenBaars (F'05) is a Professor of materials and electrical and computer engineering, and the Co-Director of the Solid State Lighting and Display Center, at the University of California, Santa Barbara.

His research areas are in MOCVD growth of widebandgap semiconductors (GaN-based) and their application to blue LEDs and laser and high-power electronic devices.

Dr. DenBaars is the recipient of the Mitsubishi Chemical Endowed Chair in Solid State Lighting and Display.

Larry A. Coldren (F'82) received the Ph.D. degree in electrical engineering from Stanford University, Stanford, CA, in 1972.

He is the Fred Kavli Professor of Optoelectronics and Sensors at the University of California, Santa Barbara. After 13 years in the research area at Bell Laboratories, he joined UC-Santa Barbara in 1984 where he now holds appointments in materials and electrical and computer engineering, and is Director of the Optoelectronics Technology Center. In 1990, he co-founded Optical Concepts, later acquired as Gore Photonics, to develop novel VCSEL technology; and in 1998 he co-founded Agility Communications, recently acquired by JDSU, to develop widely-tunable integrated transmitters. He has authored or co-authored over 800 papers, five book chapters, one textbook, and has been issued 61 patents. He has presented dozens of invited and plenary talks at major conferences.

Prof. Coldren is a Fellow of OSA, and IEE, U.K., the recipient of the 2004 John Tyndall Award, and a member of the National Academy of Engineering.

Improving the Performance of Sampled-Grating DBR Laser-Based Analog Optical Transmitters

Leif A. Johansson, *Member, IEEE*, Yuliya A. Akulova, Chris Coldren, and
Larry A. Coldren, *Fellow, IEEE, Fellow, OSA*

***Abstract*—In this paper, the available analog link performance of integrated transmitters containing a sampled-grating distributed Bragg reflector laser, a semiconductor optical amplifier, and a modulator is evaluated. It is found that to provide a link gain and a low-noise figure, an RF preamplifier is required, and for this reason, spurious-free dynamic range (SFDR) including a preamplifier has been evaluated. An SFDR of 110-dBHz$^{2/3}$, a noise figure of 5.4 dB, and link gain of 6.9 dB at 5 GHz is obtained. It is further investigated how link SFDR can be improved by linearization techniques. Two novel approaches are proposed and demonstrated: first, predistortion by extraction of nonlinear components from an integrated second modulator exposed to the same wavelength, optical power and temperature for matched nonlinear terms; second, a novel linearized modulator configuration balancing electroabsorption and Mach–Zehnder modulation that can reach a null for both second- and third-order intermodulation products at a single bias point.**

***Index Terms*—Distributed Bragg grating lasers, electroabsorption, integrated optoelectronics, microwave photonics, optical communications, photonic integrated circuits.**

I. INTRODUCTION

INDIUM Phosphide (InP) integrated photonic circuits is an attractive technology for application in analog optical link applications. High-performance optical sources, modulators, and detectors are required to provide the necessarily high signal-to-noise ratio (SNR) needed for high dynamic range. The InP material system is sufficiently mature to offer these components while being compatible to low-cost production. Further, it is compatible with chipscale photonic integration of several components to form high functionality, compact transmitters, reducing overall component cost, and improving performance by cutting coupling losses between subcomponents. It has been shown how sampled-grating distributed Bragg reflector (SGDBR) lasers integrated with a semiconductor optical amplifier (SOA) and an electroabsorption modulator (EAM) forms a very attractive widely tunable optical transmitter for digital [1] and analog [2] optical link applications.

This paper builds on these previous results and summarizes recent efforts to improve the performance for analog link applications, in particular, efforts to improve link gain, noise, figure and dynamic range when applied in an analog optical link. Link gain in this paper is referred to link *power gain,* defined as the ratio of the detected RF power at the output of the link, to the link input RF power. Link noise figure is defined as the ratio of link output SNR to the input SNR, given thermal noise limit at the link input, the exact expression is $NF \equiv 10\log[N_{\rm OUT}/kTG]$, where $N_{\rm OUT}$ is output noise power, kT is input thermal noise power, and G is link power gain [3]. Spurious-free dynamic range (SFDR) here applies to the maximum achievable SNR in the optical link using a two-tone signal probe, with the restriction that the detected in-band intermodulation products remain lower or equal to the noise floor in a chosen noise bandwidth (typically normalized to 1-Hz noise bandwidth).

The paper is organized as follows. In Section II, a brief summary of baseline analog performance of SGDBR-based transmitters is given, with a particular emphasis on observed limitations to the performance, as it forms the base of the further efforts presented within this paper. This data has previously been published [2] and is here summarized as reference. Section III covers efforts to improve the noise performance of these transmitters. An improvement in link noise figure is observed by using a preamplifier. The performance at higher RF frequencies is also improved by employing optimized transmitter biasing schemes. The next two chapters are devoted to novel schemes to linearize the response of the modulator. A compensatory predistortion scheme is described in Section IV and a linearization technique employing a weak Mach–Zehnder (MZ) effect is described in Section V. The last section gives a summary of this work.

II. BASELINE PERFORMANCE

The reference device is described in detail in [1]. It consists of a SGDBR laser, an SOA, and an EAM, all integrated on the same InP chip using an offset quantum well structure to define active regions such as the laser gain section and SOA. The SG-DBR laser includes gain and phase sections positioned between two sampled grating distributed reflectors, sampled at different periods such that only one of their multiple reflection peaks can coincide at a time [4]. The overall wavelength coverage can be greater than 45 nm. The integrated SOA compensates for on-state modulator loss, and for cavity losses caused by free carrier absorption in the tuning sections, and allows wavelength independent power leveling. The EAM uses the same bulk quaternary waveguide as the tuning sections of the laser. The Franz–Keldysh effect in the bulk waveguide material provides for large spectral bandwidth and improved optical power handling capability.

The noise performance of the transmitter was limited by relative intensity noise at the RIN peak, improving with gain section injection current to at best -153 dB/Hz at 200-mA bias and room temperature. The added SOA noise could be observed in

---

Manuscript received November 20, 2006; revised July 20, 2007. This work was supported by the DARPA/MTO CS-WDM program.

L. A. Johansson and L. A. Coldren are with the Department of Electrical and Computer Engineering, University of California, Santa Barbara, CA 93106 USA (e-mail: leif@ece.ucsb.edu; coldren@ece.ucsb.edu).

Y. A. Akulova and C. Coldren are with the JDS Uniphase Corporation, Goleta, CA 93117 USA (e-mail: yuliya.akulova@jdsu.com; chris.coldren@jdsu.com).

Digital Object Identifier 10.1109/JLT.2007.916592

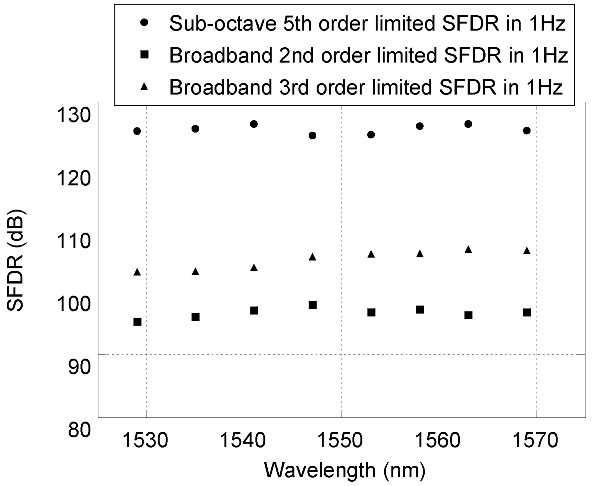

Fig. 1. Summary of measured EA SFDR when biased for broadband linear operation (minimum second-order intermodulation products) and biased for sub-octave linear operation (minimum third-order intermodulation products), normalized to 1-Hz noise bandwidth.

the noise floor away from the RIN peak, typically below 2 GHz or at high frequencies.

A link gain of −20.7 dB was obtained when using the transmitter in an analog link. The gain can be increased by terminating the detector with a higher load [3]. However, since the link noise figure is not loss limited, but primarily limited by the relative intensity noise of the laser, this will not improve the noise figure of the link. In fact, the lowest noise figure of 32 dB was obtained in "low biased" condition, with lower link gain, but where the relative modulator slope sensitivity is greater. The potential for generating positive link gain was found to be severely limited by absorbed photocurrent in the modulator. In fact, the EA slope efficiency will asymptotically approach the limit given by one absorbed electron per photon, much like 100% quantum efficiency in a laser or a photodiode. This will make it challenging to reach positive loop gain (and low noise figure) when optical losses are present.

Like most optical modulators, the EAM has an inherently nonlinear response. Optimized linearity can be obtained by careful selection of the EA bias point, though. For broadband, second-order intermodulation limited operation, the optimum bias point is found around the highest absolute slope. The spurious-free dynamic range (SFDR, a common measure of analog link performance [3]) at 1552 nm was here 97 dB $\cdot$ Hz$^{1/2}$ second-order limited or 106 dB $\cdot$ Hz$^{2/3}$ third-order limited. A summary of the measured SFDR is found in Fig. 1. For sub-octave applications, where even-order intermodulation products can be filtered, the EA exhibits an optimum bias point where third-order intermodulation products in general can be cancelled out. The dynamic range is 126 dB $\cdot$ Hz$^{4/5}$, fifth-order limited, at this bias point and 1552 nm. It should be pointed out that the rapid growth of higher order intermodulation products with drive power still limits the available linear modulation depth, even at this bias point. Further, the SFDR was measured at 0.5 GHz, well below the RIN peak. With unoptimized laser bias, the SFDR can be degraded up to 10 dB at the peak RIN frequency.

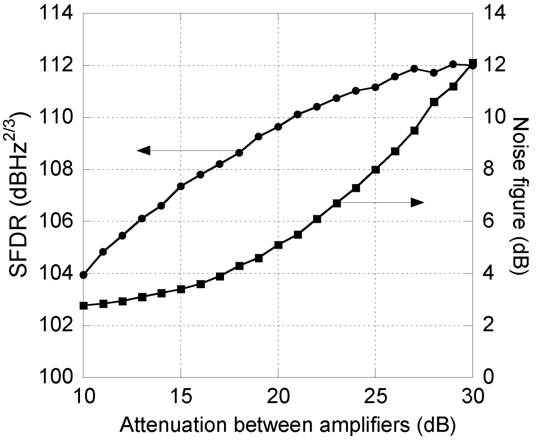

Fig. 2. Spurious-free dynamic range and link noise figure as a function of preamplification gain at 500-MHz modulation frequency.

III. PREAMPLIFIED LINK PERFORMANCE

Obtaining a low noise figure in a simple optical link using this type of transmitter is currently not possible. Therefore, in most high-performance analog applications, the transmitter will be preceded by an electronic amplified to improve link gain and noise figure, and the transmitter performance in the presence of this amplifier must be considered.

As is well known, adding an amplifier in a microwave transmission system will in most cases degrade the dynamic range in the system [5]. This is also true here. Care must be taken in selecting preamplifiers such that the benefits in improved link gain and noise figure does not come at the cost of a greatly reduced dynamic range. This can be understood from the background of achieving a low noise figure. As the gain of the preamplifier is increased to reduce noise figure, the amplifier noise gradually starts to dominate the output noise floor with a resulting degradation in dynamic range. This is illustrated by the experimental data shown in Fig. 2. To obtain this data, two amplifiers were cascaded at the input of the transmitter. Both amplifiers have a gain of 29 dB, a noise figure of 2.4 dB and output IP3 of +43.5 dBm at 500 MHz. A 6-dB attenuator had to be placed between the last stage amplifier and the modulator in order to reduce RF reflections due to imperfect modulator matching. The overall preamplifier gain was then regulated by placing an adjustable RF attenuator between the two amplifiers. It can be observed that at high attenuation, the detected noise floor is predominantly RIN limited and the SFDR approaches the limit given by the combined nonlinearities of amplifiers and modulator, here at around 112 dB $\cdot$ Hz$^{2/3}$. As the preamplification gain is increased, the noise figure asymptotically approaches that of the first amplifier with an increasingly steep dynamic range penalty as the amplifier noise starts to dominate. In the following, an overall noise figure lower that 6 dB is targeted, to limit the dynamic range penalty.

In Fig. 2, the SFDR is third-order intermodulation limited, even in the sub-octave case. Without preamplification, the EAM can be biased such that third-order intermodulation products are cancelled out over a realistic bandwidth, given that some care is taken to produce an input two-tone probe signal free from distortion. In the preamplified case, the effect of cascaded nonlinearities and their cross-terms leads to a strong frequency

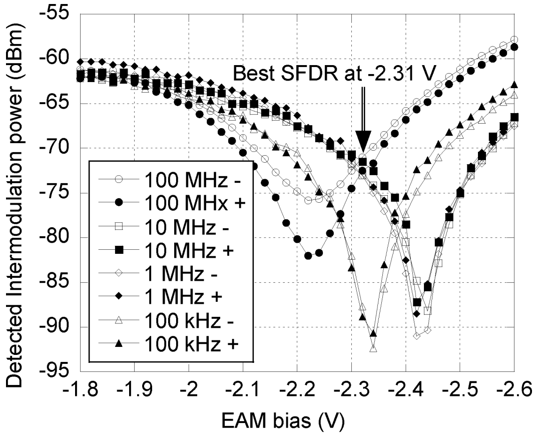

Fig. 3. Power of the third EAM order intermodulation products as a function of modulator bias for different RF frequency offset of a two-tone probe signal centered around 500 MHz.

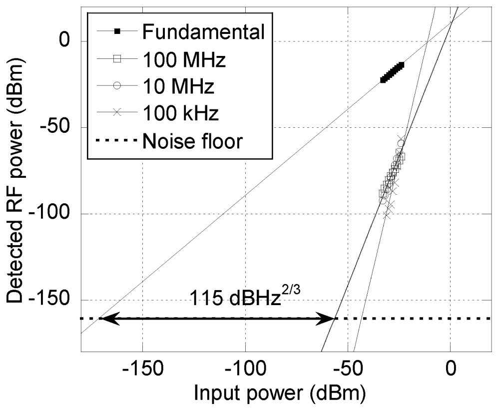

Fig. 4. Measured power of fundamental and third-order intermodulation terms and the corresponding SFDR around 500 MHz and for different separation between RF tones.

dependence on the bias point of minimum third-order distortion. Additional possible contributors to the wandering third-order minimum include internal effects in the optical transmitter, as frequency dependence at the difference frequency f1 − f2, including thermal effects at small frequency separations. This is all illustrated by the results in Fig. 3, where the power of the third-order intermodulation products is recorded as a function of two-tone RF frequency offset from 500 MHz. We can observe that the minimum varies over a 0.2-V range. The sharp dips where fifth-order limited performance is obtained cannot be maintained over a realistic RF bandwidth, and the overall performance of the preamplified transmitter will effectively be best characterized by an SFDR with a third-order intermodulation limitation.

The resulting SFDR when biased at -2.31 V is shown in Fig. 4, where intermodulation terms are taken at a range of separation frequencies of a two-tone probe signal around 500 MHz. The resulting SFDR is 115 dB $\cdot$ Hz$^{2/3}$. To obtain this value, both gain section and SOA were biased at 200 mA at 18 °C at a wavelength of 1547 nm. The preamplifier gain was adjusted to balance the SFDR penalty and noise figure such that the overall link gain was $+10.5$ dB with a link noise figure of 5 dB for this result.

These results have all been taken at the moderate frequency of 500 MHz. At higher frequencies, above 2 GHz, the increased RIN has been shown to degrade the dynamic range of these transmitters [2]. To provide high performance over a wider frequency range, 5-GHz operation frequency is here targeted, the laser must be more aggressively biased. In accordance with previous observations [2], [6], the RIN peak is shifted to higher frequencies and increased damping of the RIN resonance is observed with increasing laser injection current. At room temperature and 200-mA injection current, the RIN was here measured at -154 dB/Hz at 5 GHz, as shown in Fig. 5. The measured low frequency noise can be controlled by using more quiet current drivers and improved decoupling to the tuning sections of the SGDBR laser. Increasing the injection current to 300 mA reduced the RIN level to -158 dB/Hz. Lowering the temperature from room temperature to 0 °C produced a similar improvement at 5 GHz from increased injection efficiency. Combining reduced temperature with higher injection current finally pushed the RIN down to -160 dB/Hz, sufficient to produce a respectable dynamic range even at this frequency.

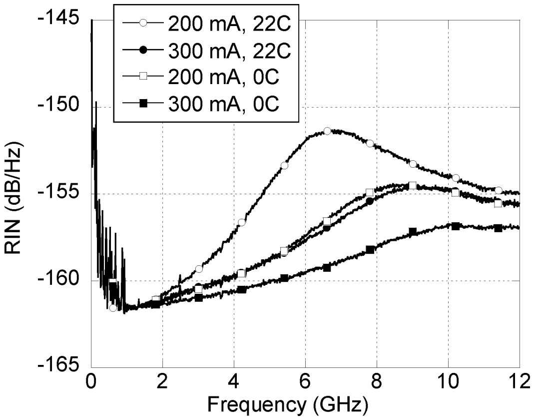

Fig. 5. Measured RIN at 200 and 300 mA and at 20 °C and 0 °C.

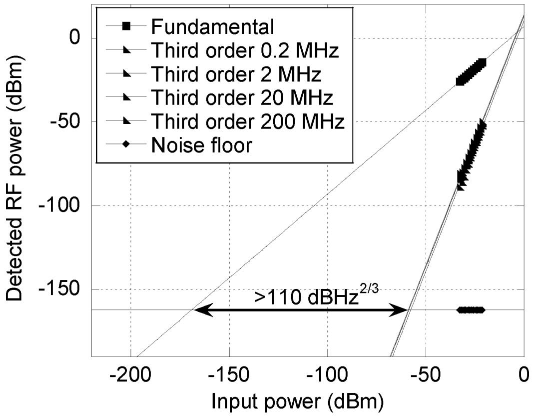

Fig. 6. Measured power of fundamental and third-order intermodulation terms and the corresponding SFDR around 5 GHz and for different separation between RF tones.

A similar arrangement was built to produce a preamplified transmitter at 5 GHz as is used for the 500-MHz results presented above. A dual amplifier configuration with adjustable overall gain is used. The first amplifier has a noise figure of 2 dB and an IP3 of 30 dBm, and the second amplifier has a noise figure of 5 dB and an IP3 of 38 dBm. Again, a small attenuator (3 dB) was placed in-between the last stage amplifier and the modulator to control reflections. Fig. 6 shows the power of

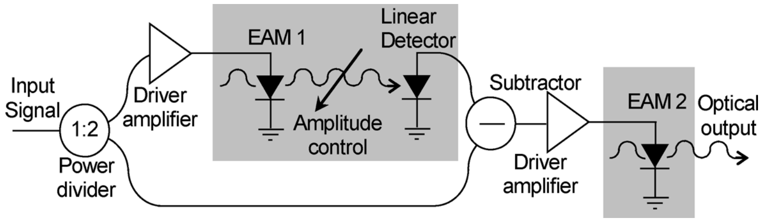

Fig. 7. Operational schematic of broadband linearization scheme. Shaded areas are integrated on the single InP chip shown in Fig. 8.

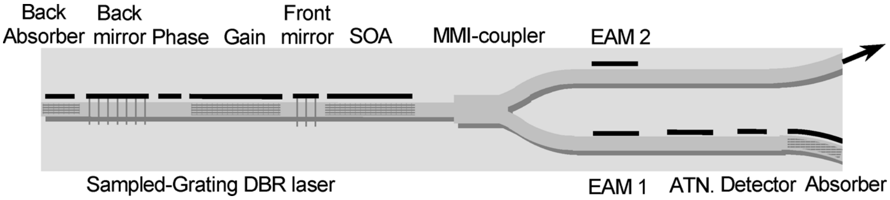

Fig. 8. Schematic of integrated photonic circuit.

the fundamentals and intermodulation terms at a range of separations of the two-tone probe. The preamplification gain was adjusted to produce a link noise figure of 5.4 dB and a link gain of 6.9 dB, resulting in an SFDR of 110 dB $\cdot$ Hz$^{2/3}$, limited by the nonlinearities of amplifiers and the modulator.

IV. COMPENSATORY PREDISTORTION

In the previous section, it was showed how the link gain and NF could be improved by adding preamplification. The high-performance frequency range was also extended by optimizing the drive conditions of the laser. However, no significant improvement in the dynamic range was generated in comparison to previous work [2].

Several linearization schemes can be considered to improve the linearity of these optical transmitters, not all are suitable for the particular requirements of a widely tunable transmitter that need to be compatible to a WDM environment. Perhaps the commercially most successful is using predistortion where improvements in performance can be achieved using an inexpensive and power efficient electronic circuit [7]. This approach can typically not adapt to changing operating conditions and requires that the response of the transmitter stays constant. It is, therefore, not suitable for integration with a widely tunable transmitter and a modulator that has wavelength-dependent response. An alternative is using feed-forward linearization where the modulated signal is tapped off and compared to the input to form a correcting signal to be added to the output [8]. In this way, any variations of the response are automatically corrected. However, the added signal must be separated in wavelength to avoid coherence effects, and is, therefore, not compatible to a WDM environment.

In the investigated approach, a predistortion circuit is constructed by measuring the nonlinearities of a first optical modulator to provide the predistorted input to a second modulator. This approach combines dynamic extraction of nonlinear response and WDM compatibility. Past demonstrations of this approach has typically been limited by the need to use two separate transmitters with slightly different response [9]. Here, the two modulators are integrated closely on a single chip, sharing a single optical source. Any variations in chip temperature, input power or wavelength now affect both modulators equally and can be dynamically compensated for.

Fig. 7 shows a schematic of the demonstrated predistortion arrangement. The input signal is split in a 2:1 ratio, where the lesser part is used to drive the predistortion link. The output of the link is then subtracted from the remainder of the input signal to form the predistorted input to the second transmitter. A driver amplifier and an optical attenuator are included in the link to ensure that the input power to the two transmitters stays equal for optimum distortion cancellation. In this demonstration, two discrete connectorized driver amplifiers are used. However, to fully take advantage of the linearization scheme, more integrated driver amplifiers should be used, preferably using two similar amplifiers sharing a common heat-sink.

Fig. 8 shows a schematic of the fabricated integrated photonic circuit. It is similar to the base device used previously with the difference that the power from the source is split into two EA modulators located in close proximity on the chip. The optical 3-dB bandwidth of this modulator is 8 GHz. A second reversed biased passive section acts as an optical attenuator and the detector then completes the on-chip optical link in one of the two waveguide paths. The second waveguide forms the optical output.

The SFDR of EAM2 in Fig. 8 without activating the predistortion path or using a driver amplifier is measured at 98 dBHz$^{2/3}$, when biased at maximum slope. This is about 7 dB lower than devices incorporating a single EA modulator [2], which can be attributed to the lower transmitted power of this particular prototype device. Connecting a driver amplifier to EAM2 with low power consumption ($\sim$ 800 mW) and low third-order intercept point (+15 dBm), the overall link gain is improved at the expense of a penalty in SFDR, now 93 dBHz$^{2/3}$. The left plot of Fig. 9 shows the captured RF spectrum around 500 MHz, where third-order intermodulation terms can be clearly observed.

Activating the on-chip predistortion link to compensate for nonlinearities, the third-order intermodulation terms can be reduced. The right plot of Fig. 9 shows the captured spectrum

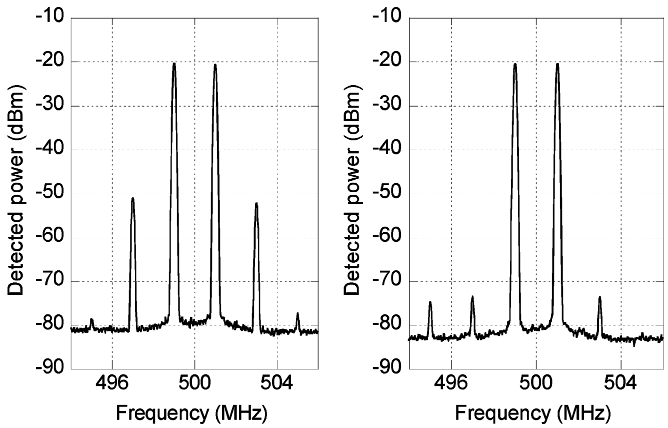

Fig. 9. RF spectra around 500 MHz for transmitter with and without predistortion.

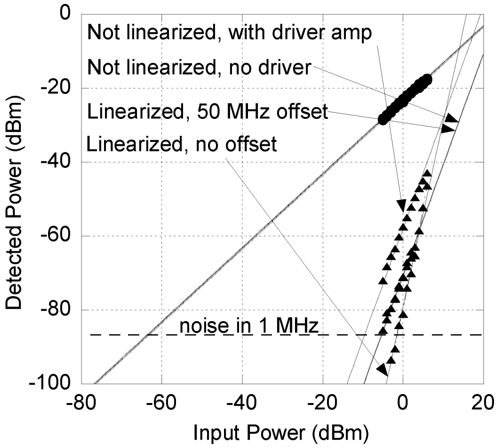

Fig. 10. SFDR of the predistorted transmitter with and without 50-MHz frequency offset from setting, and not predistorted with and without driver. The input power has been adjusted to facilitate comparison. The curves "Not linearized, no driver" and "Linearized, 50 MHz offset" overlap on this scale.

where the amplitude and phase response of the predistortion circuit has been matched. More than 20-dB suppression of third-order intermodulation terms is observed. This corresponds to a closely matched phase and amplitude in the summation of signal and predistortion link output. To generate 20 dB of intermodulation suppression, the power must be matched within 0.3 dB. A small penalty in higher order intermodulation terms is observed. This is a common effect in many linearization schemes and must be controlled so that it does not lead to a penalty. The measured SFDR at 500 MHz is compared to the uncompensated case in Fig. 10 where a fifth-order intermodulation-limited SFDR of 110 dBHz$^{4/5}$ is obtained, more than compensating for the nonlinearities of the driver amplifier.

Like any linearization scheme that relies on gain matching, the effective bandwidth of the linearization is limited due to variations in frequency response. To investigate the effective bandwidth, the center frequency was shifted while keeping all adjustments in the predistortion part constant. The results are shown in Fig. 11, where the dynamic range is plotted as a function of frequency offset. A noise bandwidth of 1 MHz was chosen to take into account the varying slope of the intermodulation terms with modulation power. It is observed that a 10-MHz frequency offset corresponds to only a 2-dB penalty in SFDR, while the added distortion of the driver amplifier is compensated for within a 50-MHz single-sided bandwidth. This fractional bandwidth can be improved by using more uniform response RF components or an equalizing circuit [10].

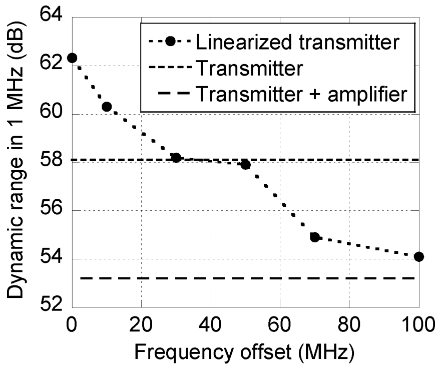

Fig. 11. Measured dynamic range in 1 MHz of the linearized transmitter as a function of shift in operating frequency.

Even at zero frequency offset, the performance of the linearized transmitter does not reach the 115 dBHz$^{2/3}$ measured in Fig. 4, using a single preamplified EAM. This is because of lower baseline performance of the optical and electrical devices, not an inherent limitation of the linearization technique. The 9-dB improvement in SFDR in 1-MHz bandwidth still represents a realistic number for the SFDR improvement practically achievable using careful amplitude and phase matching in this linearization scheme.

This linearization scheme has been shown to provide a limited amount of improvement in linearity in a compensatory manner. It is compatible with a widely tunable laser in that the generated predistorted signal is compensating for any wavelength dependence in the EA response. It has also been shown capable of compensating for amplifier nonlinearities, an important capability for application in realistic link applications, where the response of the amplifier also needs to be considered when low link noise figure is required. Here, this was limited by the use of discrete amplifier modules where the nonlinear terms not necessarily match. Ideally more closely integrated driver amplifiers with closely matched response should be used. One option is then to trade off the amplifier performance to reduce the power consumption of the transmitter, and compensating the loss of linearity. A highly linear amplifier can easily dominate the power budget of an analog transmitter. For automatic linearization over the entire tuning range, automatic predistortion gain control will need to be implemented to compensate for the variations in EA slope sensitivity with wavelength.

V. LINEARIZED MODULATOR

The compensatory predistortion presented above is well suited to reach a high level of linearization over a narrow band or a moderate level of linearization over moderate band. The problem with this approach is gain imbalance due to very slight variations in the frequency response of the modulators. The cancellation then only takes place within this limited frequency

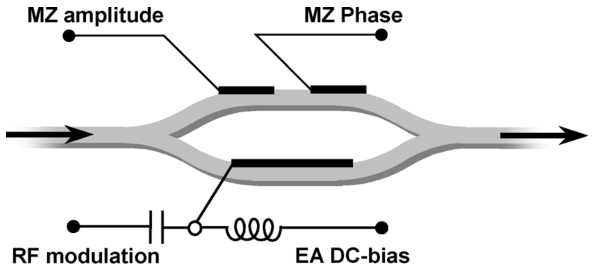

Fig. 12. Simple schematic of proposed modulator.

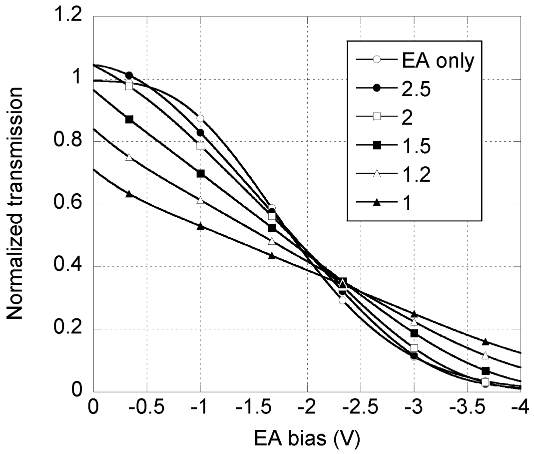

Fig. 13. Simulated linearized DC extinction curves for different ratios of equivalent EAM $V\pi$ to MZ $V\pi$.

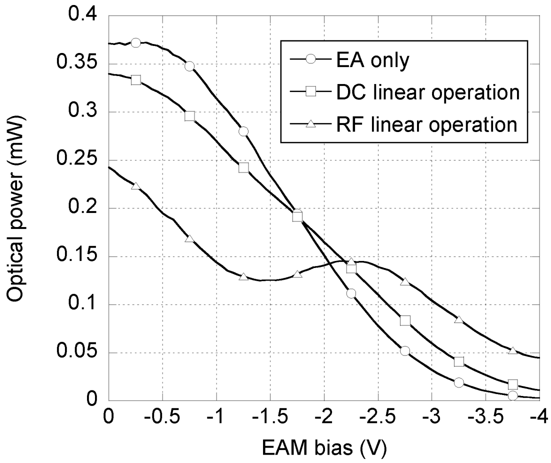

Fig. 14. Measured modulator DC extinction curves using the EAM only, and for the bias points (MZ phase + MZ balance) for a linearized DC transfer function and the transfer function where linearized RF modulation is observed.

range. We here propose and demonstrate a modulator structure that uses a single electrode to produce two modulation effects, which are then adjusted to produce an overall linearized response. Since only one electrode is being modulated, a linearized response over a wide frequency range can be expected.

The linearized modulator is based on a standard EAM. The EAM is inserted in a MZ configuration, where the other arm of the MZ is not being modulated. This produces a composite response which is given by the combination between electroabsorption and interference within the MZ modulator structure given by the electrorefraction in the modulator. Fig. 12 shows a simple schematic of the proposed modulator. The electroabsorption is modeled after the response of a Franz–Keldysh modulator, where both phase and amplitude is modulated. The total response of the modulator is then a combination of EA and MZ modulation. The EA modulator is biased at maximum slope sensitivity with minimum second-order intermodulation products. The phase control of the MZ is regulated to the corresponding operating point, with minimized second-order intermodulation but at opposite slope. A linearized response is then generated by regulating the amplitude balance between the two arms, such that third-order intermodulation products of the EA and MZ are cancelled out.

Fig. 13 shows a sample of simulated linearized responses for different ratio between the equivalent $V\pi$ of the EAM and MZ $V\pi$. For a high ratio, the power of third-order intermodulation products generated by the MZ is large relative to those produced by the EAM. In this case, a highly unbalanced MZ is required for third-order intermodulation cancellation. As the $V\pi$ ratio decreases, the voltage range where a constant slope is obtained increases as the cancellation of higher order intermodulation terms also improves. Reducing the $V\pi$ ratio even more, a penalty in overall slope sensitivity appears, as the absolute slope of the MZ becomes comparable to that of the EAM. A $V\pi$ ratio of 2 represents a good operating point with low penalty in slope sensitivity, and still a wide voltage range with constant slope.

Further, in addition to simultaneous cancellation of second and third-order intermodulation, the model shows that careful adjustment of the three DC controls would allow additional cancellation of fourth-order intermodulation products. In practice below, this operating point was never reached.

The device used to experimentally verify the proposed linearized modulator configuration is similar to that described in [11]. It consists of a widely tunable sampled grating DBR laser, a semiconductor amplifier (SOA) and a MZ modulator, all integrated on the same InP chip. The modulator consists of multimode interference (MMI) sections and 600-μm-long lumped electrodes. The laser-modulator uses a common waveguide structure, where passive sections, such as used in the MZ modulator, is defined by selective removal of an offset active quantum-well material. The bulk material of the electrodes of the MZ exhibit both electrorefraction and electroabsorption at reverse applied bias. This makes the MZ a suitable candidate for demonstration of the above linearization scheme, which requires both effects. MZ amplitude control is then achieved when reverse bias is applied to the second MZ electrode, absorbing part of the light. Amplitude independent phase control is obtained in a separate phase control section, using carrier injection phase tuning.

Fig. 14 shows the DC extinction at 1542-nm wavelength. The extinction of EA only is obtained when the second electrode of the MZ is deeply reverse biased (< -6 V) for full absorption. With the correct balance between EA and MZ effects, an overall linearized response at DC is obtained, shown in Fig. 14. This operating point is not the same as for linear operation at RF modulation. The response at DC is affected by slow thermal effects that do not affect the response at RF mod-

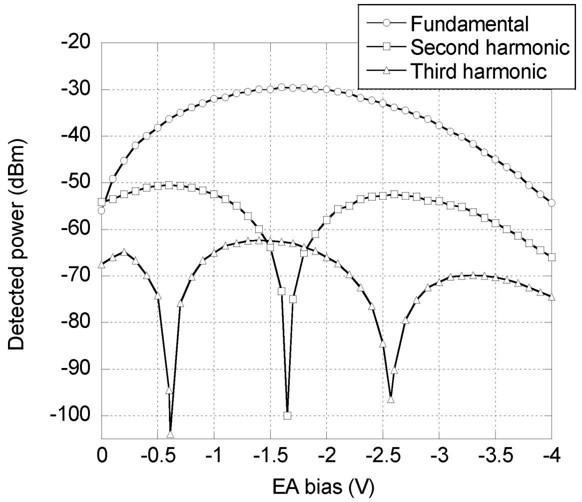

Fig. 15. Detected power of fundamental and intermodulation products using EA modulation only for 4-dBm modulation power per tone and at 1542 nm.

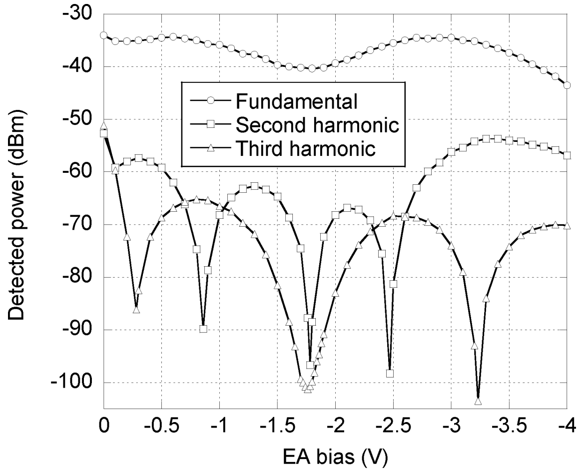

Fig. 16. Detected power of fundamental and intermodulation products using the linearized modulator for 4-dBm modulation power per tone and at 1542 nm.

ulation around a constant DC bias point. The DC response obtained at the linear bias point for RF, shown in Fig. 14, indicates that the electrorefractive effect is relatively more affected by slow heating, with a higher effective $V\pi$ at RF than is indicated by DC data. Currently, the SOA bias current was reduced to limit MZ input optical power so that the I–V product of each MZ electrode remained less than 100 mW at -6 V, I being the absorbed photocurrent. The reduced optical power also limited the total link gain and available SFDR. The spurious-free dynamic range (SFDR) was evaluated using two-tone modulation at f1, f2 $=$ 500 ± 10 MHz. Odd-order intermodulation products were measured either at either 2f1 $-$ f2 or 2f2 $-$ f1, whichever term was the greatest. Even-order intermodulation products were measured at f1 $+$ f2.

Figs. 15 and 16 shows a comparison between EA only and the linearized modulator of the power of fundamental and intermodulation products as a function of applied electrode bias. Using EA modulation only, a characteristic behavior for most modulators is observed, where at maximum slope, second-order intermodulation products are minimized, while third-order intermodulation products are prevalent. For the linearized modulator, local minima for both odd and even order products are obtained at the same bias voltage, -1.67 V. This represents the central advantage of this type of linearized modulator, the ability to linearize the response for broadband application. Due to slow thermal effects, the power of the fundamental does not stay constant over a wide DC voltage range, as would be expected form a linearized behavior. Instead, a local minimum with a slight curvature is found around the linear bias point.

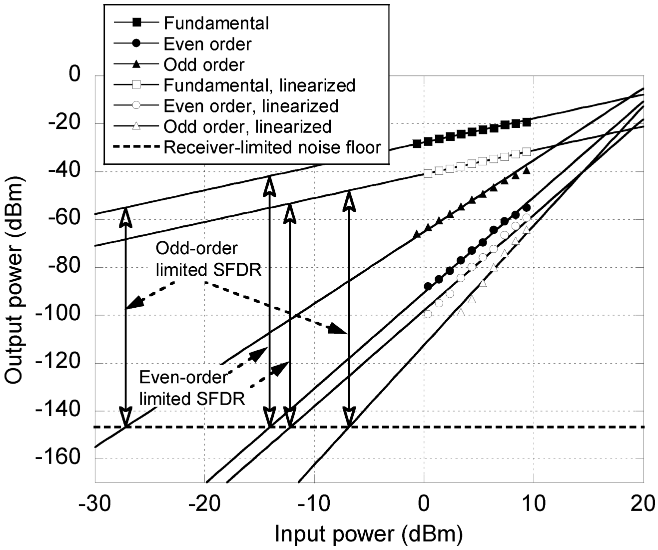

Fig. 17. Measured SFDR, limited by even or odd-order intermodulation products for the EAM and for the linearized modulator at 1542 nm and for receiver limited noise floor.

The measured SFDR is shown in Fig. 17 for both EAM and the linearized modulator. For the EAM, second-order intermodulation was cancelled at maximum slope. The SFDR, as limited by odd and even order products was $91.9\ \mathrm{dB}\cdot\mathrm{Hz}^{2/3}$ and $104.9\ \mathrm{dB}\cdot\mathrm{Hz}^{3/4}$, respectively. For the linearized modulator, both second and third-order intermodulation products could be cancelled, and odd-order limited SFDR increased to $98.9\ \mathrm{dB}\cdot\mathrm{Hz}^{4/5}$. Even-order limited SFDR was reduced to $93.4\ \mathrm{dB}\cdot\mathrm{Hz}^{3/4}$. The main reason for reduction is lower slope sensitivity of the linearized modulator. The noise floor was in all cases limited by receiver noise.

Linearized modulation was obtainable over the entire tuning range of the integrated SGDBR laser. To investigate the dependence on emission wavelength, the laser was tuned to the extremes of the tuning range and the SFDR was measured. The results are summarized in Table I. The linearization can reduce the relative power of third-order intermodulation products to a higher degree than second-order intermodulation, as the EA was biased for minimum second-order intermodulation to start with. However, the modulation sensitivity was reduced by more than 10 dB over the tuning range, resulting in a very modest improvement in SFDR. The cause of this is the nonoptimized balance between the relative effect of MZ and EA modulation. Potentially, with the right modulator material parameters, there could be a very low penalty in overall slope sensitivity, resulting in a broadband enhancement in odd-order limited SFDR by greater

TABLE I
SFDR LIMITED BY ODD (2f1 − f2) OR EVEN (f1 + f2) ORDER INTERMODULATION PRODUCTS FOR LINEARIZED AND NOT LINEARIZED EAM AT DIFFERENT WAVELENGTHS

Wavelength	EA-modulator		Linearized EA-modulator	
	SFDR (2f1-f2)	SFDR (f1+f2)	SFDR (2f1-f2)	SFDR (f1+f2)
1520.9 nm	89.9 dB·Hz$^{2/3}$	103.5 dB·Hz$^{3/4}$	97.8 dB·Hz$^{4/5}$	92.7 dB·Hz$^{3/4}$
1542.0 nm	91.9 dB·Hz$^{2/3}$	104.9 dB·Hz$^{3/4}$	98.9 dB·Hz$^{4/5}$	93.4 dB·Hz$^{3/4}$
1574.4 nm	91.7 dB·Hz$^{2/3}$	104.5 dB·Hz$^{3/4}$	99.3 dB·Hz$^{4/5}$	92.2 dB·Hz$^{3/4}$

than 10 dB with no penalty in even-order limited SFDR. However, unless overall slope sensitivity is sacrificed, a high-chirp EA must be developed that corresponds to a highly efficient MZ effect.

VI. CONCLUSION

In this paper, we have performed further investigations in transmitters formed by the integration of a widely tunable SGDBR laser with an SOA and modulator for analog optical link applications. It has been shown that by adding a preamplifier to the transmitter, low noise figure and optical link gain can be achieved. It is also shown that in a practical link application, with preamplification, a fifth-order dependence of intermodulation terms will practically not be reached, as a strong dependence of linear bias point to frequency separation using a two-tone probe signal is observed. The preamplified sub-octave SFDR was 115 dBHz$^{2/3}$ (5 dB-NF and 10.5-dB link gain) at 500 MHz and 110 dBHz$^{2/3}$ (5.4 dB-NF and 6.9-dB link gain) at 5 GHz, using a low-RIN operating point.

Improved dynamic range can be achieved using any of a number of linearization schemes. Two novel approaches have been investigated in this work. The first uses an compensatory predistortion scheme where an integrated second modulator is used to extract nonlinear terms. 20-dB suppression of intermodulation terms has been demonstrated. This approach will respond to any changes in modulator response due to wavelength, temperature and other factors. It has also been shown to be capable of providing linearization of preamplifiers, allowing the use of more nonlinear but efficient amplifiers. The main drawback of this approach is the requirement for gain matching over the operating frequency range, making this approach most attractive for narrowband applications.

The second linearization approach investigated is a linearized modulator fashioned from a combination of electroabsorption and MZ modulation that can null both third and second-order intermodulation products at a single bias point. This approach has the potential for wideband linearization, being a single electrode approach with no requirement for gain matching. The limitation is here the requirement for triple bias control; EA bias, MZ phase, and MZ balance. These must be further adjusted for any changes in modulator response due to input wavelength, temperature, etc.

REFERENCES

[1] L. A. Johansson, J. T. Getty, Y. A. Akulova, G. A. Fish, and L. A. Coldren, “Sampled Grating DBR laser-based analog optical transmitters,” *J. Lightw. Technol.*, vol. 21, no. 12, pp. 2968–2976, Dec. 2003.

[2] Y. A. Akulova, G. A. Fish, P. C. Koh, C. Schow, P. Kozodoy, A. Dahl, S. Nakagawa, M. Larson, M. Mack, T. Strand, C. Coldren, E. Hegblom, S. Penniman, T. Wipiejewski, and L. A. Coldren, “Widely-tunable electroabsorption-modulated sampled grating DBR laser transmitter,” *IEEE J. Sel. Topics Quant. Electron.*, vol. 8, no. 6, pp. 1349–1357, Nov./Dec. 2002.

[3] E. I. Ackerman and C. H. Cox, “RF fiber-optic link performance,” *IEEE Microw. Mag.*, vol. 2, no. 4, pp. 50–58, Dec. 2001.

[4] V. Jayaraman, Z.-M. Chuang, and L. A. Coldren, “Theory, design, and performance of extended tuning range semiconductor laser with sampled grating,” *IEEE J. Quant. Electron.*, vol. 29, no. 6, pp. 1824–1834, Jun. 1993.

[5] C. H. Cox, *Analog Optical Links: Theory and Practice*. Cambridge, U.K.: Cambridge Univ. Press, 2004, ch. 3.

[6] H. Shi, D. Cohen, J. Barton, M. Majewski, L. A. Coldren, M. C. Larson, and G. A. Fish, “Relative intensity noise measurements of a widely tunable sampled-grating DBR laser,” *IEEE Photon. Technol. Lett.*, vol. 14, no. 6, pp. 759–761, Jun. 2002.

[7] G. C. Wilson, T. H. Wood, M. Gans, J. L. Zyskind, J. W. Sulhoff, J. E. Johnson, T. Tanbun-Ek, and P. A. Morton, “Predistortion of electroabsorption modulators for analog CATV systems at 1.55 μm,” *J. Lightw. Technol.*, vol. 15, pp. 1654–1662, Sep. 1997.

[8] T. Ismail, C. P. Liu, J. E. Mitchell, and A. J. Seeds, “Interchannel distortion suppression for broadband wireless over fibre transmission using feed-forward linearised DFB laser,” in *Proc. IEEE Int. Topical Meeting Microwave Photonics*, Oct. 4–6, 2004, pp. 229–232.

[9] J. Yu, T. Y. Chang, G. C. Wilson, T. H. Wood, N. J. Sauer, J. E. Johnson, T. Tanbun-Ek, and P. A. Morton, “Linearization of 1.55-μm electroabsorption modulated laser bydistortion emulation and reversal for 77-channel CATV transmission,” *IEEE Photon. Technol. Lett.*, vol. 10, no. 3, pp. 433–435, Mar. 1998.

[10] R. Sadhwani, J. Basak, and B. Jalali, “Adaptive electronic linearization of fiber optic links,” in *Proc. Optical Fiber Communications Conf.*, Mar. 2003, vol. 2, pp. 477–479.

[11] Y. A. Akulova, G. A. Fish, P. Koh, P. Kozodoy, M. Larson, C. Schow, E. Hall, M. Marchand, P. Abraham, and L. A. Coldren, “10 Gb/s Mach–Zehnder modulator integrated with widely-tunable sampled-grating DBR laser,” presented at the Optical Fiber Communication Conf., Washington, DC, 2004, TuE4, on CD-ROM.

Leif A. Johansson (M’04) received the Ph.D. degree in engineering from University College London, London, U.K., in 2002.

He is currently a Research Scientist at the University of California, Santa Barbara. His current research interests include design and characterization of integrated photonic devices for analog and digital applications and analog photonic systems and subsystems.

Yuliya A. Akulova, photograph and biography not available at the time of publication.

Chris Coldren, photograph and biography not available at the time of publication.

Larry A. Coldren (S'67–M'72–SM'77–F'82) received the Ph.D. degree in electrical engineering from Stanford University, Stanford, CA, in 1972.

He is the Fred Kavli Professor of Optoelectronics and Sensors at the University of California, Santa Barbara (UCSB). HeAfter 13 years in the research area at Bell Laboratories, he joined UCSB in 1984, where he now holds appointments in Materials and Electrical and Computer Engineering and is the Director of the Optoelectronics Technology Center. In 1990, he co-founded Optical Concepts, later acquired as Gore Photonics, to develop novel VCSEL technology, and, in 1998, he co-founded Agility Communications, recently acquired by JDS Uniphase Corporation (JDSU), Goleta CA, to develop widely tunable integrated transmitters. At Bell Labs, he initially worked on waveguided surface-acoustic-wave signal processing devices and coupled-resonator filters. He later developed tunable coupled-cavity lasers using novel reactive-ion etching (RIE) technology that he created for the then new InP-based materials. At UCSB, he continued work on multiple-section tunable lasers, inventing the widely tunable multielement mirror concept in 1988, which is now used in some JDSU products. During the late 1980s, he also developed efficient vertical-cavity multiple-quantum-well modulators, which led to novel vertical-cavity surface-emitting laser (VCSEL) designs that provided unparalleled levels of performance. He continues to be active in developing new photonic integrated circuit (PIC) and VCSEL technology, including the underlying materials growth and fabrication techniques. In recent years, for example, he has been involved in the creation of efficient all-epitaxial InP-based and high-modulation speed GaAs-based VCSELs, as well as a variety of InP-based PICs incorporating numerous optical elements for widely tunable integrated transmitters, receivers, and wavelength converters operating up to 40 Gb/s. He has authored or coauthored over 800 papers, five book chapters, one textbook, and has been issued 61 patents.

Prof. Coldren has presented dozens of invited and plenary talks at major conferences. He is a Fellow of OSA and IEE, a member of the National Academy of Engineering, and the recipient of the 2004 John Tyndall Award.

Optical Phase Demodulation of a 10GHz RF Signal using Optical Sampling

Anand Ramaswamy, Leif A. Johansson, Jonathan Klamkin, Darko Zibar, Larry A. Coldren, Mark J. Rodwell and John E. Bowers
Department of Electrical and Computer Engineering, University of California, Santa Barbara, CA 93106, USA
anand@ece.ucsb.edu

Abstract: For the first time we demonstrate sampling downconversion of a 10GHz phase modulated optical signal using an integrated coherent receiver with feedback. At a downconverted frequency of 100 MHz we measure 19dB improvement in SIR.

OCIS codes: (060.1660) Coherent communications; (130.0250) Optoelectronics; (120. 5060) Phase Modulation

1. Introduction

The need for extreme linearity and low noise figure in certain analog link applications has resulted in an increased interest in optical links that employ phase modulation [1]. However, the challenge in leveraging the potential benefits of such links resides in the receiver architecture where standard interferometer based demodulation of phase generates a sinusoidal response between input phase and output photocurrent. Our effort to generate a linear response uses a feedback loop to a linear tracking phase modulator [2]. Other efforts include linearization of the receiver response using digital signal processing [3]. However, both these approaches suffer from bandwidth limitations when the input frequencies are in excess of a few GHz. In the former approach, even with compact integration of electronics and photonics, physical delays in the feedback path limit the stable loop bandwidth.

In this paper we demonstrate optical down-sampling [4] as a viable technique for extending the input frequency range of a coherent integrated receiver. By downconverting a 10GHz input signal to baseband, we are able to utilize the feedback architecture of the receiver to linearly demodulate the phase of the carrier frequency even though it exceeds the bandwidth of the receiver.

2. Optical Sampling Experiment

In this technique a train of short optical pulses from a high repetition rate pulsed optical source (typically a mode-locked laser (MLL)) is used to sample the optical phase of the input RF signal via an optical phase modulator as shown in Figure 1, right. The input signal is sampled at a rate that's close to its RF period, the pulses are integrated by the detector capacitance and a downconverted frequency component, is obtained. The frequency of this component is the difference between the pulse rate and the input signal frequency (f_{pulse}-$f_{1,2}$). The optoelectronic integrated receiver uses this downconverted signal to linearly demodulate the phase encoded carrier signal as described in [5].

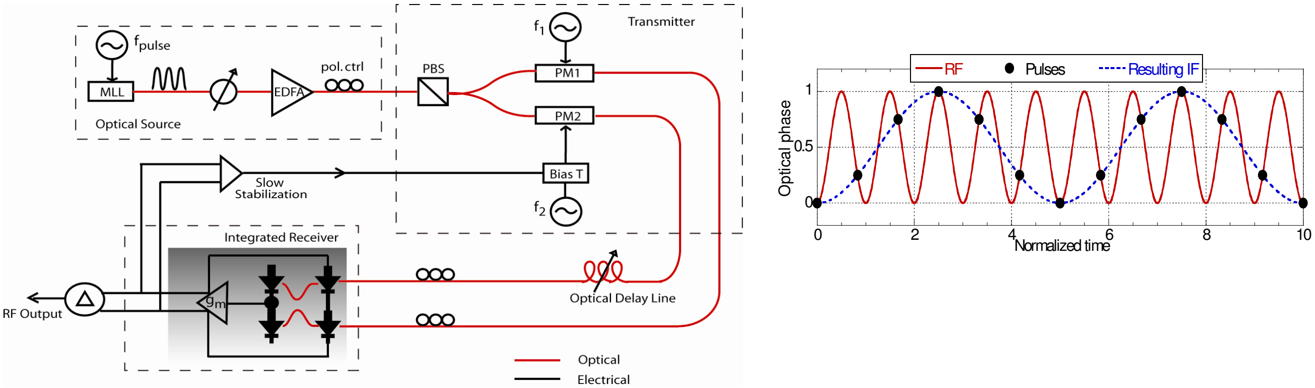

Fig. 1. Left: Experimental link. Right: Optical Sampling of phase modulated signal using pulse source

Figure 1, left shows a schematic of the experimental link used to demonstrate optical sampling. A commercial MLL with f_{pulse}=9.95327GHz and pulse width<1.4ps is used. The path lengths in the two arms of the fiber interferometer need to be accurately matched in order to ensure temporal overlap of the optical pulses from the signal and reference path. Here, an optical delay line is used for path length matching. Polarization maintaining fiber and components are used for stability. Currently, we do not have an optical filter that has high bandwidth and high power handling capability (>26dBm) to filter out ASE noise from the EDFA. Consequently, this limits the noise performance of the receiver. Another limitation to receiver performance arises from the super mode noise generated in the laser cavity about -60dBc.

3. Results

Figure 2, left shows the detected fundamental power and the power of the intermodulation distortion terms as a function of modulator drive power at a downconverted frequency of 100MHz. The input RF tones (f_1=9.852GHz and f2=9.853GHz) are applied to the transmitter phase modulators whose V_π's are 4.4V and 5.5V, respectively. When the receiver is operated without any feedback (open loop) the SIR is measured to be 35dB for an input power of 6.75dBm. When the receiver is operated closed loop with feedback in effect several observations can be made. First, for a higher input power (9.75dBm) the SIR is 19dB higher. This gives a clear indication that the reference phase modulator in the feedback path is linearly tracking the sampled incoming signal phase at a frequency of 100MHz. Second, the output RF power is nearly 20dB lower than the open loop case. This can be explained by noting that when feedback is in effect, there is a net decrease in phase swing across the phase demodulator resulting in a lower output power. Also, the signal is now tapped at the input of the reference phase modulator, not the output of the balanced detectors as in the open loop case. Figure 2, right shows the degradation in SIR at higher downconverted frequencies under closed loop operation. This is consistent with the baseband measurements of [2] where at higher frequencies, the feedback gain decreases resulting in reduced phase tracking.

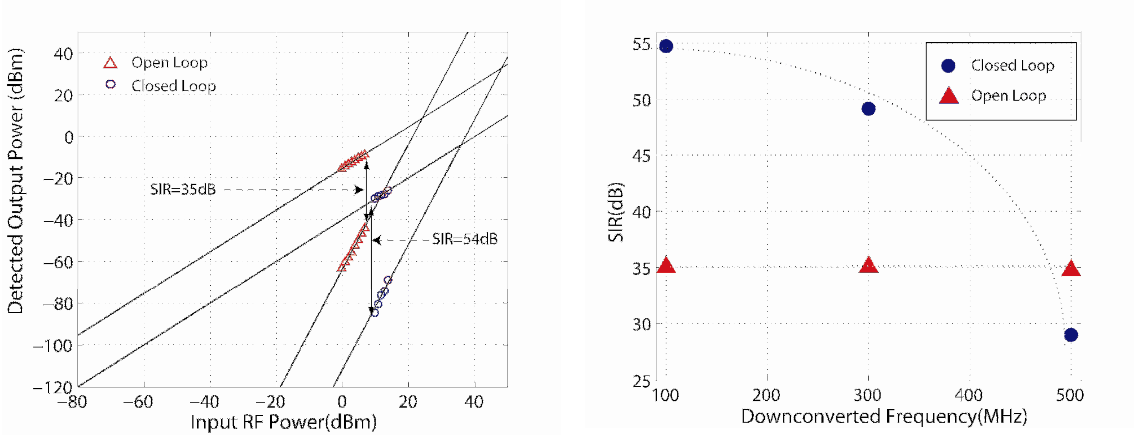

Fig. 2.Left: Measured power of fundamental and IMD3 at 100MHz. Right: SIR as a function of downconverted frequency.

The measured noise (-120dBm/Hz) is relatively high and can be attributed to noise contributions from both the EDFA and the MLL.

4. Summary

In this paper we demonstrate photonic downconversion using an integrated coherent receiver with feedback. The 19dB improvement in SIR realized at 100MHz downconverted frequency suggests that this method can be used for linear optical phase demodulation at carrier frequencies in excess of the bandwidth of the receiver.

Acknowledgment

The authors would like to thank Northrop Grumman Space Technologies for providing the electronic IC. This work was supported by the DARPA PHOR-FRONT program under United States Air Force Contract FA8750-05-C-0265.

References

[1] F. Bucholtz, V.J. Urick, M.S. Rogge and K.J. Williams, OSA COTA 2006, CFA6, Whistler, BC, Canada June 2006
[2] A. Ramaswamy, *et al.* Optical Fiber Communication (OFC), paper no. PDP3, Anaheim,CA, March 2007.
[3] T.R. Clark and M.L. Dennis, IEEE Photonics Technology Letters, Vol. 19, Issue 16, pp. 1206-1208, Aug. 15, 2007
[4] P.W. Juodawlkis, et al., IEEE Journal of Lightwave Technology, Vol. 21, No. 12, pp. 3116-3124, Dec. 2007
[5] A. Ramaswamy, et al., IEEE Journal of Lightwave Technology, Vol. 26, No. 1, pp. 209-216, Jan. 2008

Optical Phase Demodulation using a Coherent Receiver with an Ultra-Compact Grating Beam Splitter

Chin-Hui Chen[1], Anand Ramaswamy[1], Jonathan Klamkin[2], Leif A. Johansson[1], John E. Bowers[1], and Larry A. Coldren[1,2]
[1]*Electrical and Computer Engineering Department, University of California, Santa Barbara, CA 93106*
[2]*Material Department, University of California, Santa Barbara, CA 93106*
Phone: 805.893.7163, Fax: 805.893.4500, Email: janet@ece.ucsb.edu

Abstract: We describe the design and fabrication of an integrated coherent receiver incorporating a novel grating beam splitter for linear optical phase demodulation. The open loop behavior of the receiver is measured in a link experiment.

OCIS codes: (130.6622) Subsystem integration and techniques; (130.3120) Integrated optics devices

1. INTRODUCTION

Linear demodulation of phase modulated optical signals is needed to realize the extremely high dynamic range afforded by phase modulated analog photonic links. Interferometer based optical phase demodulators have a sinusoidal response that limits their performance [1]. In order to overcome the inherent nonlinearity associated with the phase recovery process we have utilized a phase locked loop (PLL) [2, 3]. The utilization of a PLL sets stringent requirements on the delay of each element in the feedback path. To operate at microwave frequencies, an integrated platform that is four orders of magnitude more compact than fiber optics is required [2]. Using an InP integration platform we were able to realize compact integration of electronics and photonics and measure an SFDR of 125dB.Hz$^{2/3}$ at 300 MHz under closed loop operation [4]. However, to achieve sufficient loop gain for a SFDR of 130dB.Hz$^{2/3}$ at 1 GHz, the loop delay must be <15ps to maintain stability.

In this paper we demonstrate open loop behavior of an integrated receiver with an ultra-compact grating beam splitter in an analog link experiment to show the potential for linear phase demodulation. We describe the design and fabrication of the novel grating-based beam splitter that can replace conventional directional couplers or multi-mode interference (MMI) based couplers in applications that require ultra-compact beam splitting [5]. This beam splitter is integrated with detectors and modulators to form the coherent integrated receiver.

2. GRATING-BEAM SPLITTER BASED INTEGRATED RECEIVER

Fig. 1 (a) shows the configuration of the balanced receiver in which the grating beam splitter is integrated with MQW phase modulators and uni-traveling-carrier photodiodes (UTC-PDs). The beam splitter includes a quasi-free space region and a short interference region consisting of grating grooves. The quasi-free space region allows the input and output beams to diverge freely in the lateral direction, confining them in the transverse direction only. The grating region splits an incoming beam into transmissive (undiffracted) and reflective (diffracted) beams.

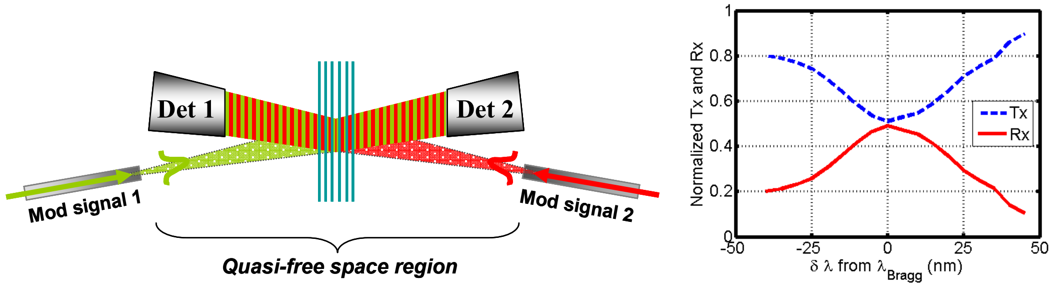

(a) (b)

Fig. 1. (a) Schematic of integrated receiver with grating-based beam splitter. (**b)** Splitting ratio of grating-based beam splitter versus wavelength. Nearly equal splitting is observed at the Bragg wavelength.

In order to avoid the mode degradation due to oblique incidence of finite beams onto thick gratings, we firstly design the incident waveguides with a small angle that is sufficiently large to distinguish beams in the quasi-free space region. An angle of 10° from normal incidence is selected and is a reasonable compromise for short total propagation length. Secondly, to also achieve the targeted splitting with an ultra-short coupling length, a highly reflective Bragg grating for 1550 nm wavelength is utilized. Thirdly, the unique quasi-free space region is introduced in order to expand the incoming beams to be comparable or wider than the grating length. The divergence in the quasi-free space region is faster than that in the traditional adiabatic flaring so that the traveling distance can be kept as short as possible. The performance of an equal splitting grating-based beam splitter is shown in Fig. 1 (b).

The integrated receiver as shown in Fig. 2 consists of a balanced UTC-PD, a compact 2x2 grating-based beam splitter, and MQW phase modulators. The device platform and fabrication process used is similar to that reported in [6]. To form the deep gratings, a SiO_2 mask was patterned with holographic lithography. The gratings were then transferred into the MQW waveguide core with methane/hydrogen/argon/oxygen-based reactive ion etching with an alternating etching and oxygen descumming process [5]. The largest index contrast in the grating is achieved when the slab waveguide layer is completely etched through. The etch of the deep grating grooves is followed by a blanket p^+ - InP cladding and p^{++} - InGaAs contact layer regrowth. This regrowth yields no apparent air voids, which suggests low scattering losses in the grating region.

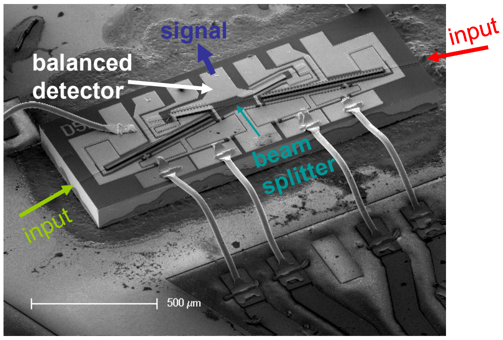

Fig. 2. SEM of integrated coherent receiver on carrier. The RF signal in-between a pair of balanced UTC-PD and gratings are indicated. Two fiber coupled incoming beams are illustrated with arrows in red and green.

3. OPTICAL PHASE DEMODULATION EXPERIMENT

Fig. 3 shows an experimental analog link that was built to evaluate the integrated receiver performance under open loop operation. The optical source consists of a tunable c.w. laser operating at 1545nm. The details of the link are described in [4]. In order to characterize the third order intermodulation distortion generated in the receiver we apply a two tone probe signal at the transmitter. However, as described in [4] we apply them separately to two $LiNbO_3$ modulators. Since, the grating is sensitive to the polarization of the incident light, the polarization controllers located before the device allow the polarization to be optimized for highest splitting ratio. The grating coupler in conjunction with the balanced photodiode forms an optical mixer that can demodulate the incoming signal phase applied at the transmitter.

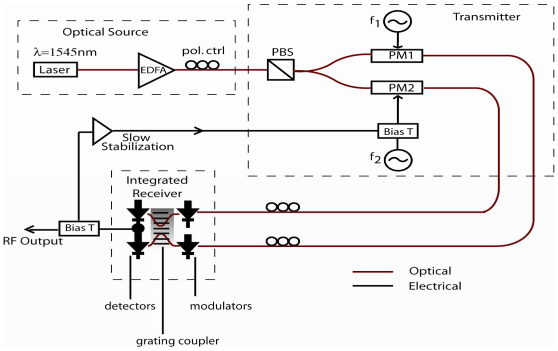

Fig. 3. Schematic of experimental analog link

Fig. 5. shows the power spectra at the output of the receiver under open loop operation. The frequencies of the two tones are 300 MHz and 302 MHz. The measured signal to intermodulation ratio (SIR) is 28.9dB for an input power

of 10dBm. As mentioned earlier, standard interferometer based demodulation of phase results in a sinusoidal relation between the detected photocurrent and incoming signal phase. Consequently, the linearity of the receiver is severely degraded by the phase recovery process. Fig. 5 (b) shows an SFDR of 86dB.Hz$^{2/3}$ at 300 MHz with 10mA of photocurrent per individual photodiode. The measured noise in the receiver was -127dBm/Hz and can be attributed to the spontaneous emission noise from the EDFA.

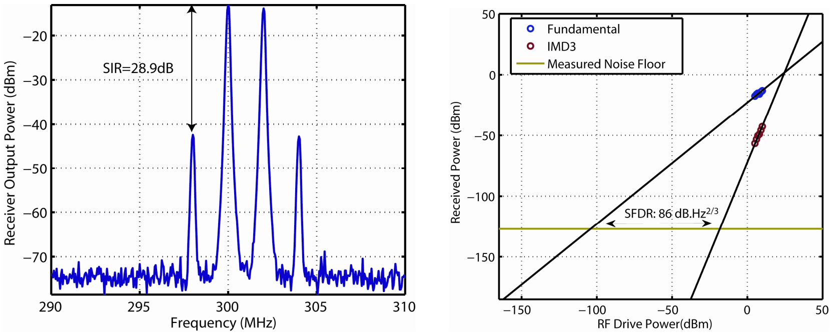

(a) (b)

Fig. 4. (a) Receiver output power spectra for open loop. **(b)** SFDR at 300MHz, 10mA photocurrent

The demonstrated open loop operation of the receiver illustrates the ability of the receiver to demodulate optical phase. The grating-based beam splitter successfully combines and splits the two incident optical beams so that the balanced UTC-PD demodulates the microwave signal phase. This demodulated signal can be amplified and fed back to the integrated phase modulators to perform linear optical phase demodulation.

4. CONCLUSION

In summary, we have demonstrated phase demodulation with a coherent integrated receiver incorporating a novel grating-based beam splitter. When combined with feedback, this receiver will realize short feedback loop delays in order to perform linear optical phase demodulation at microwave frequencies.

ACKNOWLEDGEMENT

This work was supported by DARPA via the PHOR-FRONT program under the United States Air Force Contract FA8750-05-C-0265

REFERENCES

[1] F. Bucholtz, V.J. Urick, M.S. Rogge and K.J. Williams, OSA COTA 2006, CFA6, Whistler, BC, Canada June 2006.

[2] H-F Chou, et al., "SFDR Improvement of a Coherent Receiver Using Feedback," OSA topical meeting of Coherent Optical Techniques and Applications (COTA), Whistler, BC, 2006.

[3] Y. Li *et al*., "Receiver for a coherent fiber-optic link with high dynamic range and low noise figure", *International Topical Meeting on Microwave Photonics (MWP '05)*, Seoul, Korea, 2005.

[4] A. Ramaswamy, et al., "Coherent Receiver Based on a Broadband Optical Phase-Lock Loop," *Optical Fiber Communication (OFC) conference* post deadline paper, 2007.

[5] C. H. Chen, et al., "Design and Implementation of Ultra-compact Grating-based 2x2 Beam Splitter for Miniature Photonic Integrated Circuits," OTuC5, *Optical Fiber Communication conference (OFC)*, 2008.

[6] J. Klamkin *et al.*, "Monolithically Integrated Coherent Receiver for Highly Linear Microwave Photonic Links," ME2, The 20th Annual Meeting of IEEE *LEOS* 2007.

Filter Designs for a Reconfigurable Photonic Integrated Circuit

Yujia Wang, John J. Shynk, Larry A. Coldren
Department of Electrical and Computer Engineering
University of California
Santa Barbara, CA 93106-9560

***Abstract*— This paper presents non-classical bandpass filter designs for a reconfigurable photonic integrated circuit (PIC). Because the designs must be realizable for a high frequency range in a new optical device, we consider digital infinite-impulse response filters that avoid lasing for a specific unit cell configuration. In order to accommodate the architecture of the PIC, we describe a design procedure for bandpass filters in the 10 GHz frequency range based on a prototype filter constructed from second-order sections.**

I. INTRODUCTION

For future signal processing platforms, it will be necessary to design filter structures that operate at frequencies near 10 GHz and with bandwidths around 50 MHz. Although optical infinite-impulse-response (IIR) and finite-impulse-response (FIR) filter architectures have previously been proposed [1]–[4], no photonic integrated circuits (PICs) have been physically realized. However, with recent advances in PIC technology, it is anticipated that filters in this frequency range can be implemented using a cascade of unit cells. In order to model such devices, we consider bandpass filter designs that fulfill these requirements while maintaining normal operation without lasing.

For a reconfigurable PIC, device elements that provide independent control of the magnitude and phase of the poles and zeros of an IIR system are needed. To achieve this, the unit cell is integrated with the following elements as shown in Figure 1: multi-mode interference (MMI) coupler [5], semiconductor optical amplifier (SOA) [6], and phase modulator (PM) [7]. The component operations can be described as functions of the input signal wavelength, yielding optical-response characteristics. To match the response of the physical device to that of a digital filter design, we employ a z-transform model to derive the correct mapping of the PIC parameters. The mapping is based on the bilinear transform, which connects the digital and analog domains via the sampling frequency f_s, which in turn is related to the free spectral range (FSR) of the optical system [8], [9]. For the particular unit cell considered here, we assume that $f_s = 25$ GHz.

A PIC operating in the frequency range of 10 GHz is vulnerable to lasing, which is the condition where the device operates as a laser rather than yielding an optical signal that can be processed [10]. Methods of mapping between the optical and signal processing domains were explored in [8], [9], but the need to avoiding lasing for our particular device has not been examined. We have developed mapping strategies for the unit cell, which are independent of the results in [8], [9]. At the desired operating frequency range and with a sufficiently large sampling frequency, classical IIR filter designs result in poles that are very close to the unit circle. These poles in turn correspond to component parameters of the PIC that can cause lasing. To address this issue, we modify the poles and zeros that result from classical designs, such as the elliptic filter, to obtain a magnitude response that has a suitable passband, while avoiding lasing.

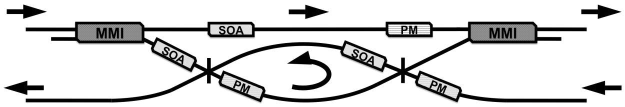

Fig. 1. Unit cell configuration and its signal flow.

The rest of this paper is organized as follows. Section II explains the basic operation and structure of a PIC unit cell, and briefly describes its components. This section also provides an overview of the basic Fabry-Perot etalon [11]. Section III presents filter design techniques and a parameter mapping for governing the behavior of the physical unit cell. The Fabry-Perot etalon is used to demonstrate the relationship between an optical scattering coefficient and the z-domain transfer function. Example results of the designs and responses of the PIC are shown in Section IV, and Section V provides a summary of the filter design.

II. PHOTONIC FILTER OVERVIEW

A PIC processes information signals carried on optical wavelengths in the visible spectrum. The structure under consideration here consists of a cascade of unit cells, each of which can be viewed as the basic building block of the overall system. A unit cell functions similar to a second-order IIR system providing individually controllable poles and zeros, and has the three previously-mentioned components: MMI, SOA, and PM. The MMI is an optical device that splits or combines its input signals [5], and is characterized by a transmission coefficient and a coupling coefficient. The SOA provides a signal gain, whereas the PM changes the phase [6], [7]. The arrangement of the MMI, SOA, and PM for the unit cell considered here is shown in Figure 1. With these

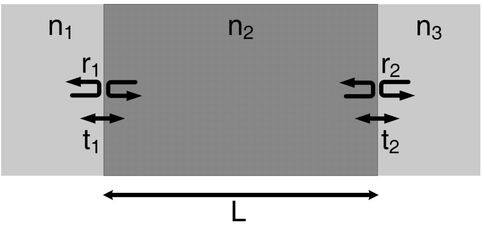

Fig. 2. Fabry-Perot etalon and its signal flow.

three components, feedforward and feedback structures can be implemented and reconfigured to process optical signals.

The input-output relationship of an optical system is modeled by a scattering coefficient [11]. To demonstrate the use of a scattering coefficient for signal processing, we examine a basic optical element known as the Fabry-Perot etalon, which functions as a simple optical narrowband filter. It is characterized by two sets of reflection and transmission coefficients $\{t_1, r_1, t_2, r_2\}$, the length L of the device, and the propagation constant $\tilde{\beta}$ of the material [11]. Figure 2 shows a block diagram of the Fabry-Perot etalon and its signal flow.

The etalon is typically made of two reflecting surfaces. When an incident signal $s(t)$ strikes the interface of the etalon from either material with index n_1 or n_3, part of the signal will reflect according to $rs(t)$, while the rest transmits through as $ts(t)$, where r and t satisfy $r^2 + t^2 = 1$. Inside the etalon, the signal magnitude and phase will change due to properties of the material according to $e^{-j\tilde{\beta}L}$, where $\tilde{\beta}$ is the complex propagation constant of the material with index n_2. Example indices are $n_1 = n_3 = 1.0003$ for air and $n_2 = 4.24$ for silicon. For a symmetric ($r_1 = r_2$) and lossless ($\beta_i = 0$) Fabry-Perot etalon, Figure 3 shows the optical response of the structure conveyed by the transmission coefficient S_{21} described in the next section. Observe that it is a periodic function of βL where β is the attenuation component of $\tilde{\beta}$.

The spacing between two adjacent resonator modes, known as the free spectral range (FSR) [11], is given by $\mathrm{FSR} = c/2nL$ where c is the speed of light, n is the index of the material, and L is the length of the device. As seen in Figure 3, the FSR corresponds to one period of the plot; the repeating nature of the optical pole graph translates to an inherent sampling frequency of $f_s = \mathrm{FSR}$. With knowledge of the parameters of the device and its optical behavior, we can establish a correspondence between the optical response and a z-domain transfer function and thus the corresponding frequency response.

The problem of lasing must be considered when designing digital filters for the unit cell. Because feedback is needed to create an IIR filter response, the unit cell contains a loop configuration in the design. Since a loop results in an internal power loss for the optical signal, an SOA is integrated into the design. Lasing refers to the condition when the gain and loss within the loop are equal, resulting in an output that is independent of the input. The effect of lasing is closely related to the instability of a digital filter with feedback. Therefore, one must design the IIR filter poles to be sufficiently within the unit circle in the z-plane. For our unit cell, we have determined that the pole magnitudes should be constrained to be < 0.995 in order to provide a margin of safety.

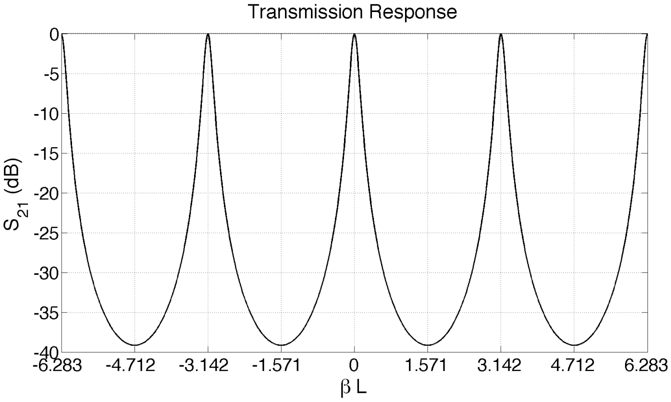

Fig. 3. Fabry-Perot transmission response showing pole locations.

III. PHOTONIC INTEGRATED CIRCUIT

A. Basic Filter Design

The bandpass filter design requirements of interest are the following: 10 GHz center frequency, 50 MHz resolution, and 60 dB stopband attenuation. Using a twelfth-order elliptic filter and a 40 ps sampling period, we are able to meet the design criteria. However, the resulting classical filter structure has pole magnitudes exceeding 0.995, which may cause the PIC to exceed the lasing threshold. As a result, we use the elliptic filter for a prototype design and derive a suboptimal filter by adjusting the pole magnitudes.

B. Cascade System

The design is based on a cascade of second-order elliptic filter sections. The transfer function of a second-order all-pole system can be written in the s-domain as

$$H(s) = \frac{1}{s^2 + 2\zeta\omega_o s + \omega_o^2}, \tag{1}$$

which is characterized by the cutoff frequency ω_o (natural frequency) and the sharpness of the peak ζ (damping ratio). Since the poles occur as a complex conjugate pair of the form $-\sigma \pm j\omega$, (1) can be written as

$$H(s) = \frac{1}{s^2 + 2\sigma s + (\sigma^2 + \omega^2)} \tag{2}$$

where

$$\sigma = \zeta\omega_o \tag{3}$$
$$\omega = \omega_o\sqrt{1 - \zeta^2}. \tag{4}$$

A cascade of second-order sections translates to fabricated unit cells with a more rapid and stable configuration than that possible using coupled resonators. The architecture of the unit cell is based on using a second-order section as the basic component of the filter design.

C. *Pole Constraint*

In the digital filter design, we must take into consideration that the pole magnitudes should not exceed 0.995 in the z-domain in order to avoid lasing. To determine the corresponding constraint on the pole locations, we start with the bilinear transform that connects a digital design to the poles in the s-domain, i.e.,

$$\begin{aligned} z &= \frac{1+\frac{T_s}{2}s}{1-\frac{T_s}{2}s} \\ &= \frac{1-\sigma\frac{T_s}{2}+j\omega\frac{T_s}{2}}{1+\sigma\frac{T_s}{2}-j\omega\frac{T_s}{2}} \end{aligned} \tag{5}$$

where T_s is the sampling period. Since the magnitude of z is < 0.995, this corresponds to

$$\frac{\sqrt{\left(1-\sigma\frac{T_s}{2}\right)^2+\left(\omega\frac{T_s}{2}\right)^2}}{\sqrt{\left(1+\sigma\frac{T_s}{2}\right)^2+\left(\omega\frac{T_s}{2}\right)^2}} < 0.995. \tag{6}$$

After a few equation manipulations, we arrive at the following expression:

$$\left(\sigma-\frac{398}{T_s}\right)^2+\omega^2 < \frac{397.995^2}{T_s^2}, \tag{7}$$

which we see is the equation of a circle. As shown in Figure 4, the region of the constrained poles is entirely to the left of the imaginary axis, which is required for general stability, and is vertically centered about the real axis to allow for a complex conjugate pair. Observe that the poles are constrained to be further away from the imaginary axis with increasing frequency.

D. *Parameter Mapping*

We can establish a connection between the optical characteristics of the unit cell and its z-domain response by examining the Fabry-Perot etalon. The signal flow of this device is modeled using scattering coefficients [11], which provide the relationships between signals at the input and output ports. Although the etalon has two input ports and two output ports (such that a signal can enter or exit the device from material n_1 or n_3), initially we are interested in the relationship between input port 1 and output port 2, as indicated in Figure 2. The other input and output ports typically involve feedback signals in a cascade structure, and thus they are not of interest for a standalone etalon. The scattering coefficient from port 1 to port 2 is

$$S_{21} = \frac{t_1t_2e^{-j\tilde{\beta}L}}{1-r_1r_2e^{-2j\tilde{\beta}L}} \tag{8}$$

where $\{t_1, t_2\}$ are the transmission coefficients, $\{r_1, r_2\}$ are the reflection coefficients, and

$$\tilde{\beta} = \beta + j\beta_i \tag{9}$$

is the propagation constant of the material characterized by the attenuation constant β and the phase constant β_i. The real part of $e^{-2j\tilde{\beta}L}$ can be factored out such that

$$S_{21} = \frac{t_1t_2e^{\beta_iL}e^{-j\beta L}}{1-r_1r_2e^{2\beta_iL}e^{-2j\beta L}}, \tag{10}$$

and since $t_1^2+r_1^2 = t_2^2+r_2^2 = 1$, we can write

$$S_{21} = \frac{\sqrt{1-r_1^2}\sqrt{1-r_2^2}e^{\beta_iL}e^{-j\beta L}}{1-r_1r_2e^{2\beta_iL}e^{-2j\beta L}}. \tag{11}$$

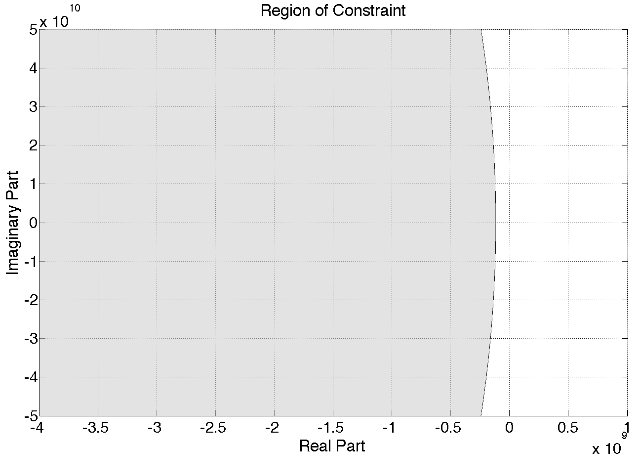

Fig. 4. Constrained pole region in the s-plane due to (7) with $T_s = 40$ ps.

The scattering coefficient S_{21} describes the relationship between the input signal and the output signal as a function of wavelength. When designing a digital filter, we are interested in the z-domain response. To obtain the proper conversion, note that the smallest unit of time is the delay of a signal through the etalon of length L. Thus, βL is the fundamental frequency of the system, so that in z-domain we have the transfer function

$$H_{21}(z) = \frac{\sqrt{1-r_1^2}\sqrt{1-r_2^2}e^{\beta_iL}z^{-T}}{1-r_1r_2e^{2\beta_iL}z^{-2T}} \tag{12}$$

where z^{-T} corresponds to the fundamental delay of the system. For this particular structure, there is a single zero $z_1 = 0$ and two poles $p_{1,2} = \pm\sqrt{r_1r_2}e^{\beta_iL}$. The Fabry-Perot etalon is a simple structure that demonstrates how to map from a scattering coefficient to the transfer function in the z-domain. The process can be extended to the more complicated unit cell used in the PIC and derived from a combination of MMIs, SOAs, and PMs. These elements allow for control of the pole and zero locations in the PIC, and thus we can design digital filters that model and govern the behavior of the optical system.

IV. EXAMPLE RESULTS

The following filter design results were obtained by first constructing an elliptic filter with six cascaded second-order sections, and then adjusting the pole magnitudes. The angular locations of the poles were kept the same while the ζ value for each section was modified to meet the magnitude constraint to avoid lasing. The zeros were then moved to different frequencies so that their effect on the rise of the passband

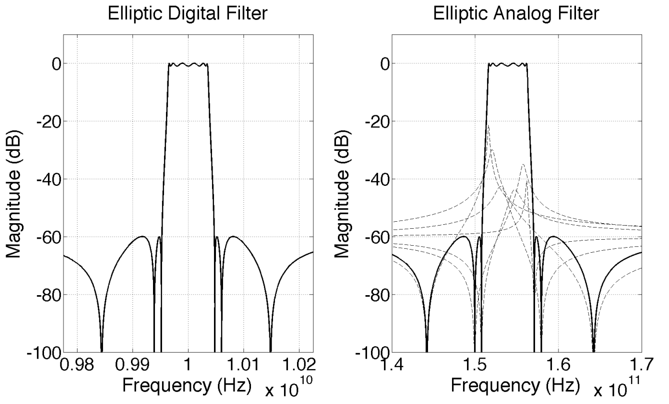

Fig. 5. Digital and analog elliptic filter designs. The dotted lines indicate the responses for the second-order sections.

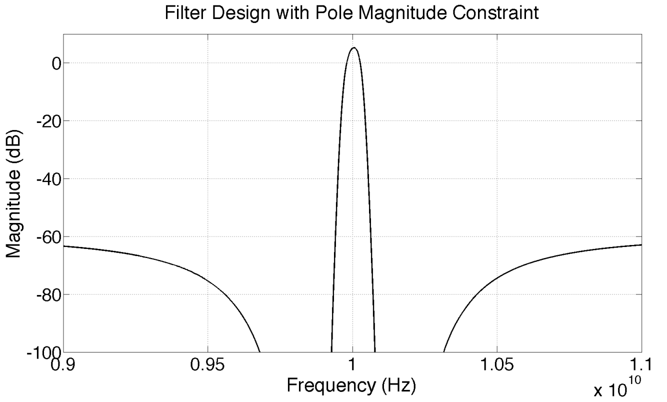

Fig. 6. Frequency response of the filter design with a pole magnitude constraint.

was minimized. Figure 5 shows the original digital and analog designs; the resulting filter response that meets the 0.995 magnitude constraint is provided in Figure 6. Figure 7 shows the transmission response of the unit cell (similar to that in Figure 3), and Figure 8 is the corresponding digital filter frequency response.

V. CONCLUSION

We considered design methods for a reconfigurable optical filter consisting of unit cells that contain SOAs, MMIs, and PMs. As demonstrated with the Fabry-Perot etalon, the signal flow characteristic of a PIC can be mapped to a transfer function in the z-domain by examining a scattering coefficient. In order to model and govern the PIC's operation, we considered a twelfth-order elliptic bandpass filter with a 10 GHz center frequency, a 50 MHz resolution, and a 60 dB stopband attenuation. However, due to the possibility of lasing in the device, we derived a suboptimal filter from this prototype design that constrains the pole magnitudes to be < 0.995. This design that can be physically realized in an optical filter operating in the 10 GHz range without causing lasing.

VI. ACKNOWLEDGMENTS

The authors would like to thank J. Bovington, H.-W. Chen, A. Fang, and R. Guzzon for helpful discussions. This work was supported by the Defense Advanced Research Projects Agency under Grant HR0011-08-1-0006.

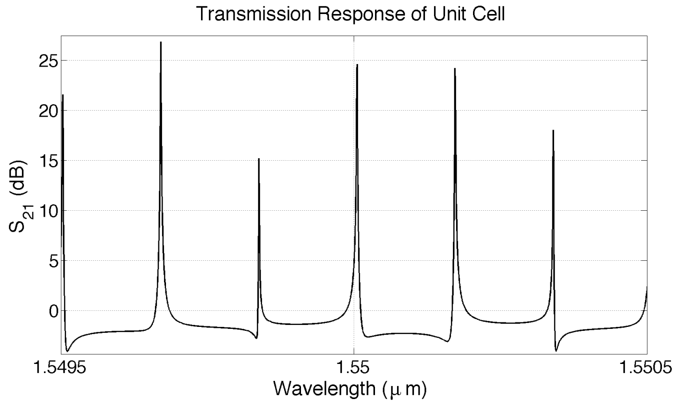

Fig. 7. Unit cell transmission response showing the pole locations.

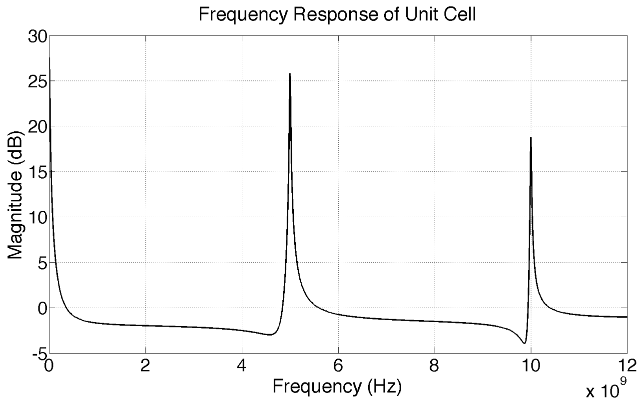

Fig. 8. Unit cell frequency response showing the pole locations.

REFERENCES

[1] J. E. Bowers, S. A. Newton, W. V. Sorin, and H. J. Shaw, "Filter response of single-mode fibre recirculating delay lines," *Electronics Letters*, vol. 18, pp. 110–111, Feb. 1982.

[2] M. Tur, J. W. Goodman, B. Moslehi, J. E. Bowers, and H. J. Shaw, "Fiber-optic signal processor with applications to matrix-vector multiplication and lattice filtering," *Optics Letters*, vol. 7, pp. 463–465, Sept. 1982.

[3] Y. Fainman and S. H. Lee, "Experimental evaluation of Mangin mirror performances for optical processing with feedback," *Optical Engineering*, vol. 24, pp. 535–540, 1985.

[4] H. Rajbenbach, Y. Fainman, and S. H. Lee, "Optical implementation of an iterative algorithm for matrix inversion," *Applied Optics*, vol. 26, pp. 1024–1031, 1987.

[5] L. B. Soldano and E. C. M. Pennings, "Optical multi-mode interference devices based on self-imaging: Principles and applications," *Journal of Lightwave Technology*, vol. 13, no. 4, pp. 615–627, Apr. 1995.

[6] M. J. Connely, *Semiconductor Optical Amplifiers*. New York: Springer, 2002.

[7] K.-P. Ho, *Phase-Modulated Optical Communication Systems*. New York: Springer, 2005.

[8] C. K. Madsen and J. H. Zhao, *Optical Filter Design and Analysis: A Signal Processing Approach*. New York: Wiley, 1999.

[9] G. Pasrija, Y. Chen, B. Farhang-Boroujeny, and S. Blair, "DSP approach to the design of nonlinear optical devices," *EURASIP Journal on Applied Signal Processing*, vol. 10, pp. 1485–1497, 2005.

[10] W. Koechner, *Solid-State Laser Engineering*. New York: Springer, 2006.

[11] L. A. Coldren and S. W. Corzine, *Diode Lasers and Photonic Integrated Circuits*. New York: Wiley, 1995.

TuR3
2:00 PM – 2:15 PM

Three-Tone Characterization of High-Linearity Waveguide Uni-Traveling-Carrier Photodiodes

Anand Ramaswamy[1], Jonathan Klamkin[2], Nobuhiro Nunoya[1], Leif A. Johansson[1],
Larry A. Coldren[1,2] and John E. Bowers[1]
[1]University of California Santa Barbara, ECE Department, Santa Barbara, CA 93106, USA
[2]University of California Santa Barbara, Materials Department, Santa Barbara, CA 93106, USA
Email: anand@ece.ucsb.edu

The IMD3 of waveguide UTC photodiodes are characterized using a three-tone technique that is independent of harmonics from the optical sources. At 1 GHz, an OIP3 of 46.2dBm at 60mA of photocurrent is measured.

High-performance analog optical links require photodiodes (PDs) that have high power handling capability as well as high linearity. Waveguide PDs are of particular interest because they can be monolithically integrated with optical modulators and couplers to realize complex receiver functionality [1]. Uni-traveling carrier PDs (UTC-PDs) [2], which were designed for high speed and high current operation, have shown very high output saturation and linearity characteristics [3, 4]. Recently, we reported on waveguide UTC-PDs with OIP3s in excess of 40dBm for up to 80mA of photocurrent, measured at 1GHz [4]. Various techniques have been suggested to characterize the third-order intermodulation distortion (IMD3) generated by PDs [5]. Typically, a two-tone setup is used where the outputs of two commercial DFB lasers operating at ~1.5µm are externally modulated with optical intensity modulators biased at quadrature. The modulated signals are combined and amplified using a fiber amplifier before being coupled into the device. One of the drawbacks of this approach is that harmonics from the optical source (i.e. modulators) interact with the fundamental signals (at f_1 and f_2) to generate distortion terms at the IMD3 frequencies ($2f_2$-f_1 and $2f_1$-f_2). When the distortion of the device under test (DUT) is very low, such as in [4], the nonlinear contributions from the optical sources become significant. Consequently distortion characterization is limited by the distortion of the measurement system itself. An alternate approach to the two-tone technique is to use three tones to measure IMD3 [5, 7]. In this technique the third order non-linear distortion components are independent of the harmonics originating in the optical modulators and signal generators. Consequently, the IMD3 measured at these frequency components can be attributed to the DUT. Fig. 1 shows a schematic of the experimental setup.

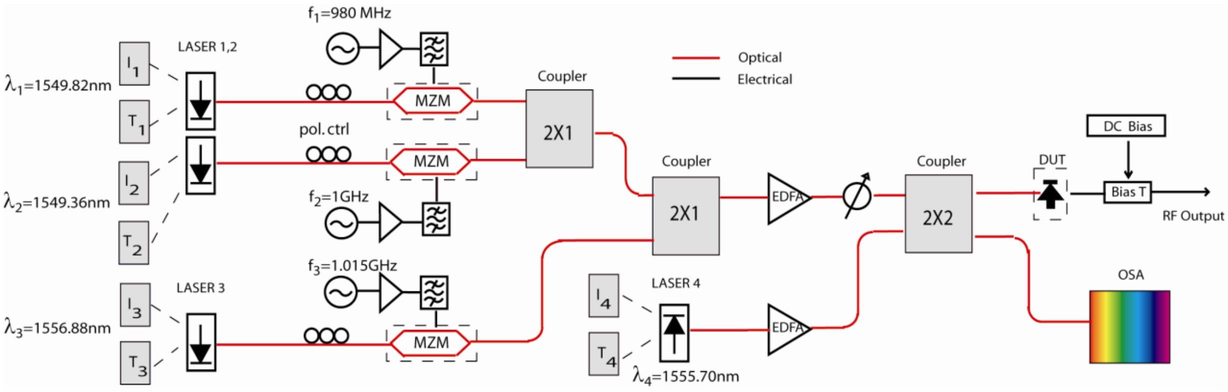

Fig. 1. Schematic of 3 tone experimental setup

The output of three CW lasers with differing wavelengths (Δλ ~0.5-7nm) are modulated separately at frequencies f_1=980MHz, f_2=1GHz and f_3=1.015GHz. The three optical signals carrying RF modulation are combined and amplified. An attenuator is used at the output of the EDFA to control the modulation index of the three tones. A fourth CW laser is used to ensure that the optical power and hence, photocurrent in the device remains unchanged as the optical modulation index is varied. For this experiment the optical modulation index is varied between approximately 20-30%. Additionally, an optical spectrum analyzer (OSA) is used to monitor the spectral content of the optical signal to ensure that four-wave mixing does not occur for the high optical powers used in this experiment.

The third order non-linear distortion components are measured at frequencies f_3–(f_1+f_2), f_2–(f_1+f_3) and f_1–(f_2+f_3). As outlined in [5] the three-tone IMD3 is 6dB larger than the ideally measured two-tone IMD3 and the three-tone IP3 is

978-1-4244-1932-6/08/$25.00 ©2008 IEEE

3dB smaller than the two-tone IP3. This distinction is more clearly illustrated in Fig. 2a). A factor of 3dB is added to the three-tone IP3 to relate this to the more commonly used two-tone IP3. Using this technique we measure the IMD3 of a UTC-PD that has a 1dB compression current of 80mA [4]. At a photocurrent level of 60mA the device has a two-tone OIP3 of 46.2dBm as shown in Fig. 2b).

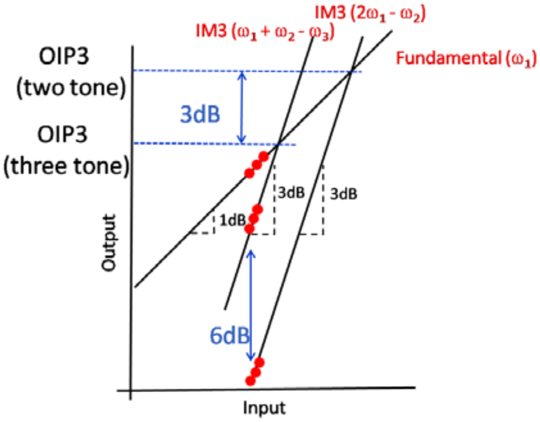

Fig. 2a). Relation between two-tone & three-tone IP3

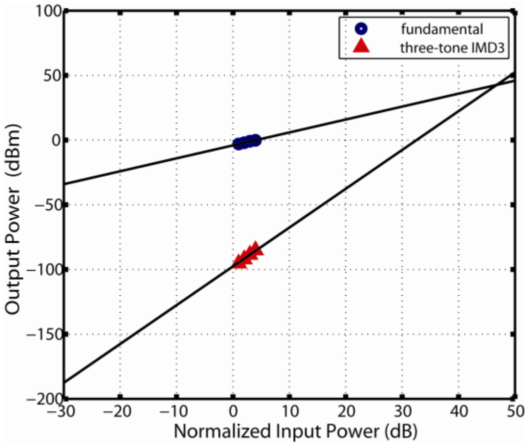

2b). Three-tone IMD3 measurement at 60mA

In order to verify the measurements we compared results from different devices that were measured using both techniques. In Fig. 3 it can be seen that when the distortion of the DUT is comparatively higher (lower IP3), the two measurements yield nearly the same result, as for Device 1. However, when the distortion of the PD is very low (OIP3 > 40dBm) we observe a significant difference in the measured distortion. It can be concluded that the measurements using the two-tone technique are limited by the measurement system when the DUT exhibits very low distortion. Therefore alternate techniques such as the three-tone approach are necessary to characterize the distortion of highly linear PDs.

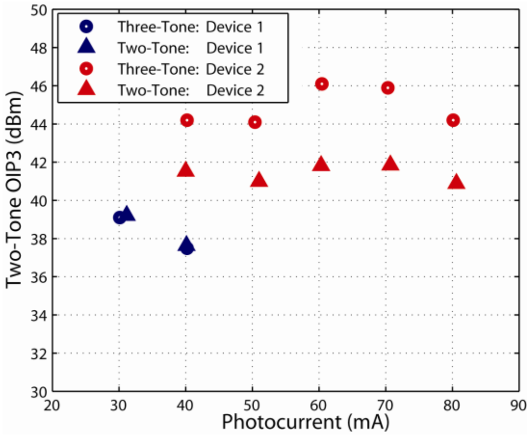

Fig. 3. Results from Two-tone & Three-tone Measurement

This work was supported by the DARPA PHOR-FRONT program under US Air Force Contract FA8750-05-C-0265.

[1] A. Ramaswamy, *et al.*, “Coherent Receiver Based on a Broadband Optical Phase-Lock Loop,” Optical Fiber Communications Conference. (OFC). Postdeadline Technical Digest. Opt Soc. America. PDP3, 2007.

[2] T. Ishibashi, *et al.*, “InP/InGaAs uni-traveiling-carrier photodiodes,” *IEICE Trans. Electron.*, vol. E83-C, pp. 938-949, Jun. 2000

[3] J. Klamkin *et al.*, “High Output Saturation and High-Linearity Uni-Traveling-Carrier Waveguide Photodiodes,” *IEEE Photonics Technol. Lett.*, vol. 19, no. 3, pp. 149-151, Feb. 2007.

[4] J. Klamkin *et al.*, “Uni-Traveling-Carrier Waveguide Photodiodes with>40dBm OIP3 for up to 80mA of Photocurrent”, Device Research Conference (DRC). Late News Jun. 2008.

[5] T. Ohno, *et al.*, “Measurement of intermodulation distortion in a unitraveling-carrier refracting-facet photodiode and a p-i-n refracting facet photodiode,” *IEEE Photonics Technol. Lett.*, vol. 14, no. 3, pp. 375-377, Mar. 2002.

[6] K.J. Williams and R.S. Esman,”Design Consdierations for high-current photodetectors,” *J. Lightw. Technol.*,vol. 17, no.8, pp. 1443-1454, Aug. 1999.

[7] T. Ohno and E.H. Hara., “Measurement of nonlinear distortion in photodiodes,” *Electron. Lett,* vol. 12, pp. 80-90, 1976.

II. Vertical-Cavity Surface-Emitting Lasers

1.5mW/Gbps Low Power Optical Interconnect Transmitter Exploiting High-Efficiency VCSEL and CMOS Driver

Shigeru Nakagawa[1], Daniel Kuchta[2], Clint Schow[2], Richard John[2]
[1] IBM Tokyo Research Laboratory, 1623-14 Shimo-tsuruma, Yamato, Kanagawa 242-0852, Japan
[2] IBM T. J. Watson Research Center, 1101 Kitchawan Road, Yorktown Heights, NY 10598, USA
e-mail: snakagw@jp.ibm.com

Larry A. Coldren, Yu-Chia Chang
Department of Electrical and Computer Engineering, University of California, Santa Barbara, CA 93106 USA

Abstract: We demonstrate a low power optical interconnect transmitter which employs a 990nm VCSEL with high efficiency and low threshold current, and a 130nm CMOS driver. The power dissipated by the transmitter is 15.1 mW at 10 Gbps.

OCIS codes: (060.2360) Fiber optics links and subsystems; (200.4650) Optical Interconnects;

1. Introduction

Requirements for interconnects in computing systems are getting harder to satisfy without employing optical technologies, as the performance keeps growing with the evolution of CMOS technologies as well as system architectures. The emphasis of system designs has been shifting toward reducing power consumption from increasing performance. The total system power, including the power required for cooling as well as for computation, is reaching to or even exceeding the limit of power supply when the system performance is increased. One main advantage of optical compared to electrical interconnects, in addition to the benefit of long-distance transmission at high data rate with optics, is a high data rate density, which provides large bandwidth through a small volume or area. This results in an efficient flow of cooling air through systems as well as tight integration of optical interconnects with electronic chips. As the bandwidth and channel count of interconnects has to be increased for evolving system performance and architecture, these benefits of optical interconnects are crucial.

Reduction of the power consumed by optical interconnects is critical to increase the aggregate interconnect bandwidth for further system performance improvement. Several efforts have been made to realize high data rates with low power dissipation, and recent breakthroughs have been made by deploying CMOS technology for high-speed laser diode drivers (LDDs) and high-speed transimpedance amplifiers plus limiting amplifiers (TIA/LIAs) [1, 2]. VCSELs have already demonstrated their inherent advantage of low-power and high-speed operation, suited for light sources of optical interconnects, and more emphasis has been placed on design optimization for high-speed operation [3]. In this talk, we design and demonstrate a very low power optical interconnect by focusing on reducing the power dissipation of the whole optical link, instead of decreasing the power consumed by each component individually. More specifically, we focus on the design of optical transmitters, which consist of the VCSELs and LDDs, to realize high optical modulation amplitude (OMA) with small modulation current, enabling reductions of the power dissipated by the LDD and TIA/LIA. The low power design presented in this talk can be also applied to any short-reach datacom and telecom transmitters based on VCSELs.

2. Low power optical interconnect design

An optical interconnect, shown in Fig. 1, has to be designed to meet the requirements of input and output electrical signals, such as a voltage amplitude and data rate. The VCSEL drive current and the optical link budget, however, have more freedom to be designed as long as error-free transmission is achieved and the swing voltage requirements are met. One approach to minimize the total power dissipation of an optical interconnect is to decrease the VCSEL modulation current, while simultaneously increasing the transmitted OMA. The reduced modulation current lowers the power dissipated by the LDD both in the pre-driver and output stages. Increased OMA further enables a reduction in the TIA/LIA power consumption due to lower required gain. Increasing the differential quantum efficiency (DQE) of a VCSEL provides larger OMA with smaller modulation current. One way to increase the DQE of a VCSEL is to decrease its internal loss, which also reduces its threshold material gain. The reduced threshold gain results in decreased power dissipation in the LDD output stage due to lowered bias current while supporting high-speed operation and enough optical average power. The DQE of a VCSEL can also be increased by decreasing the reflectivity of the output mirror, but at the expense of increased bias current.

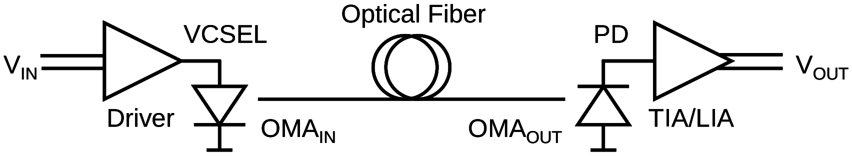

Fig.1. Optical interconnect diagram.

3. Results

One of the authors' group has demonstrated high-efficiency and high-speed 990nm VCSELs [4]. The low internal loss attributed to a short tapered oxide aperture brings both high DQE and high modulation efficiency. The VCSELs were characterized at room temperature before building a transmitter module as shown in Fig. 2. The detailed performance of the VCSELs has been already described in [4]. Some key characteristics for a 6μm-aperture device are the DQE at a bias current of 2.0 mA = 56 %, the threshold current = 0.35 mA, the threshold current density = 1.2 kA/cm^2, the series resistance at 2.0 mA = 150 Ω, and the 3dB modulation bandwidth at 2.0 mA = 11.5 GHz. The measured emission wavelength was 987 nm.

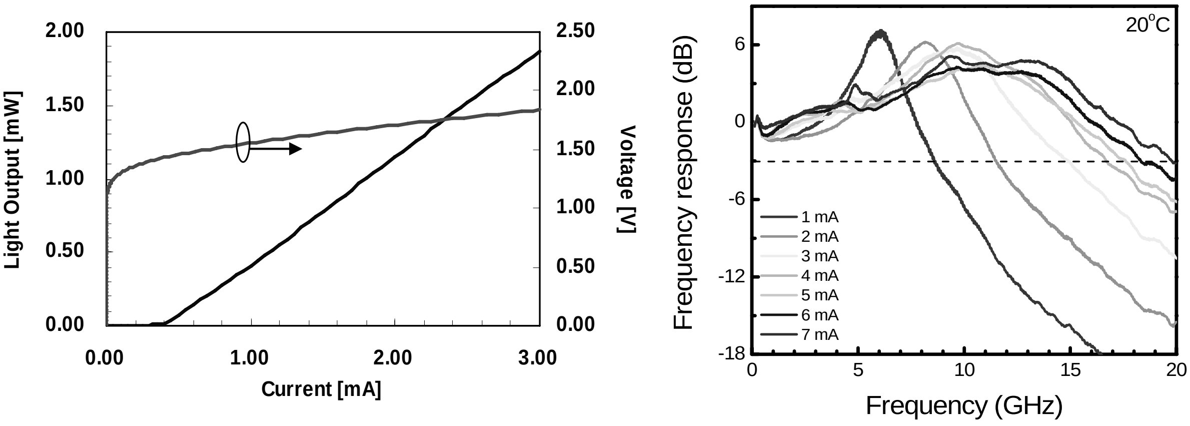

(a) (b)

Fig.2. (a) DC LIV characteristics, and (b) small-signal frequency response of 990nm, 6-μm aperture, bottom emitting VCSEL.

A transmitter module was built with a LDD fabricated in the IBM CMOS8RF technology (130 nm) and a 6μm-aperture VCSEL, both mounted on a test card. The VCSEL is backside emitting, so the card was modified by drilling a 1mm-diameter hole. The light coming out of the VCSEL through the hole was collected with a lensed multimode fiber. High-speed electrical signals were fed into the LDD using a Cascade GSSG air-coplanar probe. RF electrical signals were generated by an SHF 40 G/s pattern generator, while optical signals were detected by a 17-GHz bandwidth Newport photodiode and characterized with a Tektronics digital signal analyzer.

Optical eye diagrams were taken with various operational conditions of the transmitter. Fig. 3(a) was taken at 10 Gbps with supply voltages of the LDD pre-amplifier and output stage of 1.2 V and 2.4 V, respectively. The OMA was -0.8 dBm, and the extinction ratio was 4.0 dB. Such large OMA decreases the required receiver gain, which likely translates into a reduction of receiver power dissipation. The light was obtained through 500μm-thick substrate, and the OMA can be larger if the VCSEL is top emitting. For the 10Gb Ethernet eye mask, no mask hits were detected with +15% margin for 2^7 -1 PRBS over 100 waveforms. The measured current of the pre-amplifier and the output stages was 4.0 mA and 4.3 mA, respectively, meaning the total power dissipation of the transmitter was 15.1 mW, or 1.5 mW/Gbps at 10 Gbps. This is the lowest power dissipation for a 10-Gb/s-class optical transmitter ever reported [2]. The LDD utilized in this experiment was not specifically designed for such low modulation and bias currents, and therefore may be optimized in future LDD designs for further power reduction. Further power reduction is expected by employing 90nm CMOS technology instead of 130nm to achieve higher speed and lower power.

The optical eye diagram was measured also for a transmitter with a 4μm-aperture device and the same CMOS LDD. Fig. 3(b) is the eye diagram at 15 Gbps, and at this rate, the total power consumption is 13.6 mW, or 0.9 mW/Gbps, with an OMA of -1.6 dBm. Although the observed eye diagram is relatively noisy, which may be attributed to modal noise, this result indicates the potential of optical interconnect transmitters operating beyond 10 Gbps and dissipating power less than 1.0 mW/Gbps.

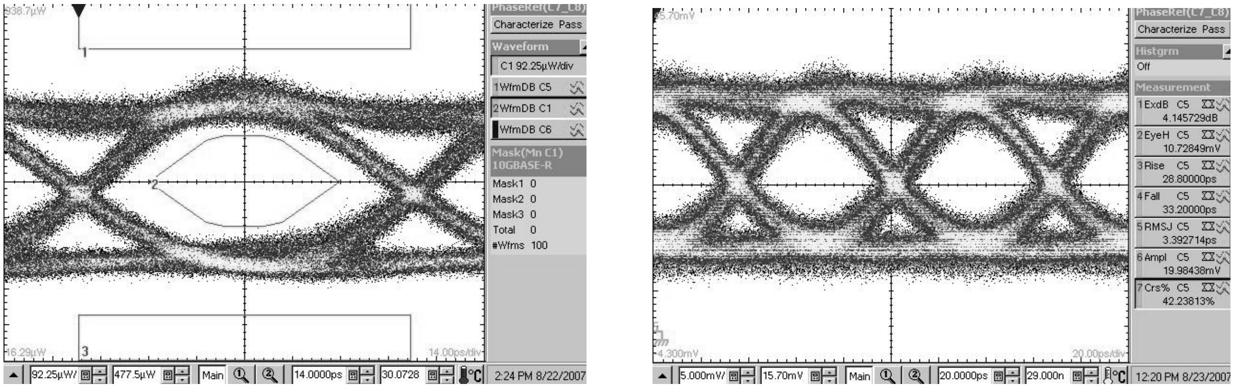

Mask1 0
Mask2 0
Mask3 0
Total 0
#Wfms 100

1 ExdB C5 4.145729dB
2 EyeH C5 10.72849mV
3 Rise C5 28.80000ps
4 Fall C5 33.20000ps
5 RMSJ C5 3.392714ps
6 Ampl C5 19.98438mV
7 Crs% C5 42.23813%

(a) 10Gbps eye diagram with 6μm VCSEL

(b) 15Gbps eye diagram with 4μm VCSEL

Fig.3. Measured optical eye diagrams of transmitters with two sizes of VCSELs and the same CMOS LDD with bias conditions optimized for low power dissipation. (a) is with 10Gb Ethernet mask with +15% margin.

4. Conclusion

We have demonstrated a low power optical interconnect transmitter exploiting a high-efficiency VCSEL and a CMOS LDD. In this experiment, a 990nm VCSEL with a DQE of 56% is employed, and operation at 10 Gbps with an OMA of -0.8 dBm was demonstrated at a record-low power dissipation of 15.1 mW, or 1.5 mW/Gbps. The transmitter also indicated the potential of the 15Gbps operation at a power dissipation of 0.9 mW/Gbps. The low power optical interconnect design approach discussed in this paper can be applied to any level of optical interconnects, such as discrete optical transceiver modules or waveguide-based optical interconnects on printed circuit boards [5, 6], and it will accelerate the deployment of optical interconnects into high-performance computing systems. The low power design presented in this talk also enables the power reduction of VCSEL-based optical transmitters for short-reach datacom and telecom.

This work was partially supported by NEDO under Optical waveguide technology for low-power ultra-high-speed interconnect project, and DARPA under contract MDA972-03-3-0004.

5. References

[1] C. Schow, F. Doany, O. Liboiron-Ladouceur, C. Baks, D. Kuchta, L. Schares, R. John, and J. Kash, “160-Gb/s, 16-channel full-duplex, single-chip CMOS optical transceiver,” in *Tech. Dig. Optical Fiber Communication Conf.*, Anaheim, CA, March 2007.

[2] C. Kroemer, G. Sialm, C. Berger, T. Morf, M. L. Schmatz, F. Ellinger, D. Erni, G.-L. Bona, and H. Jackel, “A 100-mW 4 x 10 Gb/s transceiver in 80-nm CMOS for high-density optical interconnects,” *IEEE J. Solid-State Circuits*, **40**, pp. 2667-2679, 2005.

[3] N. Suzuki, H. Katakeyama, K. Fukatsu, T. Anan, K. Yashiki, and M. Tsuji, “25-Gbps operation of 1.1-mm-range InGaAs VCSELs for high-speed optical interconnects,” in *Tech. Dig. Optical Fiber Communication Conf.*, Anaheim, CA, March 2006.

[4] Y.-C. Chang, C. S. Wang, and L. A. Coldren, “High-efficiency, high-speed VCSELs with 35 Gbit/s error-free operation,” *Electron. Lett.*, **43**, pp. 1022-1023, 2007.

[5] F. E. Doany, “160-Gb/s, bidirectional parallel optical transceiver module for board-level interconnects using a single-chip CMOS IC,” in *Proc. 57th Electron. Comp. and Technol. Conf.*, Reno, NV, May 2007.

[6] S. Nakagawa, Y. Taira, H. Numata, K. Kobayashi, K. Terada, Y. Tsukada, “High-density optical interconnect exploiting build-up waveguide-on-SLC board,” submitted to *58th Electron. Comp. and Technol. Conf.*, Lake Buena Vista, FL, May 2008.

Small Optical Sources with Improved Speed/Power Dissipation

Larry A. Coldren and Yu-chia Chang
ECE and Materials Depts., University of California, Santa Barbara, CA
coldren@ece.ucsb.edu

For optical interconnects it is desirable to maximize the date rate for a given power dissipation. In our recent work we have managed to obtain a record data-rate/power dissipation value of 3.5 Gps/mW in a novel VCSEL that was transmitting 35 Gps data at an optical power level of 2.5 mW . At somewhat lower powers a bandwidth/$\sqrt{\text{current}}$ of 17 GHz/mA$^{1/2}$ was also found. These results were obtained by engineering the VCSEL cavity to have low optical loss, low parasitics, and a small volume. This involved the use of optimized tapered oxide apertures, additional deep oxidation layers, and carefully engineered compositions and dopings in the mirrors. This talk will discuss the design principles involved.

In the past several years, vertical-cavity surface-emitting lasers (VCSELs) have received renewed interest for their potential applications in optical interconnects. Compared with edge emitters, VCSELs are preferable due to their small footprint, ease of fabrication in arrays, on-wafer testing, high-speed operation at lower power dissipation, and cost effectiveness.

Figure 1 illustrates some of our results for a device with a 3μm aperture. Details of the device structure and fabrication can be found in refs. [1, 2]. The design of the structure involves many trade-offs, including electrical resistance vs.optical absorption loss and mode confinement vs. optical scattering loss. A new blunter taper was used compared to our prior work[3]. The voltage, output power, and temperature rise against current (L-I-V-T) curves show a very low threshold current of 0.144 mA and a high slope efficiency of 0.67 W/A. This low threshold as well as high efficiency indicates that our short tapered oxide aperture does not introduce excess optical loss even down to 3 μm diameter range. However, it does result in a modal volume reduction factor of 1.73, corresponding to a 31% increase in intrinsic bandwidth. The bit-error-rate curve at 35 Gb/s was taken with a non-retrun-to-zero signal having a 2^7-1 word length. The bias current was 4.4 mA and the RF voltage swing was ~0.84 V$_{p\text{-}p}$. The inset shows the optical eye diagram and the eye is clearly open with an extinction ratio of 5.4 dB, despite a relatively low 25 GHz bandwidth reciever that limited the measurement. The VCSEL power dissipation, excluding the RF circuitry, is only 10 mW. This corresponds to the highest data-rate/power-dissipation ratio of 3.5 Gbps/mW.

[1] Y.-C. Chang, C.S. Wang and L.A. Coldren: “High-efficiency, high-speed VCSELs with 35 Gbit/s error-free operation,” *Electron. Lett.*, **43** (9) pp. 1022–1023, 2007.

[2] Y.-C. Chang, C.S. Wang, L.A. Coldren: “Small-dimension power-efficient high-speed vertical-cavity surface-emitting lasers,” *Electron. Lett.*, **43** (7) pp. 396–397, 2007.

[3] E.R. Hegblom, D.I. Babic, B.J. Hibeault, and L.A.Coldren: “Scattering losses from dielectric apertures in vertical-cavity lasers,” *IEEE J. Sel. Topics Quantum Electron.*, **3**, pp. 379–389, 1997.

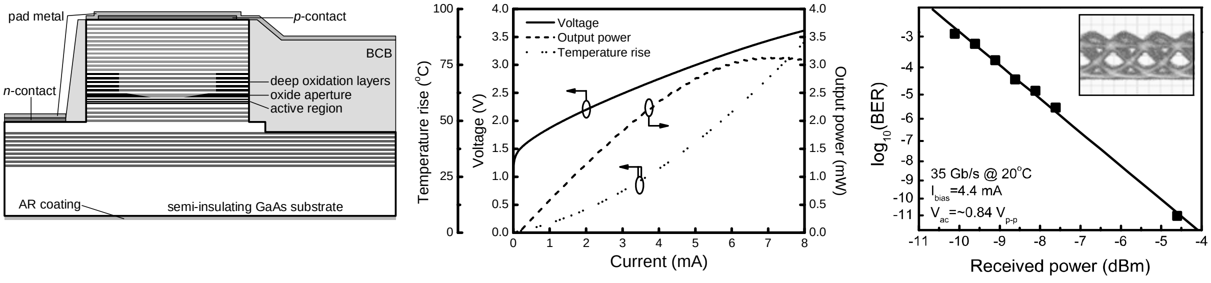

Figure 1: Tapered-oxide-aperture VCSEL and results.

Ultra-fast VCSELs promise to turbocharge chip communication

The copper interconnects that route chip-to-chip data transfer are starting to reach their speed limit. But this looming bottleneck can be overcome by switching to ultra-fast VCSELs with tiny threshold currents, say **Yu-Chia Chang** and **Larry Coldren** from the University of California, Santa Barbara.

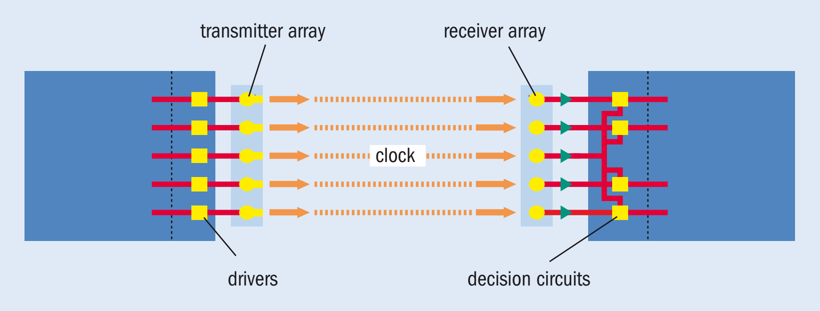

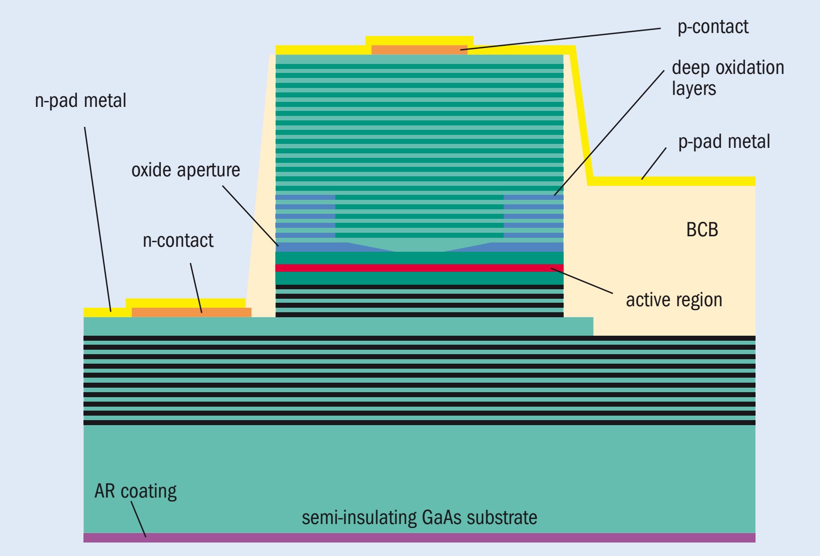

Fig. 1. (top) UCSB's VCSEL could be used to form an array of transmitters that provide chip-to-chip interconnects. **Fig. 2.** (bottom) The UCSB InGaAs/GaAs quantum-well design features a blunter tapered aperture that enables very high modulation speeds at acceptable optical losses.

Finally the silicon folks might actually need us. The copper interconnects that they are using are running out of steam, and this is starting to obstruct their advances in interchip communication. It's a weakness that's even threatening to bump Moore's law off course because the electrical input and output functions needed in tomorrow's state-of-the-art microprocessors will dissipate more power and demand a greater share of a chip's real estate. Even today data transfer is a complicated task. Loss, dispersion and cross-talk have to be addressed with predistortion and sophisticated pulse recovery techniques in the transmit and receive stages, respectively.

Against this background of increasing complexity, optical interconnection schemes look like a good bet for the future. This technology offers several key advantages over copper, such as lower signal delay, higher bandwidth, reduced power consumption and freedom from electromagnetic interference. In addition, it has the potential to deliver intrachip communication.

However, optical interconnects will only offer a practical solution if improvements are made to devices and interface systems. Copper is a viable solution at speeds of up to 10 Gbit/s, so data rates must be at least 20 Gbit/s for optoelectronics to be considered an option. Low power consumption is another prerequisite, alongside the ability to be integrated with silicon electronics. But there is no point in trying to meet any of these goals unless the emitters and detectors can be manufactured in large volumes with high yields.

At the University of California, Santa Barbara (UCSB), we are working on a device that could be the key component in chip-to-chip optical interconnects – a miniature, high-speed, efficient VCSEL. It has evolved out of our part of the US Defense Advanced Research Projects Agency's chip-to-chip optical interconnects program, which also supports IBM's "Terabus" project. It aims to demonstrate complete optical links between chips using polymer waveguides (figure 1). It's a technology that's competing with silicon photonics, but which offers lower power dissipation – the primary limiter for continued scaling of processor speed.

There are several benefits that VCSELs offer over their edge-emitting cousins for optical interconnect applications: they are smaller; they are easier to fabricate in arrays; they support on-wafer testing; they offer high-speed operation at lower power consumption; and they are cheaper. However, many of the VCSELs that have been designed for optical interconnects have large diameter apertures – typically

Fig. 3. (right) This cross-sectional scanning electron image reveals key features in the UCSB VCSEL – five deep oxidation layers and a tapered oxide aperture. **Fig. 4.** (far right) UCSB's high-speed VCSELs are fabricated with the following process steps: **(a)** mesa etch, **(b)** oxidation, **(c)** n-metal deposition, **(d)** p-metal deposition, **(e)** n-contact removal, **(f)** patterning with a low-dielectric resin, **(g)** pad metal deposition, and **(h)** adding an anti-reflection coating.

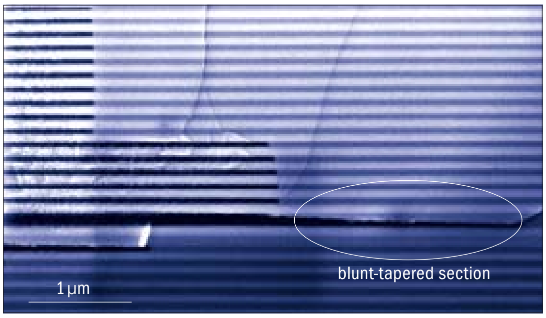

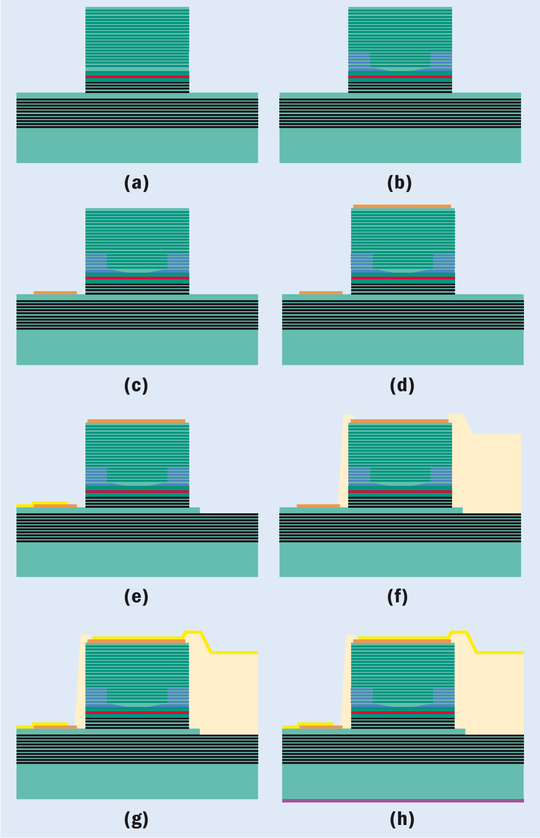

5–8 µm – that drive up the bias current required for a high modulation bandwidth. We avoid this pitfall by scaling down the VCSEL size. Although this leads to a power drop of 50%, it cuts power dissipation and increases the bandwidth, while maintaining acceptable optical losses.

The devices that we have made are 980 nm bottom-emitting VCSELs with a tapered oxide aperture and a contact inserted within the n-type cavity (figure 2, p29). The standard emission wavelength of 850 nm was not selected because the strained InGaAs/GaAs quantum wells (QWs) that produce 980 nm emission deliver a higher intrinsic modulation bandwidth thanks to higher gain at lower carrier densities. Some studies suggest that InGaAs QW-lasers are more reliable. But more importantly, this particular design is compatible with bottom-emission thanks to GaAs' transparency at 980 nm.

Bottom emission means that flip-chip bonding can be used to integrate our VCSELs with electronics. This eliminates wire bond inductance and the need for wire bonding. Backside microlenses can be added to collimate the output beam, which improves alignment tolerance and cuts packaging costs. This combination of advantages should equip our devices with the compatibility required for advanced computer and processor interconnection architectures and other datacom applications.

Our VCSEL's key feature compared with prior art is a blunter tapered aperture and a larger oxide thickness next to the active region (figure 3). This provides a high degree of optical confinement and enables our laser to combine high speeds with acceptable optical losses. Employing a longer tapered section would reduce optical losses even further, but this results in larger mode volumes with an unacceptable penalty of much slower modulation speeds.

The parasitic capacitance of a relatively thin oxide aperture can restrict the modulation bandwidth of oxide-confined VCSELs. The capacitance is often reduced by proton implantation, which creates a thick, highly resistive region. However, this highly effective method requires additional process steps that threaten reliability, and increase fabrication costs and parasitic resistance.

We get around this problem by creating additional deep oxidation layers above the confining aperture, which lower the parasitic capacitance. By increasing the aluminum fraction of the AlGaAs layers in the first several periods of the top distributed Bragg reflector, we can simultaneously form deep oxidation layers along with the oxide aperture.

It is easy to incorporate this simple approach into oxide-confined VCSELs with semiconductor mirrors. No modifications to the fabrication techniques are required, and it increases the refractive index contrast in the unoxidized region where optical modes exist, thanks to the layers with higher aluminum content. This means that mode volume is cut because the longitudinal mode is more confined. On top of this, reductions in parasitic resistance are delivered with minimal impact to optical loss, thanks to high-quality engineering of the band-structure and the p-doping profiles in the top mirror.

Our approach to VCSEL fabrication is compatible with existing manufacturing processes and begins with MBE growth of the epitaxial structure on semi-insulating (100) GaAs substrates (see figure 4 for an overview). Etching creates cylindrical mesas that expose the n-GaAs contact layer, before wet oxidation forms oxide apertures and deep oxidation layers. Metal evaporation adds the p-type Ti/Pt/Au and n-type Au/Ge/Ni/Au contacts.

Pad capacitance is reduced by removing the part of the n-GaAs contact layer (RF-ground) that lies beneath the p-pad metal (RF-signal). The low dielectric constant resin benzocyclobutene is inserted in its place before vias are opened to expose the contacts and Ti/Au is deposited for the pad metals. Finally, an anti-reflection coating is

> "This device's bandwidth makes it the fastest ever 980 nm VCSEL."

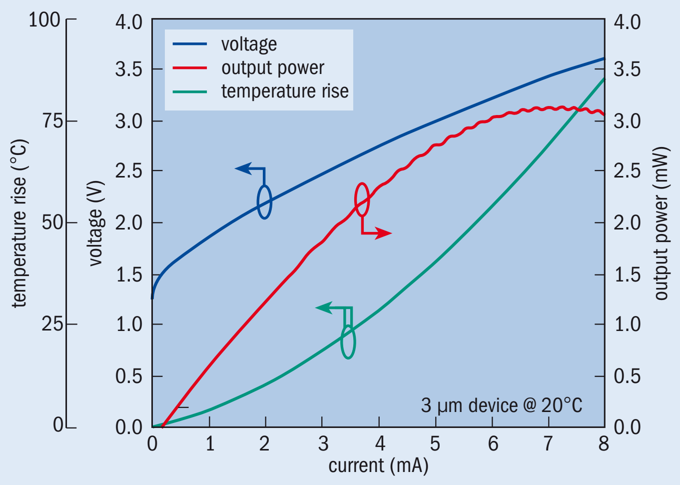

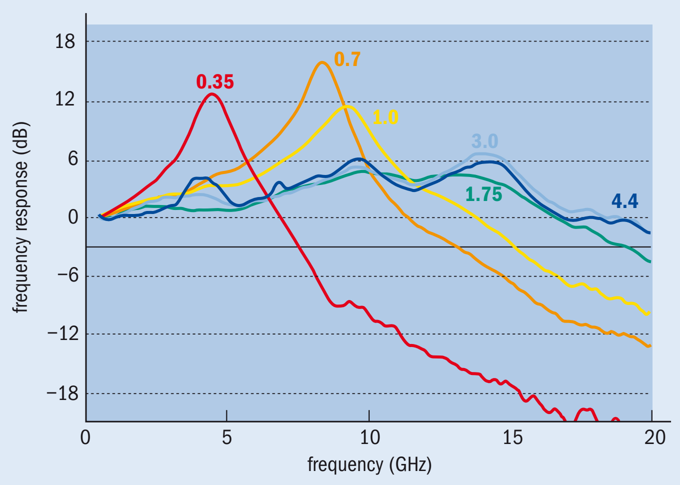

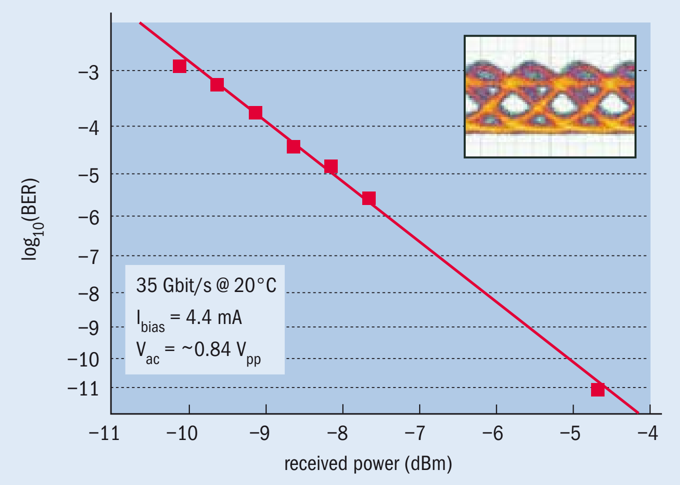

Fig. 5. (top left) UCSB's 3 µm diameter aperture VCSELs deliver up to 3 mW at 20 °C. This laser has a series resistance of approximately 250 Ω at 4.4 mA bias current, the conditions that are used for the large signal experiments. Thermal impedance is 3.3 °C/mW and the temperature rise is 33 °C at this current, but improvements may be possible through refinements in the design of the VCSELs. **Fig. 6.** (top right) Adjustments in bias current from 0.35–4.4 mA alter the modulation speed of the 3 µm diameter device, which is highest at 4.4 mA. At this bias the modulation exceeds 20 GHz, which is a record for 980 nm VCSELs. **Fig. 7.** (left) Bit error rates (BERs) were measured for UCSB's 35 Gbit/s, 3 µm diameter device at 20 °C. This VCSEL was biased at 4.4 mA and a peak-to-peak voltage swing of 0.84 V was used. The input was a non-return-to-zero signal with 2^7−1 word length. Eye diagrams are shown in the inset figure, which reveal that the eye is clearly open. The extinction ratio is 5.4 dB. In the BER curve, a variable optical attenuator (VOA) was used to take all but the lowest data point. Poor detector responsivity and a 3 dB insertion loss of the VOA prevented the measurement of BERs between 10^{-4} and 10^{-7}. To ensure measurement accuracy, the lowest data point was gated for 30 minutes with a total of 583 errors.

applied to reduce backside reflection.

We have produced 3 µm diameter aperture VCSELs with this process. These emitters have a slope efficiency of 0.67 W/A, which corresponds to a differential quantum efficiency of 54% (figure 5). Threshold current is just 0.144 mA, which is comparatively low for high-speed VCSELs as they usually have threshold currents of at least 0.4 mA. Peak wall-plug efficiency is 31%, maximum output power is 3.1 mW and the threshold voltage is just 1.47 V – very low for such a small device as it is only 220 meV larger than the photon energy.

Small-signal modulation measurements on our 3 µm aperture emitter revealed that it could respond to frequencies beyond 20 GHz, the upper detection limit for our instrument (figure 4). This device's bandwidth clearly exceeds that frequency, which makes it the fastest ever 980 nm VCSEL.

We evaluated this device's suitability for real-world systems with large-signal digital modulation experiments. At 20 °C and a modulation rate of 35 Gbit/s, our 3 µm diameter device produced bit error rates as low as 10^{-11} over a couple of meters of fiber, which demonstrates that it is suitable for high-quality interchip communication. The VCSEL power dissipation, excluding RF circuitry, is only 10 mW, which corresponds to the highest data rate/power-dissipation ratio that has ever been obtained for any type of laser source.

We are now targeting data rates of 40 Gbit/s, which can be reached by simply extending our existing techniques. However, we are also engaged in another project that has the potential to get us to the 100 Gbit/s range with a single channel. If such high speeds could be achieved, then this will further enhance the attractiveness of employing VCSELs for chip-to-chip interconnects. ●

Further reading

T Anan 2007 *Proc. International Symposium on VCSELs and Integrated Photonics* E3.
Y-C Chang *et al.* 2006 *Electron. Lett.* **42** 1281.
Y-C Chang *et al.* 2007 *Electron. Lett.* **43** 1022.
E Hegblom *et al.* 1997 *IEEE J. Select. Topics Quantum Electron.* **3** 379.
A A L-Omari *et al.* 2004 *IEEE Photon. Technol. Lett.* **16** 969.
L Schares *et al.* 2006 *IEEE J. Sel. Topics Quantum Electron.* **12** 1032.
E Strzelecka *et al.* 1995 *Electron. Lett.* **31** 724.

About the authors

Larry Coldren (left) is the Fred Kavli professor of optoelectronics and sensors at UCSB, and the director of the university's Optoelectronics Technology Center. He joined UCSB in 1984 after spending 13 years as a researcher at Bell Laboratories. **Yu-Chia Chang** (right) is a PhD student in the electrical and computer engineering department at UCSB. His research interests include the design, growth and characterization of high-speed VCSELs.

Optimization of VCSEL Structure for High-Speed Operation

Yu-Chia Chang and Larry A. Coldren
ECE Department, University of California, Santa Barbara, CA 93106 USA
TEL: (805) 893-7065, FAX: (805) 893-4500, email: yuchia@engr.ucsb.edu

Abstract—**The optimization of our tapered-oxide-apertured VCSEL structure for high-speed operation is presented. Using a new aperture design and *p*-doping recipe in the top mirror, bandwidths $>$ 20 GHz and 35 Gb/s error-free operation has been demonstrated.**

I. INTRODUCTION

In the past several years, vertical-cavity surface-emitting lasers (VCSELs) have received renewed interest for their potential applications in optical interconnects. Compared with edge emitters, VCSELs are preferable due to their small footprint, ease of fabrication in arrays, on-wafer testing, high-speed operation at lower power dissipation, and cost effectiveness. Last year, we first demonstrated 35 Gb/s error-free operation on 3 μm diameter high-speed VCSELs [1]. This achievement was enabled by the optimization of several key components of our VCSEL structure, especially tapered oxide aperture and *p*-doping in the top mirror, in order to minimize cavity loss and mode volume.

II. DEVICE DESIGN

We use *n*-intracavity, bottom-emitting, tapered-oxide-apertured VCSEL structure emitting at 980 nm wavelength. Details of the device structure and fabrication can be found in [1], [2]. The design of the structure involves many trade-offs and one of them is the electrical resistance and optical loss by doping concentration. Bandgap-engineering is commonly used to simultaneously achieve low resistance and low loss. Due to higher free carrier absorption loss and lower mobility of holes, we mainly focused on the optimization of the *p*-mirror. Fig. 1(a) plots the average doping concentration for each DBR period. Three different doping levels are used to approximate the calculated ideal doping profile. The doping is the lowest near the active region for low optical loss and increases as moving towards the top contact layer. Fig. 1(b) shows the low-doped DBR design within the period. At the standing-wave peaks, bi-parabolic grade and modulation doping is used to flatten the valence band [3]. On the other hand, uni-parabolic scheme is used at the standing-wave nulls so that holes are accumulated at the interfaces to reduce the resistance without adding extra losses [4].

Another trade-off is the mode confinement and optical scattering loss by aperture design. Fig. 2(a) shows two tapered oxide aperture designs. The top one is our original design which yields negligible optical scattering loss down to 1.5 μm diameter devices. However, it does not provide enough mode confinement for efficiently achieving high bandwidth. To optimize the aperture design, we simulated round-trip scattering loss and effective mode radius as a function of the taper length for a $\lambda/2$ thick aperture based on the model in [5]. The results are plotted in Fig. 2(b). Taper length of 4 μm was chosen and the final design is shown in the bottom of Fig. 2(a). Compared with our original design for 3 μm diameter devices, the effective mode radii reduced from 2.64 to 2.01 μm, corresponding to a 1.73 time mode volume reduction, which should give a 31% increase in relaxation resonance frequency and bandwidth. At the same time, the optical scattering loss does not increase noticeably.

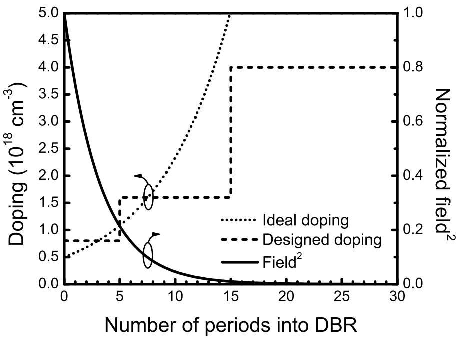

(a) Average doping profile

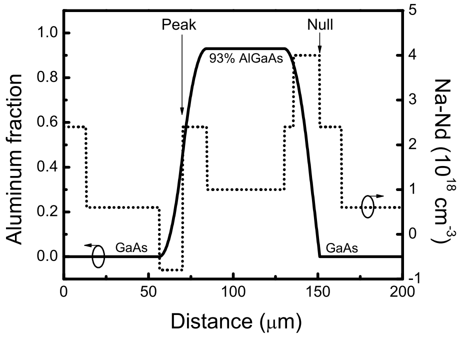

(b) Doping/grading within one period

Fig. 1: Optimization of the doping in the *p*-mirror.

III. RESULTS

Fig. 3 shows the voltage, output power, and temperature rise against current (L-I-V-T) curves for a 3 μm diameter device. The device has a very low threshold current of 0.144 mA and a high slope efficiency of 0.67 W/A. This low threshold as well as high efficiency indicates that our short tapered

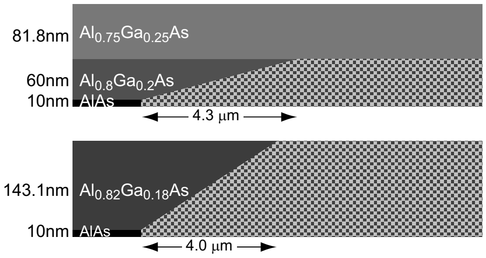

(a) Top: long taper design and bottom: short taper design.

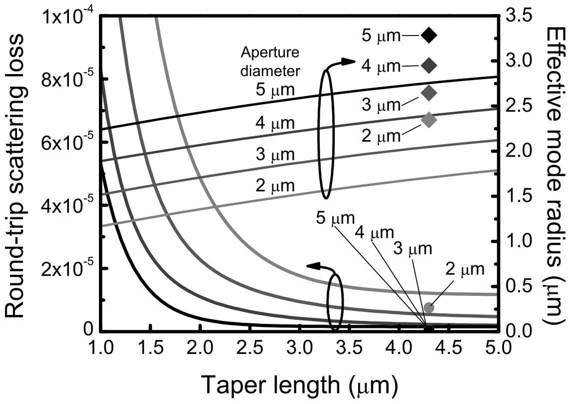

(b) Simulated optical scattering loss and effective mode radius as a function of taper length for the devices with diameters ranging from 2 to 5 μm. Superimposed are the results for the long taper aperture: diamonds (effective mode radius) and circles (scattering loss).

Fig. 2: Optimization of tapered oxide aperture.

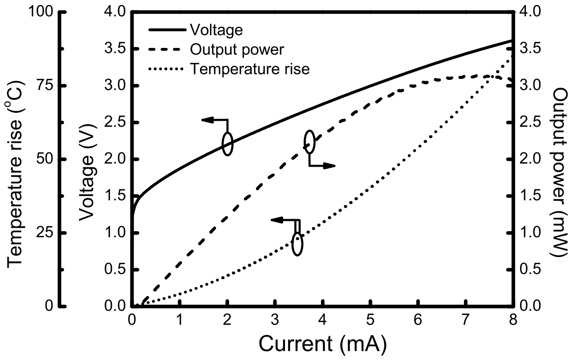

Fig. 3: L-I-V-T curves for 3 μm diameter device.

oxide aperture indeed does not introduce excess optical loss even down to 3 μm diameter range. The threshold voltage is only 1.47 V, 220 meV larger than the photon energy. This low threshold voltage is the consequence of the optimized *p*-doping scheme and the low threshold current. The series resistance is approximately 250 Ω at a bias current of 4.4 mA, where large-signal modulation experiments were performed. The peak wall-plug efficiency is 31% and the maximum output power is 3.1 mW. The thermal impedance of the devices is 3.3°C/mW.

Fig. 4(a) plots the 3-dB frequency versus $(I - I_{\text{th}})^{1/2}$. A bandwidth exceeding 20 GHz is achieved at bias currents > 2 mA. This is the highest bandwidth for 980 nm VCSELs. The modulation current efficiency factor (MCEF) of this device is 16.7 GHz/mA$^{1/2}$, very close to the highest 16.8 GHz/mA$^{1/2}$ for QW-based VCSELs [6]. This high MCEF is the consequence of better lateral mode confinement from our short tapered oxide aperture. Fig. 4(b) plots the bit-error-rate curve at 35 Gb/s for a 3 μm diameter device [1]. The input was a non-retrun-to-zero signal with 2^7-1 word length. The bias current was 4.4 mA and the RF voltage swing was ~ 0.84 $V_{\text{p-p}}$. The inset shows the optical eye diagram and the eye is clearly open with an extinction ratio of 5.4 dB. The VCSEL power dissipation, excluding the RF circuitry, is only 10 mW. This corresponds to the highest data-rate/power-dissipation ratio of 3.5 Gbps/mW.

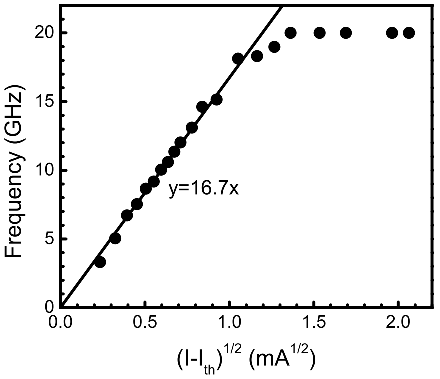

(a) 3-dB frequency vs. $(I - I_{\text{th}})^{1/2}$

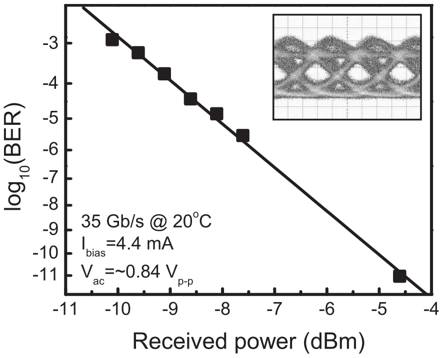

(b) Bit-error-rate curve

Fig. 4: High-speed performance for 3 μm diameter device.

IV. CONCLUSION

By carefully designing the *p*-doping profile in the top mirror as well as the shape of the tapered oxide aperture, we demonstrate an improvement in our VCSELs' high-speed performance without compromising the static performance. Modulation bandwidth exceeding 20 GHz at bias currents $>$ 2 mA has been achieved. Moreover, data rate up to 35 Gb/s is demonstrated for only 10 mW power dissipation.

REFERENCES

[1] Y.-C. Chang *et al.*, *Electron. Lett.*, vol. 33, pp. 1022–1023, 2007.
[2] Y.-C. Chang *et al.*, *Electron. Lett.*, vol. 43, pp. 396–397, 2007.
[3] M.G. Peters *et al.*, *Appl. Phys. Lett.*, vol. 63, pp. 3411–3413, 1993.
[4] K.L. Lear *et al.*, *Appl. Phys. Lett.*, vol. 68, pp. 605–607, 1996.
[5] E.R. Hegblom *et al.*, *IEEE J. Sel. Topics Quantum Electron.*, vol. 3, pp. 379–389, 1997.
[6] K.L. Lear *et al.*, *Electron. Lett.*, vol. 32, pp. 457–458, 1996.

III. Cavity QED and Single-Photon Emitters

WY1 (Invited)
3:30 PM – 4:00 PM

High frequency single photon sources

Stefan Strauf[1,2], Matthew T. Rakher[1], Nick G. Stoltz[3] , Larry A. Coldren[3,4], Pierre M. Petroff[3,4], and Dirk Bouwmeester[1,5]

1. Department of Physics, University of California, Santa Barbara, CA 93106, USA
2. Department of Physics and Engineering Physics, Stevens Institute of Technology, Hoboken, NJ 07030, USA
3. Department of Materials, University of California, Santa Barbara, CA 93106, USA
4. Department of Electrical Engineering, University of California, Santa Barbara, CA 93106, USA
5. Huygens Laboratory, Leiden University, P.O. Box 9504, 2300 RA Leiden, The Netherlands

Recent years have shown tremendous progress in the fabrication of single photon sources (SPS) based on quantum dots (QDs) embedded in semiconductor micro and nanocavities which are of interest for applications in quantum information science [1].

Here we will review our recent work on high-frequency single photon sources operating at single photon emission rates above 100MHz. To effectively harvest the radiative recombination of QD excitons and to overcome the total internal reflection losses of high index semiconductor materials the emission can be coupled into a cavity mode. We have characterized the single photon emission of individual QDs from two types of cavities: Photonic crystal nanocavities with quality factors up to 18000 [2] and oxide apertured microcavities with quality factors up to 50000 [3,4]. Comparing the emission of QDs inside the cavity region with those in the unprocessed areas we find typical geometrical enhancement factors of 12-fold for photonic crystals and 45-fold for apertured microcavities. Measured values of the zero delay time peak are of the second-order correlation function are typically 3-7% at low pump powers. The comparison has been made for QDs with measured radiative lifetimes of about 1 ns, i.e. for those QDs which do not show a Purcell effect due to spatial and/or spectral mismatch between emitter and mode. Characterizing hundreds of devices and tuning mode and emitter into spectral resonance we typically do not find a Purcell enhancement for the photonic crystals due to the extremely small spatial mode extend and low areal density of QDs leading to a radiative lifetimes which is often inhibited up to an order of magnitude [2,5]. In contrast, about half of the fabricated oxide apertured microcavites devices display a 3-fold spontaneous emission enhancement [4-6] with best values up to a Purcell-factor of six [5]. From a technological point of view the oxide-tapered microcavities are preferred since they display larger geometrical enhancement factors, are mechanically rugged, can be easily coupled to an optical fiber, and provide an additional Purcell enhancement without the need for a sophisticated nanofabrication technique to actively match the mode and emitter spatial resonance condition.

In general, random carrier capture can lead to the occupation of bright and dark neutral exciton states within the QD. Formation of a dark state limits the ability of a SPS to emit single photons at higher repetition rates. In fact, while QD lifetimes down to about 50 ps have been measured and SPS have been triggered with GHz repetition rates, measured single photon count rates are typically limited to the kHz regime. We have recently demonstrated that utilization of negatively charged excitons can further improve the performance of SPS since formation of dark states will be suppressed to some degree. To this end we have developed a novel trench design allowing to introduce oxide tapered apertures as well as an electrical gate in close proximity to the active QD layer within a microcavity structure [6]. Applying a bias voltage to the back gate increases the QD emission by a factor of five. Utilizing negatively instead of neutral

978-1-4244-1932-6/08/$25.00 ©2008 IEEE

excitons improved the single photon count rate by another factor of three. In culmination, these effects contribute to a measured record high rate of single photons on demand up to 31 MHz, and promise rates above 116 MHz as probed by cw experiments [6]. We have furthermore achieved an on-chip voltage-control of the spectral resonance condition between mode and emitter as well as an on-chip control of the emitted linear polarization state of the single photons.

References:

[1] A.J. Shields, *Semiconductor quantum light sources*, Nature Photonics **1**, 215 (2007), and references therein.

[2] Strauf, S., K. Hennessy, M.T. Rakher, Y.-S. Choi, A. Badolato, L.C. Andreani, E.L. Hu, P.M. Petroff, and D. Bouwmeester, *Self-tuned quantum dot gain in photonic crystal lasers*. *Phys. Rev. Lett.* **96**, 127404 (2006).

[3] N. G. Stoltz, M. Rakher, S. Strauf, A. Badolato, D.D. Lofgreen, P.M. Petroff, L.A. Coldren, and D. Bouwmeester; *High-quality factor optical microcavity using oxide apertured micropillars,* Appl. Phys. Lett. **87**, 031105 (2005).

[4] N. G. Stoltz, M. Rakher, S. Strauf, D. Bouwmeester, P. M. Petroff, and L. A. Coldren, *Quantum Dot Spontaneous Emission Lifetime Modification in Optical Microcavities using Oxide Apertured Micropillars,* Proc. SPIE **6101**, 61010W, (2006).

[5] M. T. Rakher, S. Strauf, Y. Choi, N.G. Stolz, K.J. Hennessey, H. Kim, A. Badolato, L.A. Coldren, E.L. Hu, P.M. Petroff, D. Bouwmeester, *Cavity QED with quantum dots in semiconductor microcavities,* Proc. SPIE **6481**, 648109 (2007)

[6] S. Strauf, N.G. Stoltz, M.T. Rakher, L.A. Coldren, P.M. Petroff, and D. Bouwmeester, *High-frequency single photon source with polarization control*, Nature Photonics **1**, 704 (2007).